Antiferromagnetic nanodiscs with perpendicular magnetic anisotropy for biological applications

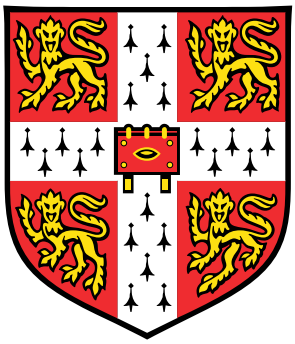

Emma Nicola Welbourne

Supervisor: Prof. R. P. Cowburn

Department of Physics
University of Cambridge

This dissertation is submitted for the degree of
Doctor of Philosophy

Sidney Sussex College

December 2020

Declaration

I hereby declare that except where specific reference is made to the work of others, the contents of this dissertation are original and have not been submitted in whole or in part for consideration for any other degree or qualification in this, or any other University. This dissertation is the result of my own work and includes nothing which is the outcome of work done in collaboration, except where specifically indicated in the text. This dissertation contains fewer than 65,000 words including appendices, bibliography, footnotes, tables and equations and has less than 150 figures.

Emma Nicola Welbourne
December 2020

Abstract

Magnetic particles have been widely implemented across research areas in liquid and biological environments, such as cancer therapy, drug delivery and cell sorting. Perpendicularly magnetised (PM) synthetic antiferromagnetic (SAF) particles exhibit a range of desirable properties that make them strong candidates for applications in fluid. These include a zero remanence state, sharp and tunable switching, and a high and variable saturation magnetisation.

This thesis will first continue to explore the flexibility of the SAF particle design. Through engineering of the SAF thin film, the basis of the particles, this work demonstrates the ability to tune the SAFs towards a suite of applications. In addition, a novel take on the fabrication of thin film based magnetic nanoparticles is presented. This method is capable of efficient and effective production of particularly high yields of well-defined nanodiscs with robust magnetic properties.

The magnetic behaviour of the PM SAF particles, and the thin films they are created from, is analysed with particular focus on the characteristics displayed in a fluidic environment. This leads to the discovery of novel magneto-mechanical transitions of SAF particles in liquid and continues to demonstrate the applicability of SAFs across a spectrum of applications.

Application of the PM SAF particles is examined in the context of cancer therapy. Previous studies into SAFs in cancer therapy utilised them in the magneto-mechanical destruction of tumour cells. Leading on from this work, the concept of integrating SAF microdiscs with iron oxide nanoparticles (IONPs) in a 'magnetic combination therapy' is explored. This preliminary study reveals interesting inter-particle interactions between the SAFs and IONPs and shows the potential for a synergistic effect in the combined therapy.

This work provides a robust toolbox for the fabrication of tailored nanodiscs for use in a range of fluidic and biological applications.

Acknowledgements

First of all I would like to thank Prof. Russell Cowburn, for giving me the opportunity to do a PhD, and for all of the support and guidance over the last few years. His research group has been a fantastic place to learn and work. Special mentions go out to the shrimp tank, after lunch crossword sessions, and of course, cake Monday.

I would particularly like to thank Dr. Tarun Vemulkar for passing on all of his knowledge, from the growth of a (nearly) perfect SAF to the intricacies of handling Bertha. His help and advice over the course of my PhD has been invaluable. I'd also like to show my appreciation to Dr. Dorothée Petit, for all of her input over the years, and especially for her patience over the last few months.

Thank you to all of my Cambridge friends, for absolutely making my time here. I must also mention the wonderful community of SSBC: all of the early mornings were very much worth it, as rowing has gifted me with some of my best memories of Cambridge.

Finally, my biggest thanks go out to my family—Mum, Dad, Kerry and Alex—for their unwavering support. My parents have no doubt played a massive part in me getting where I am today, and I am forever grateful for their belief in me. And my husband, Alex, has been there for me every step of the way, providing me with the wisdom, guidance and faith that I absolutely couldn't have achieved this without.

Contents

Nomenclature

Acronyms / Abbreviations

β	Degree of ferrimagnetism
H_C	Coercive field
H_J	Coupling field
H_K	Anisotropy field
J	Exchange coupling energy
J/Kt	Coupling to anisotropy ratio
K	Effective anisotropy
M_S	Saturation magnetisation
t_{Pt}	Pt interlayer thickness
AC	Alternating current
AF	Antiferromagnetic
AFM	Atomic force microscope
AP	Anti-parallel
DC	Direct current
dex	Dextran
EA	Easy axis
EBL	Electron beam lithography
EC	Exchange coupling
FM	Ferromagnetic
FWHM	Full width half maximum
HFLF	High frequency, low field

HMCL	Hole-mask colloidal lithography
HP	Hard plane
IONPs	Iron oxide nanoparticles
IP	In plane
MCA	Magnetocrystalline anisotropy
MDs	Microdiscs
MMD	Magneto-mechanical destruction
MOKE	Magneto-optical Kerr effect
MV	Magnetic-vortex
NIL	Nanoimprint lithography
NSCs	Neural stem cells
NSL	Nanosphere lithography
OM	Optical microscopy
OOP	Out of plane
P	Parallel
PM	Perpendicular anisotropy
PMA	Perpendicular magnetic anisotropy
PS	Polystyrene
PSDF	Power spectral density function
Py	Permalloy
RKKY	Ruderman-Kittel-Kasuya-Yosida
RMS	Root mean squared
RT	Room temperature
SAF	Synthethic antiferromagnetic
SAR	Specific absorption rate
SEM	Scanning electron microscopy
SFi	Synthetic ferrimagnetic

SPIONs	Superparamagnetic iron oxide nanoparticles
SQUID	Superparamagnetic quantum interference device
SRHF	Slow rotation, high field
SRT	Spin reorientation transition
VSM	Vibrating sample magnetometry

Chapter 1

Introduction

1.1 Magnetic particles in biological applications

Simple superparamagnetic, paramagnetic and ferromagnetic nanoparticles have been employed across a diverse array of applications in the field of biology [47, 48]. These types of particle are fabricated via colloidal chemistry, or the dispersion of powders or flakes derived from macroscopic materials [21], which offer controllable sizing and scalability for commercialisation. Their relatively simple magnetic states give rise to a selection of particle properties that have been exploited by a spectrum of applications, including zero remanence states and tunable moments. One branch of research makes use of the inherent ability of the particles to respond to an external magnetic field, in technologies such as cell separation, bio-molecule isolation and purification [23, 37, 46, 47, 51]. These particles have also been employed in medical imaging, primarily with superparamagnetic iron oxide nanoparticles (SPIONs) as magnetic resonance imaging contrast agents [45], but also more recently in the novel modality of magnetic particle imaging [17], where the direct mapping of magnetic material is used to generate images. SPIONs are also well-established in the field of cancer therapy, as agents in magnetic hyperthermia [50], where the cytotoxic heating of cells is induced via the heating of the particles under the application of high frequency AC magnetic fields. Another branch of research into the use of magnetic particles in biological applications exploits the ability to magnetically actuate the particles and hereby apply forces to soft matter systems. This property is employed in a range of techniques, for the manipulation of cells and other biological molecules, in areas including tissue engineering and drug delivery [13, 48].

1.1.1 Remote control of soft matter systems

Magnetic particles offer a powerful tool to remotely control and manipulate specific components of a soft matter system, through the application of external magnetic fields. Additionally, the coupling of the field to the particles is possible regardless of intervening structures (e.g. biological tissue), which is a distinct advantage for *in vivo* applications. Nanomagnetic actuation offers particularly high levels of precision:

by coupling magnetic nanoparticles with functional molecules (e.g. antibodies) it is possible to target, manipulate and activate individual ion channels or surface receptors on specific cells [13]. This method is also capable of exerting higher torques than other strategies [16], with simple tunablility through the strength of the applied field. These characteristics lend the concept to a suite of different applications across biomedical and biotechnology research areas: from the investigation of cellular functions, to soft robotic devices, to the development of novel medical treatments.

The work in this field was pioneered by investigations into the rheological properties of cellular cytoplasm under an applied stress [12, 22, 55]. Later on, research was expanded into the concept of magnetic 'twisting' [57–59], employing magnetic particles to exert torques, which launched the exciting prospect of noninvasive probing of cellular activity and mechanics. Since then, this concept has been developed such that it has been possible to bind magnetic particles to individual integrin receptors on the cellular membrane and quantify the mechanical properties of the cytoskeleton [42, 65, 66] (see Figure 1.1(a)).

Progress in magnetic actuation methods has lead to a series of alternative methods, which employ high-gradient magnetic fields that lead to the exertion of translational forces rather than torques. One example of this is the indirect activation of mechanosensitive ion channels [3, 4, 18, 19, 52] (see Figure 1.1(b)). This was achieved again through the attachment of magnetic particles to membrane receptors. The application of a high-gradient magnetic field then induces a deformation of the cell membrane, which activates nearby stretch-gated ion channels. The possibility of directly activating specific ion channels has also been shown using a similar methodology (see Figure 1.1(c)). Here, a magnetic particle (generally sub micron sized) must make a direct attachment with the ion channel itself, which is achieved via an appropriate antibody. That ion channel can then be activated by applying a magnetic force to the particle [27]. The third high-gradient field method of magnetic actuation requires the use of smaller magnetic particles, which can be attached to receptor complexes in the cell membrane (see Figure 1.1(d)). It is then possible to promote receptor clustering by applying a focused, high-gradient field [41], which triggers a specific intracellular signaling pathway [38].

1.1.2 Magnetic actuation in biomedicine and biotechnology

All of these techniques highlight the unique opportunity that magnetic actuation offers for the examination of the mechanical and kinetic properties of soft matter systems, as well as for the potential to control system components and processes, including specific cellular signaling pathways [13, 48]. In biomedicine, one way that magnetic actuation has been implemented is in applications in tissue engineering and regenerative medicine. There has been particular success in the directed differentiation of mesenchymal stem cells, where it has been shown that mechanical cues are particularly

important in generating bone, muscle and connective tissue [68]. Subsequent studies of one group have employed the indirect and direct activation of ion channels to stimulate tissue growth, stimulate intracellular calcium stores, change membrane potential, upregulate genes related to bone and cartilage formation, and initiate and promote bone matrix mineralisation [15, 25–27, 32, 56]. The same research group has since had similar success with magneto-mechanically controlled differentiation of bone marrow stromal cells [24, 28], which possess a high potency for evolving into or repairing other tissues due to their greater range of plasticity [5, 11, 20]. Overall, this research has strong implications in the development of personalised therapeutics, for the growth of functional replacement tissue from a patient's own cells, either *ex vivo* or *in vivo* [13].

Another therapeutic application uses the localised torques exerted via magnetic particles to destroy cancer cells. The pioneering work employed permalloy magnetic vortex microdiscs (MDs) [31], engineered to possess a zero remanence state to prevent particle agglomeration, which could limit effective dispersion across a population of

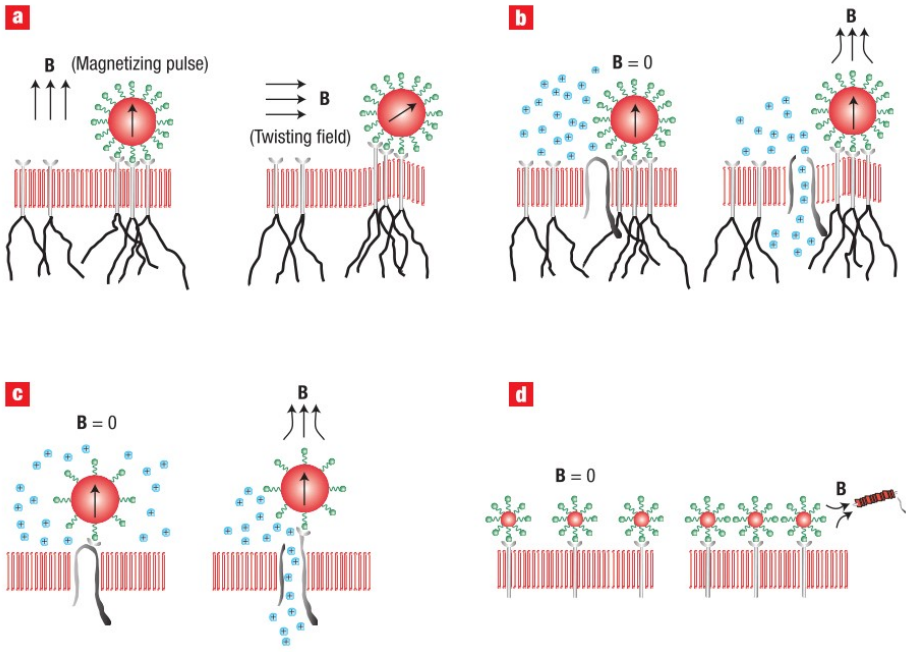

Figure 1.1: Figure taken from [13]. A schematic representation of different types of magnetic particle actuation methods for cells. (a) The magnetic twisting cytometry. Magnetic microparticles are functionalised against integrin receptors on the cell membrane, which are linked to actin filaments (black lines). A magnetising pulse, followed by an orthogonal 'twisting field' induces a torque on the system. (b) Activation of mechanosensitive ion-channels. Receptor bound magnetic microparticles are 'pulled' under the application of a high-gradient magnetic field, deforming the cell membrane and activating adjacent mechanosensitive ion channels. (c) Targeted ion-channel activation. Magnetic nanoparticles are attached directly to ion-channels via antibodies. The application of a high-gradient magnetic field pulls the particle and forces the channel open. (d) Receptor clustering. Magnetic nanoparticles are bound to receptor complexes, which are spaced across the membrane surface. The application of a high-gradient magnetic field causes the receptors to cluster near to the field source, which can trigger intracellular signaling.

cells, but could also lead to the clogging of blood vessels if this therapy was applied through injection into the blood stream [14]. The MDs were taken up by tumour cells and actuated via the application of an oscillating magnetic field, which caused them to transmit a force. It was suggested that the mechanical disruption caused by the MDs both compromised the integrity of the cell membranes and affected the ionic exchange of mechanosensitive channel, which triggered programmed cell death in tumour cells. This method has also been translated by our research group to an *in vivo* model, generating significant brain tumour reduction and increased survival rate in mice [10]. This type of cancer therapy overcomes a lot of the challenges presented by the more heavily researched magnetic hyperthermia, including the non-specificity of the effect leading to the potential damage of healthy tissue [14, 48].

Outside of biomedicine, remotely controlled magnetic actuation strategies offer appealing solutions to a wide range of soft matter applications. This includes a selection of biotechnologies, which are being driven towards lab-on-chip style of devices. An example of this is the mixing of reagents in micro fluidic devices. On the macroscale, mixing is often achieved via magnetic stirrers. On the microscale, turbulent mixing offers somewhat of a challenge [60], meaning that an additional stimulus is required to mix reagents. Magnetic particles have been shown to provide this in the form of valves, mixers and pistons [40, 54]. Another application is magnetic transport, e.g. the magnetically directed movement of catalytic nanomotors [8, 33], where the ability to control the directionality and speed of components of a soft matter system offers considerable promise in a variety of biotechnologies [64]. The technique of magnetic labeling has also seen widespread implementation across biological research, with extensions to the sensing, separation, isolation and purification of specific biological entities from either liquid suspensions or their native environment [47, 48, 63]. Here, applied magnetic fields, often with some type of gradient, are employed to capture or measure the particles and in turn the components they are tagging. Finally, static and dynamic assemblies of magnetic particles offer novel types of magneto-mechanical actuation. These assemblies may be generated by functional linkers, a polymer matrix or inherent magnetic interactions. In particular, dynamic self-assemblies of magnetic particles, tuned by the application of external magnetic fields, is of interest to applications such as soft robotics, microfluidic mechanical devices, assembly of complex architectures and the organisation of soft matter systems [67].

1.2 Antiferromagnetically coupled particles with perpendicular magnetic anisotropy

1.2.1 Drawing from magnetic memory technologies

In developing a novel type of particle for use in biological applications, the group's research looked to the fields of magnetic memory and spintronics, where more complex

magnetic systems are employed. These systems are created through the engineering of multilayer heterostructure thin films, which offer key magnetic properties that can be manipulated for specific technologies based around magnetic actuation.

Thin films with perpendicular magnetic anisotropy (PMA), an interfacial effect originating from spin-coupling interactions between layers of ferromagnetic (FM) and heavy metal materials (e.g. Co and Pt) [7], have proved to be an important area of research from the perspective of technological applications. PMA tends to be strong, which means that the energy barrier that prevents a FM bit from thermally switching its magnetic configuration is high, hence providing relatively stable states for the storage of information. The strength of PMA also makes it more robust to downscaling, making it possible to manufacture devices with sub-40 nm bit sizes. This is the lower limit for bits fabricated from in-plane magnetic materials, as these rely on shape anisotropy, which is dependent on the magnetisation volume [30]. Strong PMA induces narrow domain walls, and these domain walls propagate with high velocities [43]. These properties have been exploited in hard drive discs [9], and domain wall logic and memory architectures [1].

Antiferromagnetic (AF) interlayer exchange coupling, driven by an Ruderman-Kittel-Kasuya-Yosida (RKKY) interaction [29, 53, 69], can be used to create synthetic antiferromagnetic (SAF) thin films that exhibit a zero remanence state [6]. The presence of this state means that SAFs have an extinguishable magnetostatic stray field and are less susceptible to effects arising from a non-zero demagnetising field [35]. This has lead to SAF films being introduced into magnetic memory research for the development of data storage devices with higher thermal stability. In particular, they have seen use in in-plane spin-valve read heads [35]. Furthermore, the SAF configuration has been shown to increase the reversal field of the hard layer in PMA based magnetic tunnel junctions, as well as minimising dipolar interactions between storage and reference layers, thus improving thermal stability and data retention times [2]. SAF architectures with PMA have also shown potential in memory logic devices such as those that exploit domain wall motion [49] and three dimensional shift registers [34].

1.2.2 Highly tunable, remotely actuated magnetic particles

Perpendicularly magnetised (PM) SAFs offer a selection of desirable characteristics that could be exploited in the field of biomedicine, particularly in applications that involve mechanical actuation [62]. By combining a top-down lithography process with the PM SAF thin films, a new family of planar magnetic particles with strong uniaxial anisotropy and tunable properties was created. The planar discs with PMA offer a unique system for the control of particle orientation with an applied magnetic field, which is efficient at transducing torque because of its uniaxial symmetry. The RKKY coupling induces a zero remanence state, which prevents magnetic aggregation outside of applied fields. Crucially, the magnitude of the PMA and RKKY coupling are tunable through the adjustment of the thin film structure and are not affected by the particle

shape. Furthermore, it is relatively straightforward to increase the magnetic moment of the thin film system without compromising the magnetic properties, through repeating the PM SAF bilayer motif [62]. Overall these particles present as strong candidates for applications such as magnetic sorting and actuation of biological systems.

An investigation into PM SAF microdiscs (MDs) in liquid, under the influence of a uniaxial magnetic field, revealed some novel magneto-mechanical behaviours. Here, the additional degree of freedom, in the form of physical orientation, gives the MDs the ability to minimise their energy through accessing different parts of the easy axis and hard plane saturation processes through mechanical rotations. In a liquid suspension of MDs, this lead to the formation of dynamic, reconfigurable magnetic chains [61]. These types of behaviour are potentially interesting for applications in areas such as soft robotics and the dynamic self-assembly of complex architectures.

PM SAF MDs have also have been demonstrated as strong candidates in the magneto-mechanical destruction of tumour cells under the application of a low frequency, high strength rotating magnetic field [36, 39, 44]. It has been shown that they offer a more effective therapeutic effect than magnetic vortex MDs, due to their uniaxial anisotropy [39]. Additionally, a study into a potential combination therapy found a synergistic effect between the application of PM SAF MDs and radiotherapy. Specifically, the gold-coated MDs both radiosensitised the cancer cells, acting as intracellular emitters of secondary electrons, as well as providing their characteristic mechanical damage through exertion of torque [36].

1.3 Thesis aims

The goal of this thesis is to build on the pioneering research that has developed PM SAF particles and begun to investigate how they may be manipulated and exploited. We highlight the ability to engineer the properties of magnetic particles and discuss how this can be highly advantageous across a range of biological applications, particularly those involving mechanical actuation. We also characterise our particles extensively in a liquid environment, to gain understanding of their behaviour and how it might be of interest to a number of applications. Overall, this work provides a robust toolbox for the fabrication of tailored magnetic nanodiscs, to be employed by a spectrum of biotechnology and biomedical applications.

Initially we will cover an in depth study of PM multilayer heterostructures and continue to explore the flexibility of the AF coupled system, in particular through the exploitation of tunable RKKY coupling. We engineer an assortment of these thin films, demonstrating their variation in magnetic hysteresis and discussing their interest to specific applications. Moving on to the patterning of these films, we will present a novel take on the fabrication of planar nanoparticles. Here, we show that this method is capable of efficiently producing particularly high yields of well-defined nanodiscs, without compromising our carefully engineered magnetic properties.

An investigation into the behaviour of PM AF coupled discs in liquid suspen-

sions, under the influence of a magnetic field, leads to the discovery of novel magneto-mechanical transitions. We study how the design of our thin film can affect the configurations and transitions exhibited by the particles. Furthermore, we reveal variation in how the particles behave with a dependence on measurement parameters, such as field sweep rate.

Finally, we examine a specific application of our PM SAF particles, in the area of cancer therapy. We put forward the concept of a 'magnetic combination' cancer treatment, integrating the magneto-mechanical destruction effect of PM SAFs with magnetic hyperthermia via iron oxide nanoparticles. Our preliminary study presents interesting inter-particle interactions between the two particle types and indicates potential for an effective combined therapy.

References

[1] D. A. Allwood, G. Xiong, C. C. Faulkner, D. Atkinson, D. Petit, and R. P. Cowburn. Magnetic domain-wall logic. *Science*, 309(5741):1688–1692, sep 2005.

[2] S. Bandiera, R. C. Sousa, Y. Dahmane, C. Ducruet, C. Portemont, V. Baltz, S. Auffret, I. L. Prejbeanu, and B. Dieny. Comparison of Synthetic Antiferromagnets and Hard Ferromagnets as Reference Layer in Magnetic Tunnel Junctions With Perpendicular Magnetic Anisotropy. *IEEE Magnetics Letters*, 1:3000204–3000204, 2010.

[3] Andreas R. Bausch, Ulrike Hellerer, Markus Essler, Martin Aepfelbacher, and Erich Sackmann. Rapid Stiffening of Integrin Receptor-Actin Linkages in Endothelial Cells Stimulated with Thrombin: A Magnetic Bead Microrheology Study. *Biophysical Journal*, 80(6):2649–2657, jun 2001.

[4] Andreas R. Bausch, Winfried Möller, and Erich Sackmann. Measurement of Local Viscoelasticity and Forces in Living Cells by Magnetic Tweezers. *Biophysical Journal*, 76(1):573–579, jan 1999.

[5] Paolo Bianco, Mara Riminucci, Stan Gronthos, and Pamela Gehron Robey. Bone Marrow Stromal Stem Cells: Nature, Biology, and Potential Applications. *Stem Cells*, 19(3):180–192, may 2001.

[6] P. Bruno. Theory of interlayer exchange interactions in magnetic multilayers. *Journal of Physics Condensed Matter*, 11(48):9403–9419, 1999.

[7] Patrick Bruno. Tight-binding approach to the orbital magnetic moment and magnetocrystalline anisotropy of transition-metal monolayers. *Physical Review B*, 39(1):865–868, 1989.

[8] Jared Burdick, Rawiwan Laocharoensuk, Philip M. Wheat, Jonathan D. Posner, and Joseph Wang. Synthetic Nanomotors in Microchannel Networks: Directional

Microchip Motion and Controlled Manipulation of Cargo. *Journal of the American Chemical Society*, 130(26):8164–8165, jul 2008.

[9] Claude Chappert, Albert Fert, and Frédéric Nguyen Van Dau. The emergence of spin electronics in data storage. *Nature Materials*, 6(11):813–823, nov 2007.

[10] Yu Cheng, Megan E. Muroski, Dorothée C.M.C. Petit, Rhodri Mansell, Tarun Vemulkar, Ramin A. Morshed, Yu Han, Irina V. Balyasnikova, Craig M. Horbinski, Xinlei Huang, Lingjiao Zhang, Russell P. Cowburn, and Maciej S. Lesniak. Rotating magnetic field induced oscillation of magnetic particles for in vivo mechanical destruction of malignant glioma. *Journal of Controlled Release*, 223:75–84, feb 2016.

[11] Michael Chopp and Yi Li. Treatment of neural injury with marrow stromal cells. *The Lancet Neurology*, 1(2):92–100, jun 2002.

[12] F.H.C. Crick and A.F.W. Hughes. The physical properties of cytoplasm. *Experimental Cell Research*, 1(1):37–80, 1950.

[13] Jon Dobson. Remote control of cellular behaviour with magnetic nanoparticles. *Nature Nanotechnology*, 3(3):139–143, mar 2008.

[14] Jon Dobson. Cancer therapy: A twist on tumour targeting. *Nature Materials*, 9(2):95–96, 2010.

[15] Jon Dobson, Sarah H. Cartmell, Ahmed Keramane, and Alicia J. El Haj. Principles and design of a novel magnetic force mechanical conditioning bioreactor for tissue engineering, stem cell conditioning, and dynamic in vitro screening. *IEEE Transactions on Nanobioscience*, 5(3):173–177, 2006.

[16] Randall M. Erb, Joshua J. Martin, Rasam Soheilian, Chunzhou Pan, and Jabulani R. Barber. Actuating Soft Matter with Magnetic Torque. *Advanced Functional Materials*, 26(22):3859–3880, 2016.

[17] Bernhard Gleich and Jürgen Weizenecker. Tomographic imaging using the nonlinear response of magnetic particles. *Nature*, 435(7046):1214–1217, 2005.

[18] M. Glogauer, J. Ferrier, and C. A. McCulloch. Magnetic fields applied to collagen-coated ferric oxide beads induce stretch-activated Ca2+ flux in fibroblasts. *American Journal of Physiology-Cell Physiology*, 269(5):C1093–C1104, nov 1995.

[19] Michael Glogauer and J. Ferrier. A new method for application of force to cells via ferric oxide beads. *Pflügers Archiv*, 435(2):320, 1997.

[20] Joanna E. Grove, Emanuela Bruscia, and Diane S. Krause. Plasticity of Bone Marrow-Derived Stem Cells. *Stem Cells*, 22(4):487–500, jul 2004.

[21] S. P. Gubin, Yu A. Koksharov, G. B. Khomutov, and G. Yu Yurkov. Magnetic nanoparticles: Preparation, structure and properties. *Uspekhi Khimii*, 74(6):539–574, 2005.

[22] A Heilbronn. Eine neue methode zur bestimmung der viskosität lebender protoplasten. *Jahrb. Wiss. Bot.*, 61(284), 1922.

[23] Wolf K. Hofmann, Sven De Vos, Martina Komor, Dieter Hoelzer, William Wachsman, and H. Phillip Koeffler. Characterization of gene expression of CD34 + cells from normal and myelodysplastic bone marrow. *Blood*, 100(10):3553–3560, 2002.

[24] Bin Hu, Jon Dobson, and A J El Haj. Control of smooth muscle α-actin (SMA) up-regulation in HBMSCs using remote magnetic particle mechano-activation. *Nanomedicine: Nanotechnology, Biology, and Medicine*, 10(1):45–55, 2014.

[25] Bin Hu, A J El Haj, and Jon Dobson. Receptor-targeted, magneto-mechanical stimulation of osteogenic differentiation of human bone marrow-derived mesenchymal stem cells. *International Journal of Molecular Sciences*, 14(9):19276–19293, 2013.

[26] Steven Hughes, Jon Dobson, and Alicia J. El Haj. Magnetic targeting of mechanosensors in bone cells for tissue engineering applications. *Journal of Biomechanics*, 40:S96–S104, jan 2007.

[27] Steven Hughes, Stuart McBain, Jon Dobson, and A J El Haj. Selective activation of mechanosensitive ion channels using magnetic particles. *Journal of the Royal Society, Interface / the Royal Society*, 5(25):855–63, 2008.

[28] J M Kanczler, H S Sura, J Magnay, D Green, R O Oreffo, J P Dobson, and A J El Haj. Controlled differentiation of human bone marrow stromal cells using magnetic nanoparticle technology. *Tissue Eng Part A*, 16(10):3241–3250, 2010.

[29] Tadao Kasuya. A Theory of Metallic Ferro- and Antiferromagnetism on Zener's Model. *Progress of Theoretical Physics*, 16(1):45–57, 1956.

[30] Andrew D. Kent and Daniel C. Worledge. A new spin on magnetic memories. *Nature Nanotechnology*, 10(3):187–191, 2015.

[31] Dong-Hyun Kim, Elena a Rozhkova, Ilya V Ulasov, Samuel D Bader, Tijana Rajh, Maciej S Lesniak, and Valentyn Novosad. Biofunctionalized magnetic-vortex microdiscs for targeted cancer-cell destruction. *Nature materials*, 9(2):165–71, feb 2010.

[32] G R Kirkham, K J Elliot, M Knight, A Keramane, B Akhtar, D M Salter, J Dobson, A J El Haj, and S H Cartmell. Electrophysiological responses of HMSCs and bone cells to magnetic particle tagging. *Tissue Engineering*, 13:1684, 2007.

[33] Timothy R. Kline, Walter F. Paxton, Thomas E. Mallouk, and Ayusman Sen. Catalytic Nanomotors: Remote-Controlled Autonomous Movement of Striped Metallic Nanorods. *Angewandte Chemie International Edition*, 44(5):744–746, jan 2005.

[34] Reinoud Lavrijsen, Ji Hyun Lee, Amalio Fernández-Pacheco, Dorothée C.M.C. Petit, Rhodri Mansell, and Russell P. Cowburn. Magnetic ratchet for three-dimensional spintronic memory and logic. *Nature*, 493(7434):647–650, 2013.

[35] J. L. Leal and M. H. Kryder. Spin valves exchange biased by Co/Ru/Co synthetic antiferromagnets. *Journal of Applied Physics*, 83(7):3720–3723, 1998.

[36] Selma Leulmi Pichot, Sabrina Bentouati, Saif S. Ahmad, Marios Sotiropoulos, Raj Jena, and Russell Cowburn. Versatile magnetic microdiscs for the radio enhancement and mechanical disruption of glioblastoma cancer cells. *RSC Advances*, 10(14):8161–8171, 2020.

[37] Paul A. Liberti, Chandra G. Rao, and Leon W.M.M. Terstappen. Optimization of ferrofluids and protocols for the enrichment of breast tumor cells in blood. *Journal of Magnetism and Magnetic Materials*, 225(1-2):301–307, jan 2001.

[38] Robert J. Mannix, Sanjay Kumar, Flávia Cassiola, Martín Montoya-Zavala, Efraim Feinstein, Mara Prentiss, and Donald E. Ingber. Nanomagnetic actuation of receptor-mediated signal transduction. *Nature Nanotechnology*, 3(1):36–40, jan 2008.

[39] Rhodri Mansell, Tarun Vemulkar, Dorothée C. M. C. Petit, Yu Cheng, Jason Murphy, Maciej S. Lesniak, and Russell P. Cowburn. Magnetic particles with perpendicular anisotropy for mechanical cancer cell destruction. *Scientific Reports*, 7(1):4257, 2017.

[40] James E. Martin and Kyle J. Solis. Quantifying vorticity in magnetic particle suspensions driven by symmetric and asymmetric multiaxial fields. *Soft Matter*, 11(36):7130–7142, 2015.

[41] Benjamin D. Matthews, David A. Lavan, Darryl R. Overby, John Karavitis, and Donald E. Ingber. Electromagnetic needles with submicron pole tip radii for nanomanipulation of biomolecules and living cells. *Applied Physics Letters*, 85(14):2968–2970, 2004.

[42] Christian J. Meyer, Francis J. Alenghat, Paul Rim, Jenny Hwai-Jen Fong, Ben Fabry, and Donald E. Ingber. Mechanical control of cyclic AMP signalling and gene transcription through integrins. *Nature Cell Biology*, 2(9):666–668, sep 2000.

[43] T. A. Moore, I. M. Miron, G. Gaudin, G. Serret, S. Auffret, B. Rodmacq, A. Schuhl, S. Pizzini, J. Vogel, and M. Bonfim. High domain wall velocities

induced by current in ultrathin Pt/Co/AlOx wires with perpendicular magnetic anisotropy. *Applied Physics Letters*, 93(26):262504, dec 2008.

[44] Megan E. Muroski, Ramin A. Morshed, Yu Cheng, Tarun Vemulkar, Rhodri Mansell, Yu Han, Lingjiao Zhang, Karen S. Aboody, Russell P. Cowburn, and Maciej S. Lesniak. Controlled Payload Release by Magnetic Field Triggered Neural Stem Cell Destruction for Malignant Glioma Treatment. *PLOS ONE*, 11(1):e0145129, jan 2016.

[45] Tobias Neuberger, Bernhard Schöpf, Heinrich Hofmann, Margarete Hofmann, and Brigitte von Rechenberg. Superparamagnetic nanoparticles for biomedical applications: Possibilities and limitations of a new drug delivery system. *Journal of Magnetism and Magnetic Materials*, 293(1):483–496, may 2005.

[46] O Osman, S Toru, F Dumas-Bouchiat, N M Dempsey, N Haddour, L-F Zanini, F Buret, G Reyne, and M Frénéa-Robin. Microfluidic immunomagnetic cell separation using integrated permanent micromagnets. *Biomicrofluidics*, 7(5):54115, jan 2013.

[47] QA A Pankhurst, J Connolly, S K Jones, and J Dobson. Applications of magnetic nanoparticles in biomedicine. *Journal of Physics D-Applied Physics*, 36(13):R167–R181, 2003.

[48] Quentin A. Pankhurst, N. T. K. Thanh, S. K. Jones, and Jon Dobson. Progress in applications of magnetic nanoparticles in biomedicine. *Journal of Physics D: Applied Physics*, 42(22):224001, nov 2009.

[49] S. S.P. Parkin, N. More, and K. P. Roche. Oscillations in exchange coupling and magnetoresistance in metallic superlattice structures: Co/Ru, Co/Cr, and Fe/Cr. *Physical Review Letters*, 64(19):2304–2307, 1990.

[50] E. A. Périgo, G. Hemery, O. Sandre, D. Ortega, E. Garaio, F. Plazaola, and F. J. Teran. Fundamentals and advances in magnetic hyperthermia. *Applied Physics Reviews*, 2(4):041302, dec 2015.

[51] Jochen F. Peter, Angela M. Otto, and Bernhard Wolf. Magnetic particles as Powerful Purification Tool for High Sensitive Mass Spectrometric Screening Procedures. *Proteomics*, 2009.

[52] H Pommerenke, E Schreiber, F Dürr, B Nebe, C Hahnel, W Möller, and J Rychly. Stimulation of integrin receptors using a magnetic drag force device induces an intracellular free calcium response. *European journal of cell biology*, 70(2):157–164, jun 1996.

[53] M A Ruderman and C Kittel. Indirect Exchange Coupling of Nuclear Magnetic Moments by Conduction Electrons. *Physical Review*, 96(1):99–102, oct 1954.

[54] T. Sawetzki, S. Rahmouni, C. Bechinger, and D. W. M. Marr. In situ assembly of linked geometrically coupled microdevices. *Proceedings of the National Academy of Sciences*, 105(51):20141–20145, dec 2008.

[55] William Seifriz. An Elastic Value of Protoplasm, with Further Observations on the Viscosity of Protoplasm. *Journal of Experimental Biology*, 2(1):1 LP – 11, oct 1924.

[56] H S Sura, J Magnay, J Dobson, and A J El Haj. Gene expression in stem cells following stimulation using magnetic particle technology. *Tissue Eng*, 13:1699, 2007.

[57] P.A. Valberg and J.P. Butler. Magnetic particle motions within living cells. Physical theory and techniques. *Biophysical Journal*, 52(4):537–550, oct 1987.

[58] P.A. Valberg and H.A. Feldman. Magnetic particle motions within living cells. Measurement of cytoplasmic viscosity and motile activity. *Biophysical Journal*, 52(4):551–561, oct 1987.

[59] Peter A. Valberg and David F. Albertini. Cytoplasmic motions, rheology, and structure probed by a novel magnetic particle method. *Journal of Cell Biology*, 101(1):130–140, 1985.

[60] Alexander van Reenen, Arthur M. de Jong, Jaap M. J. den Toonder, and Menno W. J. Prins. Integrated lab-on-chip biosensing systems based on magnetic particle actuation - a comprehensive review. *Lab Chip*, 14(12):1966–1986, 2014.

[61] T. Vemulkar, E. N. Welbourne, R. Mansell, D. C. M. C. Petit, and R. P. Cowburn. The mechanical response in a fluid of synthetic antiferromagnetic and ferrimagnetic microdiscs with perpendicular magnetic anisotropy. *Applied Physics Letters*, 110(4):042402, 2017.

[62] T Vemulkar, R Mansell, D C M C Petit, R P Cowburn, and M S Lesniak. Highly tunable perpendicularly magnetized synthetic antiferromagnets for biotechnology applications. *Applied Physics Letters*, 107(1):012403, jul 2015.

[63] Elina A Vitol, Valentyn Novosad, and Elena A Rozhkova. Microfabricated magnetic structures for future medicine: from sensors to cell actuators. *Nanomedicine*, 7(10):1611–1624, 2012.

[64] Joseph Wang and Kalayil Manian Manesh. Motion Control at the Nanoscale. *Small*, 6(3):338–345, feb 2010.

[65] N. Wang, J.P. P Butler, and D.E. E Ingber. Mechanotransduction across the cell surface and through the cytoskeleton. *Science (New York, N.Y.)*, 260(5111):1124–1127, 1993.

[66] Ning Wang and Donald E. Ingber. Probing transmembrane mechanical coupling and cytomechanics using magnetic twisting cytometry. *Biochemistry and Cell Biology*, 73(7-8):327–335, jul 1995.

[67] George M. Whitesides. Self-Assembly at All Scales. *Science*, 295(5564):2418–2421, mar 2002.

[68] Malcolm Wright, Paresh Jobanputra, Charles Bavington, Donald M. Salter, and George Nuki. Effects of Intermittent Pressure-Induced Strain on the Electrophysiology of Cultured Human Chondrocytes: Evidence for the Presence of Stretch-Activated Membrane Ion Channels. *Clinical Science*, 90(1):61–71, jan 1996.

[69] Kei Yosida. Magnetic Properties of Cu-Mn Alloys. *Physical Review*, 106(5):893–898, jun 1957.

Chapter 2

Theory and background

2.1 Theory

This section discusses some of the theory that underpins the experimental results in this thesis. We first focus on the two key phenomena of our thin films: interfacial perpendicular magnetic anisotropy and Ruderman-Kittel-Kasuya-Yoshida coupling. We then go on to outline the macrospin model that will be used to understand the magnetic reversal of our perpendicularly magnetised, synthetic antiferromagnetic systems.

2.1.1 Perpendicular magnetic anisotropy

The multilayer thin films grown and studied in this work all exhibit perpendicular magnetic anisotropy (PMA). This is a uniaxial, interfacial anisotropy, which causes the magnetisation of ferromagnetic (FM) layers to orient perpendicular to the plane of the thin film.

Magnetocrystalline anisotropy

Magnetocrystalline anisotropy (MCA) encompasses the energy contribution from the atomic structure and bonding in a FM material. It generates hard and easy axes of magnetisation, meaning that it takes more or less energy to magnetise the material in certain directions. It was theorised that the origin of MCA, in cubic FM crystals, was spin-orbit coupling [1]. This is a relativistic effect, where the spin dipole magnetic moment of the electrons couples with the magnetic field generated by their orbital motion. In turn, this induces a small orbital momentum, which couples the magnetic moment to the crystal axes [13]. There is therefore a strong connection between the MCA energy and the orientation of the orbitals, or magnetisation, relative to the crystal axes, which reflects the symmetry of the crystal [7, 13]. At the interface of a FM material there is a lowered symmetry, which strongly modifies the MCA compared with the bulk. This generates a partial quenching of the angular momentum, causing the out of plane (OOP) orbitals to dominate and yielding a so-called interface anisotropy [2].

PMA in CoFeB/Pt thin films

A dominant interfacial anisotropy may be induced in thin films when they are grown below a critical thickness, known as the spin reorientation transition (SRT) [21, 28]. The volume contribution of the anisotropy (K_V) in a thin film originates from dipolar interactions and favours in plane (IP) magnetisation. This is referred to as shape anisotropy, as it the result a demagnetising energy term that is associated with sample shape [20]. Conversely, the interfacial contribution to the anisotropy (K_S), from the MCA discussed above, favours a normal alignment of the magnetisation to the surface of a thin film. The thin films studied in this thesis are all $Co_{60}Fe_{20}B_{20}$/Pt multilayer heterostructures. Here, symmetry breaking at the interface between the Co and the Pt, enhanced by hybridisation of the Co 3d and Pt 5d orbitals [10, 12, 15], induces the PMA.

The effective anisotropy, K_{eff}, of the thin film system obeys [13]:

$$K_{eff} = K_V + 2K_S/t \tag{2.1}$$

Here, K_V is negative and K_S is positive such that $K_{eff} < 0$ gives IP magnetisation and $K_{eff} > 0$ gives PMA. As t represents the thickness of the FM layer, in the case of ultrathin films K_{eff} is dominated by K_S, leading to PMA. This happens below the SRT, when there are relatively few bulk atoms, causing the atoms at the interface to dominate the behaviour of the film. This effect has been documented previously in Co/Pt [6, 8, 21] and CoFeB/Pt [28] thin films. The angle dependent energy density in an applied field is a combination of the anisotropy (1st term) and Zeeman (2nd term, originating from the alignment of the magnetisation with the field) contributions:

$$E = \left(K_i - 2\pi M_S^2\right)\sin^2\theta - M_S H cos(\alpha - \theta) \tag{2.2}$$

where θ and α denote the angles subtended by the magnetisation and field, respectively, and the film normal, and K_i is the intrinsic anisotropy (including the interfacial and bulk contribution). The magnetostatic energy contribution, $2\pi M_S^2$ (where M_S is saturation magnetisation) arises from the demagnetising field, which favours an IP magnetisation. The effective anisotropy of the thin film is thus:

$$K_{eff} = K_i - 2\pi M_S^2 \tag{2.3}$$

For PMA, where $K_{eff} > 0$, this gives $K_i > 2\pi M_S^2$.

Experimentally, magnetic anisotropy is extracted from hard plane (HP) magnetisation measurements. For our CoFeB/Pt thin films, which exhibit strong PMA, we obtain a value of K_{eff} from the HP saturation field, or anisotropy field $H_K = 2K_{eff}/M_S$ [13]. Using equation 2.1 we can also then use HP saturation field to measure the interfacial contribution to the anisotropy, K_S. A plot of $K_{eff}t$ versus t gives a linear relationship that, upon extrapolation to $t = 0$, yields $2K_S$.

2.1.2 Ruderman-Kittel-Kasuya-Yoshida coupling

A large proportion of the thin films in this thesis utilise antiferromagnetic (AF) interlayer exchange coupling (EC) between pairs of FM layers through a non-magnetic space layer. We engineer this into our CoFeB/Pt multilayer heterostructures via an AF Ruderman-Kittel-Kasuya-Yoshida (RKKY) type coupling layer: an interlayer of Ru sandwiched between the FM CoFeB pairs.

The manifestation of RKKY coupling

The microscopic origin of this phenomenon was initially studied by Ruderman and Kittel, who theorised the EC of nuclear magnetic moments of atoms in a metal by means of the hyperfine interaction with the surrounding conduction electrons [3]. Kasuya [4] and Yosida [5] went on to explain the interaction between conduction electrons and unfilled inner shell electrons, the $s-d$ interaction, in a transition metal and its implication in the EC of FM materials. This RKKY interaction is an indirect EC because it does not involve any direct coupling between magnetic moments: a localised magnetic moment spin-polarises the conduction electrons, which in turn couples to a neighbouring localised magnetic moment a distance r away [20]. The r-dependent EC coefficient, $J(r)$, is given by:

$$J(r) \propto \frac{\cos(2k_F r)}{r^3} \tag{2.4}$$

at large r, where k_F is the Fermi wavevector. The EC thus manifests as oscillatory with r (going back and forth between FM and AF in character) and of decreasing strength as r increases

We can extend the treatment of two localised spins to two FM layers with a uniform areal spin distribution separated by a non-magnetic metal layer in the z direction [14]. The EC coefficient from one layer on the next is then J_{12}, and at large z it is represented by:

$$J_{12} \propto \frac{\sin(2k_F z)}{z^2} \tag{2.5}$$

This relationship represents an oscillating spin density of conduction electrons in the non-magnetic spacer layer [22], which generates the EC between the two adjacent FM layers. Hence, the EC between two FM layers may be FM or AF in nature, and is mediated by the thickness of the non-magnetic spacer.

Quantification of RKKY coupling

In our thin films with PMA, where we have two FM layers AF coupled via the RKKY interaction, the additional energy term per unit area is described by [17]:

$$E(\theta) = J\cos(\theta_2 - \theta_1) \tag{2.6}$$

where J is the RKKY coupling energy per unit area, and θ_1 and θ_2 are the angles between the FM layer magnetisations and the EA of the film. J may also be represented as an effective coupling field between two FM layers, H_J:

$$J = H_J M_S t \tag{2.7}$$

where t is the thickness of the layer that is being acted on (although for this discussion the two FM layers will be of the same thickness). At remanence, a pair of RKKY coupled FM layers exhibit an anti-parallel (AP) configuration, where their layer magnetisations point in opposite directions. At a critical field (applied along the EA), called the saturation field (H_S), the moments switch into a parallel (P) configuration, such that both layer moments align with the field direction. In the case of non-coercive switching, the saturation field is the coupling field (see Figure 2.1a). Experimentally, H_J may be extracted from a measurement of the minor loop of the thin film, which corresponds with the magnetic reversal of the softer of the two FM layers (even if the layers are nominally grown identical, they will not be so experimentally). In a real, coercive system, the effective coupling field on the softer layer from the magnetisation of the harder layer, H_J, is determined as the field by which the minor loop is shifted (see Figure 2.1b). The saturation field is $H_S = H_J + H_C$, where H_C is the coercive field [27].

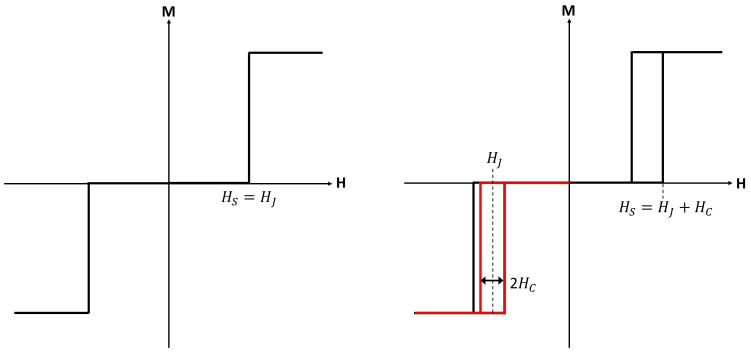

(a) Non-coercive (b) Coercive

Figure 2.1: Schematics of the (a) non-coercive and (b) coercive EA M-H response, with critical fields noted.

2.1.3 Zero temperature macrospin model

In this thesis, investigations into the behaviour of magnetic systems with PMA and AF coupling through simulations were conducted using a zero temperature macrospin model. Coercivity was not included in the model, making it an absolute energy minimum model [9]. We found the absolute minimum of the system for each value of applied field using Monte Carlo simulated annealing, this method allows the exploration of multilayer systems without a dramatic increase in computation time and memory requirements. From this, we generated minimum energy diagrams and corresponding magnetic hysteresis loops for easy, hard and global (mechanically unconstrained)

saturation processes. The global responses provided key insight into the magneto-mechanical behaviour of our magnetic particle systems.

Schematics of our bilayer system of two AF coupled FM layers with PMA are shown in Figure 2.2. The thicknesses of the FM layers, M_1 and M_2, are t_1 and t_2 respectively. The layer magnetisations form the angles θ_1 and θ_2 with the EA. In order to simulate the fluidic environment, we allow the system to rotate freely, such that its EA can be at any angle, α, to the applied field, H. As all of the thin films grown in this work use the same magnetic material for both FM layer (CoFeB), we assume that M_S is the same for both layers. For our system, we write the total energy per unit area as a summation of the PMA, AF EC and Zeeman energy contributions:

$$E = \begin{array}{cc} K_1 t_1 \sin^2(\theta_1) + K_2 t_2 \sin^2(\theta_2) & PMA \\ +J\cos(\theta_2 - \theta_1) & EC \\ -HM_S\left[t_1\cos(\alpha-\theta_1) + t_2\cos(\alpha-\theta_2)\right] & Zeeman \end{array} \tag{2.8}$$

The effective anisotropies, K_1 and K_2, of each FM layer with PMA are assumed to be equal and are extracted from the saturation field (H_{Sat}) of the HP thin film measurement. The HP saturation process ($\alpha = \frac{\pi}{2}$), as illustrated in Figure 2.3a, occurs via the canting of the two FM layers towards the field direction. To achieve saturation, the system must overcome both the anisotropy field (H_K) and the effective coupling field (H_J) such that $H_{Sat} = H_K + 2H_J$, where $H_K = 2K/M_S$. As the bilayer systems we study all undergo EA saturation via the spin-flip regime (see below), we can extract H_J from a minor loop of the thin film EA response, as is described in Section 2.1.2. From this, we can calculate the RKKY coupling energy per unit area, J, using the relationship $J = H_J M_S t$ where t is the average thickness of the two FM layers.

The EA saturation process ($\alpha = 0$) of an AF coupled system depends on the ratio between anisotropy and EC. The spin-flip regime (see Figure 2.3b) is a single stage process that presents in a system where $K > J/2t$ [9, 11]. It is characterised by a direct switch of the AF coupled layer moments from the AP ($\theta_1 = 0$, $\theta_2 = \pi$) to the P ($\theta_1 = \theta_2 = 0$) configuration. In a non-coercive system, this switch occurs when the

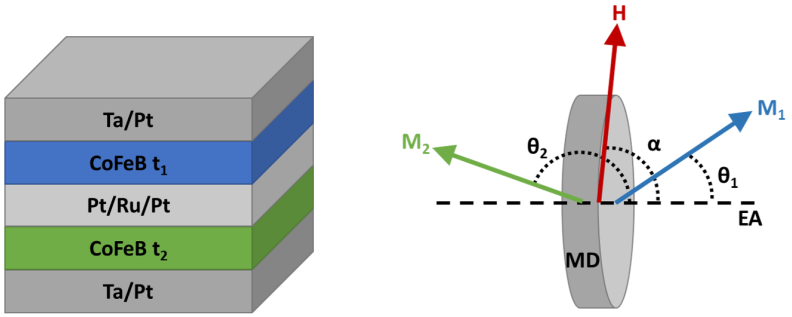

(a) Stack schematic (b) Bilayer system

Figure 2.2: Schematics of (a) the thin film structure and (b) the bilayer system for a magnetic disc (MD) with an EA and AF coupled FM layers.

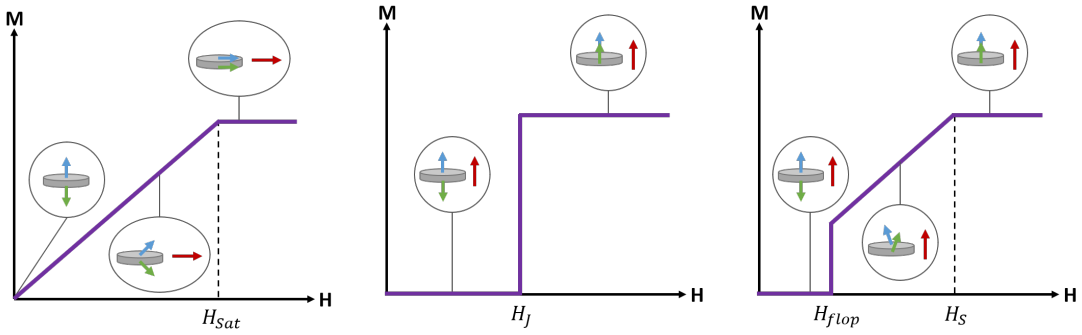

(a) HP (b) Spin-flip (c) Spin-flop

Figure 2.3: The (a) HP saturation process, and (b) spin-flip and (c) spin-flop EA saturation processes. The arrows represent layer moment and field directions, analogously to the scheme in 2.2b.

applied field is equal to H_J. A spin-flop regime manifests when $K < J/2t$ and is a two step transition process [9, 11] (see Figure 2.3c). The first step of the transition occurs at the critical field $H_{flop} = \frac{2}{M_S}\sqrt{K(K + \frac{J}{t})}$: the FM layers go from the 0, π AP configuration to a θ, $-\theta$ alignment with the field. The second step occurs at the saturation field $H_S = \frac{2}{M_S}(K + \frac{J}{t})$: the layer moments rotate continuously until they reach the P configuration.

2.2 Background

The development of perpendicularly magnetised (PM), synthetic antiferromagnetic (SAF) particles for the use in biomedical and biotechnology applications has been pioneered by researchers in the Cowburn group. The work presented in this thesis builds on the innovation and discoveries that had previously been accomplished. This section is dedicated to reviewing the published work from the group in this research area.

2.2.1 PM SAF microdiscs — the particle architecture

Thin film design

Vemulkar et al determined that PM SAF thin films, with their more complex magnetic behaviour than traditionally used superparamagnetic nanoparticles, offered some highly desirable properties for biological applications [35]. The motif of the magnetic multilayer stack used in this work is shown in Figure 2.4a and is described by $Ta/Pt/CoFeB/Pt/Ru/Pt/CoFeB/Pt$. A polar magneto-optical Kerr effect (MOKE) easy axis (EA) hysteresis loop of a single bilayer of this form is shown in Figure 2.4b.

SAF films are characterised by a zero remanence state (the apparent non-zero magnetisation at remanence is Figure 2.4b is due to the depth dependence of the MOKE signal), which is generated by RKKY coupling of the magnetic layers through a Ru interlayer, as discussed in Section 2.1.2. This is a crucial property in biological or other

liquid applications as it prevents magnetic particles from agglomerating and maintains their stability in solution. The low susceptibility of the system under low fields is also useful here: particles with high susceptibility have been shown to stay agglomerated after the application of an applied field [25, 32]. The sharp switch to full magnetisation allows efficient access to the saturation moment. Furthermore, by tuning the strength of the RKKY coupling through the thickness of the Pt interlayers (either side of the Ru) it is possible to tune the switching field [28]. This provides greater flexibility for tailoring towards applications such as sorting and purification [29]. The film is also characterised by strong PMA, and hence an EA of magnetisation. This is generated by interfacial spin-orbit interactions between the CoFeB and Pt layers, as discussed in Section 2.1.1. This property allows an effective transduction of torque from a rotating magnetic field.

For applications that utilise the transduction of mechanical force via magnetic particles, maximising the total magnetic moment of the particles is important. Vemulkar et al demonstrated that it is possible to increase the magnetic moment of a PM SAF film simply by stacking up repeats of the bilayer motif. Figure 2.4c schematically shows the composition of a 12 times repeated bilayer and the resulting easy axis EA vibrating sample magnetometry (VSM) loop is shown in Figure 2.4d. There is no degradation in the saturation magnetisation or significant change in the layer anisotropy. The switch to saturation occurs by a more slanted transition. This due to slight variation in the RKKY coupling across the individual bilayers, as well as an increase in magnetostatic interactions and domain formation [23, 24]. Nevertheless, the overall hysteresis is sim-

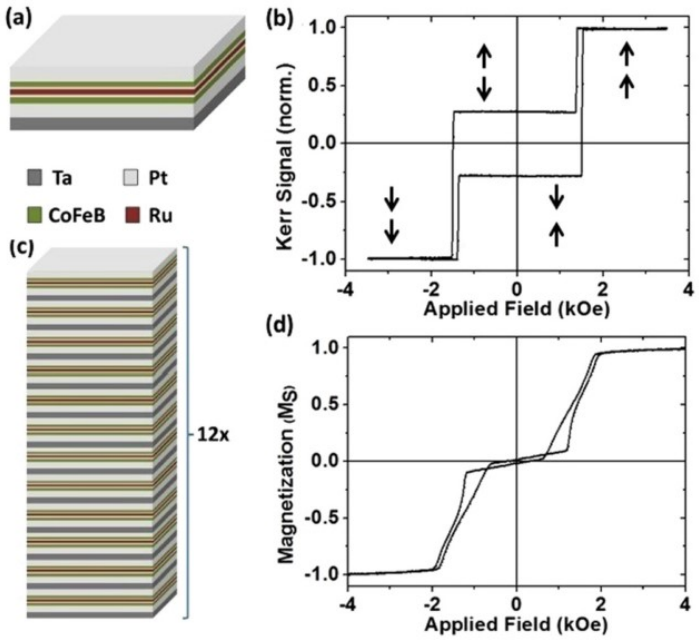

Figure 2.4: Figure and caption taken from [35]. (a) The single coupled bilayer motif. (b) Polar MOKE hysteresis loop of the single bilayer. The arrows show the magnetisation direction of each CoFeB layer perpendicular to the plane of the film. (c) The multilayer stack used to create the magnetic particles, where the basic motif is stacked 12 times. (d) VSM easy axis hysteresis loop of the 12 repeat motif multi- layer stack.

ilar to that of a single bilayer, with the desirable PM SAF properties conserved.

Translation into microdiscs

To fabricate magnetic microdiscs (MDs) from a PM SAF film, Vemulkar et al employed a simple optical lithography method: the multilayer stack was sputtered on top of silicon substrates that had been patterned with 2 μm diameter photoresist pillars [35]. The MDs were then released into solution by dissolving the pillars with acetone. Characterisation of the MDs on substrate (released and redeposited) by polar MOKE loop reveals a very similar magnetic response to that the nominally identical thin film, as shown in Figure 2.5a. Furthermore, a VSM measurement of a liquid suspension of the MDs, as shown in Figure 2.5b, demonstrates that the key PM SAF properties translate well into water [35].

This work illustrates PM SAFs as strong candidates for use in biological applications, with their range of desirable characteristics and the advantage of precise tunability of a number of key parameters.

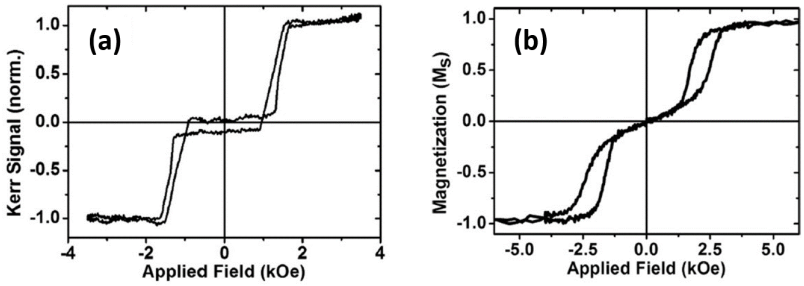

Figure 2.5: Figure adapted from [35]. (a) Polar MOKE hysteresis loop of a single particle. (b) VSM hysteresis loop of the particles in water.

2.2.2 PM SAF transitions in liquid

The suspension of magnetic particles in a fluid environment provides them with an additional degree of freedom: the ability to move. This alters the energy landscape of single particles, which induces changes in their magnetic response, and gives them the possibility to form inter-particle interactions, which leads to magnetic self-assembly. Work by Vemulkar et al probed the specific behaviour exhibited by PM SAFs upon subjection to a uniaxial magnetic field sequence [39]. This work lead to the emergence of novel magneto-mechanical transitions, which manifested via the mechanical rotations of particles as they accessed magnetic saturation processes that minimise their energy. Furthermore, it revealed the formation of dynamic, reconfigurable magnetic chains.

Experimental results

Vemulkar et al began the investigation into the behaviour of PM AF coupled particles in liquid, under applied fields, with a study of SAF MDs [39]. Here, the magnetic layers are balanced such that the system exists in a net zero moment AP state in zero field.

A set of 2 μm discs was fabricated from a SAF thin film of the form $[Ta(2)/Pt(2)]_3/[Ta(2)/Pt(2)/CoFeB(1.2)/Pt(0.5)/Ru(0.9)/Pt(0.5)/CoFeB(1.2)/Pt(2)]_2/Ta(2)/[Pt(2)/Ta(2)]_3$, with thicknesses in nm [39]. The liquid VSM response of these MDs suspended in water is shown in Figure 2.6a. The magnetic saturation process was found to be characterised by a linear response at low fields, followed by a distinct switch to saturation. Optical microscopy (OM) images of the MD suspension under applied fields are displayed in Figures 2.6b–2.6d. It was discovered that these particles exhibit three distinct regimes, manifesting through different configurations relative to the field direction, which lead to dynamic self-assembly behaviour [39].

Firstly, in a very low field regime, as seen in Figure 2.6b, the particles are randomly oriented with respect to the field and are well dispersed: the induced moment in the MDs is negligible due to the AF coupling. Next, as the field is increased to a value corresponding with the linear response in the hysteresis, the discs mechanically rotate and align their HP parallel to the field direction (see Figure 2.6c). They also begin to form edge-to-edge assemblies in chains along the field direction. Finally, as the field is increased such that it exceeds the saturation field the particles undergo an abrupt 90° rotation, which aligns their EAs parallel with the field direction (see Figure 2.6d) In

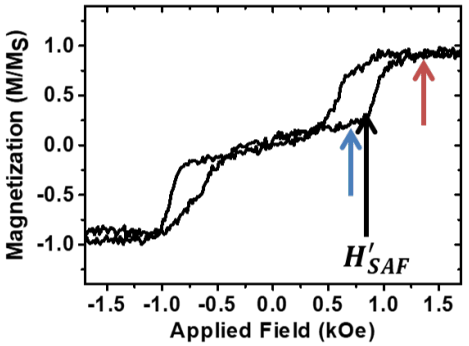

(a) Discs in liquid

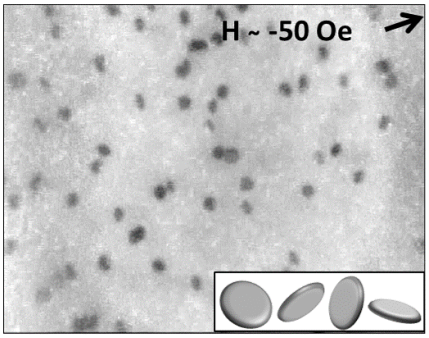

(b) -50 Oe

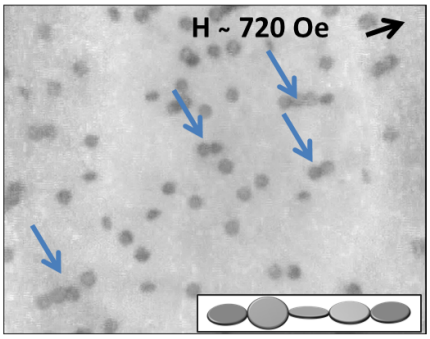

(c) 720 Oe

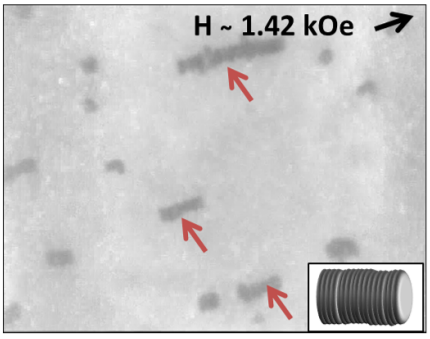

(d) 1420 Oe

Figure 2.6: Figure adapted from [39]. (a) The liquid VSM loop of the SAF MDs in water. The particle saturation field, H'_{SAF}, is indicated by the black arrow. 100× OM images of the SAF disc suspension under applied fields of (b) ~ -50 Oe, (c) ~ 720 Oe and (d) ~ 1.42 kOe (field direction in plane, as indicated by the black arrows). The blue and red arrows in (a) indicate the fields in (c) and (d) respectively. The inset schematics depict the particle configurations.

this saturated regime, the chains snap together such that the discs are in a face-to-face configuration.

Simulations

Vemulkar et al simulated the response of a single SAF disc in liquid, under the influence of a uniaxial magnetic field, by utilising the macrospin model outlined in Section 2.1.3. This revealed the magneto-mechanical behaviour behind the transitions observed in the experimental work [39].

Figure 2.7 shows the energy and magnetisation plots for the EA, HP and rotationally unconstrained global responses of a SAF system, as generated by the simulation. Along the EA, saturation is achieved via a spin-flip transition, whereas the HP saturation process occurs via the canting of the two layer moments towards the HP direction.

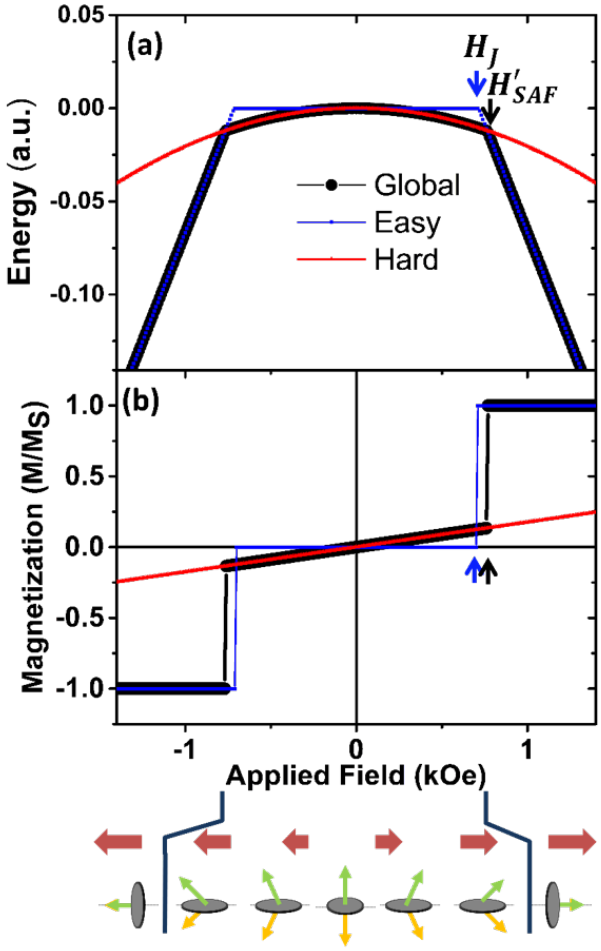

Figure 2.7: Figure taken from [39]. (a) Minimum energy curves along the EA (blue), HP (red) and global (black) for a SAF system with the magnetic parameters extracted from the film in Figure 2.6. (b) The corresponding simulated hysteresis loops for each response type. Below, a schematic depicts the orientation of an individual disc and its layer moments (green and yellow arrows) with respect to the applied field (red arrows). The blue and black arrows indicate the coupling field, H_J, and critical SAF field, H'_{SAF}, respectively.

The global energy response forms a superposition of the EA and HP processes, with its path following that of the minimum energy. At low fields, the HP process has the lower energy, which induces a torque on the particles to align their HP with the field [16, 18], reflecting the particle configuration found in Figure 2.5c. As the field rises, the layer moments continuously cant towards the HP, as they would in a HP saturation process. At a critical field, H'_{SAF}, the EA process becomes the lower in energy. This causes the discs to abruptly rotate 90° into the configuration found in Figure 2.5d, as the layer moments simultaneously flip into a parallel state with each other, the EA and the field. These magneto-mechanical transitions lead to the reconfiguration of the disc chains as they interact via dipolar coupling [39]. The behaviour demonstrated by this work is potentially interesting for applications in the fields of soft robotics, fluid-based micro- and nanodevices and dynamic self-assembly.

2.2.3 Magnetic particles in mechanical cancer cell destruction

Magnetic-vortices and in-plane SAFs

The use of magnetic particles in the magneto-mechanical destruction of cancer cells was first demonstrated with magnetic-vortex (MV) permalloy (Py) MDs by Kim et al [26]. Here, $\sim$ 90% cancer cell destruction was achieved through two key effects: compromising the integrity of cellular membranes and initiation of programmed cell death. Further research on this topic includes: the triggering of apoptosis in renal cancer cells through the vibration of cell membrane attached MV MDs [34], and the *in vivo* destruction of malignant glioma through the oscillation of MV MDs in a rotating magnetic field [36].

Leulmi et al compared the potential of MV MDs with in-plane SAF MDs for the purpose of biological applications [32]. The in-plane (IP) SAFs that were considered in this work were formed by antiferromagnetically coupling a pair of Py layers. This study concluded that, in principle, the IP SAF particles could produce larger torques, which would make them more efficient in the destruction of cancer cells. However, IP SAFs were deemed more challenging to produce than MV particles and moreover, they have been found to exhibit self-polarisation under certain conditions [25, 32] (see Section 6.4.1 for more details).

PM SAFs

PM SAFs were first implemented into a cancer therapy on malignant glioma cells by Muroski et al in a collaboration with the Cowburn lab [37]. Here, the 12 times bilayer stack patterned into 2 μm discs, as developed by Vemulkar et al [35], was employed. Neural stem cells (NSCs) have been shown to be promising candidates for the targeted delivery of therapeutics to cancers, because of their inherent tumour-tropic migratory behaviour [19]. The delivery of nanoparticles has previously been applied to

several cancer types, including malignant gliomas [30, 31, 33]. However, limitations of stem cell delivery of nanoparticles include the inefficiency of drug release and inability to remotely trigger a timed release. Accordingly, the study by Muroski et al first demonstrated the magnetic field triggered destruction of NSCs: PM SAF MDs that had been internalised by the NSCs were remotely triggered by a 1 T rotating magnetic field, rupturing the cell membranes and releasing the MDs. They then showed that the glioma cells were also able to internalise the MDs, which indicates the potential for efficient drug delivery. A second dose of the magnetic field treatment was then determined to induce apoptosis, through the rotation of the MDs, which lead to over 50% of glioma cell death.

Mansell et al demonstrated the effectiveness of PM SAF MDs, in comparison with MV MDs, at transducing torque and at inducing death of glioblastoma cells [38]. Both types of MD were created with a diameter of 2 μm, with the PM SAFs being nominally the same as that described in [35]. The particles have some similar magnetic properties: both characterised by a zero remanence state and they have similar HP saturation fields. However, their magnetic anisotropies exhibit crucially different symmetries: the PM SAFs have an easy out-of-plane magnetisation axis, while the MV MDs have an easy magnetisation plane. This leads to a significant difference in behaviour under the application of a rotating magnetic field, as is shown schematically in Figure 2.8, which subsequently causes a substantial difference in the effectiveness of torque application between the two particles. In an *in vitro* study, the glioblastoma cells were incubated with each type of particle and then subjected to a 1 T rotating field. The MV MDs killed just 12% of cells, while the PM SAF MDs were able to kill 62% [38]. This shows that, despite the fact that MV MDs were capable of a much larger maximum torque [38], it is the symmetry considerations that are key to effective magneto-mechanical destruction.

Most recently, Leulmi et al implemented PM SAF MDs in a combination cancer therapy [40]. This study demonstrated the MDs as enhancers of the traditional radiotherapy method, on top of their induction of mechanical damage via exertion of torque.

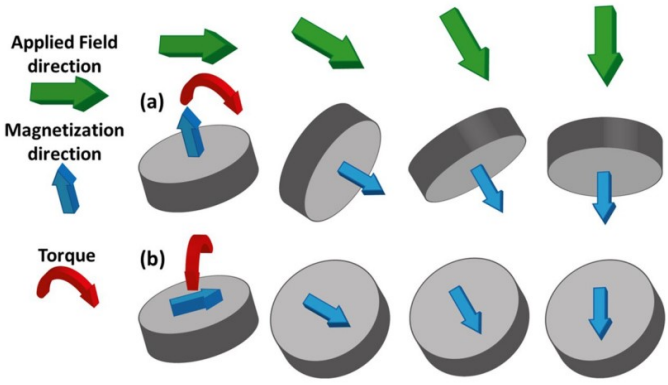

Figure 2.8: Figure taken from [38]. Schematic showing the magnetisation direction and torques on (a) PM SAF particles and (b) MV particles under an applied rotating field.

A large increase in DNA damage and reduction in glioblastoma colony formation was found for cells that had been incubated with the MDs, in comparison to conventional radiotherapy, which indicates that the MDs play a synergistic role in enhancing the killing of tumour cells with radiotherapy. This could make it possible to use lower energy radiation sources, which are required for intra-opertaive therapy and also desirable for minimising negative effects to healthy tissue, without compromising the therapeutic effect. With their additional ability to damage cancer cells mechanically, MDs offer an attractive platform for a potentially highly effective cancer therapy.

References

[1] J. H. Van Vleck. On the anisotropy of cubic ferromagnetic crystals. *Physical Review*, 52(11):1178–1198, 1937.

[2] Louis Néel. Anisotropie magnétique superficielle et surstructures d'orientation. *Journal de Physique et le Radium*, 15(4):225–239, 1954.

[3] M A Ruderman and C Kittel. Indirect Exchange Coupling of Nuclear Magnetic Moments by Conduction Electrons. *Physical Review*, 96(1):99–102, oct 1954.

[4] Tadao Kasuya. A Theory of Metallic Ferro- and Antiferromagnetism on Zener's Model. *Progress of Theoretical Physics*, 16(1):45–57, 1956.

[5] Kei Yosida. Magnetic Properties of Cu-Mn Alloys. *Physical Review*, 106(5):893–898, jun 1957.

[6] P. F. Carcia. Perpendicular magnetic anisotropy in Pd/Co and Pt/Co thin-film layered structures. *Journal of Applied Physics*, 63(10):5066–5073, may 1988.

[7] Patrick Bruno. Tight-binding approach to the orbital magnetic moment and magnetocrystalline anisotropy of transition-metal monolayers. *Physical Review B*, 39(1):865–868, 1989.

[8] S. Hashimoto, Y. Ochiai, and K. Aso. Perpendicular magnetic anisotropy and magnetostriction of sputtered Co/Pd and Co/Pt multilayered films. *Journal of Applied Physics*, 66(10):4909–4916, 1989.

[9] B. Dieny and J P Gavigan. Minimum energy versus metastable magnetisation processes in antiferromagnetically coupled ferromagnetic multilayers. *J. Phys.:Condens. Matter*, 2(1):187–194, 1990.

[10] D. Weller, H. Brändle, and C. Chappert. Relationship between Kerr effect and perpendicular magnetic anisotropy in Co1-xPtx and Co1-xPdx alloys, 1993.

[11] P. J. H. Bloemen, H. W. van Kesteren, H. J. M. Swagten, and W. J. M. de Jonge. Oscillatory interlayer exchange coupling in Co/Ru multilayers and bilayers. *Physical Review B*, 50(18):13505–13514, nov 1994.

[12] D. Weller, Y. Wu, J. Stöhr, M. G. Samant, B. D. Hermsmeier, and C. Chappert. Orbital magnetic moments of Co in multilayers with perpendicular magnetic anisotropy. *Physical Review B*, 49(18):12888–12896, may 1994.

[13] M T Johnson, P J H Bloemen, F J A den Broeder, and J J de Vries. Magnetic anisotropy in metallic multilayers. *Reports on Progress in Physics*, 59(11):1409–1458, 1996.

[14] J A C Bland. Chapter 15 Ultrathin magnetic structures-magnetism and electronic properties. In D A King and D P B T The Chemical Physics of Solid Surfaces Woodruff, editors, *Growth and Properties of Ultrathin Epitaxial Layers*, volume 8, pages 583–634. Elsevier, 1997.

[15] N Nakajima, T Koide, T Shidara, H Miyauchi, H Fukutani, A Fujimori, K Iio, T Katayama, M Nývlt, and Y Suzuki. Perpendicular Magnetic Anisotropy Caused by Interfacial Hybridization via Enhanced Orbital Moment in Co/Pt Multilayers: Magnetic Circular X-Ray Dichroism Study. *Physical Review Letters*, 81(23):5229–5232, dec 1998.

[16] Jian Gang Zhu, Youfeng Zheng, J. G. Zhu, and Y. Zheng. Characteristics of AP bias in spin valve memory elements. *IEEE Transactions on Magnetics*, 34(4 PART 1):1063–1065, 1998.

[17] P. Bruno. Theory of interlayer exchange interactions in magnetic multilayers. *Journal of Physics Condensed Matter*, 11(48):9403–9419, 1999.

[18] Jian Gang Zhu. Spin valve and dual spin valve heads with synthetic antiferromagnets. *IEEE Transactions on Magnetics*, 35(2 PART 1):655–660, 1999.

[19] K S Aboody, A Brown, N G Rainov, K A Bower, S Liu, W Yang, J E Small, U Herrlinger, V Ourednik, P M Black, X O Breakefield, and E Y Snyder. Neural stem cells display extensive tropism for pathology in adult brain: evidence from intracranial gliomas. *Proceedings of the National Academy of Sciences of the United States of America*, 97(23):12846–12851, nov 2000.

[20] S Blundell. *Magnetism in Condensed Matter*. Oxford UNiversity Press, Oxford, UK, 2001.

[21] M. Kisielewski, A. Maziewski, M. Tekielak, A. Wawro, and L. T. Baczewski. New possibilities for tuning ultrathin cobalt film magnetic properties by a noble metal overlayer. *Physical Review Letters*, 89(8):087203/1–087203/4, 2002.

[22] J Stöhr and H C Siegmann. *Magnetism: From Fundamentals to Nanoscale Dynamics*. Springer Berlin Heidelberg, Berlin, Heidelberg, 2006.

[23] V Baltz, A Bollero, B Rodmacq, B Dieny, J.-P. Jamet, and J Ferré. Multilevel magnetic nanodot arrays with out of plane anisotropy: the role of intradot magnetostatic coupling. *The European Physical Journal - Applied Physics*, 39(1):33–38, 2007.

[24] Olav Hellwig, Andreas Berger, Jeffrey B. Kortright, and Eric E. Fullerton. Domain structure and magnetization reversal of antiferromagnetically coupled perpendicular anisotropy films. *Journal of Magnetism and Magnetic Materials*, 319(1-2):13–55, dec 2007.

[25] H. Joisten, T. Courcier, P. Balint, P. Sabon, J. Faure-Vincent, S. Auffret, and B. Dieny. Self-polarization phenomenon and control of dispersion of synthetic antiferromagnetic nanoparticles for biological applications. *Applied Physics Letters*, 97(25):253112, 2010.

[26] Dong-Hyun Kim, Elena a Rozhkova, Ilya V Ulasov, Samuel D Bader, Tijana Rajh, Maciej S Lesniak, and Valentyn Novosad. Biofunctionalized magnetic-vortex microdiscs for targeted cancer-cell destruction. *Nature materials*, 9(2):165–71, feb 2010.

[27] Volume 62. In R E Camley and R L Stamps, editors, *Solid State Physics*. Academic Press, 2011.

[28] R. Lavrijsen, A. Fernández-Pacheco, D. Petit, R. Mansell, J. H. Lee, and R. P. Cowburn. Tuning the interlayer exchange coupling between single perpendicularly magnetized CoFeB layers. *Applied Physics Letters*, 100(5):052411, jan 2012.

[29] Elina A Vitol, Valentyn Novosad, and Elena A Rozhkova. Microfabricated magnetic structures for future medicine: from sensors to cell actuators. *Nanomedicine*, 7(10):1611–1624, 2012.

[30] Yu Cheng, Ramin Morshed, Shih-Hsun Cheng, Alex Tobias, Brenda Auffinger, Derek A Wainwright, Lingjiao Zhang, Catherine Yunis, Yu Han, Chin-Tu Chen, Leu-Wei Lo, Karen S Aboody, Atique U Ahmed, and Maciej S Lesniak. Nanoparticle-programmed self-destructive neural stem cells for glioblastoma targeting and therapy. *Small (Weinheim an der Bergstrasse, Germany)*, 9(24):4123–4129, dec 2013.

[31] Xinglu Huang, Fan Zhang, Hui Wang, Gang Niu, Ki Young Choi, Magdalena Swierczewska, Guofeng Zhang, Haokao Gao, Zhe Wang, Lei Zhu, Hak Soo Choi, Seulki Lee, and Xiaoyuan Chen. Mesenchymal stem cell-based cell engineering with multifunctional mesoporous silica nanoparticles for tumor delivery. *Biomaterials*, 34(7):1772–1780, feb 2013.

[32] S. Leulmi, H. Joisten, T. Dietsch, C. Iss, M. Morcrette, S. Auffret, P. Sabon, and B. Dieny. Comparison of dispersion and actuation properties of vortex and

synthetic antiferromagnetic particles for biotechnological applications. *Applied Physics Letters*, 103(13):132412, 2013.

[33] Rachael Mooney, Yiming Weng, Revathiswari Tirughana-Sambandan, Valerie Valenzuela, Soraya Aramburo, Elizabeth Garcia, Zhongqi Li, Margarita Gutova, Alexander J Annala, Jacob M Berlin, and Karen S Aboody. Neural stem cells improve intracranial nanoparticle retention and tumor-selective distribution. *Future Oncology*, 10(3):401–415, feb 2014.

[34] Selma Leulmi, Xavier Chauchet, Melissa Morcrette, Guillermo Ortiz, Hélène Joisten, Philippe Sabon, Thierry Livache, Yanxia Hou, Marie Carrière, Stéphane Lequien, and Bernard Dieny. Triggering the apoptosis of targeted human renal cancer cells by the vibration of anisotropic magnetic particles attached to the cell membrane. *Nanoscale*, 7(38):15904–15914, 2015.

[35] T Vemulkar, R Mansell, D C M C Petit, R P Cowburn, and M S Lesniak. Highly tunable perpendicularly magnetized synthetic antiferromagnets for biotechnology applications. *Applied Physics Letters*, 107(1):012403, jul 2015.

[36] Yu Cheng, Megan E. Muroski, Dorothée C.M.C. Petit, Rhodri Mansell, Tarun Vemulkar, Ramin A. Morshed, Yu Han, Irina V. Balyasnikova, Craig M. Horbinski, Xinlei Huang, Lingjiao Zhang, Russell P. Cowburn, and Maciej S. Lesniak. Rotating magnetic field induced oscillation of magnetic particles for in vivo mechanical destruction of malignant glioma. *Journal of Controlled Release*, 223:75–84, feb 2016.

[37] Megan E. Muroski, Ramin A. Morshed, Yu Cheng, Tarun Vemulkar, Rhodri Mansell, Yu Han, Lingjiao Zhang, Karen S. Aboody, Russell P. Cowburn, and Maciej S. Lesniak. Controlled Payload Release by Magnetic Field Triggered Neural Stem Cell Destruction for Malignant Glioma Treatment. *PLOS ONE*, 11(1):e0145129, jan 2016.

[38] Rhodri Mansell, Tarun Vemulkar, Dorothée C. M. C. Petit, Yu Cheng, Jason Murphy, Maciej S. Lesniak, and Russell P. Cowburn. Magnetic particles with perpendicular anisotropy for mechanical cancer cell destruction. *Scientific Reports*, 7(1):4257, 2017.

[39] T. Vemulkar, E. N. Welbourne, R. Mansell, D. C. M. C. Petit, and R. P. Cowburn. The mechanical response in a fluid of synthetic antiferromagnetic and ferrimagnetic microdiscs with perpendicular magnetic anisotropy. *Applied Physics Letters*, 110(4):042402, 2017.

[40] Selma Leulmi Pichot, Sabrina Bentouati, Saif S. Ahmad, Marios Sotiropoulos, Raj Jena, and Russell Cowburn. Versatile magnetic microdiscs for the radio enhancement and mechanical disruption of glioblastoma cancer cells. *RSC Advances*, 10(14):8161–8171, 2020.

Chapter 3

Experimental methods

This chapter details the experimental techniques used in this work. This begins with fabrication methods used to create magnetic thin films and particles. Next, the key techniques used to analyse the magnetic behaviour are described. This includes magnetometry systems for the assessment of magnetic reversal of films and particles, as well as some customised set ups for the study of the magneto-mechanical configurations of particles in liquid. Finally, the materials and methods used in our *in vitro* research are discussed.

3.1 Fabrication

3.1.1 Sputtering

Direct current (DC) magnetron sputtering is a standard physical vapour deposition method used for the growth of magnetic thin films. Here, a process gas (in our case, Ar) flows between a pair of electrodes, creating a DC plasma of gaseous ions. The plasma is accelerated towards a 'target' of desired material, which is situated at the cathode, and the ions bombard the target causing the emission, or 'sputtering', of target atoms and secondary electrons. Magnets of alternating polarity sit below the cathode and force the secondary electrons to follow the magnetic field lines, confining them in the area just above the target [5]. This increases the Ar plasma density close to the target, by increasing the ionisation of Ar via collision with secondary electrons, and thus increases the efficiency of the target sputtering. Placing a substrate at the anode results in target atoms favourably traveling towards and condensing on the surface, which leads to the growth of a thin film of the desired material.

The magnetic multilayers, and Al films, fabricated for this thesis were made using a Kurt Lesker DC magnetron sputtering system, which comprises of a high vacuum chamber with six target positions, all angled towards a rotating sample stage (spinning at 20 rpm to smooth out deposition thickness), and an adjacent load-lock. The typical base pressure of the system was $\sim 2 - 8 \times 10^{-8}$ mbar. The thin film stacks were grown at room temperature (RT) and under a working pressure of $7 - 9 \times 10^{-3}$ mbar. The sputtering rate of each target was calibrated by growing a sample for a set amount of

time, giving a film thickness between $20 - 30$ nm. These samples were grown on Si chips $1 - 4$ cm^2 patterned with a cross in marker pen. Dissolving the ink in acetone, thus lifting off the material on top, created steps in the film. The thickness of the deposition was then measured using an atomic force microscope (AFM), allowing the calculation of a growth rate for each target. Increments in growth time was limited to 1 s by the system and minimum growth time was additionally limited by the ~ 1 s shutter time of the magnetrons. Rate of growth could be controlled by varying the magnetron power, these were set between $30 - 300$ W, depending on the inherent target growth speed, desired thickness and precision requirements.

3.1.2 Ion milling

Ion milling is a physical etching technique used for the controlled removal of material to a desired depth. A typical system accelerates ions of an inert gas (Ar in our system) from a wide beam source towards a sample surface. The ions bombard the surface atoms and expel them, slowly removing layers of the material. Ion milling is a preferential method to chemical etching alternatives as it is cleaner (due to being performed under vacuum), more universal and doesn't exhibit under-cutting [8]. In our system, the sample was rotated during milling, to increase the uniformity of the etching. The speed of etching may be controlled by variation of the beam parameters, particularly the beam current.

The Ar ion milling system used for this project was situated in the main chamber of the sputterer, with the ion source positioned in the centre of the chamber. It was utilised in the fabrication of magnetic particles, for lithography methods that implemented a mask for the 'cutting out' of particles from a continuous thin film: the unprotected film was etched away, leaving behind the material covered by the mask. The majority of milling was conducted under an Ar pressure of $\sim 1.6 \times 10^{-4}$ mbar, using a beam current of 28 mA and a beam voltage of 600 V.

To calculate typical milling rates under these conditions, calibration samples were produced in the form of continuous films with photoresist hall bars patterned on top. After a known period of milling time, the hall bars were dissolved away and AFM was used to assess the step height between the milled and masked areas of the film. To work out how long it took to mill through a single SAF bilayer a few identical samples, with a prescribed total bilayer thickness, were prepared and milled simultaneously. Periodically, one of the samples had the hall bars removed and was measured by AFM, until the step height matched the bilayer thickness. It was determined that a typical SAF stack took ~ 40 s to mill through and Al milled at a rate of 0.32 nm/s. For one experiment we reduced the beam current to 10 mA (keeping the voltage the same), which increased the time to mill through a typical SAF to ~ 180 s. These numbers were utilised in the minimisation of milling time for the fabrication of magnetic discs.

3.2 Magnetometry

3.2.1 Polar magneto-optical Kerr effect

Broadly, magneto-optical effects are established by dielectric properties of media, which are controlled by electron dynamics [11]. The magneto-optical Kerr effect (MOKE) describes the change in polarisation of light that is reflected by a magnetic medium, which originates with spin orbit interactions [2, 4].

The light utilised in MOKE measurements is linearly polarised. This is a superposition of equal amplitude, right and left circularly polarised light. Magnetic materials exhibit off-diagonal elements in their dielectric tensor, which leads to an anisotropic response in the electric field of a reflected light wave [9, 11]: there is a difference in the refractive index between the left and right circular polarisations of light propagating through a magnetic material. This anisotropy manifests in two effects: Kerr ellipticity and Kerr rotation. Kerr ellipticity is the ellipticity in the reflected light, due to an induced dichoism: a difference in absorption of the left and right circularly polarised components creates a difference in their amplitudes. Kerr rotation is the rotation from the axis of the incident to the reflected light; the magnetic material causes a birefringence, an anisotropy in refractive index, which creates phase difference between the two light components. When light is at a perpendicular incidence to the surface of a magnetic material, Kerr ellipticity, ε_K, and Kerr rotation, θ_K are given by:

$$\tan\left[\varepsilon_K(\omega)\right] = \frac{r_+(\omega) - r_-(\omega)}{r_+(\omega) + r_-(\omega)} \tag{3.1}$$

$$\theta_K(\omega) = -\frac{1}{2}\left[\varphi + (\omega) - \varphi_-(\omega)\right] \tag{3.2}$$

where

$$\tilde{r}_\pm(\omega) = r_\pm(\omega) exp\left[i\varphi_\pm(\omega)\right] \tag{3.3}$$

are the reflection coefficients for right (+) and left (–) circularly polarised light [6]. Here, ω and $\varphi_\pm$ denote the frequency and phase of the reflected light respectively.

MOKE magnetometry offers a rapid technique for obtaining local magnetic information of thin film samples. Although it cannot provide any quantification of a sample's magnetisation, it is a powerful tool for recording the magnetisation dynamics. The MOKE used for this work is a NanoMOKE3 system from Durham Magneto Optics Ltd, set up in the polar configuration for the measurement of easy axis (EA) behaviour of magnetic thin films and disc-shaped particles with out of plane (OOP) anisotropy. Here, the laser, a linearly polarised beam with spot size $10 - 15$ μm, is directed perpendicular to the sample surface and thus parallel with it's EA. The maximum applied magnetic field for this system is ~ 0.6 T with a controllable field sweep rate (minimum frequency 0.005 Hz). This set up was also implemented in the collection of domain images, utilising the scanning laser microscopy and CCD camera functions

in the software, which were processed using a purpose built MATLAB application [10]. [1] provides a complete explanation of the analysis and noise considerations during the set up of a MOKE system.

3.2.2 Vibrating sample magnetometry

Vibrating sample magnetometry (VSM) is a complementary method to MOKE for the assessment of the magnetic behaviour of thin films: it provides quantitative measurements of bulk samples, namely saturation magnetisation, M_S. The set up utilises a slow ramped magnetic field, as opposed to the higher sweep rate used for quick MOKE measurements. Additionally, it is possible to reach higher applied fields, which allows us to assess hard plane (HP) measurements of our high anisotropy thin films.

In a VSM, a magnetic sample is attached to the end of a rigid, rod-shaped sample holder and vibrated sinusoidally, at a fixed frequency and perpendicular to an applied magnetic field. As the field is slowly ramped in specified increments, the stray field from the oscillating sample induces a voltage in a set of stationary pick up coils. This measured voltage is directly proportional to the magnetic moment of the sample, by Faraday's law of induction [3]. A lock in amplifier is used to amplify the signal picked up by the coils, with reference to the driving frequency of the sample holder. From Faraday's law, the voltage, V, induced in a coil with a single turn due to a local change in net flux follows [7]:

$$\oint E \cdot ds = -\frac{\delta\phi}{\delta t} \tag{3.4}$$

i.e.

$$V = -\frac{d\phi}{dt} = -\frac{d\phi}{dx} \cdot \frac{dx}{dt} \tag{3.5}$$

By the Biot-Savart law we can relate the flux, ϕ, produced by a sample's magnetic dipole moment, $\boldsymbol{m}$, to a field, $\boldsymbol{B}$, produced by a current, I, in the pick up coils:

$$\boldsymbol{B} \cdot \boldsymbol{m} = I\phi \tag{3.6}$$

If we assume that the sample is undergoing simple harmonic motion with amplitude A and frequency ω:

$$\frac{dx}{dt} = A\omega\cos(\omega t) \tag{3.7}$$

By combining equations 3.5–3.7 we show that the induced voltage is shown to be proportional to moment, and hence sample magnetisation:

$$V = \frac{d}{dx}\left[\frac{\boldsymbol{B}(\boldsymbol{r}) \cdot \boldsymbol{m}}{I}\right] A\omega\cos(\omega t) = G(\boldsymbol{r})mA\omega\cos(\omega t) \tag{3.8}$$

where $G(\boldsymbol{r})$ is a geometrical factor representing the spatial distribution of the coil sensitivity [7]. A more detailed description of the principles of VSM can be found in

[3] and [7].

In this work an EZ7 VSM from Microsense is used, with samples attached to a quartz rod sample holder, vibrated at 75 Hz and measured at RT. The maximum applied field of the system is 1.75 T. Background from the sample holder (a linear, diamagnetic response) is subtracted from the measured signal, prior to analysis. This system was used for both EA (OOP) and HP (IP) measurements of PM thin films, and additionally for the evaluation of particles in liquid. In this case a small vial, designed for use with a VSM, was filled with a particle suspension and attached to a normal quartz sample holder for measurement. Background signal from a water only filled vial was then removed. This allowed us to probe the magnetic response of particles in liquid, under an applied field, and lead to key insight into their novel switching behaviour.

3.3 Magneto-mechanical analysis

3.3.1 Particle imaging

Observations of magnetic particles in liquid under applied fields were performed via two optical microscope (OM) magnet set ups. The majority of the images and videos in this work were taken using the set up displayed in Figure 3.1. A few microlitres ($\sim$ 5 µl) of particle suspension is deposited on a Si chip; the Si is lightly plasma ashed beforehand to make it more hydrophilic, which allows the droplet to wet the surface more, making it flatter and easier to focus through. A sample holder, with x, y and z translation, positions the chip between the pole pieces of a dipole electromagnet (GMW 3470), which is capable of a maximum applied field of $\sim$ 5 kOe at a 25 mm pole piece separation or $\sim$ 8 kOe at a 12 mm separation. A 5 megapixel colour video camera built into a custom Olympus BXFM modular mount for reflected light microscopy is then

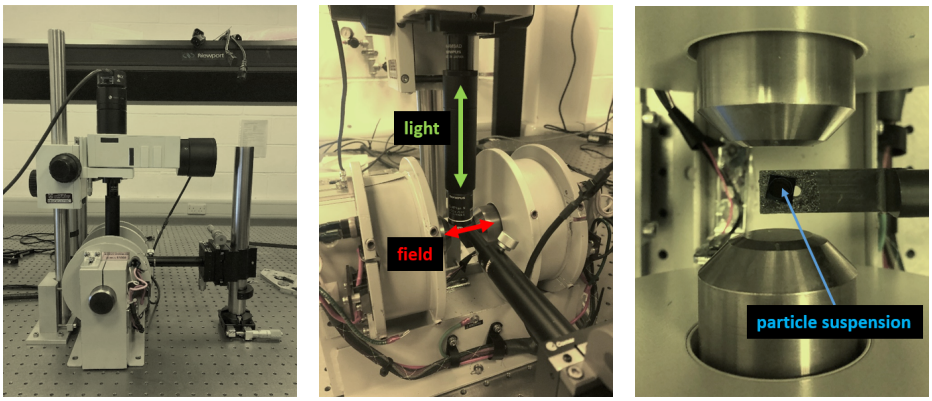

(a) (b) (c)

Figure 3.1: Photos of the OM-dipole set up. (a) The full set up. (b) The positioning of the objective above the dipole and sample holder: arrows indicate the directions of light and applied magnetic field. (c) The positioning of a sample between the pole pieces.

used to record the particle behaviour perpendicularly to the applied field direction. The use of long working distance objectives makes it possible to image the liquid samples with a range of magnifications without the objectives making contact with the water and whilst maintaining the sample in the centre of the dipole (minimum pole piece separation ~ 24 mm). In this work 50× and 100× objectives were employed, to image both micro and nanoparticles. The resolution of these are 0.79 and 0.46 μm respectively, based on the use of 550 nm light: our set up uses white light for illumination, so these resolutions are approximate.

A small proportion of the particle imaging was done via an earlier OM-magnet set up, which was built in a similar configuration as the new version, such that imaging was perpendicular to field direction. Here, the many body and objectives (50×, 100×) of a standard reflected light microscope were used in conjunction with a quadrupole, borrowed from a Durham Magneto Optics Ltd. NanoMOKE3 system, which was capable of a maximum applied field of ~ 1.2 kOe in the x and y directions.

3.3.2 Reflectivity measurements

To analyse the spatial configuration of magnetic nanodiscs, which are challenging to focus on with an optical microscope due to their particularly small thickness (10–20 nm), reflectivity measurements were employed. These were performed using the Durham Magneto Optics Ltd. NanoMOKE3 system, which can be set up to record reflectivity data, in its high-field polar configuration. A small reconfiguration of the set up was made to align the MOKE laser perpendicular to the field direction and maximise the potential reflectivity signal: the laser was directed vertically, such that it had normal incidence on the bottom of a cuvette (designed for optical measurements e.g. spectrophotometery) containing the particle suspension, as shown in Figure 3.2. The principle of these reflectivity measurements is that maximum signal is acquired

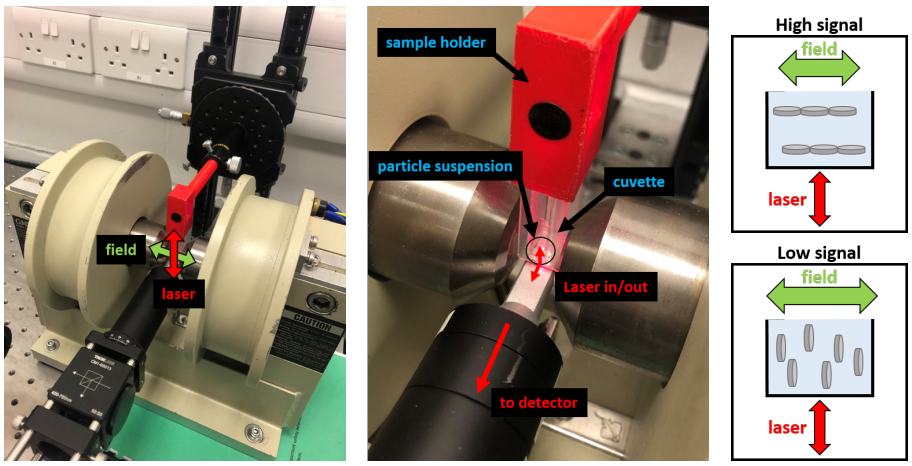

(a) (b) (c)

Figure 3.2: Photos of the reflectivity measurement set up with (a) the light and field directions and (b) the sample position indicated. (c) A schematic of the hard (top) and easy (bottom) axis alignments of the nanodiscs relative to the laser and field.

when the nanodiscs align their hard axis with the applied field (faces perpendicular to the laser) and a minimum signal corresponds with an easy axis alignment with the applied field (edges perpendicular to the laser, see Figure 3.2c).

References

[1] D. A. Allwood, Gang Xiong, M. D. Cooke, and R. P. Cowburn. Magneto-optical Kerr effect analysis of magnetic nanostructures. *Journal of Physics D: Applied Physics*, 36(18):2175–2182, 2003.

[2] Petros N. Argyres. Theory of the Faraday and Kerr effects in ferromagnetics. *Physical Review*, 97(2):334–345, 1955.

[3] Simon Foner. Versatile and sensitive vibrating-sample magnetometer, 1959.

[4] H. R. Hulme. The Faraday Effect in Ferromagnetics. *Proceedings of the Royal Society A: Mathematical, Physical and Engineering Sciences*, 135(826):237–257, 1932.

[5] P. J. Kelly and R. D. Arnell. Magnetron sputtering: A review of recent developments and applications. *Vacuum*, 56(3):151–226, 2000.

[6] Petr Kielar. Magneto-optical polar Kerr effect and dispersion relations. *Journal of the Optical Society of America B*, 11(5):854, 1994.

[7] Robert Luscombe. *Design and Development of a Vibrating Sample Magnetometer for High Magnetic Field Measurements of Superconductors*. Masters thesis, Durham University, 1994.

[8] P Norgate and V J Hammond. Ion beam etching. *Physics in Technology*, 5(3):186–203, 1974.

[9] Z Q Qiu and S. D. Bader. Surface magneto-optic Kerr effect. *Review of Scientific Instruments*, 71(3):1243, 2000.

[10] Alexander Welbourne. MOKE Image Analysis (https://uk.mathworks.com/matlabcentral/fileexchange/72494-moke-image-analysis?s_tid=prof_contriblnk), MATLAB Central File Exchange, 2020.

[11] J. Zak, E. R. Moog, C. Liu, and S. D. Bader. Universal approach to magneto-optics. *Journal of Magnetism and Magnetic Materials*, 89(1-2):107–123, 1990.

Chapter 4

Engineering magnetic thin films

4.1 Introduction

The use of perpendicularly magnetised (PM) materials and synthetic antiferromagnets (SAFs) have been important in the area of spintronics. The key benefits that PM materials offer are large retention times and fast domain wall speeds [12]. The added complexity of a SAF brings additional magnetic properties, such as an antiparallel (AP) state and tunable switching, that can be further exploited to create efficient data storage and logic devices [9, 18]. It has been shown that PM SAFs, and the extensive research that has been made into them in spintronics, may be exploited for the purpose of creating highly tunable magnetic particles for biological applications [17]. The architecture of a PM SAF results in a number of characteristics that are desirable for applications in biological, or more generically liquid, environments. These include a zero remanence state, sharp and efficient switching, and a relatively high saturation magnetisation. Additionally, the method used for engineering the magnetic stack offers a significant degree of flexibility and control of these characteristics, which is highly beneficial in tailoring magnetic particles towards a particular application [17].

The general structure of the PM SAFs is this work is $Ta/Pt/CoFeB/Pt/Ru/Pt/CoFeB/Pt/Ta$. A 2 nm layer of amorphous Ta provides a relatively smooth buffer to deposit the rest of the film on top of. As the magnetic properties of a PM SAF are strongly dependent on the interfaces within the multilayer stack, a smooth seed layer promotes robust properties, which includes sharp switching [16]. Layers of Pt sandwich the magnetic CoFeB, which is kept at a thickness below the spin reorientation transition (SRT) (see 2.1.1), which pulls the magnetisation out of plane (OOP) through spin-orbit interactions [6] (further info in Section 2.1.1). The $Pt/Ru/Pt$ motif provides tunable antiferromagnetic (AF) coupling: the Ru providing a Ruderman-Kittel-Kasuya-Yosida (RKKY) interaction [5, 14], which may be modulated through the thickness of the Ru or the Pt interlayers [1, 8].

This chapter will start with introducing the $Pt/CoFeB/Pt$ motif, which is the building block of the PM SAF thin film. It will then go on to study the architecture and magnetic behaviour of PM SAFs, exploring ways of engineering the thin film

to produce a range of tunable properties. This design flexibility demonstrates the potential for tuning a PM SAF towards a diverse selection of applications, including those in biological research areas.

4.2 CoFeB/Pt multilayers

4.2.1 Uncoupled CoFeB

Single layers

A series of PM uncoupled CoFeB stacks were sputtered in the form $Ta(2)/Pt(2)/CoFeB(x)/Pt(2)/Ta(2)$, with thicknesses in nm and where $x = 0.6 - 1.4$. To investigate the variation in magnetic behaviour with CoFeB thickness, t_{CoFeB}, polar MOKE was used to measure the easy axis (EA) hysteresis of the samples. The resulting loops, presented in Figure 4.1a, show the characteristic square shape with relatively sharp transitions that is expected for single PM CoFeB layers with t_{CoFeB} under the SRT. By extracting the coercive field, H_C, from the MOKE loops we reveal its relationship with t_{CoFeB}; Figure 4.1b shows that H_C increases with decreasing t_{CoFeB}. This likely stems from increasing roughness as the CoFeB gets thinner, inducing more defects in the thin film, which leads to an increase in domain wall pinning during magnetic transitions. This shows coercivity to not only be a key measure of the magnetic properties of a film, but also to be a reflection of other conditions, such as growth quality and texturing.

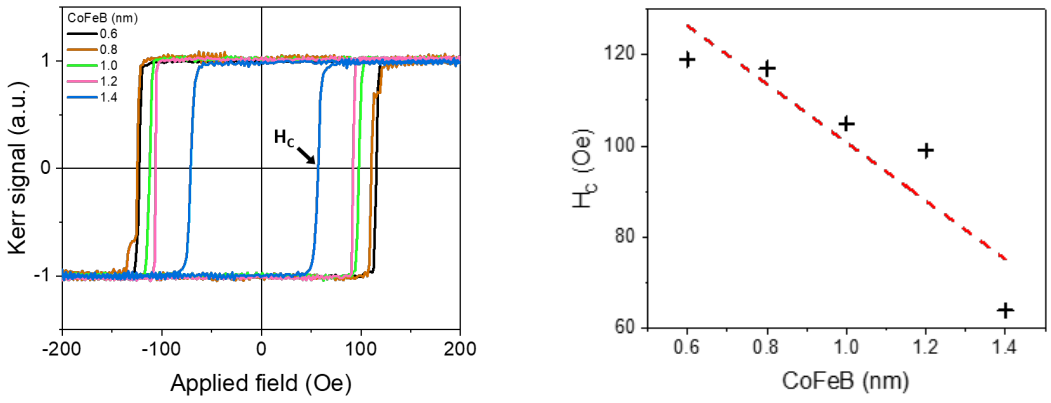

(a) EA MOKE

(b) Coercivity

Figure 4.1: (a) Polar MOKE easy axis loops and (b) coercive fields (H_C) of single, perpendicular layers of CoFeB. A linear fit is added to guide the eye. The films were grown in the form $Ta(2)/Pt(2)/CoFeB(x)/Pt(2)/Ta(2)$, where CoFeB thickness, x, was varied from $0.6 - 1.4\,nm$.

Multilayer stacks

A magnetic particle under an applied field experiences a torque that is proportional to its total magnetic moment. Therefore, moment is a key parameter to control for the purpose of liquid applications. There is a limit to how much the thickness of a CoFeB layer can be increased in a PM sample: if the thickness exceeds the SRT, the magnetic moment lies in the plane of a film. Accordingly, to increase the moment of a film we engineer heterostructured multilayers comprising of repeats of CoFeB layers, with ultrathin Pt layers inserted in between to conserve the PM state. To investigate the effect that this has on the magnetic reversal of a thin film, a series of samples were grown in the form $Ta(2)/Pt(2)/CoFeB(1)/[Pt(0.8)/CoFeB(1)/]_{n-1}Pt(2)/Ta(2)$, with thicknesses in nm and where the number of repeats $n = 1-5$. The OOP MOKE loops taken from the series are presented in Figure 4.2, alongside a graph of H_C versus n. Here, H_C is taken as the field required to complete a full magnetic reversal. Clearly,

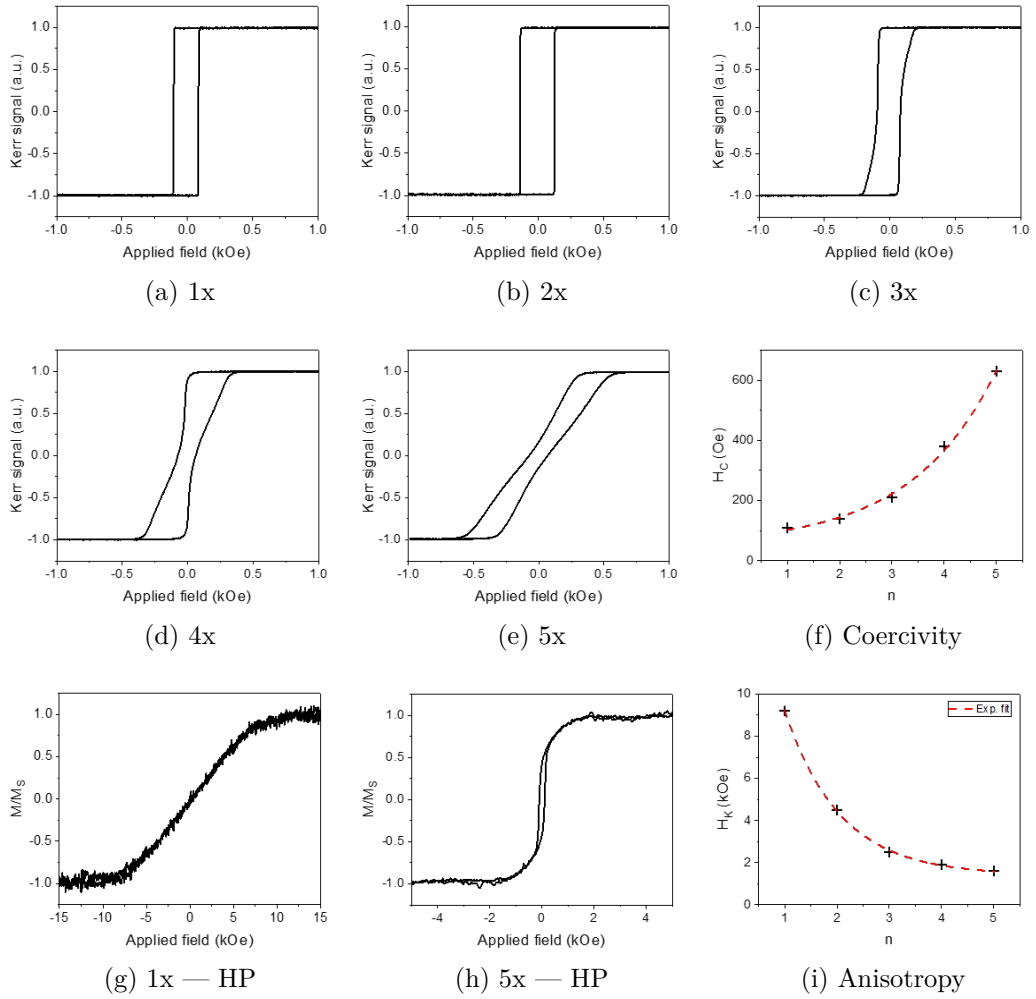

Figure 4.2: (a)–(e) MOKE loops from an uncoupled CoFeB layer series grown in the form $Ta(2)/Pt(2)/CoFeB(1)/[Pt(0.8)/CoFeB(1)/]_{n-1}Pt(2)/Ta(2)$, where the number of repeats, n, ranges from $1-5$. (f) The relationship between number of repeats and coercivity field (H_C). The exponential fit is added to guide the eye only. (g) and (h) HP loops of the $n = 1$ and 5 samples. (i) The relationship between number of repeats and anisotropy field (H_K), with exponential fit to guide the eye.

there is significant increase in H_C with increasing n, with an apparent exponential relationship. We can see from the MOKE that a key contributor to this behaviour is the change from sharp, EA transitions at the lower end to highly sloped transitions with the higher number of repeats. The major reason for this change in switching behaviour is that there is a trade off between surface area and total volume of magnetic material: as n is increased an effective SRT for the whole stack is neared. This causes the magnetic reversal to change from nucleation limited, where there is rapid domain wall motion once a few domains have nucleated, to become increasingly dominated by a collective propagation of reverse stripe domains [5]. This is the consequence of the balance between the Zeeman, domain wall and magnetostatic energies. The result is an increase in the switching field of the film as the transitions become significantly more sloped.

In plane (IP) hysteresis loops were measured via VSM. The results for the $n = 1$ and 5 cases are shown in Figures 4.2g and 4.2h respectively. For $n = 1$, the curve is sigmoidal in shape, with no hysteresis and a particularly high saturation field. For $n = 5$ we still find a sigmoidal shape, however, there is hysteresis around remanence and the saturation field is significantly lower. Therefore, we again see a change in the switching behaviour with an increase in n: the film changes from a fully HP-like reversal to something which displays more EA characteristics.

The anisotropy field (H_K) of all five samples was taken from the respective HP loops, generating the H_K versus n graph shown in Figure 4.2i. There is a very clear decrease in H_K with increasing n, corresponding with the progressively stronger easy axis behaviour in the IP direction, which lowers the strength of the anisotropy along the OOP axis.

4.2.2 Synthetic antiferromagnets

The insertion of Ru between layers of PM CoFeB induces their coupling via an RKKY interaction [5, 14]. Pt interlayers, added either side of the Ru, act to stabilise the PM state [1]. In this case a thin film is in the form $Ta/Pt/CoFeB/Pt/Ru/Pt/CoFeB/Pt/Ta$. This leads to the formation of a PM SAF, which exhibits a characteristic EA hysteresis as shown in Figure 4.3a. As depicted by the blue arrows, which represent the magnetisation in the two coupled CoFeB layers, an antiparallel (AP) state is formed at remanence where the net moment is zero. In the case of a MOKE hysteresis loop, as in Figure 4.3a, this is not represented by zero Kerr signal due to the depth dependence of the measurement, which is caused by the skin-depth of the probe laser. As the strength of an applied magnetic field is increased from remanence, along the easy axis of the SAF, there is a sharp switch to the parallel (P) state at the saturation field of the sample. When the magnetic field is then ramped back down there is another sharp switch back to the AP state. By measuring a minor loop of the SAF (as discussed in Section 2.1.2, Red in Figure 4.3a) we can calculate the coupling field, H_J, and coercive field, H_C, of the each of the layers. The HP behaviour

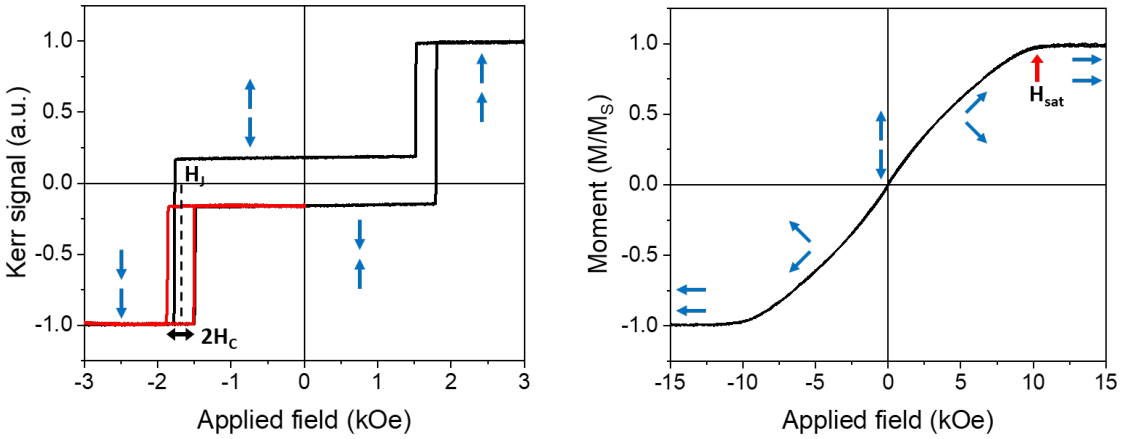

(a) EA (b) HP

Figure 4.3: (a) An EA polar MOKE loop of a SAF film, with coupling field (H_J) and coercivity field (H_C) indicated. (b) A HP VSM loop of a SAF film, normalised by magnetic saturation, with the saturation field (H_{sat}) indicated. The blue arrows represent the direction of magnetisation of each of the CoFeB layers.

of a SAF takes the shape shown in Figure 4.3b. There is a non-hysteretic, sigmoidal transition from one saturation point, H_{sat}, to the other, via a zero remanence state. This is the result of the moments of the two coupled CoFeB layers canting between the easy and hard axes, as shown by the blue arrows.

The distinct hysteresis behaviour exhibited by a SAF provides a number of highly desirable characteristics for device applications, particularly those involving magnetic particles in a fluid environment [17]. Firstly, the zero remanence state of the system prevents inter-particle interactions in the absence of applied fields, which precludes SAF particles from aggregating. The low susceptibility of the system in low fields also limits the agglomeration of particles after the application of a field [7]. This is reinforced by the exhibition of relatively high coupling fields, in comparison to dipolar fields between particles, preventing self-polarisation (see Section 6.4.1). The strong EA anisotropy of the PM SAF leads to sharp switches between the AP and P states and therefore efficient activation and deactivation. Additionally, in applications involving rotating fields, transduction of torque is more effective from an easy axis than an easy plane [11]. Tunable switching, through the $Pt/Ru/Pt$ interlayer, provides flexibility in the system and an ability to tailor it towards particular applications. Finally, there is potential for varying the moment, by simply building up repeats of the SAF motif, without compromising key properties including the zero remanence state [17].

In this section, these magnetic properties will be explored further, to illustrate the extent of the tunability of the PM SAF system. This will demonstrate a full suite of thin films that may be utilised in magnetic particles across a wide range of biological and other fluid applications.

RKKY coupling — AF peaks

The thickness of the Ru (t_{Ru}) modulates the RKKY coupling strength: the coupling oscillates between peaks of strong AF and ferromagnetic (FM) coupling, with a reduction in peak strength as t_{Ru} increases [1, 2, 14]. To probe the two strongest AF peaks, a series of SAFs with ultrathin Pt interlayers (to maximise coupling and therefore workable range) were grown in the form $Ta(2)/Pt(2)/CoFeB(1)/Pt(0.4)/Ru(t_{Ru})/Pt(0.4)/CoFeB(1)/Pt(2)/Ta(2)$, with thicknesses in nm. This series was split into two groups of films: one with t_{Ru} centred around 0.9 nm, the first expected AF peak, and the other centred around 2 nm, the second expected AF peak [1]. The EA MOKE measurements of the films are presented in Figure 4.4, alongside a plot of H_J versus t_{Ru}. We clearly see a rise and fall in the coupling with increasing t_{Ru} for both sets of SAFs, with a much larger range of H_J for the set with smaller values of t_{Ru}. This translates into the characteristic pair of steep asymmetric peaks in the coupling plot, centred around the strongest and second strongest AF coupling values of $t_{Ru} = 0.9$ and 2.0 nm respectively.

This illustrates the ability to utilise Ru thickness as a parameter for, at least, the coarse tuning of SAF switching fields. Engineering magnetic films or particles towards saturating at particular fields, such that they are suitable for different applications, is quite desirable. Furthermore, optimising films to saturate in relatively high or low applied fields, through this coarse tuning ability, could prove to be very useful in biomedical device design: a large H_J would prevent particle activation until it was required, even in environments with low field backgrounds, whereas a low H_J would be very useful in the creation of devices without bulky or expensive field application systems.

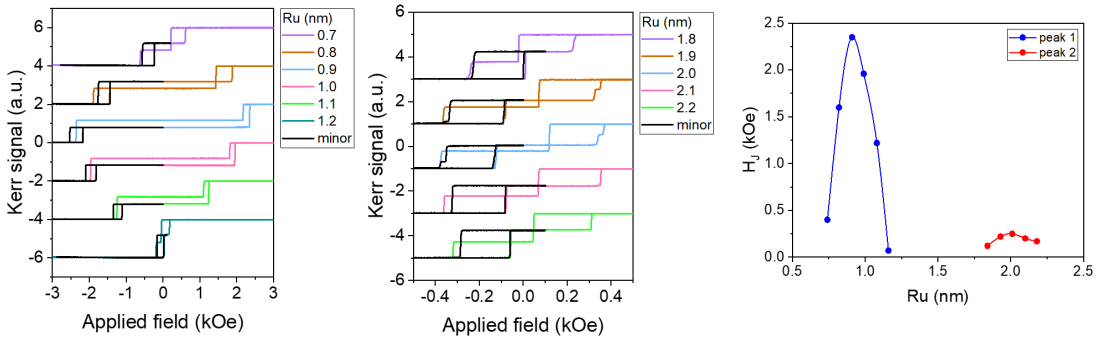

(a) 1st peak (b) 2nd peak (c) Coupling field

Figure 4.4: MOKE loops of SAF films coupled with different thicknesses of Ru: (a) around the first peak and (b) around the second peak. (c) Shows the peaks produced for H_J vs. t_{Ru}.

Tuning coupling with the Pt interlayer

An additional method of tuning the coupling strength of a SAF is via the Pt interlayer thickness (t_{Pt}): the insertion of Pt between CoFeB and Ru limits the interlayer interac-

tion, with coupling strength being inversely proportional to t_{Pt} [8]. Figure 4.5a displays the MOKE loops taken from a series of SAFs grown on the first Ru peak, in the form $Ta(2)/Pt(2)/CoFeB(0.9)/Pt(t_{Pt})/Ru(0.9)/Pt(t_{Pt})/CoFeB(0.9)/Pt(2)/Ta(2)$, with thicknesses in nm and $t_{Pt} = 0.37 - 0.69$. The sharp transitions in the MOKE loops are indicative of switching in the spin-flip regime (see Section 2.1.3).

As expected, the saturation fields of the SAFs distinctly reduce as the t_{Pt} is increased. By calculating the H_J for each sample from the minor loops and plotting against t_{Pt} we find the characteristic exponential decrease. This relationship is of the form $H_J = Ae^{-t_{Pt}/t_d}$, where A is the amplitude and t_d is the characteristic decay length of the coupling field. In our case we extract $A = 17 \pm 3$ kOe and $t_d = 0.19 \pm 0.02$ nm: this decay length is comparable with that found in the literature ($t_d = 0.16 \pm 0.01$ nm in [8]). To compare our amplitude with that found in the literature we must adjust for CoFeB thickness (t_{CoFeB}), as coupling energy $J = H_J M_S t_{CoFeB}$ (see Section 2.1.2). We therefore obtain $At_{CoFeB} \approx 15$ kOe nm, which is higher than that in [8]: $At_{CoFeB} \approx 7$ kOe nm. Due to the exponential nature of the relationship between H_J and t_{Pt}, small changes in the magnetic properties of the thin films can have a large effect on the amplitude of the data fit. For example, we have assumed that the M_S of our CoFeB is identical to that in the literature. Additionally, all of our films are switching via a spin-flip transition, while those in the literature [8] switch via a mixture of spin-flip and spin-flop transitions. Most significantly, we have made no consideration of disparity in Ru thickness (we use 0.9 nm, while the previous study uses 1.5 nm), which we have just shown has a large effect on the coupling. The fact that our samples are grown with a Ru thickness closer to the 1st AF peak is consistent with us achieving larger coupling strengths.

In comparison with the relationship between H_J and Ru thickness, t_{Pt} has a much more moderate effect on the coupling of a SAF, making it a better candidate for the fine

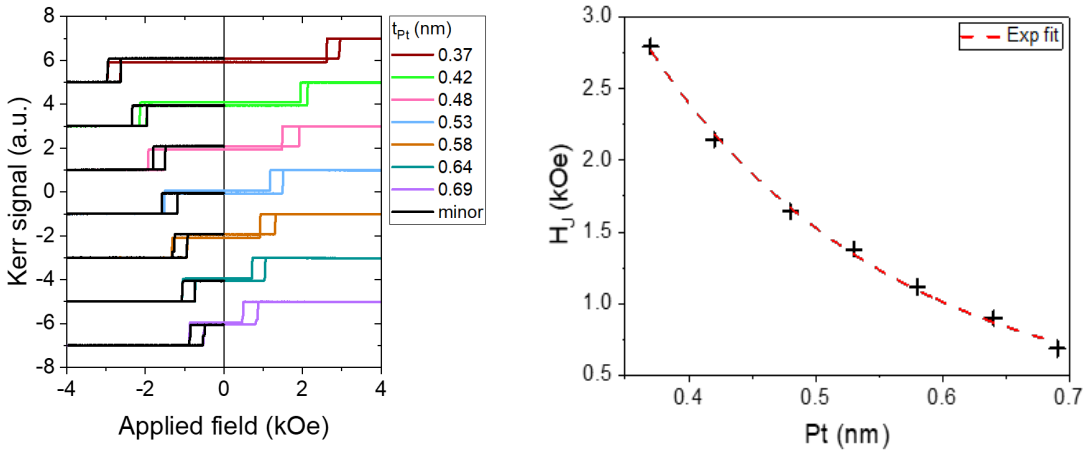

(a) Pt series (b) Coupling field

Figure 4.5: (a) MOKE loops from a SAF film series grown with the form $Ta(2)/Pt(2)/CoFeB(0.9)/Pt(t_{Pt})/Ru(0.9)/Pt(t_{Pt})/CoFeB(0.9)/Pt(2)/Ta(2)$ for a range of t_{Pt}. The effect of t_{Pt} on H_J is shown in (b).

tuning of magnetic switching. This would be highly beneficial for sorting or purification type applications.

4.2.3 SAF stacks with repeats

Increasing moment

As has been discussed previously, increasing the moment, and thus the force/torque, that can be applied on magnetic particles could be beneficial to their application. To increase the moment of a SAF stack, without losing the PM state by crossing the SRT, we can repeat the main motif to create a film in the form $Ta/[Pt/CoFeB/Pt/Ru/Pt/CoFeB/Pt/Ta]_n$, where n is the number of repeats. To investigate the effect that this has on the hysteretic behaviour of a SAF, a series of films were grown in the form $Ta(2)/[Pt(2)/CoFeB(1)/Pt(0.4)/Ru(0.9)/Pt(0.4)/CoFeB(1)/Pt(2)/Ta(2)]_n$, with thicknesses in nm.

The EA MOKE loops for each samples are presented in Figure 4.6a. As we previously observed with the uncoupled CoFeB layers in Section 4.2.1, the increase in n causes the magnetic transitions to lose sharpness. We quantify this through the spread in switching field, as shown in Figure 4.6b, which shows a distinct increase with n. At the two ends of the spectrum, the switch of $n = 1$ sample starts at ∼1.63 kOe and finishes at ∼1.66 kOe, while the $n = 10$ switching occurs across ∼ 1.54–1.98 kOe. Additionally, we can see in Figure 4.6b that the alterations to the shape of the hysteresis translates through to the effective coupling H_J, which decreases with increasing n. Contrary to the uncoupled CoFeB stacks, the strongest contributor to the changes in

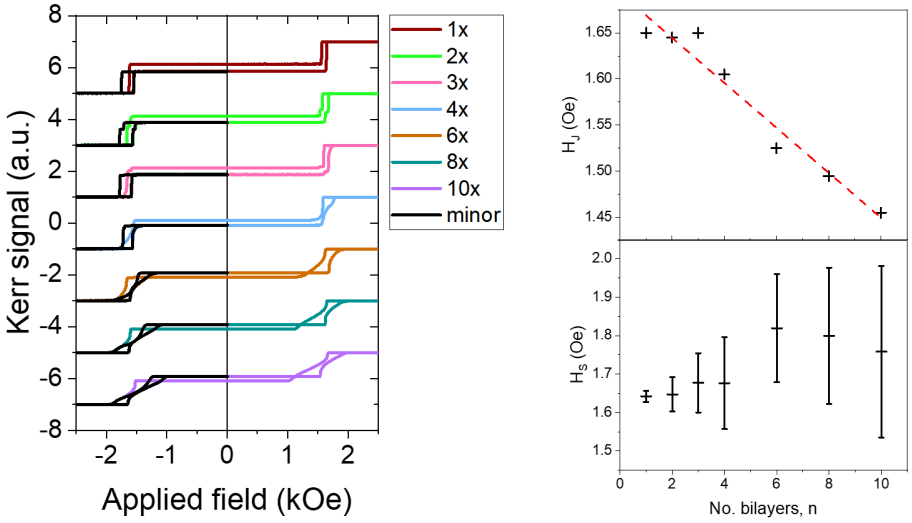

(a) MOKE (b) Fields

Figure 4.6: (a) MOKE loops of a SAF stack series, with film grown in the form $Ta/[Pt/CoFeB/Pt/Ru/Pt/CoFeB/Pt/Ta]_n$, where n is the number of repeats. (b) The trends in (top) effective coupling field H_J and (bottom) switching field H_S (bottom) with n. For H_J, a linear fit is added to guide the eye. The error bars for H_S represent the range of field from the start to the end of the magnetic switches.

hysteresis of the SAF multilayers is roughness. The Ta/Pt buffer motif magnetically decouples each SAF layer, preserving the strong magnetic anisotropy of the system and therefore the sharp, spin-flip switching. However, despite the repeats of the Ta smoothing layer, roughness will be translated up the ever increasing stack and increasing the number of defects, as has been seen in similar multilayer heterostructures [10, 15]. This leads to an increase in domain wall pinning, but also a distribution in H_J and H_C across the different CoFeB pairs. The larger the multilayer, the greater the distribution will become, which induces a smearing in the overall switching fields of the SAF film.

Nevertheless, the switching of the SAFs remains tunable and relatively efficient, the OOP anisotropy is preserved and the repeated bilayer motif successfully increases moment. These multilayer films are therefore strong candidates for the production of magnetic particles in mechanical actuation based applications e.g. magneto-mechanical destruction cancer therapies [11].

Magnetic stacks with multiple switches

For some applications, it could be beneficial to employ a film or particles that undergo multiple magnetic switches across an applied field range. This mainly includes magnetic sorting, in particular multiplexed sorting. Initially, this concept was tested with a dual bilayer, PM SAF grown in the form $Ta(2)[/Pt(2)/CoFeB(0.9)/Pt(t_{Pt})/Ru(0.9)/Pt(t_{Pt})/CoFeB(0.9)/Pt(2)/Ta(2)]_2$ with thicknesses in nm and where $t_{Pt} = 0.45$ and 0.3 nm such that the top layer exhibited stronger RKKY coupling than the bottom. The EA MOKE and VSM measurements of the sample are presented in Figures 4.7a and 4.7c respectively. We observe a conservation of the sharp switching behaviour, for two pairs of distinct switches at very different applied field values. By measuring the individual minor loops, we can calculate the coupling and coercivity for each bilayer: $H_{J1} = 1370$ Oe, $H_{C1} = 130$ Oe, $H_{J2} = 2520$ Oe and $H_{C2} = 170$ Oe, where layer 1 is in the bottom bilayer and layer 2 is in the top bilayer.

By reducing the thickness of the CoFeB layers (t_{CoFeB}) we can increase the coupling strength induced by the Ru layer: as $H_J \propto t_{CoFeB}$ (see Section 2.1.2), the RKKY coupling can be 'diluted' by increasing magnetic layer thickness [8]. This increases the range of Pt interlayer thicknesses that are accessible to us for the creation of a multilayer SAF stack with multiple coupling strengths. First, a SAF thin film comprising of three different bilayers was grown in the form $Ta(2)[/Pt(2)/CoFeB(0.6)/Pt(t_{Pt})/Ru(0.9)/Pt(t_{Pt})/CoFeB(0.6)/Pt(2)/Ta(2)]_3$, with thicknesses in nm and where $t_{Pt} =$ 0.55, 0.4, 0.3 nm. Again we observe a hysteresis loop containing distinct transitions for each of the bilayers, as shown in the MOKE and VSM in Figures 4.7b and 4.7d respectively. The two lower field switches retain their sharpness, however the highest coupled bilayer exhibits some smearing in the parallel-to-antiparallel (P–AP) transition, which is likely caused by a combination of the particularly thin Pt interlayer and increased roughness in the upper layers of the magnetic stack, which will lead to a higher chance of domain wall pinning. Despite this, it is still possible to access three

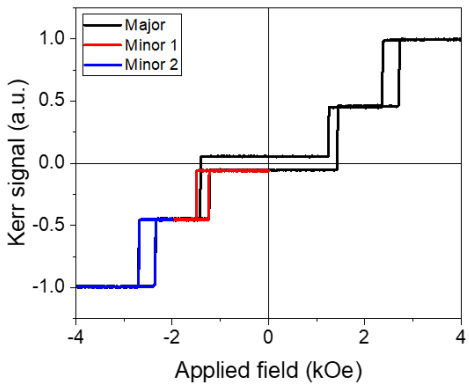

(a) MOKE

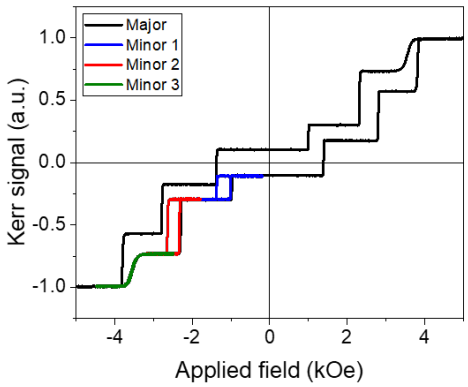

(b) MOKE

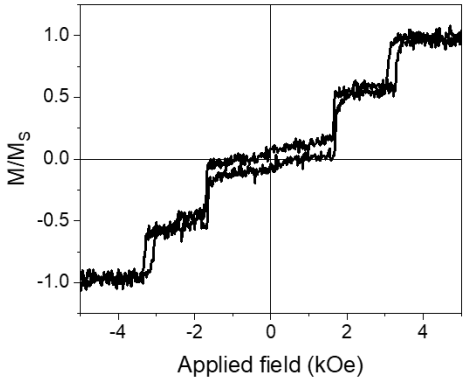

(c) VSM

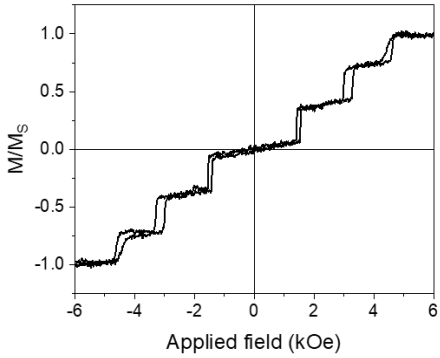

(d) VSM

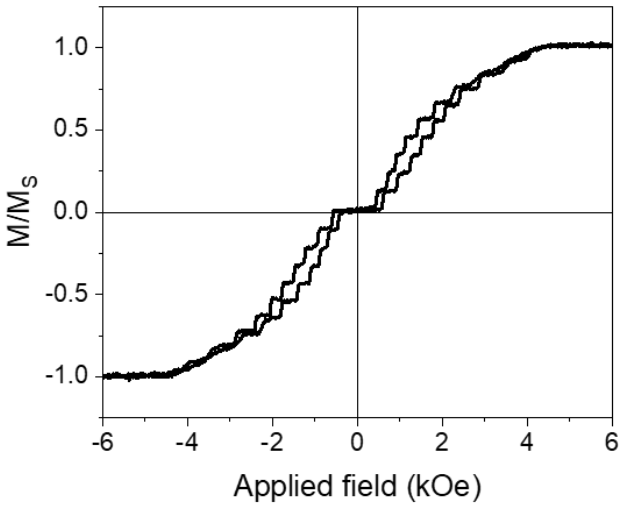

(e) VSM

Figure 4.7: The MOKE, (a) & (b), and VSM, (c) and (d), EA loops of the double and triple SAF bilayers respectively. (e) The EA VSM response of a SAF film comprised of ten bilayers with different coupling strengths.

individual MOKE loops within the sample, which allow us to calculate the field parameters for each bilayer: $H_{J1} = 1190$ Oe, $H_{C1} = 170$ Oe, $H_{J2} = 2480$ Oe, $H_{C2} = 160$ Oe, $H_{J3} = 3580$ Oe and $H_{C3} = 280$ Oe.

Finally, it was considered whether it were possible to create a multi-bilayer SAF stack comprising of a much larger number of coupled bilayers. Utilising the thinner 0.6 nm CoFeB layers and a range of Pt interlayers that theoretically provided well spaced coupling values, such that transitions did not merge, a 10× bilayer film was grown in the form $Ta(2)[/Pt(2)/CoFeB(0.6)/Pt(t_{Pt})/Ru(0.9)/Pt(t_{Pt})/CoFeB(0.6)/Pt(2)/Ta(2)]_{10}$, with thicknesses in nm and where $t_{Pt} = 0.75 - 0.3$ nm (steps of 0.05 nm). Due to the relatively large thickness of this magnetic stack, it was not possible to effectively probe all of the bilayers with our MOKE system. However, an EA VSM loop, shown in Figure 4.7e, revealed the existence of a hysteresis loop with ten individual switches in the anti-parallel-to-parallel (AP–P) direction. As observed with the triple bilayer sample, the weaker coupled layers (towards the bottom of the stack) exhibit relatively sharp switching, whilst the more highly coupled ones (towards the top of the stack) were more sloped. This is again more evident for the P–AP transitions, which has lead to some merging for the highest switching field values. By taking the derivative of the VSM loop (Savitzky Golay smoothed with polynomial order 1 and a window of 10) we find peaks that are associated with each of the transitions made by the 10× bilayer SAF. Figures 4.8 displays the results for the rising and falling field data within the $0 - 5$ kOe applied field range. The individual switches seen in the VSM loop during the AP–P transitions have translated to ten distinguishable peaks in the derivative plots (Figures 4.8a and 4.8b). The P–AP transitions only produce eight distinguishable peaks, as expected from the smearing found in the VSM loop. By applying a Gaussian fit to these peaks, as shown in blue and red, we can calculate the mean and full width half maximum (FWHM) of each of these peaks, which represent the centre and spread of each of the SAF transitions. Figure 4.8c displays the results for each of the fitted peaks in the rising and falling field data. In both cases the peaks, and thus transitions, found in the lower applied fields have narrower FWHMs (smaller error bars), while the high-

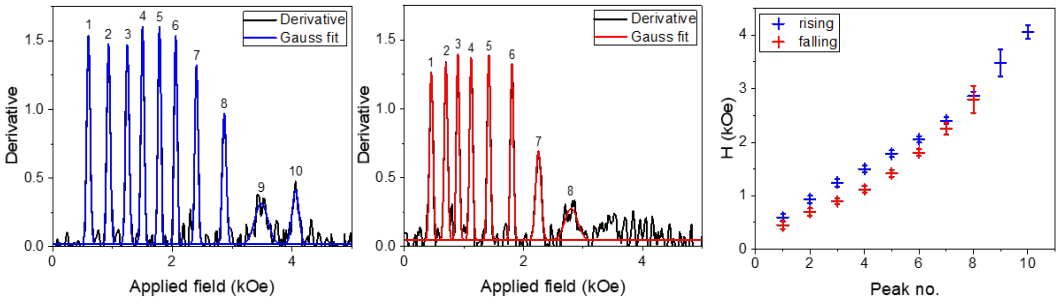

(a) Rising field (b) Falling field (c) Peak data

Figure 4.8: Plots of the derivative of the (a) rising and (b) falling field sections of the VSM data from the 10× bilayer SAF within the $0 - 5$ kOe applied field range wit Gaussian fits of the visible peaks, with the peak no. indicated above. (c) The mean field (H) for each of these peaks with the FWHMs plotted as errors.

est field transitions show a much greater spread (larger error bars). This corresponds with more extended magnetic transitions, likely due to more nucleation-dominated behaviour. This is the result of higher levels of roughness coming from two sources: the thinner Pt interlayers used to generate the higher coupled bilayers and the translation of roughness up the large SAF stack.

4.3 Effect of underlayers

Note: all evaporation of Ge for samples in this work was performed by T. Vemulkar (Prof. Cowburn's group).

The use of sacrificial underlayers are vital in the fabrication of thin film based magnetic particles for liquid applications: once produced, particles must be lifted off substrate, which requires some sort of release mechanism. In choosing a suitable sacrificial layer, two key criteria are considered: ease of removal and the effect on the properties of a film grown on top. Previously, photoresists have been utilised for this purpose, as they provide a very simple lift off process. However, the organic structure of photoresists is inherently rough, which can lead to the destruction of the smooth interfaces exploited in the design of more complex magnetic thin films (e.g. SAFs). Additionally, the solvents used to dissolve photoresists are also organic, which necessitates a series of washing steps to clean up a particle suspension that could lead to a large decrease in yield. Inorganic underlayers may provide an appropriate alternative here, namely as providers of relatively smooth substrates and thus limiting effects on magnetic properties. Furthermore, many are amenable to the same deposition methods as our thin films, which may simplify process requirements. This section will explore the use of two such candidates, Al and Ge, for the production of thin film based particles comprising PM CoFeB stacks. These are readily dissolved in basic solvents (e.g. NaOH or TMAH) or hydrogen peroxide (H_2O_2) respectively, which doesn't compromise the ease of lift off and moreover, eliminates the use of organic solvents. On this point, Ge has an advantage over Al: H_2O_2 naturally degrades to water, which eliminates the requirement of any washing steps and thus limits yield loss. By growing a selection of PM CoFeB based thin films on Al and Ge, and on Si as a reference, an investigation into the effect of these underlayers on magnetic behaviour was conducted.

4.3.1 Al vs Ge as an underlayer

A series of PM SAF coupled CoFeB bilayers were sputtered on top of sputtered Al, thermally evaporated Ge and Si to investigate the underlayer effect on their hysteresis. Two key features that we were looking to conserve, particularly as they are noted as desirable properties for magnetic particles in liquid applications, were sharp transitions and a zero remanence state. These originate from perpendicular anisotropy and RKKY coupling. The thin film stacks were grown in the form $Ta(2)/Pt(4)/CoFeB(0.9)/Pt(t_{Pt})/Ru(0.9)/Pt(t_{Pt})/CoFeB(0.9)/Pt(4)/Ta(2)$, with thickness in nm. The Pt

interlayer thickness, t_{Pt}, ranged from $0.41 - 0.69$ nm to create a series of coupling strengths. To analyse their magnetic hysteresis, the samples were measured using MOKE: the results are presented in Figure 4.9. We clearly see that the Al underlayer has a drastic effect on the easy axis behaviour of the SAFs. The sharpness of the transitions is completely lost and there is a large increase in coercivity across the range of samples. This has led to a loss of the zero remanence state in the more weakly coupled films, which is unfavourable for particles in liquid applications, as it leads to aggregation. Conversely, the Ge underlayer has a much smaller effect on the hysteresis, when compared with the Si reference samples. We observe a small decrease in the coupling fields across the series, a relatively small change in coercivity, and a conservation of the sharp transitions. These results indicate that Ge is a good, and certainly superior, option for a sacrificial layer: it appears to ensure the robustness of the thin film properties and also maintains access to a large range of SAFs with zero remanence.

To further analyse the effects that the underlayers have on the hysteresis of the SAFs, two key parameters were calculated from the minor MOKE loops: coupling field, H_J, and coercive field, H_C. In Figure 4.10a we observe the characteristic trend of exponentially decreasing H_J with linearly increasing t_{Pt} for all three sets of samples. Overall, both the Al and Ge samples exhibit slightly lower coupling than the Si counterparts, where in general $H_J(Si) > H_J(Al) > H_J(Ge)$. The difference between the Ge and Si samples decreases with increasing t_{Pt}, whereas the Al samples have a more consistent reduction in H_J from the Si equivalents. The variation of coercivity field, H_C, with t_{Pt} for the SAF series is shown in Figure 4.10b. For the Ge set, we observe values of H_C that are roughly similar to that of the Si set, with a small rise over the increasing t_{Pt} . In contrast, the H_C's of the Al samples are much higher than the others and there is a distinct increase in H_C with t_{Pt}.

By measuring the series of thin films using a VSM to obtain HP hysteresis loops, we can additionally calculate the anisotropy field, H_K. There is no particular relationship found between t_{Pt} and H_K for any of the samples. However, the samples grown on

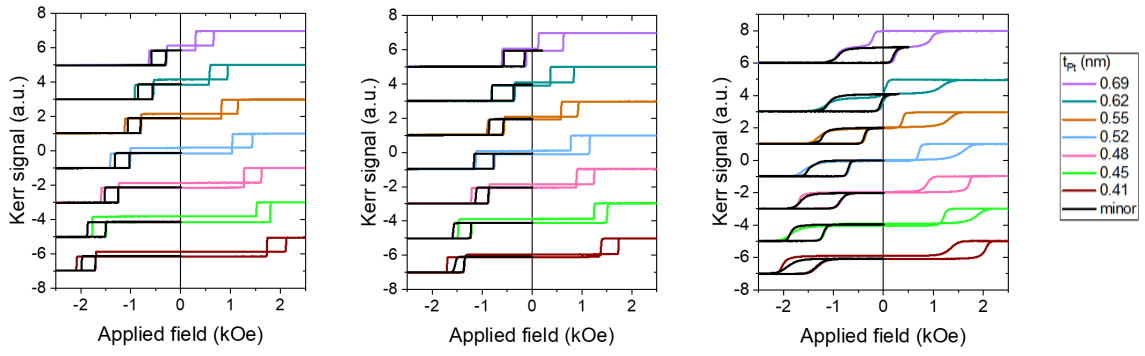

(a) Si (b) Ge (c) Al

Figure 4.9: Major and minor EA MOKE loops of a SAF film series, grown in the form $Ta(2)/Pt(4)/CoFeB(0.9)/Pt(t_{Pt})/Ru(0.9)/Pt(t_{Pt})/CoFeB(0.9)/Pt(4)/Ta(2)$, with varied Pt interlayer thickness (t_{Pt}). The series was grown on top of (a) Si, (b) Ge and (c) Al.

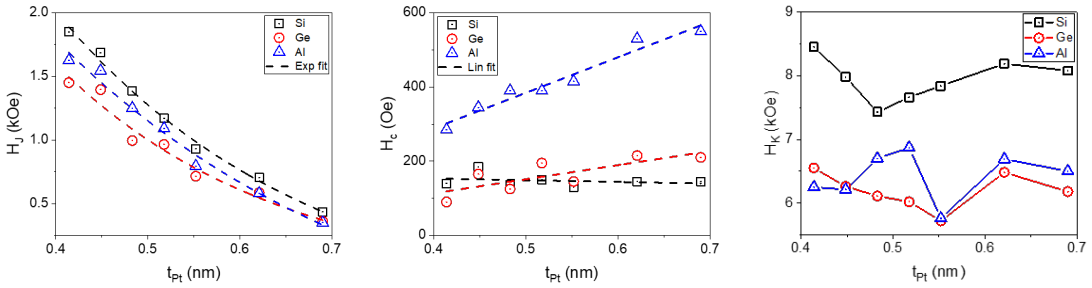

(a) H_J (b) H_C (c) H_K

Figure 4.10: Variation of (a) coupling (b) coercivity and (c) anisotropy with Pt interlayer thickness, t_{Pt}, for the SAF series grown on Si, Ge and Al.

both Ge and Al exhibit lower values of H_K than the Si counterparts. As the PM state of the system is dependent on interlayer interactions, an increase in texturing could reduce the strength of these interactions and thus the strength of the OOP anisotropy.

Roughness analysis

To probe the origin of the hysteretic changes with the different underlayers, AFM was used to assess the topography of the substrates. The images produced are presented in the top row in Figure 4.11a; we observe significantly greater texturing in the scan of the Al in comparison to Ge, with the Si appearing the smoothest. This translates into the root mean squared (RMS) roughness, calculated from the scans using *Gwyddion* analysis software and displayed in Figure 4.11a, whereby the value for Ge (1.32 nm) is slightly higher than that of Si (0.23 nm), but the Al shows much greater roughness (4.28 nm). We achieve the same findings upon the assessment of the top Ta layer of a SAF ($t_{Pt} = 0.69$ nm) grown on top of each substrate, as shown in the bottom row of Figure 4.11a.

Furthermore, *Gwyddion* was used to find the radial power spectral density function (PSDF) profiles for each of the substrate scans. As we can see in Figure 4.11b, not only does the Al sample generally exhibit higher magnitudes of roughness (W_r), it also shows a high level of roughness in the $10-20$ nm. This is significant as this is the length-scale associated with nucleation and propagation of domain walls in perpendicular films [12]. Such roughness does not manifest in the Ge sample, with values more comparable to Si. These findings account for the changes in the hysteresis loops of the SAF films grown on the different substrates: the magnetic properties of a perpendicular SAF strongly depend on the interfaces between each layer in the film. Thus, changes in roughness have a direct impact on the domain wall dynamics during magnetic reversal. Roughness on the length-scale associated with domain wall motion parameters will have an effect on whether a transition is nucleation or propagation dominated: a large number of defects will induce a more nucleation dominated transition, which characteristically has a more extended switching field, as we observed in the Al samples. A more propagation dominated transition, where the domain wall motion is rapid,

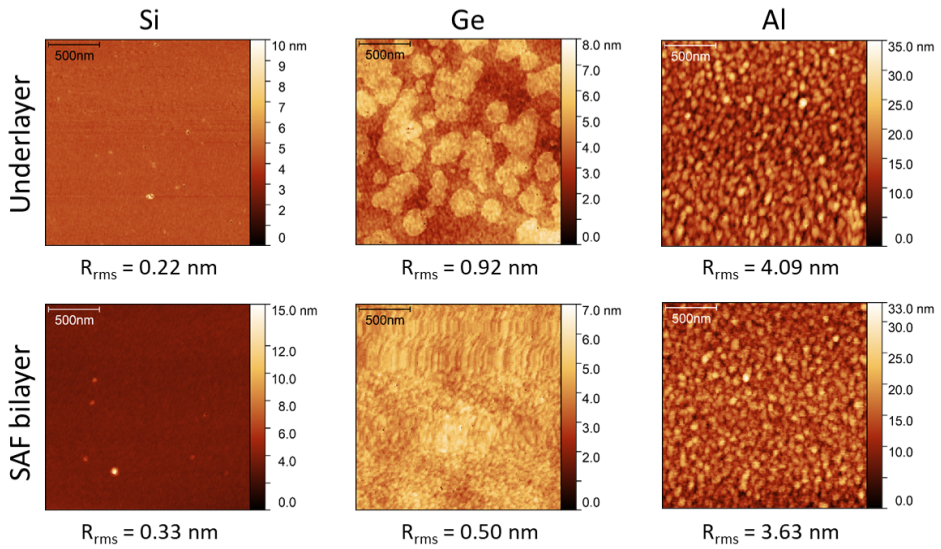

(a) Topography scans

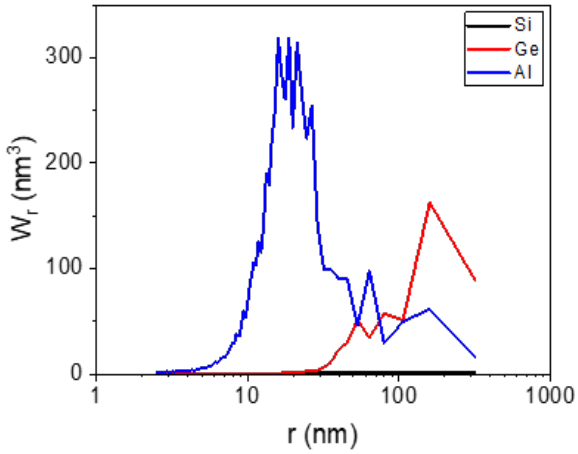

(b) PSDF

Figure 4.11: (a) AFM topography images of the substrates, Si/Ge/Al, and of the top Ta layer of a SAF bilayer (t_{Pt} = 0.69 nm) grown on top of each substrate. The root mean squared roughness (R_{rms}) is note below is respective image. (b) The radial PSDF profiles taken from each of the substrate scan in (a), where r is radius and W_r is the radial PSDF, representing roughness at different length scales.

produces sharp transitions, as observed in the Si and Ge samples. This result provides more support for Ge as suitable candidate for a sacrificial layer in the production of thin film based magnetic particles.

4.3.2 SAF behaviour on Si vs Ge

Having eliminated Al as a potential sacrificial layer, with the results in the previous section showing Ge to be a superior option, further experiments were made to investigate the effect of a Ge underlayer on the behaviour of perpendicular CoFeB films. First, single PM CoFeB layers in the form $Ta(2)/Pt(2)/CoFeB(x)/Pt(2)/Ta(2)$, with thicknesses in nm and where $x = 0.6-1.4$, were grown on top of Si and Ge. The MOKE

loops taken from each sample are presented in Figure 4.12, which show sharp transitions for all samples, alongside a graph of coercivity versus CoFeB thickness (t_{CoFeB}). From these data we find that both sets of films exhibit an decrease in H_C with increasing t_{CoFeB}. The Ge sample set gives H_C values that are consistently higher than the Si counterparts, with a slightly steeper slope compared with the Si set. This is consistent with previous findings: slightly increased roughness in the films, generated by the Ge surface, leads to greater domain wall pinning in the samples during a magnetic transition.

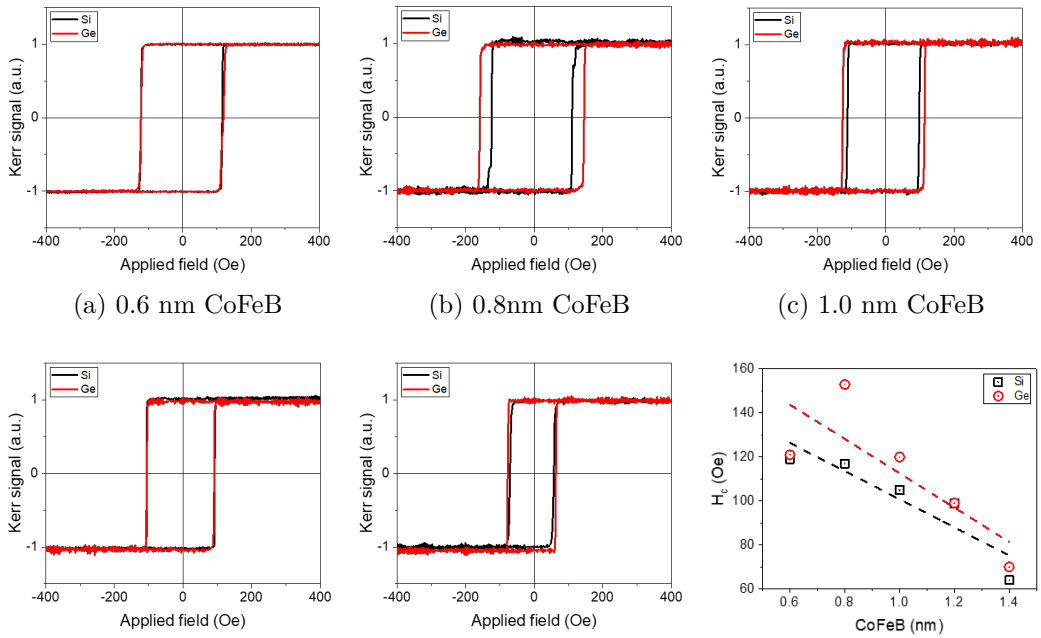

(a) 0.6 nm CoFeB (b) 0.8nm CoFeB (c) 1.0 nm CoFeB

(d) 1.2 nm CoFeB (e) 1.4 nm CoFeB (f) Coercivity

Figure 4.12: (a)–(e) MOKE loops from a single layer series grown in the form $Ta(2)/Pt(2)/CoFeB(x)/Pt(2)/Ta(2)$, where CoFeB thickness, x, was varied from $0.6 - 1.4$ nm. (f) The relationship between CoFeB thickness and H_C, with linear fits added to guide the eye.

Domain imaging

Next, domain imaging of the thin films, using polar Kerr microscopy, was used to thoroughly probe the nucleation and propagation behaviour that drive the PM CoFeB transitions. To begin with, a single layer of 0.9 nm PM CoFeB that had been grown on Si and Ge was imaged: a series of snapshots are displayed in Figure 4.13. Both sets of images show single nucleation sites, in the field of view, followed by rapid domain wall propagation; the single PM CoFeB experiences propagation-dominated switching, corresponding to the sharp MOKE switches.

Figure 4.14 shows a series of domain images from a pair of the SAF samples from Section 4.3.1 with $t_{Pt} = 0.5$ nm, taken during the AP–P transition. Here, we observe a number of nucleation sites, which are likely the result of the ultrathin Pt interlayers that will have added significant texture to the thin film. These small domains then

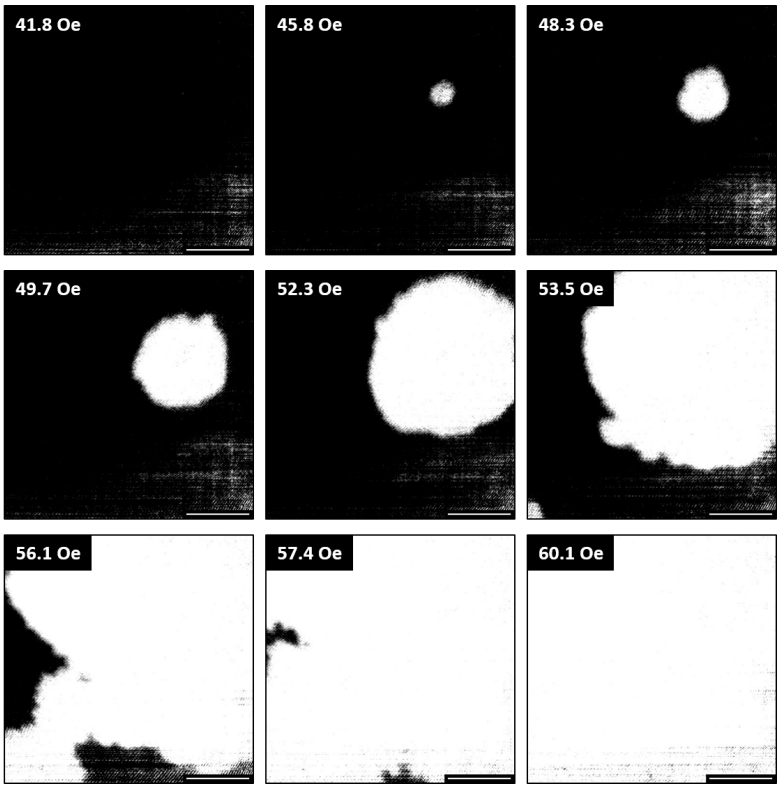

(a) Si

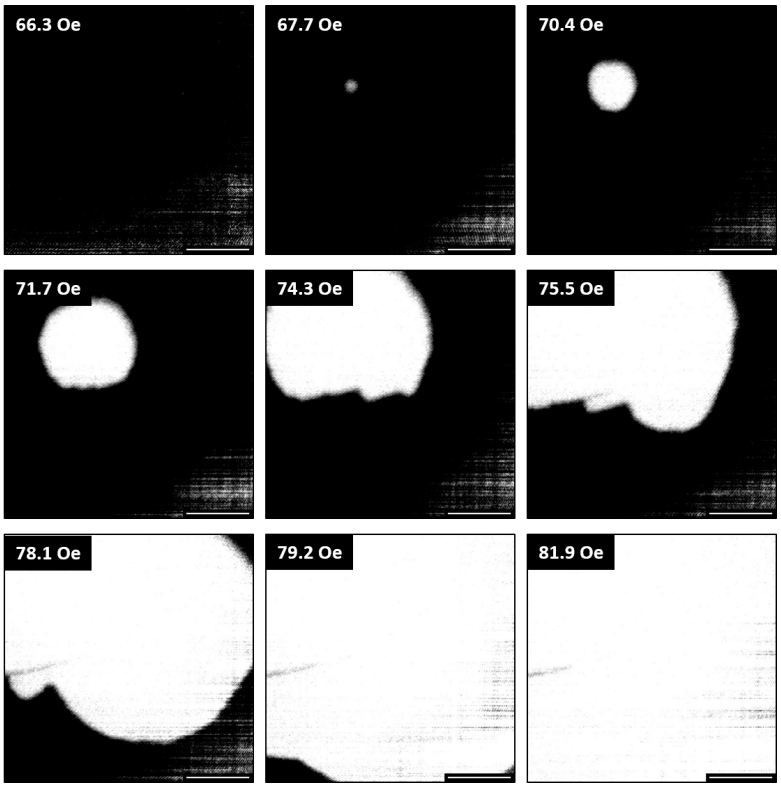

(b) Ge

Figure 4.13: The Kerr domain images of a single layer of 0.9 nm PM CoFeB grown on (a) Si and (b) Ge. Scale bar is 100 μm.

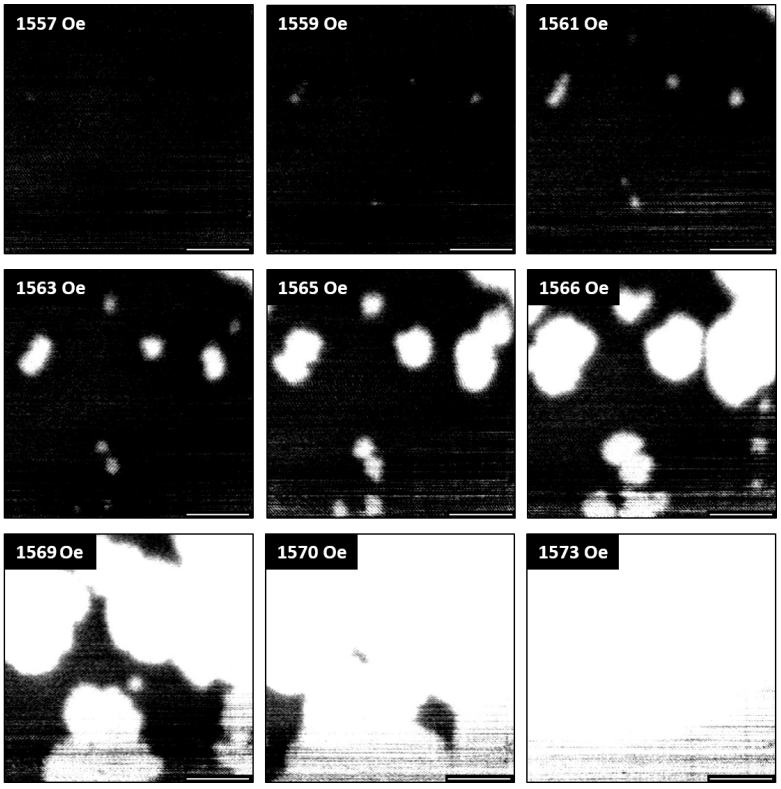

(a) Si

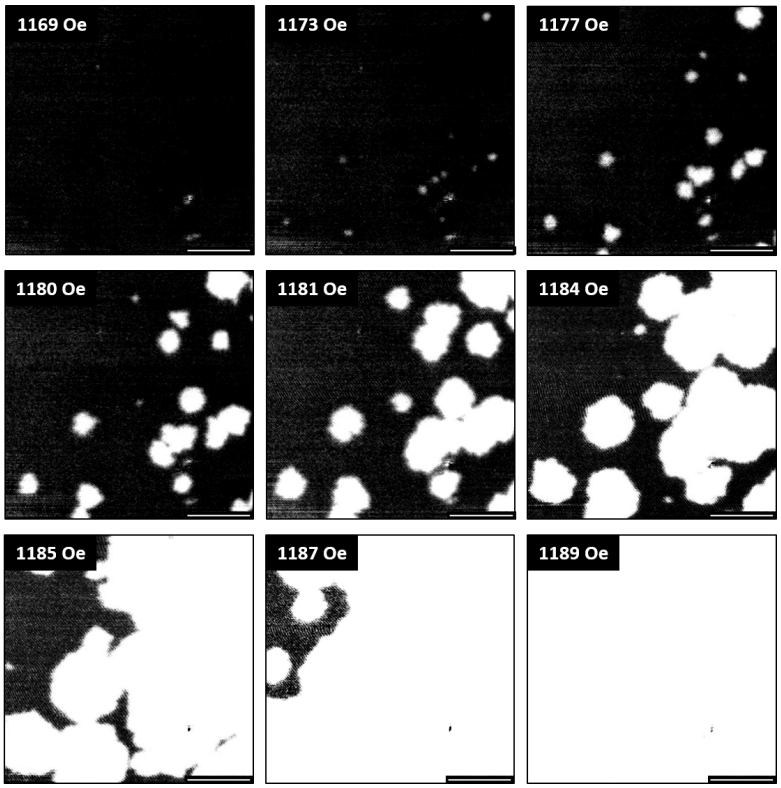

(b) Ge

Figure 4.14: Kerr microscopy domain images of SAFs switching from the AP to P state for bilayers grown on (a) Si and (b) Ge. The Pt interlayer thickness is 0.5 nm. Scale bar is 100 μm.

quickly merge together, generating the rapid domain wall propagation that results in the sharp MOKE transitions discussed previously. These results are consistent with an earlier study of domain wall dynamics in coupled CoFeB multilayers, with ultrathin Pt interlayers, where transitioning from the AP–P state was found to occur via a relatively high density of domains [10].

Comparison of SAF switches

Earlier work [10] found that there was a relationship between the thickness of the Pt interlayer and the domain wall behaviour during the AP–P transition: namely that for highly coupled films, with thinner Pt, nucleation of a higher density of domains was seen, whilst less coupled samples transitioned via single domains. Since reversal during AP–P transitions is dominated by local FM or low AF couling, this behaviour was attributed to an increased density of pinholes with decreasing Pt thickness. Additionally, the study discovered a difference in the behaviour of transitioning from the AP–P state versus the P–AP state: the P–AP transition always occurred via the nucleation of a single domain, similar to a single layer CoFeB sample. This was explained by the nature of P–AP transitions, where domain nucleation is generated by local areas of high AF coupling, which is not caused by pinholes. Using our set of SAF samples, grown on Si and Ge with a series of values of t_{Pt}, we investigated whether the Ge underlayer has an effect on these behaviours.

Figure 4.15 presents snapshots of the domain pattern of SAFs switching for both the AP–P and the P–AP transition, for five different t_{Pt}'s, comparing samples grown on Ge with those on Si. Focusing on the AP–P transition (Figure 4.15a) we observe the same relationship between t_{Pt} and domain pattern as was previously found [10]: increasing nucleation sites with decreasing t_{Pt}. This somewhat corresponds with the pattern observed in the Ge samples: there is a decrease in the number of nucleation sites between the $t_{Pt} = 0.41$ nm and $t_{Pt} = 0.48$ nm samples. However, the rest of the sample series continues to transition via multiple nucleation sites within the field of view, with not even the thickest t_{Pt} sample transitioning through the propagation of a single domain in the way that the equivalent Si sample does. This indicates that for the thinnest t_{Pt} Ge samples, the characteristics of the transition are driven by the texturing from the ultrathin Pt, which will create large numbers of defects. These growth defects are likely to manifest as pinning sites, which limit domain wall propagation, and pinholes in the interlayer motif, which create local regions of FM coupling between the CoFeB layers and thus nucleation sites for the AP–P transition. However, as t_{Pt} increases the film becomes smoother and the number of pinning sites and pinholes reduce. However, unlike in the Si samples, there is a contribution from the Ge texturing, which prevents the shift towards single nucleation sites and propagation dominated AP–P transitions.

With regards to the P–AP transition (Figure 4.15b), we again observe analogous results to the previous work for our Si substrate samples: domains propagate rapidly,

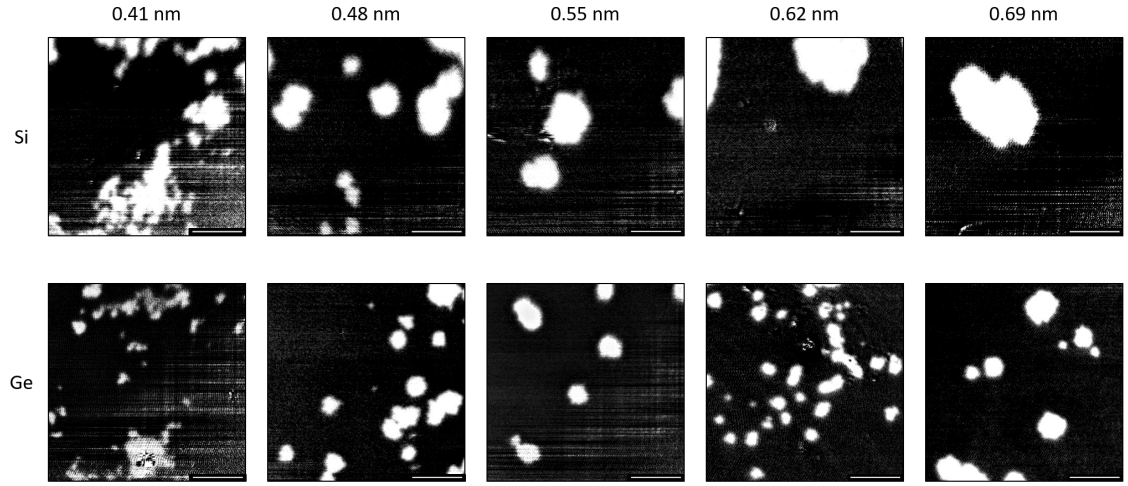

(a) AP–P

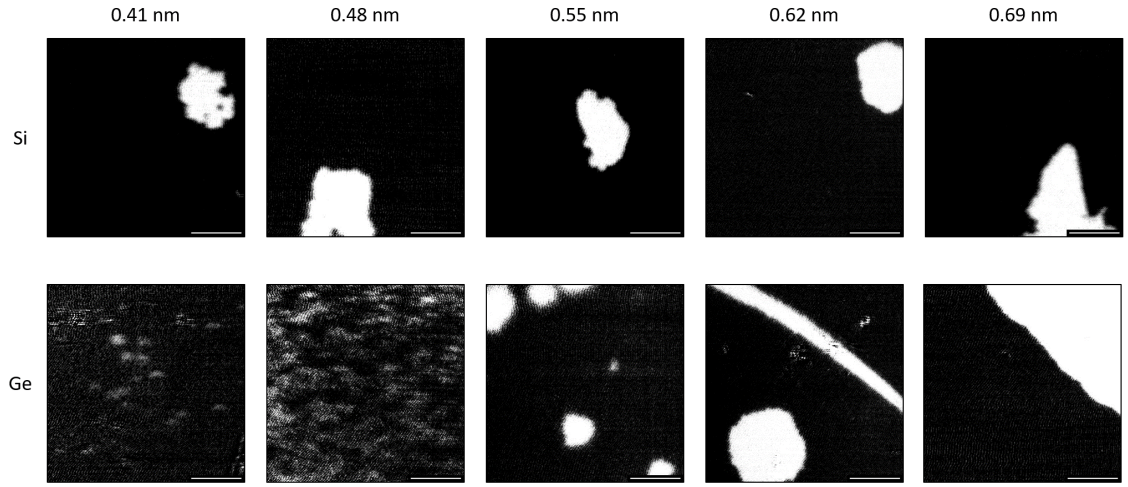

(b) P–AP

Figure 4.15: Snapshots of Kerr microscopy domain imaging of SAFs switching from the AP–P or the P -AP state. Images shown for samples grown on both Si and Ge, with a range of Pt interlayer thicknesses (noted above the images). All images are shifting from black to white. The scale bar is 100 μm.

originating from a single nucleation site in the field of view, for all values of t_{Pt} [10]. Conversely, the Ge samples exhibit variation in domain dynamics across the range of t_{Pt}. The Ge sample with the thickest Pt interlayer shows similar behaviour to the Si counterpart: a large sweeping domain appearing to originate from one local nucleation site. However, as t_{Pt} is reduced the number of nucleation sites in the field of view increases, but for thicknesses down to 0.55 nm the domains continue to propagate to complete the P–AP transition. On the other hand, the two samples with the thinnest t_{Pt} exhibit nucleation dominated transitions: speckled nucleation sites increase in number over time, with no manifestation of domain wall propagation. A possible explanation for this behaviour is orange peel coupling. Here, relatively long wavelength roughness (as was found for Ge) in a film with high OOP anisotropy creates local sites of strong AF coupling [13]. These act as nucleation sites that drive

nucleation dominated magnetic reversal. This is manifested more in the films with thinner t_{Pt} where there will be an increased number of defects (including pinning sites and local variation in coupling strength), which will cause the layer to nucleate a lot of separate domains before it can reverse completely.

4.3.3 Field sweep dependent switching of SAFs on Ge

Observation of AP–AP transitions in highly coupled SAFs

Kerr microscopy domain imaging was performed on a new series of SAF bilayers that were grown on Ge (electron beam evaporated) with the form $Ta(2)/Pt(2)/CoFeB(0.9)/Pt(t_{Pt})/Ru(0.9)/Pt(t_{Pt})/CoFeB(0.9)/Pt(2)/Ta(2)$, where t_{Pt} was in the range $0.37-0.64$ and thicknesses were in nm. Snapshots of the domain behaviour during the different transitions of each sample are displayed in Figure 4.16. As we found previously (see Section 4.3.2), there is a clear difference in domain dynamics between the AP–P and P–AP transitions: the P–AP switches are generally occurring via the propagation of large domains, while the AP–P switches involve more numerous nucleation sites. Furthermore, we discover a third transition in the three thinnest t_{Pt} samples, which exhibits a lower contrast between states; a more complete series of the domain images for the $t_{Pt} = 0.42$ nm sample can be found in Figure A.1 in the Appendix, where the contrast is kept the same across the set. The middle transition exhibits large domains with propagation driven dynamics. Additionally, we find a very similar domain pattern during the AP–P and P–AP transitions, which indicates that the same layer is switching in both cases. These results strongly suggest that this extra transition is an AP–AP transition, whereby the top and bottom CoFeB layers simultaneously switch direction.

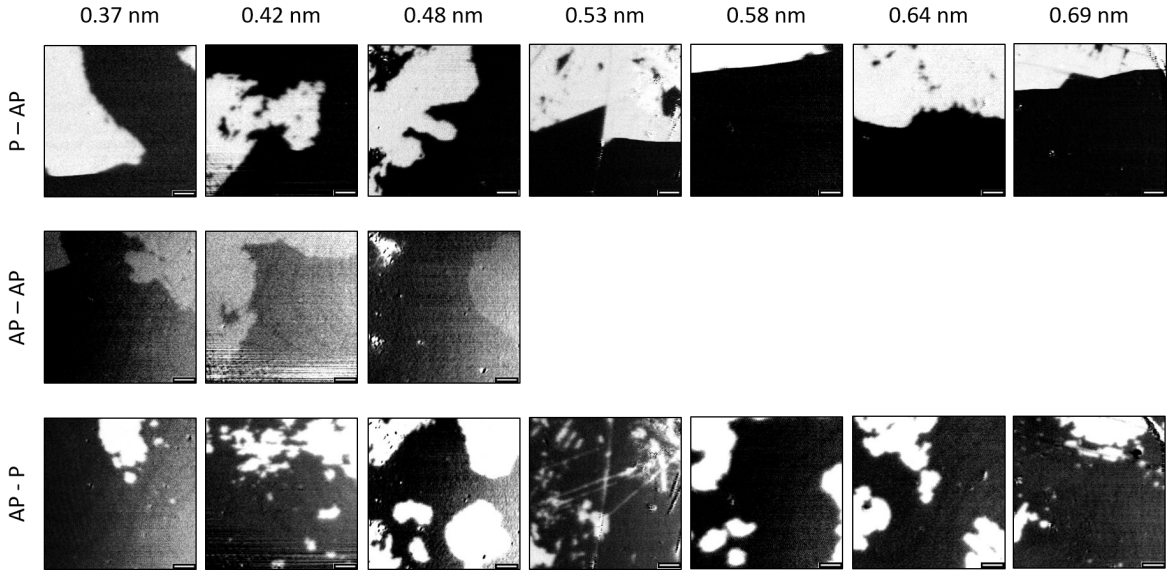

Figure 4.16: Snapshots from domain imaging of SAFs grown on Ge highlighting the P–AP, AP–P and AP–AP transitions across a range of t_{Pt} (noted above the images). All images are shifting from black to white. The scale bar is 50 μm.

The coercivity of these PM SAF systems are highly dependent on field sweep rate (FSR), due to the magnetic reversal being a thermally activated process. At low FSR the system spends more time at a particular applied field and therefore has a higher probability of switching magnetically, which induces a lower switching field and thus a lower coercivity. The FSR used while taking these domain images is particularly slow, due to the quasi-static nature of the field application. Hence, to investigate whether FSR has an effect on the presentation of the AP–AP transition, we took MOKE loops of the $t_{Pt} = 0.42$ nm sample across a range of field sweep rates, as presented in Figure 4.17. Here, the highest FSR (7.6 kOe/s) is similar to what we generally use to make MOKE measurements of our thin films, while the lowest (0.08 kOe/s) is as close as we can get to replicating the quasi-static type field application during domain imaging (using the minimum field frequency of the system, 0.005 Hz).

For the four highest FSR loops, we find the characteristic decrease in coercivity with decreasing FSR. An additional transition then appears in the 0.79 kOe/s loop. As we decrease the FSR even further, we see this additional transition slightly shift towards zero field. As MOKE is a depth dependent measurement, it allows us to distinguish the switching of the top CoFeB layer (higher Kerr signal) from the bottom CoFeB layer (lower Kerr signal). Looking at the heights of the transitions in the loops with the added switching, it appears that the larger two measure a similar level of Kerr signal, indicating that it could be the same layer switching. From this we infer that the additional, third transition is in fact an AP–AP transition and thus that both the AP–P and P–AP involve the bottom layer switching. This corresponds with the findings in the domain images.

As has been shown, both in Section 4.3.1 and in earlier work [16], underlayers can have large effects on the magnetic properties of CoFeB thin films. Here, the bottom layer of CoFeB is grown on top of the buffer layers (Ta/Pt), whilst the top layer is grown on top of the interlayers ($Pt/Ru/Pt$). By using particularly thin Pt interlayers we generate increased numbers of growth defects. Additionally, there tends to be a general degradation of structure conditions up a multilayer stack [10, 15]. We envisage that altogether, this could cause an inherent imbalance in the two CoFeB layers and leads to one of them having a slightly higher moment (M^+) than the other (M^-), an example of this is shown in Figure 4.18a. The imbalance induces differences in energy in the two AP states, under the application of a magnetic field. This gives rise to the potential for transitions between the AP states.

We have observed that the AP–AP transition is mediated by domain wall motion, however its existence is not trivial. Neither the anisotropy nor the coupling energy favour one of the two AP states, and a switch from one AP state to the other cannot be initiated by local defects with high AF or high FM strength. However, in the case of an AF coupled film with a moment imbalance, the Zeeman energy will favour the alignment of the M^+ layer with the field, and thus one of the AP states over the other. This explains why the switching of the M^+ layer might be induced, but not why M^- layer also switches.

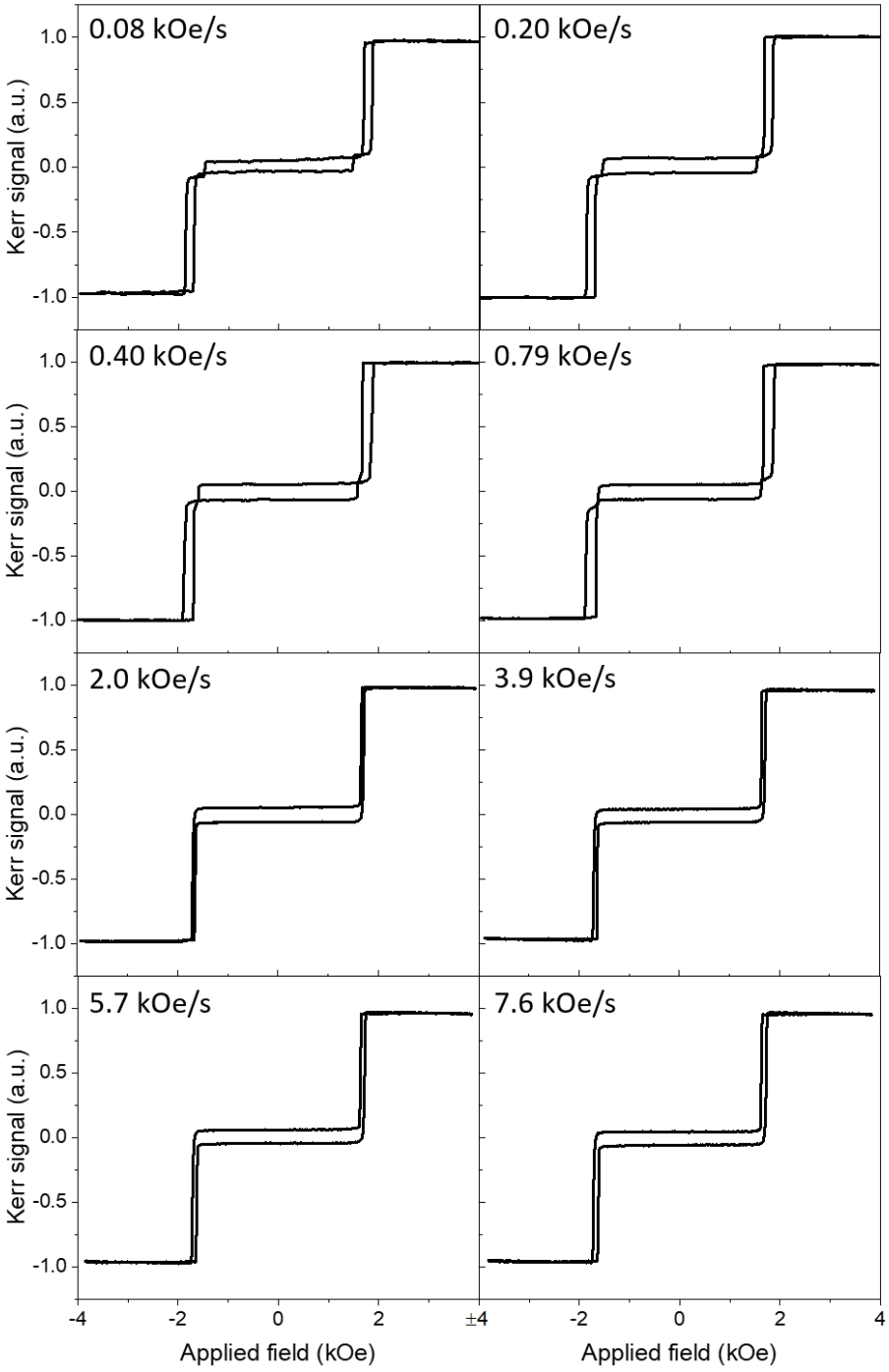

Figure 4.17: MOKE loops across a range of FSRs for the film with $t_{Pt} = 0.42$ nm.

It could be thought that an AP–AP transition might be caused by the flipping of the M^+ layer (to align with the field), immediately followed by the M^- layer due to the AF coupling making the AP state favourable. However, in a spin-flip transition, the switching field of an M^+ layer will occur at a high enough field that it would not be desirable for an M^- layer to switch into an AP alignment with the field. This concept cannot therefore explain the manifestation of an AP–AP transition.

An alternative theory starts with the assumption that there is the formation of a dual AP state at remanence: the majority of the film exists in in the top-up/bottom-down state, while a small region is in the top-down/bottom-up state. It has been

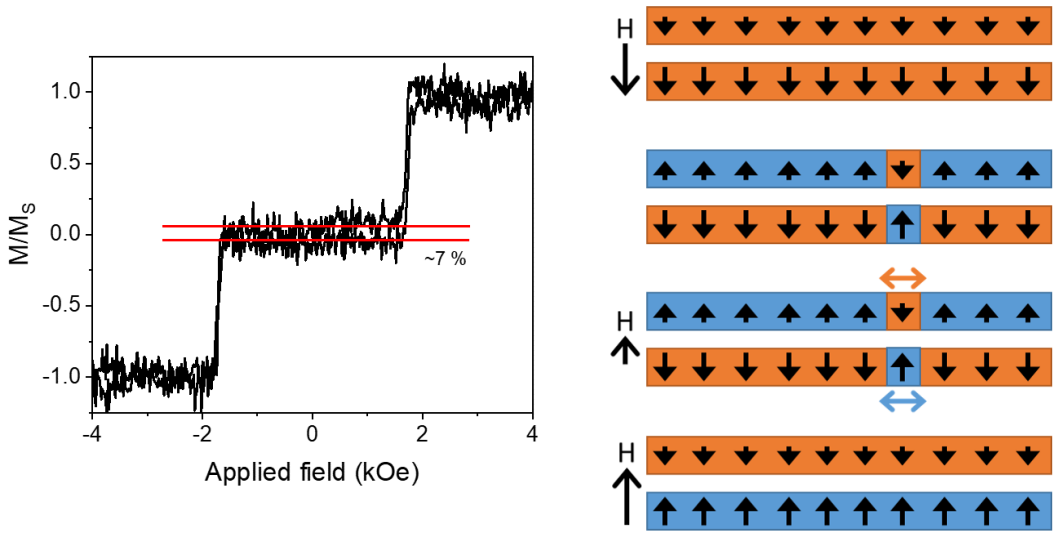

(a) VSM of imbalance (b) AP–AP mechanism 1

Figure 4.18: (a) The moment imbalance (∼7%) depicted in the VSM loop of the t_{Pt} =0.48 nm SAF from bilayer series in this section. (b) A schematic of the AP–AP transition mechanism originating from a dual AP state. The arrows in the blue (up) and orange (down) regions represent the direction of moment in the two imbalanced layers of CoFeB. H represents the applied field direction. The orange and blue arrows indicate the direction of domain wall propagation.

postulated that this could be caused by some thickness inversion in the magnetic layers, originating from growth defects [4]. This localised area of opposite AP state would cause domain walls to form in both layers and could constitute a AP–AP nucleation site. As an applied field is increased, the domain walls will want to propagate to minimise the energy of the system. Additionally, the Zeeman energy is favouring the AP state which maximises M^+ layer alignment with the field. However, the AF coupling makes it beneficial for the domain walls to remain bound, and so they propagate simultaneously, in the direction that best minimises the Zeeman energy. This model is summarised in the schematic in Figure 4.18b.

The fact that the AP–AP transition has manifested in our samples with the strongest coupling is consistent with an unpublished study [4]. The theory behind this is that for the domain walls to propagate together, they must be strongly enough coupled for this to be energetically favourable. Additionally, the FSR dependence of our AP–AP transitions, i.e. their manifestation only at sufficiently low FSR (highlighted in Figure 4.17), is also consistent with the previous study [4]. This is due to the inherent dependence of coercivity on FSR: both the AP–AP and the AP–P switches have a coercivity that decreases with decreasing FSR. As there is a greater rate of change in the AP–P coercivity, when FSR is increased there is eventually a point when the AP–P transition occurs at a lower applied field than a potential AP–AP transition. Thus, the AP–AP transition is extinguished and the AP–P transition occurs via the opposite layer, as we found.

The presence of an AP–AP transition in a PM SAF film would be interesting in

the field of magnetic memory. Domain walls between multiple AP states have already been used for race track memory [18].

Reversal of switching order in weakly coupled SAFs

A set of PM SAFs weakly coupled via the 2nd AF peak were grown on Ge with the form $Ta(2)/Pt(2)/CoFeB(t_{CoFeB})/Pt(t_{Pt})/Ru(2)/Pt(t_{Pt})/CoFeB(t_{CoFeB})/Pt(2)/Ta(2)$ where thicknesses are in nm, $t_{CoFeB} = 0.8$ or 1 and $t_{Pt} = 0.21$, 0.27 or 0.32. To assess the FSR dependence of their hysteresis, MOKE loops were measured at various field frequencies. That of each sample, taken at the minimum (0.02 kOe/s) and maximum (7.0 kOe/s) FSR, are displayed in Figures 4.19a–4.19f.

As expected, due to the particularly weak coupling of these samples, we did not find any manifestation of AP–AP transition in these samples. However, we did find some differences in switching layer order. The loops in 4.19a, c and d all display the

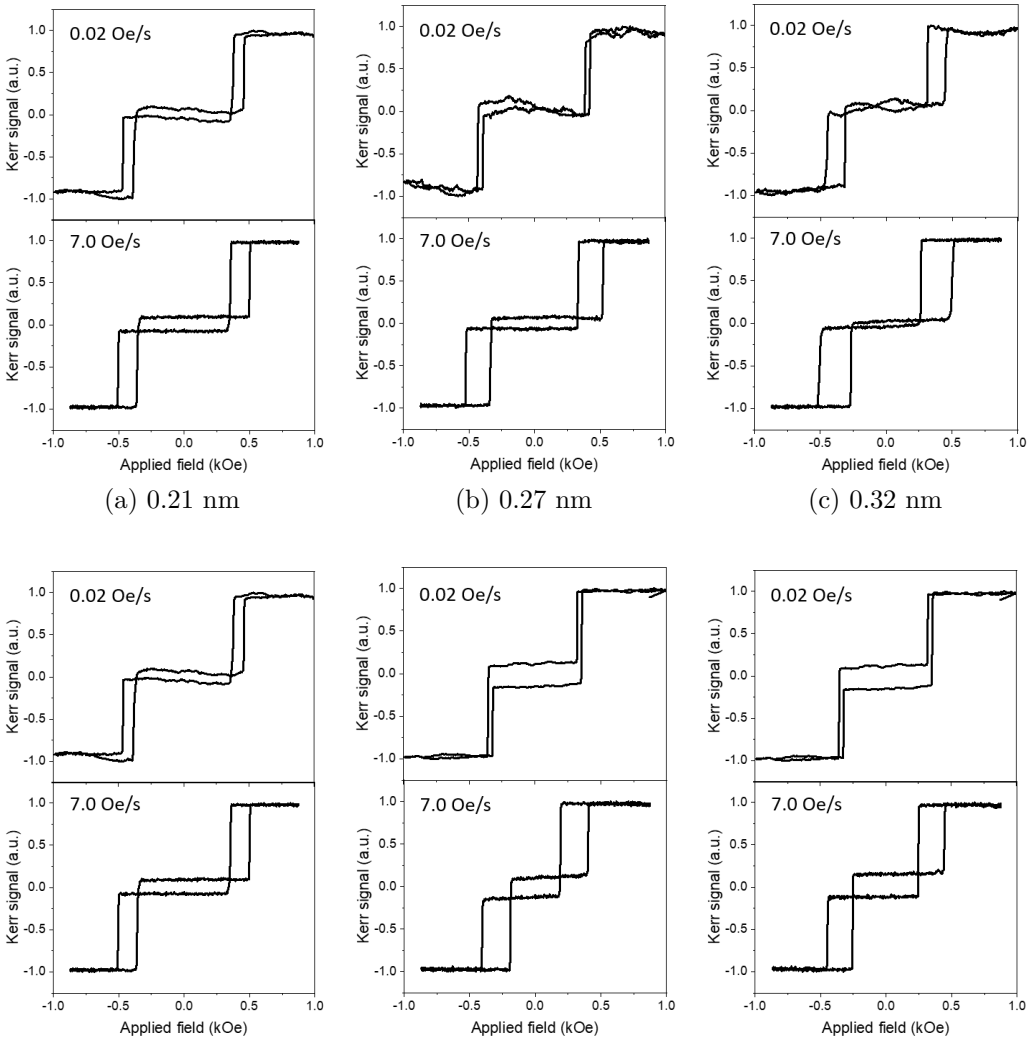

(a) 0.21 nm (b) 0.27 nm (c) 0.32 nm

(d) 0.21 nm (e) 0.27 nm (f) 0.32 nm

Figure 4.19: MOKE loops for the maximum and minimum values of FSR for the (a)–(c) 0.8 nm and (d)–(f) 1 nm CoFeB samples, across three different values of t_{Pt} (0.21 nm, 0.27 nm and 0.32 nm).

same order of switching at both values of FSR: the top CoFeB layer switches P–AP and the bottom switches AP–P. At the higher FSR, the loops in b, e and f switch in the same way: top P–AP and bottom AP–P. Conversely, at the lower FSR, the loops in b, e and f exhibit a reversal in layer switching: the bottom layer switches P–AP and the top layer switches AP–P. This indicates that we have discovered, for this small subset of 2nd AF peak PM SAFs, the potential for FSR controlled selective layer switching.

This phenomenon was previously demonstrated in AF coupled PM bilayers comprised of a Co-CoFeB layer pair, with different proximities to the SRT and an appropriate coupling value [3]. By using that particular film design, which created a highly-asymmetric SAF, an overlap in the FSR dependence curves for the two different layers was generated. This meant that at different applied field frequencies, the probability of which layer switched first was modulated, and dynamic field control of the layers was made possible.

In the case of our 2nd AF SAFs, the thin film stack has not been designed with a large asymmetry. VSM reveals a small imbalance in the CoFeB layer pairs, in the region of a 5–7% difference, as was observed in the 1st AF SAFs earlier (see Figure 4.18a). However, this is certainly not a large enough imbalance to cause a crossover in the sweep rate dependence curves like that exploited in the previous work. Nevertheless, it has been made clear that the use of particularly low t_{Pt}, which in this case is close to the atomic radius of Pt, generates large numbers of growth defects in a SAF film. These defects have significant consequences on the domain dynamics of the individual CoFeB layers, as they drive nucleation and can limit propagation. At high FSR transitions tend towards nucleation-dominated behaviour. This is due to the FSR being so high that new domains nucleate before existing domains have had the time to propagate, causing a multi-domain transition. Hence, the order of switching is determined by the layer with the lowest nucleation field. At low FSR, where the transitions are more propagation-dominated (as the FSR no longer takes over domain propagation), a large number of pinning sites might cause the order of switching to instead be determined by the layer with the lower propagation field. If the layer with the lower nucleation field does not also have the lower propagation field, this could generate an FSR dependence in switching order. This concept is consistent with the switching order observed in our MOKE loops: in the samples that exhibit a change in switching order, we find that at high FSR the top layer switches first, but at low FSR the bottom layer switches first. This makes sense, as we expect more defects to be present in the top CoFeB layer (grown on the sub-nm Pt interlayer and further from the Ta/Pt buffer), in the form of nucleation and pinning sites.

Although this phenomenon is not yet reproducible, having come about randomly through the occurrence of a series of particular defects in a sample, it seems there is the potential to recreate it seeing as it has manifested in three of the six samples analysed in this section. The ability to select the switching order of a SAF through controlling the FSR could be exploited in areas such as sensing and data storage.

4.4 Conclusion

By taking the established concept of using PM SAFs for biological applications, this chapter has demonstrated how we can build on the flexibility of this type of thin film. The findings extend the scope for tuning the properties of PM SAFs, exhibiting how they can be tailored towards different purposes.

We studied how changing different components of the multilayer stack influences its magnetic behaviour. We show that repeats of the bilayer can be used to generate an increase in magnetic moment, which could be beneficial for torque based applications. By manipulating the interlayer motif we exhibit coarse and fine control of the magnetic switching characteristics, through the Ru and Pt thicknesses respectively, which is key in fields such as magnetic sorting. This lead on to the engineering of multi-bilayer thin films with multiple switching fields, an interesting concept for multiplex sorting.

We explored the effects of additional parameters on the magnetic transitions of PM SAFs. A focus was made on underlayers due to their necessity in the fabrication of magnetic particles for liquid applications. Ge was established as a strong underlayer candidate for the production of robust SAF films. Nonetheless, it was also found to have some interesting effects on domain dynamics. Additionally, by exploiting the FSR dependence of PM SAFs, some interesting phenomena were uncovered: AP–AP transitions in highly coupled SAFs and dynamic selective switching in 2nd AF peak SAFs. Films displaying these types of behaviours could be used in applications such as race track memory or sensing and data storage respectively.

Overall this work provides a robust toolbox for the design of PM SAFs to be used in a wide range of applications, including those in a biological environment.

References

[1] S. Bandiera, R. C. Sousa, S. Auffret, B. Rodmacq, and B. Dieny. Enhancement of perpendicular magnetic anisotropy thanks to Pt insertions in synthetic antiferromagnets. *Applied Physics Letters*, 101(7):072410, aug 2012.

[2] P Bruno and C Chappert. Ruderman-Kittel theory of oscillatory interlayer exchange coupling. *Phys. Rev. B*, 46(1):261–270, 1992.

[3] A. Fernández-Pacheco, F. C. Ummelen, R. Mansell, D. Petit, J. H. Lee, H. J.M. Swagten, and R. P. Cowburn. Dynamic selective switching in antiferromagnetically-coupled bilayers close to the spin reorientation transition. *Applied Physics Letters*, 105(9), 2014.

[4] K D Hakkel. Anti-ferromagnetically-coupled domain walls in synthetic ferrimagnets. Technical report, 2016.

[5] Olav Hellwig, Andreas Berger, Jeffrey B. Kortright, and Eric E. Fullerton. Domain structure and magnetization reversal of antiferromagnetically coupled per-

pendicular anisotropy films. *Journal of Magnetism and Magnetic Materials*, 319(1-2):13–55, dec 2007.

[6] M T Johnson, P J H Bloemen, F J A den Broeder, and J J de Vries. Magnetic anisotropy in metallic multilayers. *Reports on Progress in Physics*, 59(11):1409–1458, 1996.

[7] H. Joisten, T. Courcier, P. Balint, P. Sabon, J. Faure-Vincent, S. Auffret, and B. Dieny. Self-polarization phenomenon and control of dispersion of synthetic antiferromagnetic nanoparticles for biological applications. *Applied Physics Letters*, 97(25):253112, 2010.

[8] R. Lavrijsen, A. Fernández-Pacheco, D. Petit, R. Mansell, J. H. Lee, and R. P. Cowburn. Tuning the interlayer exchange coupling between single perpendicularly magnetized CoFeB layers. *Applied Physics Letters*, 100(5):052411, jan 2012.

[9] Reinoud Lavrijsen, Ji Hyun Lee, Amalio Fernández-Pacheco, Dorothée C.M.C. Petit, Rhodri Mansell, and Russell P. Cowburn. Magnetic ratchet for three-dimensional spintronic memory and logic. *Nature*, 493(7434):647–650, 2013.

[10] J. H. Lee, R. Mansell, D. Petit, A. Fernández-Pacheco, R. Lavrijsen, and R. P. Cowburn. Domain imaging during soliton propagation in a 3D magnetic ratchet. *SPIN*, 03(04):1340013, dec 2013.

[11] Rhodri Mansell, Tarun Vemulkar, Dorothée C. M. C. Petit, Yu Cheng, Jason Murphy, Maciej S. Lesniak, and Russell P. Cowburn. Magnetic particles with perpendicular anisotropy for mechanical cancer cell destruction. *Scientific Reports*, 7(1):4257, 2017.

[12] T. A. Moore, I. M. Miron, G. Gaudin, G. Serret, S. Auffret, B. Rodmacq, A. Schuhl, S. Pizzini, J. Vogel, and M. Bonfim. High domain wall velocities induced by current in ultrathin Pt/Co/AlOx wires with perpendicular magnetic anisotropy. *Applied Physics Letters*, 93(26):262504, dec 2008.

[13] J. Moritz, F. Garcia, J. C. Toussaint, B. Dieny, and J. P. Nozières. Orange peel coupling in multilayers with perpendicular magnetic anisotropy: Application to (Co/Pt)-based exchange-biased spin-valves. *Europhysics Letters*, 65(1):123–129, 2004.

[14] S. S.P. Parkin. Systematic variation of the strength and oscillation period of indirect magnetic exchange coupling through the 3d, 4d, and 5d transition metals. *Physical Review Letters*, 67(25):3598–3601, 1991.

[15] Dorothée Petit, Reinoud Lavrijsen, Jihyun Lee, Rhodri Mansell, Amalio Fernández-Pacheco, and Russell P. Cowburn. Systematic layer-by-layer characterization of multilayers for three-dimensional data storage and logic. *Nanotechnology*, 27(15), 2016.

[16] T. Vemulkar, R. Mansell, D. C. M. C. Petit, R. P. Cowburn, and M. S. Lesniak. The effect of underlayers on the reversal of perpendicularly magnetized multilayer thin films for magnetic micro- and nanoparticles. *Journal of Applied Physics*, 121(4):043908, 2017.

[17] T Vemulkar, R Mansell, D C M C Petit, R P Cowburn, and M S Lesniak. Highly tunable perpendicularly magnetized synthetic antiferromagnets for biotechnology applications. *Applied Physics Letters*, 107(1):012403, jul 2015.

[18] See Hun Yang, Kwang Su Ryu, and Stuart Parkin. Domain-wall velocities of up to 750 m s-1 driven by exchange-coupling torque in synthetic antiferromagnets, 2015.

Chapter 5

Perpendicularly magnetised nanodiscs

5.1 Introduction

The use of magnetic particles in biological and other fluidic environments has become increasingly widespread, with applications including cancer therapy, drug delivery, contrast agents and tissue engineering [11, 22]. These applications exploit a variety of properties exhibited by magnetic particles, for example: heat generation is used for magnetic hyperthermia cancer therapy [6, 40]; mechanical activation is utilised in the manipulation and control of cells and proteins [20, 31], and also in mechanically destructive cancer therapies [26, 45]; and magnetic switching and capture has been employed across cell separation, bio-molecule isolation and purification techniques [8, 10, 23, 31, 32]. With such a diverse array of potential applications it is beneficial to be able to tailor the particles to an individual situation and maximise their efficacy and efficiency. Therefore, engineering particles that allow for flexibility in design is highly desirable. This flexibility extends not only into the magnetic properties, but the size and shape of the particles must also be considered.

When designing a magnetic particle for a particular application, there are a number of characteristics that should be considered to optimise efficacy. In biological, or other liquid, environments it is necessary to engineer particles that are stable in fluid such that they will be well dispersed and not agglomerate. Surface functionalisation techniques can be successful at minimising or eliminating dipolar interactions [9, 12, 15, 49], however, they add significant processing steps to particle production. Thus, it is more convenient to engineer particles with a net zero moment. A low susceptibility is also desirable, as this will prevent the possibility of particles staying agglomerated after the application of an applied field [25, 33]. The second key characteristic for flexible design is an easily and widely tunable particle; the potential to control multiple parameters of the magnetic state of a set of particles allows them to be used effectively for a variety of applications. Such parameters include: the magnetic moment, particularly for the purpose of applying torques; and the activation or saturation field, preferably with a sharp

and efficient switch [38]. Finally, for the purpose of transduction of torques, particles with a strong magnetic anisotropy (e.g. strong uniaxial anisotropy) are significantly more efficient [45].

So far, superparamagnetic iron oxide nanoparticles (SPIONs) have been the major candidates for biological applications [11, 14, 22]. SPIONs are produced via a relatively simple chemical synthesis method, which has been successfully industrialised, and are naturally of a biologically relevant size. However, their simplistic magnetic state limits their tunability and can also lead to some undesirable effects. As we can see from the example hysteresis loop in Figure 5.1a, SPIONs generally exhibit a zero remanent state, although high field sweep rates induce a coercivity (as exploited in magnetic hyperthermia), which could lead to particle agglomeration due to their high susceptibility [25, 49]. Additionally, SPIONs can also be prone to agglomeration through surface interactions due to their small, colloidal state, without significant engineering [9, 12, 15, 44, 49]. The simple SPION magnetic state does not allow for control when it comes to switching field, and the potential for increasing moment is very limited as it doesn't take much to transform particles into ferromagnets.

Another type of magnetic particle that has been implemented in biological applications is magnetic vortex (MV) microdiscs, favoured for their high magnetic moment and ease of fabrication [26, 31, 33, 42]. The hysteresis loop of such particles is displayed in Figure 5.1b. Here, we also have a zero remanence state and a relatively low susceptibility, which limits particle agglomeration [33]. These particles offer a range of diameters and thicknesses, although they are somewhat limited in size and aspect ratio as the existence of the vortex state is driven by the disc dimensions [5]. Namely, there is little scope for tuning of particle structure or magnetic switching.

In-plane synthetic antiferromagnetic (SAF) particles, address some of the issues seen with SPIONs and MV discs: they exhibit zero remanence, can be designed to have low field susceptibility and offer a level of tunability for applications [18, 24]. Additionally, they will, in principle, produce larger torques than MV particles [33]. However, they have been shown to suffer from self-magnetisation after the application of a magnetic field if their susceptibility is too high (see Section 6.4.1) and are more difficult to fabricate than MV discs [25, 33].

Conversely, research into perpendicularly magnetised (PM)/out of plane SAF par-

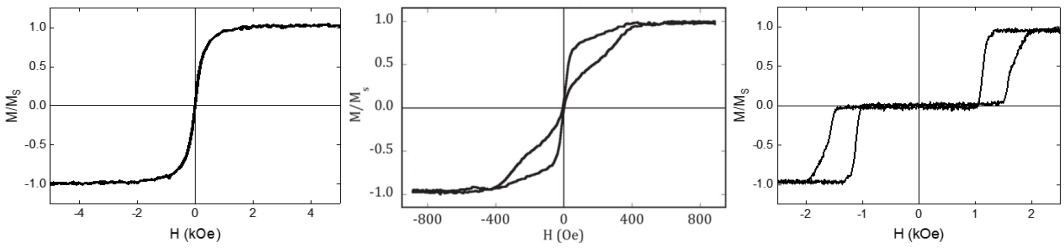

(a) Superparamagnetic (b) Magnetic vortex (c) PM SAF

Figure 5.1: Hysteresis loops of different types of magnetic particles. (b) is taken from [43].

ticles has shown them to be a promising answer to all of the desirable characteristics in liquid based applications, along with providing a flexible particle structure that allows for finer control in activation and assembly [38, 46]. The PM SAF state, as shown in Figure 5.1c, provides the key combination of zero remanence and low field susceptibility, which prevents particle agglomeration and aggregation even after application of fields. It is also relatively trivial to increase the magnetic moment of these discs, without compromising zero remanence, to maximise the transduction of mechanical forces. The strong uniaxial anisotropy exhibited by the PM state provides two advantages: the driving of sharp magnetic switches, which makes particle activation efficient; and more effective mechanical actuation and torque production under applied fields [45]. Finally, the engineered SAF state provides a high level of tunability [38], allowing the possibility to adapt particles for different applications. Previous work has demonstrated PM SAF particles as strong candidates in magneto-mechanical cancer therapies [45] and there is potential for their self-assembly behaviour in liquid to be exploited in areas such as microfluidics, biosensing or soft-robotics [46].

As previously mentioned, size and structure should also be considered when designing magnetic particles towards a particular application: it would be advantageous to be able to fabricate particles in a wide range of sizes. Particularly in biological environments, when particles may need to be taken up by cells or attached to submicroscopic proteins, the ability to create particles in the nanoscale may be necessary. To date, one limitation of PM SAF particles is size: although methods for the production of microdiscs have been well developed, obtaining good yields of well defined particles on the nanoscale has been a challenge. This chapter will discuss a new method for the fabrication of thin film based nanodiscs, which will allow access to a substantial range of disc sizes and thus enables PM SAFs to be tailored to a multitude of biological applications. The technique manufactures high yields of well-defined, magnetically robust magnetic particles on a sub-micron length-scale. PM SAF particles, created via this method, will then be characterised: including studies on how this magnetic state is effected by the patterning process and an exploration of the consequences for tunability towards liquid based applications.

5.2 Fabrication of thin film based nanodiscs

Conventional magnetic particles used for biological and fluid applications, SPIONs, are produced using a highly efficient chemical synthesis method that is successfully industrialised. Research into the use of thin film based magnetic particles has been going for a few years, which has revealed some very interesting and desirable properties for these types of applications. However, a fabrication method for such particles that is able to compete with the yields (for the purpose of therapeutic applications), the reliability and the uniformity that has been established for SPIONs has been challenging to establish. For a fabrication process to be viable for future commercialisation, the product needs to fulfill the following parameters: robust and reliable magnetic properties; a well-defined

and consistent particle shape, fit for application; a range of particle sizes, with access to the nm range; a relatively simple series of processing steps; and high yield. So far, the methods used to produce thin film particles have been successful at achieving some or most of these parameters, but never all of them. In this section, a selection of these methods will be outlined and discussed. A new fabrication methodology will then be presented, which has been designed to deliver all of the necessary requirements for the successful manufacturing of thin film based magnetic nanoparticles.

5.2.1 Lithography techniques

Optical lithography

Optical lithography is a highly efficient method for producing patterns, which is why it is widely used in both research and industry applications. This technique has been well used in this lab for high yield production of PM SAF microdiscs. Here, photoresist was patterned into pillars of ~ 2 μm diameter, a SAF stack was sputtered on top and then easily lifted off in disc form by dissolving the photoresist in acetone [38], as shown in Figure 5.2a. The main limitation of this method is size: light resolution prevents the patterning on the nanoscale. Furthermore, optical lithography is susceptible to focus and optimal proximity issues, which can create large variations and defects in the pillar patterning. Additionally, growing the particles directly on top of the pillars can cause significant defects in particle shape. This is illustrated by the scanning electron microscopy (SEM) image in Figure 5.2b, where the film deposition has coated both the top and edges of the pillars, creating large 'skirts' on the microdiscs. The second drawback of depositing onto the pillars themselves, is that it is less trivial to tune the

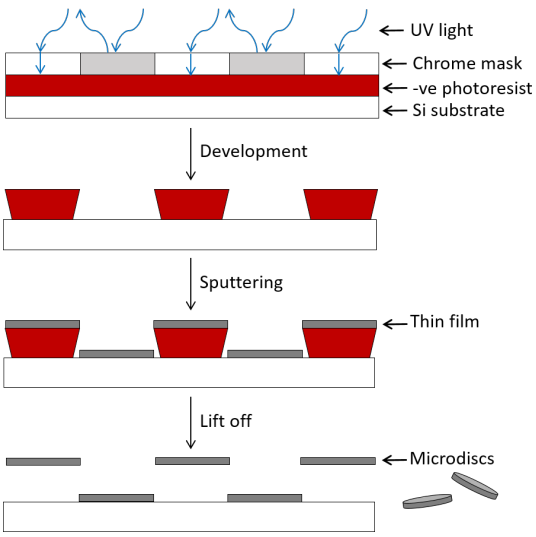

(a) Optical lithography

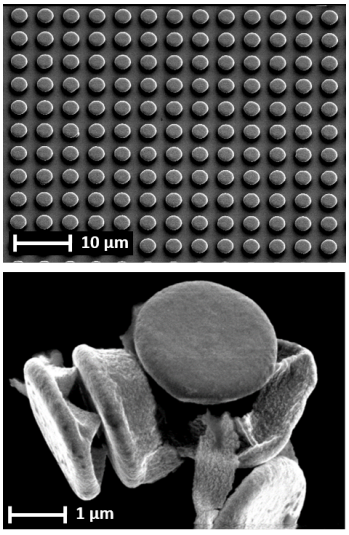

(b) Microdisc SEM

Figure 5.2: (a) A schematic describing the process for creating magnetic microdiscs on top of lithographically defined photoresist pillars. (b) SEM images of microdiscs produced by this method before (top) and after (bottom) lift off.

magnetic properties of the film. This is because there is a relatively large change in behaviour between the continuous film and the film grown on top of the pillar, which is the result of the surface topography of photoresist having a roughness wavelength on the length-scale associated with the nucleation and propagation of domain walls in perpendicular films [21].

An alternative use of optical lithography is to create a photoresist mask on top of a continuous thin film, which can favourably be engineered as desired in magnetic behaviour, and ion mill away the unmasked areas, as shown in Figure 5.3a. This leaves behind disc-shapes of the film beneath the resist pattern, on top of a chosen sacrificial layer. This modifying of the lithography method significantly improves particle shape: by eliminating the edge features it is possible to produce more uniform discs with the capability of creating very high aspect ratios (see Figure 5.3b), which may be useful for some biological applications, including those directly involving cells [19, 41]. However, the use of optical lithography still limits the resolution of the method, preventing access to the nanoscale. In addition, photoresist that has been ion milled can be challenging to remove due to cross-linking: more harmful solvents may be required to dissolve it and undesirable residues could still be left behind on particle surfaces.

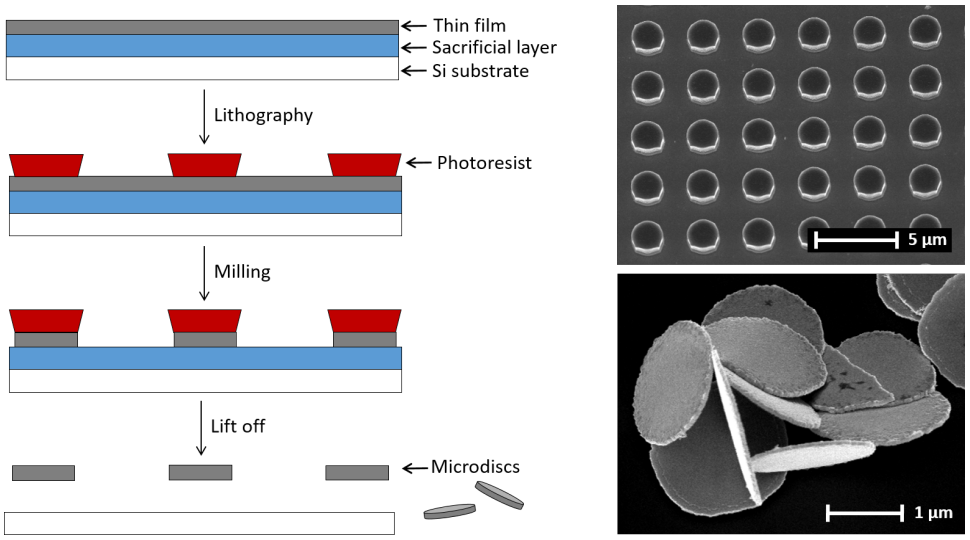

(a) Mill-mask lithography (b) Milled microdiscs

Figure 5.3: (a) A schematic describing the process of creating magnetic microdiscs from a continuous thin film, by using optical lithography to form an ion milling mask. (b) SEM images of microdiscs created this way before (top) and after (bottom) lift off.

Hole-mask colloidal lithography

A novel approach to particle fabrication is hole-mask colloidal lithography (HMCL) [17]. Here, a mask with holes is patterned on top of a sacrificial layer and material is deposited through the mask to create particles. To make the nm range accessible, a method using relatively inexpensive, colloidal polystyrene (PS) beads has been de-

veloped [43]. This method distributes PS beads, using a dropcast method, across the surface of a two part stack of sacrificial layers: PMMA on top of Ge. By sputtering the whole sample with titanium, removing the PS beads and then oxygen plasma ashing, a mask of holes is created in the PMMA layer. A thin film may then be sputtered into the holes, and removal of the PMMA layer leaves behind a array of particles on top of the second sacrificial layer, Ge, which can be dissolved to release the particles (see Figure 5.4a).

Whilst this technique provides an inexpensive option for the production of thin film based nanoparticles, it too comes with problems. Firstly, as described, the protocol is somewhat inefficient: multiple steps of deposition and etching produces a mask with a relatively low yield of holes. This is namely due to the dropcast application of the PS beads, as it is challenging to create a particularly dense monolayer of beads via this method. Secondly, the deposition of material through such small holes causes large shadowing effects and leads to discs that are not planar in shape (see Figure 5.4b).

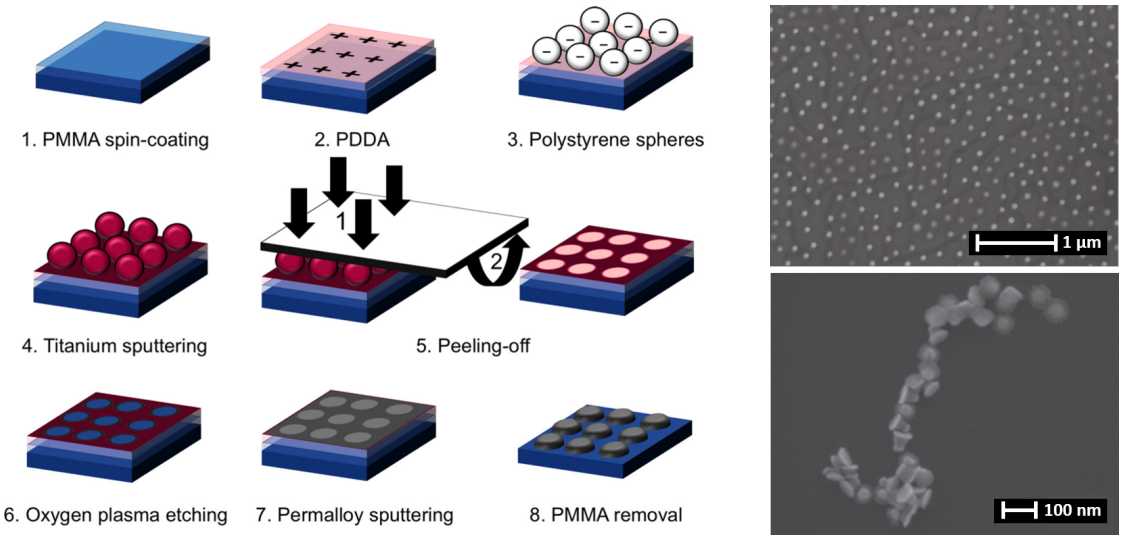

(a) HMCL (b) Nanodisc SEM

Figure 5.4: (a) Schematic of a HMCL process previously formulated to create permalloy nanodiscs. (b) SEM images of microdiscs created this way before (top) and after (bottom) lift off. All images taken from [43].

Nanoimprint lithography

Another, more widely used technique for the production of nanoparticles is nanoimprint lithography (NIL). This method uses a compression molding approach to create a thickness contrast pattern in a layer of resist (see Figure 5.5a). The pattern is then transferred through the full thickness of the resist by anisotropic etching, which removes any remaining resist in the compressed areas [4]. Nanoimprint stamps are generally made using electron beam lithography (EBL), thus allowing access to the nanoscale, but others have also been produced using self-assembled polymer spheres, which results in a much larger yield per imprint at a reduced cost [18, 27] (discussed further in the

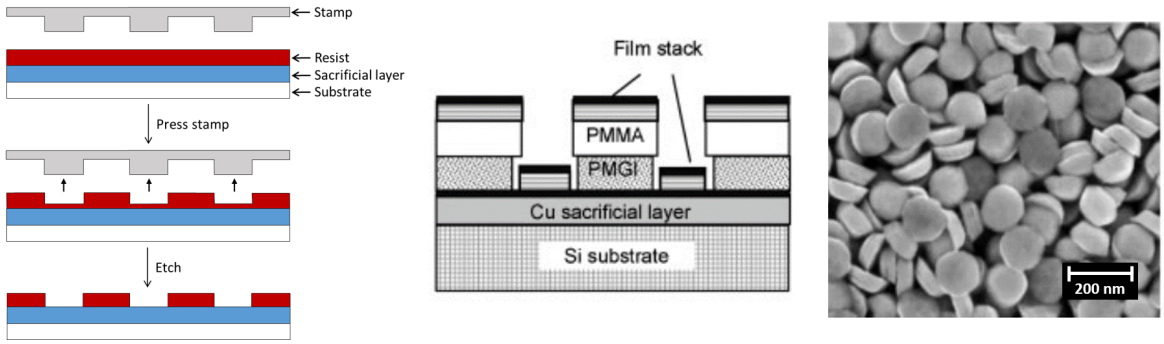

(a) NIL (b) Nanodisc fabrication (c) Nanodisc SEM

Figure 5.5: (a) A schematic of the NIL process. (b) A schematic of the fabrication of nanodiscs via NIL, after patterning and film deposition. (c) An SEM image of lifted off nanoparticles. (b) & (c) taken from [18].

next section). Additionally, the use of a pre-made, reusable stamp makes it possible to pattern with a high-throughput, making it commercially viable. By creating a mask of holes on top of a sacrificial layer, as seen previously in the HMCL method, material deposition can then be used to form releasable magnetic particles in the holes.

A previous study used NIL to create SAF nanodiscs with IP magnetisation [18]: a schematic of the fabrication process after film deposition is shown in Figure 5.5b. In this work a double resist layer, on top of a Cu sacrificial layer, was imprinted with a pattern using a quartz stamp with 100 nm diameter pillars (defined by EBL). The SAF film was then deposited through the pattern, resulting in 120 nm diameter magnetic nanoparticles, an SEM image of which is shown in Figure 5.5c. Despite the large improvement in yield from the HMCL method detailed above, the NIL technique suffers the same disadvantage: shadowing effects preventing the creation of well-defined disc shapes.

Nanosphere lithography

Nanosphere lithography (NSL, originally referred to as Natural lithography), is a fast, high throughput and low cost method for producing regular arrays of nanostructures, which can be implemented as a lithography mask [1, 2]. The process generally comprises three main steps: colloidal mask generation, diameter modulation and lift off. The HMCL process, detailed earlier, utilised a basic version of this process using the particularly inexpensive PS beads as the colloidal element [43]. However, this method does not optimise the self-assembly of the PS beads into arrays: the dropcast method of bead application limits particle yield and is not highly reproducible. The technique of spin coating beads to create a colloidal mask has been implemented in previous studies [34, 36], in particular, a model has been created for the large-area monolayer coverage of PS beads by spin coating [48]. This comes with a number of advantages: a large increase in particle yield, the use of a well established industrial technique and the simple control of array parameters through the tuning of spin speed and acceler-

ation. This study went on to utilise their colloidal masks to create different arrays of nanoholes and nanodots [48], a schematic of the nanodot fabrication process is shown in Figure 5.6. For the purpose of creating thin film based nanoparticles, this particular use of NSL suffers from the same issues with shadowing effects as discussed previously.

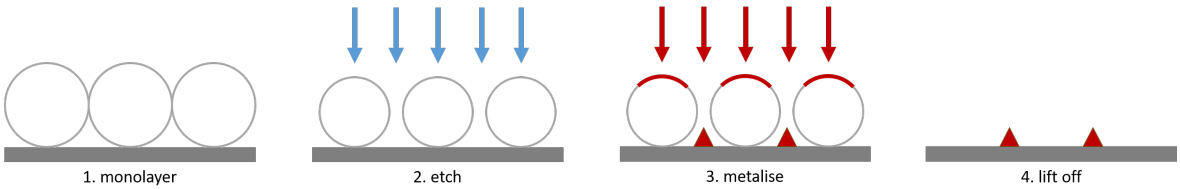

Figure 5.6: Schematic of creating nanoparticles via NSL.

One way that NSL has already been implemented into the production of thin film based nanodiscs was mentioned earlier: the self-assembly of PS beads to create NIL stamps. In one study, the colloidal mask was used directly as the stamp to produce IP SAF particles [18]. In another, a NSL mask was used to etch a stamp into a Si substrate, as shown in Figure 5.7, to again fabricate IP SAF particles.

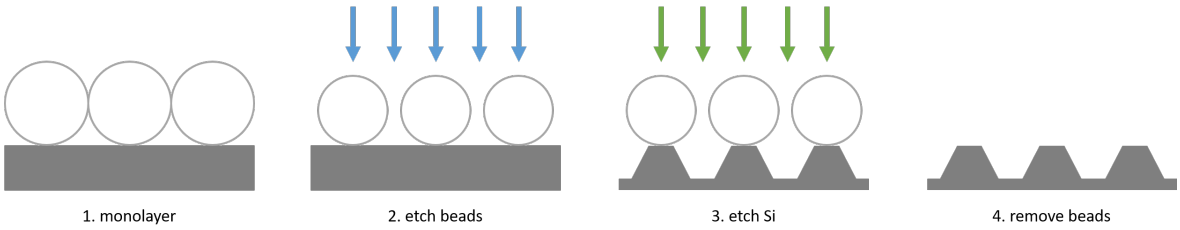

Figure 5.7: Schematic of the fabrication of a NIL stamp via NSL.

5.2.2 Nanosphere lithography with ion milling

Note: all evaporation of Ge for samples in this work was performed by T. Vemulkar (Prof. Cowburn's group).

Here I present an updated version of the cost and time-effective fabrication method, NSL with ion milling [39], and make use of a Ge sacrificial layer [43], which produces more optimal patterning of robust thin film based nanodiscs. I then demonstrate how it answers all of the key needs for effective production of SAF nanoparticles, particularly for liquid and biological based applications. By using the PS beads as a direct lithography mask, we streamline the protocol while retaining access to the nanoscale. By implementing the application of beads via spin coating [48], rather than the dropcast method [43], we significantly increase particle yield. By starting with a continuous film and using ion milling to form our discs, as was previously developed to create permalloy particles [39], we are able to create uniform discs, with the potential for high aspect ratios, from a thin film that has been carefully designed and grown before patterning. Finally, the choice of Ge as the sacrificial layer ensures that we

conserve our carefully engineered magnetic properties, without compromising ease of lift off (see Section 4.3).

The method

A schematic of the complete fabrication process designed for the production of a high yield of high aspect ratio nanodiscs with a well conserved, PM SAF state is displayed in 5.8. The first step is to deposit a layer of Ge, of thickness $50 - 100$ nm, onto a Si substrate via thermal or electron beam evaporation. Ge was chosen as the sacrificial layer for two key reasons: it's ease of removal in an inorganic solvent (particularly after ion milling) and, crucially for this application, the similarity in properties of a magnetic film grown on Ge in comparison with Si (as discussed in Section 4.3).

The PM SAF multilayer stack is then sputtered on top of the Ge. This stack can be engineered beforehand: by using a top-down approach to the fabrication process and starting with a continuous thin film, which then essentially has particles 'cut out' from it, we are able to pre-tune the magnetic properties to a greater extent. It is therefore easier to tailor the magnetic particles towards a particular application, for example by manipulating their total moment or switching field.

A thin (~ 5 nm) Al cap is added, which serves two purposes: it promotes adhesion

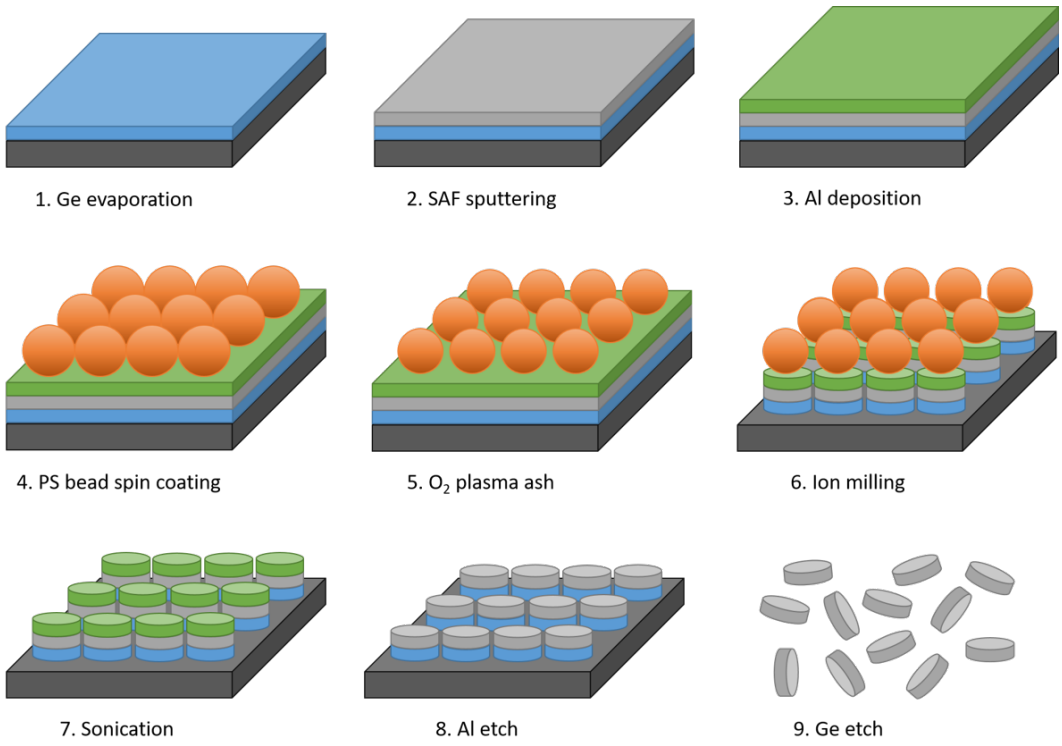

Figure 5.8: A schematic of the full protocol for the fabrication of nanodiscs. (1) Ge is evaporated onto Si. (2) The SAF film is sputtered on top of the Ge. (3) An Al layer is deposited on top of the SAF. (4) PS beads are spin coated across the surface. (5) Plasma ashing reduces the PS bead size. (6) The PS beads are used as an ion milling mask and discs of the Ge-SAF-Al stack are made. (7) Sonication in water removes the PS beads. (8) An Al etch removes the cap. (9) A Ge etch lifts off the nanodiscs into solution.

of PS beads and provides an additional sacrificial layer to allow the removal of material that is redeposited during ion milling. On the first point, the Al cap is plasma ashed prior to the application of PS beads. This oxidises the top layer of Al and creates a surface charge, which makes it hydrophilic, promoting the spread of the PS bead solution, and also attractive to the negatively charged PS beads (via the surface groups). It was observed during experiments that a good distribution of PS beads across an Al cap was easier to achieve and more consistent than on the top Ta layer of the SAF stack. The need of having the Al cap as an additional sacrificial layer is demonstrated in Figure 5.9: nanodiscs fabricated without a capping layer show distinct features on their top surfaces, caused by re-deposition of material around the base of the PS beads during the milling process, which is left behind when the lithography mask is removed. By utilising an Al capping layer, we can remove this extra material and achieve nanodiscs with relatively flat surfaces, as will be discussed later in this section (see 'Size and shape').

The next stage is the formation of the lithography mask, using NSL [48]. The PS beads used for this purpose are from Polybead®, Polysicence Inc and have a carboxylate or sulphate coating, such that they have a negative surface charge, which aids their distribution across a substrate. The beads are diluted in deionised water as necessary (see Table 5.1) and are spin coated using parameters that produce a relatively dense monolayer. The spin coating recipe consists of two stages: first a slow spin at 200 rpm to spread out the beads evenly and secondly a fast acceleration (1000 rpm/s) up to the much higher speed of 8000 rpm to order and adhere, and to remove excess beads. A bonus of this spin coating method is that it is commercially viable, easily scalable and simple to tune for particle density. Once attached, the PS beads are oxygen plasma ashed to partially shrink them, an SEM image of the resulting bead mask is shown in Figure 5.10a. The timing of this was carefully calibrated to achieve a balance between minimising size change and creating a sufficient gap between the beads to form a mask that produces individual discs (see Table 5.1).

Once the lithography mask is formed on top of the full stack, the nanodiscs can be

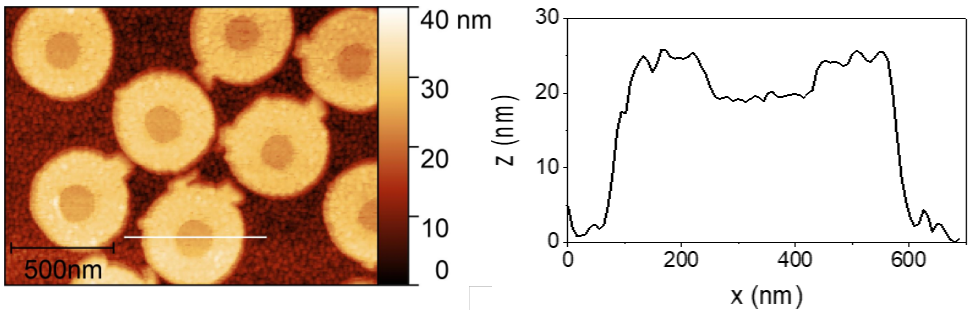

(a) 2D scan of nanodiscs (b) Line-profile of nanodisc

Figure 5.9: 2D topography scans and line profile (extracted from the white line marked in (a)) of a set of nanodiscs. Scans were taken after the removal of the lithography mask and before particle lift-off.

Diameter (nm)	100	200	500	1000
Dilution	2:1	1:1	1:0	1:0
Ash time (s)	30	60	240	300

Table 5.1: Dilution (beads : water) and plasma ashing time criteria for the PS beads of different diameters.

'cut out' of the thin film. Here, an Ar ion miller is used to etch away the unmasked regions of the film, leaving behind disc-shaped islands of the film beneath each bead. We achieve excellent pattern transfer of the 2D projection of the PS beads spherical shape onto the film. The milling time is calculated so as to just get through the SAF stack and Al cap, but not to go through the Ge layer. This is to limit the effect the ion milling has on the magnetic properties of the thin film, which is discussed in more detail in Section 5.3.1. Additionally, it prevents the melting of the PS beads, making them significantly easier to remove. Using calibration samples and AFM it was determined that the Al cap etched at ~ 0.3 nm/s and a typical SAF bilayer took ~ 40 s to etch through, when using the beam parameters of 600 V and 28 mA.

Next the lithography mask is removed. First, sonication of the sample in water removes the PS bead mask. The Al cap, and thus any redeposited material, is removed via a short (~ 60 s) chemical etch with photoresist developer (a tetramethylammonium hydroxide based solvent). This leaves behind just the SAF discs on the Si/Ge substrate, as displayed in Figure 5.10b. It is then possible to characterise the magnetic discs on chip to deduce size, structure and magnetic properties, via measurements such as MOKE and SEM.

Finally, the particles are lifted off using a H_2O_2 etch: the sample surface is first covered in a 35% H_2O_2 solution for ~ 1 hr, dissolving the Ge layer. The whole sample is then submerged in a larger volume (at least $10\times$ H_2O_2 volume) of deionisied water, to dilute the solution, and sonicated to aid the release of the discs. The suspension is then

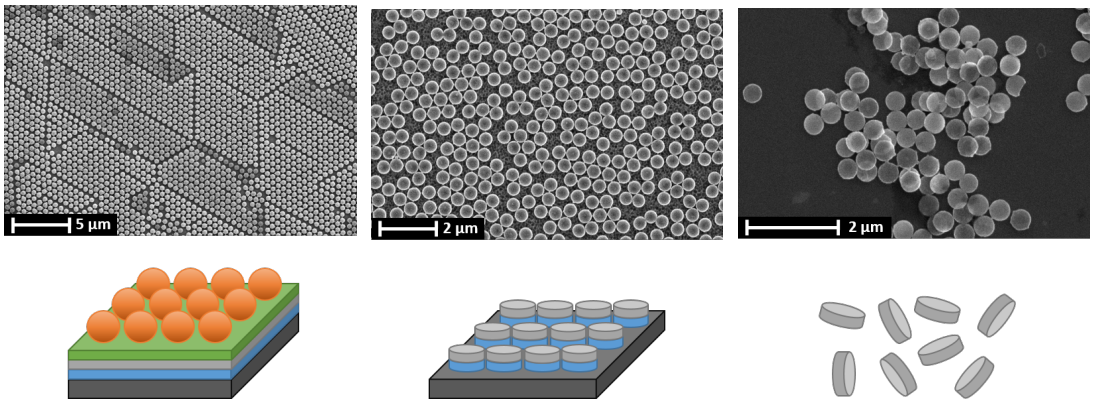

(a) Ashed PS bead mask (b) Milled discs on chip (c) Lifted discs

Figure 5.10: SEM images highlighting three key steps of the nanodisc fabrication protocol: (a) PS beads arranged as a milling mask across the surface of the Ge/SAF/Al stack; (b) milled nanodiscs, on chip, with the Al cap removed; and (c) nanodiscs that have been lifted off and redeposited for imaging.

left overnight to allow the H_2O_2 to degrade to water and for the particles to sediment out. This allows the solution to be concentrated, as required, before further processing or characterisation. An SEM image of some nanodiscs that were lifted off this way and then redeposited on a Si chip for imaging is shown in Figure 5.10c. An added bonus of this fabrication method is that the Ge lift off process fully cleans the Si substrate, leaving behind a wafer that may be reused for subsequent particle production, which is highly beneficial from the perspective of reducing manufacturing costs or limiting consumption of resources.

Size and shape

As discussed, one of the major benefits of this fabrication method is the access to the nanoscale, which is made possible by utilising colloidal PS beads for the lithography mask. Figure 5.11 shows a series of nanodiscs made using PS beads with four different diameters, demonstrating that we can produce discs from the lower limit of optical lithography, around 1 μm, all the way down to 100 nm. In these images it is seen that the use of plasma ashing, to separate out the PS beads prior to milling, produces individual discs with diameters slightly under that of the original beads.

The shape of the nanodiscs can be assessed by AFM prior to their lift off. Figure 5.12a shows a 3D view produced from a topography scan of some 500 nm discs on substrate. We see that there is some texturing in the top surface of the discs, which will mostly originate from the Ge (as discussed in Section 1.3.1). However, the discs

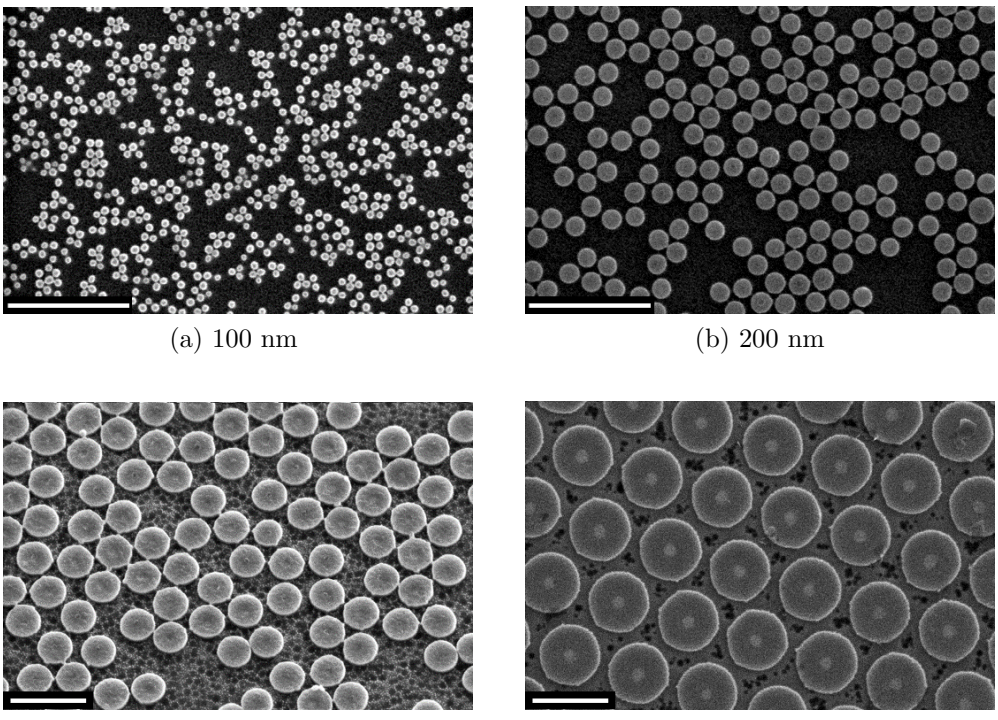

(a) 100 nm (b) 200 nm

(c) 500 nm (d) 1 μm

Figure 5.11: SEM images of SAF discs, before lift off, made with PS beads of four different diameters. All scale bars are 1 μm.

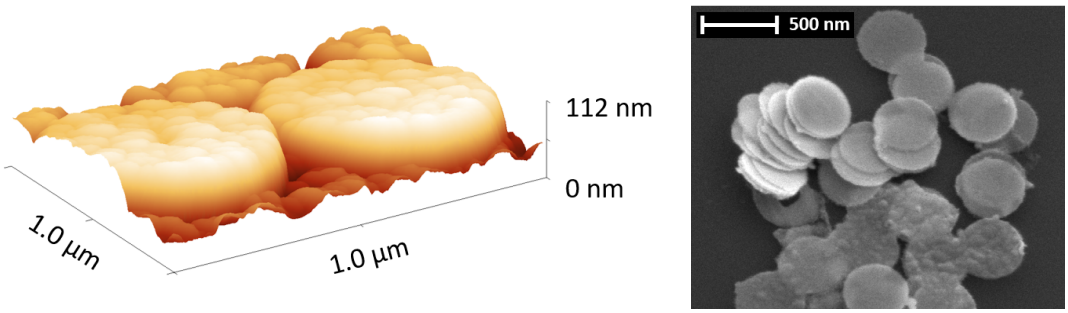

(a) AFM of discs on chip (b) SEM of lifted discs

Figure 5.12: (a) An AFM scan taken of some nanodiscs before lift off, in 3D. (b) An SEM image of some nanodiscs that have been lifted off and redeposited onto a Si chip.

have a relatively flat top surface, particularly in comparison to that shown in Figure 5.9. SEM imaging of nanodiscs after their lift off and redeposition, as shown in Figure 5.12b, reveals very close stacking of discs that are thin enough to penetrate with the electron beam (it is possible to see the outline of discs that are underneath others). This further demonstrates the capability of producing uniform and high-aspect ratio nanodiscs.

Yield

For the ideal case of hexagonal close-packed spheres of equal size in 2D (see Figure 5.13a) the packing constant is $\pi\sqrt{3}/6$ giving a surface coverage of 91%. If we take our 500 nm PS bead case, where the lithography processing (shrinkage of beads after application) leads to a particle diameter of $\sim$ 430 nm, ideal bead packing would lead to a particle surface coverage of 67%. If we compare this to areas of the most optimal packing achieved for the 500 nm beads experimentally, an example of which is shown in Figure 5.13b, Image J analysis gives a surface coverage of 55% (post-bead shrinkage). Although this is a 12% drop from the idealised case, this comparison shows that our NSL process is generating relatively high yields of particles.

Optimisation of the bead packing, during the spin coating application, is mainly

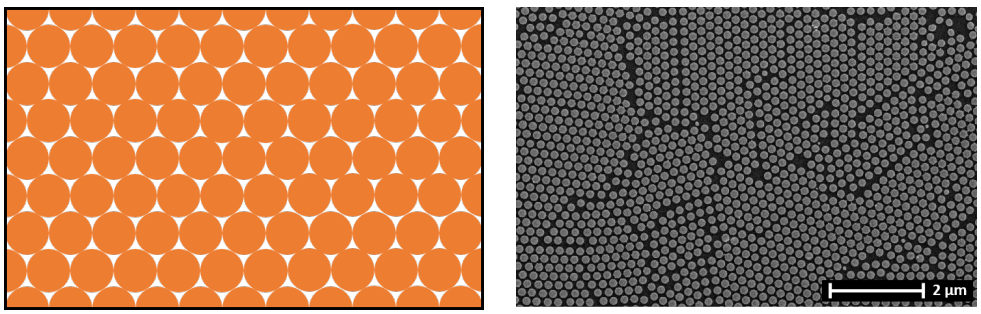

(a) Ideal packing (b) 500 nm discs

Figure 5.13: (a) A schematic of ideal, hexagonal close packing of PS beads. (b) An SEM image of 500 nm nanodiscs with relatively close packing.

achieved through the spin parameters. The key variable in the spin coating recipe, which was found to have by far the greatest effect on bead density, is the spin acceleration from the first to the second spin speed: the slower the acceleration, the denser the beads. The value of 1000 rpm/s was chosen to provide a balance between good bead density and maintaining a monolayer. The dilution of the PS bead stock solution also has an effect on the packing density: this was a parameter that was controlled for the smaller bead sizes (100 and 200 nm), as the original solutions formed multilayers even with higher spin accelerations. The SEM images in Figure 5.14 show the differences in bead density across three different dilutions of the 200 nm PS beads. We see the layering of the PS beads in the undiluted sample, whilst the 1/10 dilution shows large gaps between clusters of packed beads. The 1/2 dilution, which was chosen to be the optimal, shows some small blank areas, but the majority of the surface is covered with well packed beads.

Image J was used to analyse SEM images and calculate particle yield across a range of different disc sizes, which showed high percentages of coverage by area, as is displayed in Table 5.2. To compare with previous processes, HMCL of ~ 100 nm discs achieved around 10% coverage, yielding just a third of the number produced by this new method [43]. Furthermore, if we look at the optical lithography based, photoresist pillar method for making 2 μm discs, this gave $\sim 30\%$ coverage. This could be increased by using a lithography mask that created a hexagonal arrangement, rather than square arrangement, of pillars. Allowing for sufficient gaps between pillars (500 nm to ensure effective pattern transfer) it could be possible to achieve $\sim 58\%$ coverage. Therefore, our NSL is competitive with the traditional optical lithography technique in terms of yield, and is superior in the fabrication of discs on the nanoscale.

Size / nm	Coverage / %	Discs / mm^2
100	31	80×10^6
200	41	18×10^6
500	55	4×10^6
1000	50	8×10^5

Table 5.2: Yields achieved by patterning with different sized PS beads.

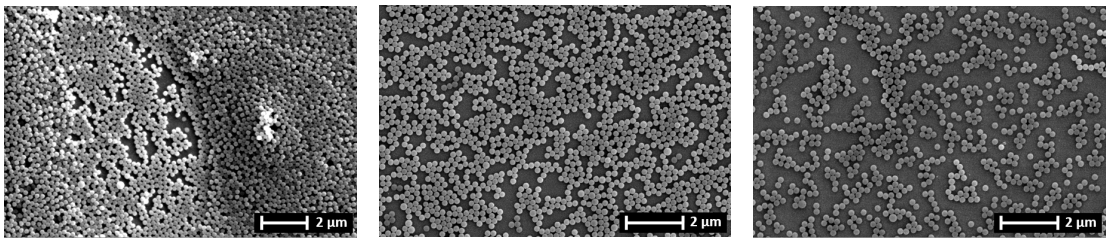

(a) No dilution (b) 1/2 dilution (c) 1/10 dilution

Figure 5.14: SEM images of spin coated 200 nm PS beads with different dilutions in DI water.

5.3 Magnetic properties of particle arrays — the effect of patterning

Note: all evaporation of Ge for samples in this work was performed by T. Vemulkar (Prof. Cowburn's group).

5.3.1 The milling process

Since we are fabricating our magnetic particles via a top-down approach, starting with a continuous film and then patterning it into discs, it is interesting to look at how the process of pattering affects magnetic behaviour. Once effort has been put into tuning the magnetic state of the film, prior to patterning, we wish to carry out the fabrication protocol with parameters that minimise change. One of the major processes during fabrication is the ion milling step: this is where the discs are 'cut out' of the film via a large bombardment of Ar ions, which has been shown to cause significant modification of thin film multilayer properties [37]. Here, the combination of heat, defect induction and a drastic change in size and shape of the film, has large consequences for the switching behaviour. This is evident in the MOKE loops taken of arrays of 500 nm discs, when compared with the original thin film, examples of which are shown in Figure 5.15. In the following sample series of 500 nm nanodiscs, we wanted to explore if the milling parameters could be altered so as to minimise the magnetic state change.

Milling power

First we looked into the effect of reducing the milling power, and thus removing the unwanted material in a more gentle manner, by lowering the ion beam current. Usually our system is used with a beam current of 28 mA, so we took a film milled with that parameter and compared it with the same film milled using a beam current of 10 mA (the lowest stable beam current we could reach on this system). We use intervals of 20 s, separated by 20 s cool down periods, the normal operating procedures adopted by the lab. The cool down periods are used to allow heat to conduct or radiate away, since there is minimal convective cooling under vacuum, which prevents the melting of the PS beads. The total milling time was 40 s or 180 s for the 28 mA or 10 mA currents respectively (see Section 3.1.2).

The MOKE loops taken of each of the resulting particle arrays are displayed in Figure 5.15, along with a loop of the original thin film which was grown in the form $Ta(2)/Pt(2)/CoFeB(1)/Pt(0.4)/Ru(0.9)/Pt(0.4)/CoFeB(1)/Pt(2)/Ta(2)$ with thicknesses in nm. There is a clear difference between the MOKE of the film compared with that of the particles, particularly when looking at the major loops: for example the discs reach full saturation at much higher applied fields than the film. However, the loops of the two different sets of particles appear to be very similar. This is reinforced when we calculate the coupling and coercivity fields of each sample: the film has a coupling field, H_J, of 1400 Oe and a coercivity field, H_C, of 110 Oe; the 28 mA milled

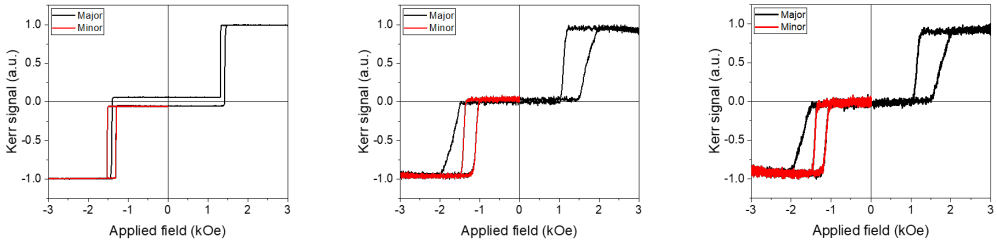

(a) Thin film (b) 28 mA (c) 10 mA

Figure 5.15: MOKE loops of a (a) thin film and corresponding 500 nm nanodiscs milled with a current of (a) 28 mA and (b) 10 mA.

discs have a H_J of 1240 Oe and a H_C of 230 Oe; and the 10 mA milled discs have a H_J of 1250 Oe and a H_C of 210 Oe. Therefore, the patterning process has slightly reduced the coupling and greatly increased the coercivity, but the change in milling power/beam current does not cause a significant change in either.

There are a few possible explanations for the changes in hysteresis found here, which could be occurring singularly or in combination. The first source of changes comes from the process we use to pattern our discs, i.e. the ion milling. Firstly, despite the use of cooling periods, the milling process will still cause some rise in temperature in the sample. This could disrupt the interfaces within the PM SAF multilayer through atomic diffusion [3, 28, 29, 50]. Secondly, the bombardment of ions could create defects in the stack in a few different ways [7, 35, 37]: Ar ion implantation, sputtering away of stack atoms or mixing of stack atoms. If defects are on the length scale that can cause domain wall pinning, this could cause an increase in coercivity and extensions of the transitions.

The other source of change in hysteresis originates from the the inherent reduction in structure size: from a continuous film to a nanostructure. The patterning of a thin film into nanodiscs reduces the likelihood of a nucleation defect being present inside the structure. This will change the switching field, but also create a spread in switching fields across the population of nanodiscs, which will cause a sloping of the transition measured by MOKE. The reduction in structure size could introduce also edge effects. In a patterned nanodisc the edge-to-area ratio increases significantly, which could introduce an increase or variation in defects. Additionally, the transformation from continuous film to nanostructures will have introduced magnetostatic interactions between the CoFeB layers within each nanodisc, and could also occur between CoFeB layers in adjacent nanodiscs on the chip. This interaction favours a parallel orientation of the moments, which will yield an effective reduction in coupling strength, and is also known to induce an increase in coercivity [16].

The fact that lowering the beam power did not reduce the effect of patterning on the nanodisc hysteresis indicates that even the lower current is above the threshold where milling causes heating and/or defects. Furthermore, it is very likely that the transformation from thin film to nanodiscs is a significant source of the loop changes.

Milling intervals

We next varied the milling intervals, i.e. the 'on' and 'off' periods (see Table 5.3), with the idea of reducing possible heating effects. The MOKE loops generated from a series of discs with different 'on/off' sequences, produced by milling with a 28 mA beam current for a total of 40 s, and their original thin film ($Ta(2)/Pt(2)/CoFeB(1)/Pt(0.4)/Ru(0.9)/Pt(0.4)/CoFeB(1)/Pt(2)/Ta(2)$ (thicknesses in nm) are shown in Figure 5.16. The coupling and coercivity fields calculated from the MOKE is displayed in Table 5.3. Again, we see a drop in H_J and an $\sim 2\times$ increase in H_C when we go from the thin film to the 500 nm discs. Additionally, there isn't a large variation in the magnetic parameters pulled out of the nanodiscs MOKE loops, suggesting that changes in milling intervals did not cause a significant effect on magnetic state.

As before, these results indicate that the beam parameters used could be above the threshold for the generation defects in the samples. Also, they support the concept that a significant source of change in the magnetic hysteresis originates from the transformation from a continuous film to a nanodisc array, including the introduction of intra-particle magnetostatic interactions.

Sample	H_J/Oe	H_C/Oe
Film	1400	110
40 on	1190	210
20 on/20off	1240	230
10 on/20 off	1240	220
5 on/20 off	1210	210
10 on/100 off	1240	220

Table 5.3: Coupling and coercivity fields for a thin film and a series of discs milled out of it under different timings.

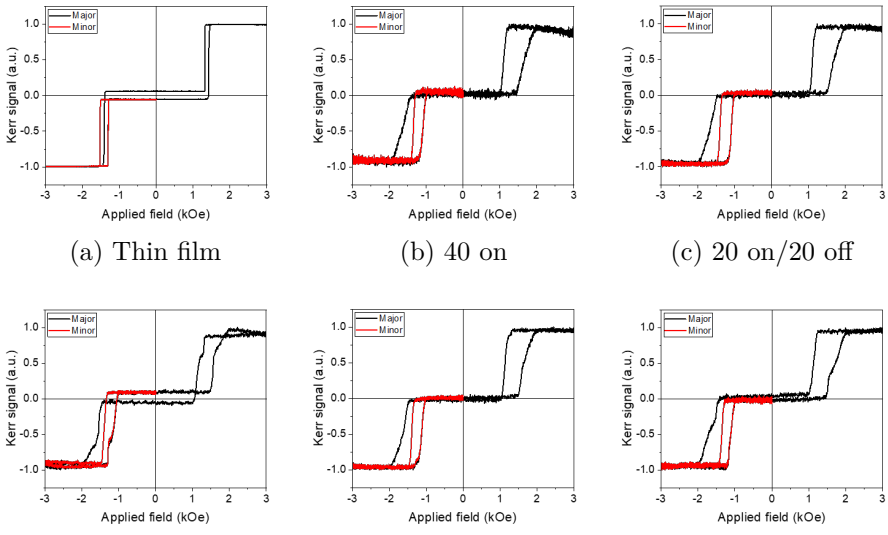

(a) Thin film (b) 40 on (c) 20 on/20 off

(d) 10 on/20 off (e) 5 on/20 off (f) 10 on/100 off

Figure 5.16: MOKE loops of a (a) thin film and (b)–(f) corresponding 500 nm nanodiscs after a series of milling time parameters.

Al cap

Finally we looked into whether the Al cap added any protection to the magnetic stack during the milling procedure, and therefore if it was increased in thickness would there be a smaller change on magnetic state during patterning. We compared three disc samples which originated from the same thin film, grown in the form $Ta(2)/Pt(2)/CoFeB(0.9)/Pt(0.4)/Ru(0.9)/Pt(0.4)/CoFeB(0.9)/Pt(2)/Ta(2)$ with thicknesses in nm, one with no Al cap, the second with a 20 nm Al cap and the third with a 40 nm Al cap. The 500 nm discs were milled using a beam current of 28 mA and a 20 s on/20 s off sequence for a total milling time of 40 s (to mill through the bilayer) plus the time needed to get through the Al, which mills at 0.32 nm/s (see Section 3.1.2). The MOKE loops from the film and the three sets of discs are shown in Figure 5.17 and the coupling and coercivity fields from each are displayed in Table 5.4. Once again we see a decrease in H_J and a very big increase in H_C through patterning. There doesn't appear to be much variation in these values between the sets of discs, although the disc sample with no Al cap seems to be slightly less affected, with the highest H_J and lowest H_C. This may be a result of the longer milling time required to get through the Al caps on the other two discs samples. This indicates that the milling process itself does contribute to the change in hysteresis: a large increase in milling time would cause a larger temperature increase and/or increase the amount of adverse ion interactions, which could create more defects on the relevant length scale for magnetic reversal.

Following from these findings about the effect of changing milling conditions on the magnetic behaviour of patterned nanodiscs, subsequent samples were prepared using a beam current of 28 mA and milling time intervals of 20 on/20 off. This was chosen to minimise processing time, while maintaining a cooling period to prevent the melting

Sample	H_J/Oe	H_C/Oe
Film	2120	160
No cap	1890	540
20 nm cap	1820	580
40 nm cap	1810	570

Table 5.4: Coupling and coercivity fields for a thin film and a series of discs milled out of it with different Al caps.

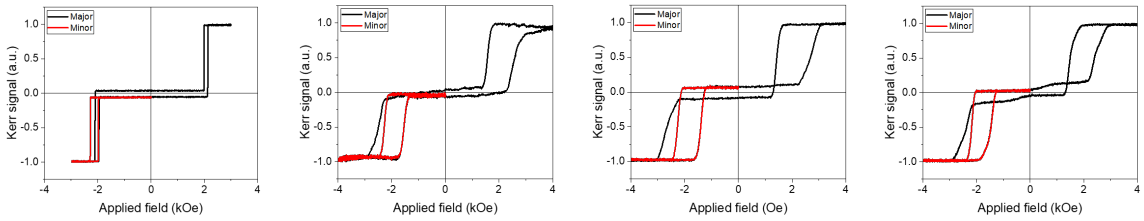

(a) Thin film (b) No Al (c) 20 nm Al (d) 40 nm Al

Figure 5.17: MOKE loops of a (a) thin film and (b)–(d) corresponding 500 nm nanodiscs milled with different Al caps.

of the PS bead mask (which would make it more difficult to remove). Furthermore, in response to the findings on the use and thickness of Al it was decided that a thin ($\sim$ 5 nm) cap would be used: this is enough to provide the layer desired for PS bead addition in the NSL step, but also minimises the added material and thus the milling time required to get through the full thin film stack.

5.3.2 Pattern size

As it is clear that the patterning process causes a major change in the magnetic state of the SAF stack, we investigated whether pattern size, or disc size had any effect on the resulting state. A thin film was grown in the form $Ta(2)/Pt(2)/CoFeB(0.9)/Pt(0.4)/Ru(0.9)/Pt(0.4)/CoFeB(0.9)/Pt(2)/Ta(2)$ with thicknesses in nm, on top of both Si and Ge coated Si. Nanodisc samples were then created using four different diameters of PS bead: 100 nm, 200 nm, 500 nm and 1 μm. MOKE loops of each thin film and milled disc sample were taken to compare their magnetic behaviour, these are shown in Figure 5.18. To measure the discs, the laser was defocused so as to sample a larger area of the pattern. H_J and H_C were extracted from the minor loops to provide a qualitative comparison of the samples, graphs of these versus pattern size are shown in Figure 5.18c and 5.18d respectively. Here, the average and standard deviation were calculated from minor loops from four different areas on each sample.

Between the thin films and associated discs, we see the characteristic drop in H_J and large increase in H_C. The first notable trend in the data is a consistent decrease in H_J of $\sim$ 200 Oe and H_C of $\sim$ 400 Oe from the Si samples to the equivalent Ge samples. If we look at the coupling from the original thin films (see Figures 5.18a and 5.18b) we see a similar difference in H_J: 2350 Oe for the Si sample and 2210 Oe for the Ge sample. So it appears that this inherent difference in coupling between the discs grown on Si and Ge is similar to that which appears in the original thin films, which results from the increased texturing of the Ge substrate (see Section 4.3.1). The only change made by patterning is a small, but equal, decrease in H_J of around $300 - 400$ Oe from films to discs.

H_C comes out as very similar for the thin films: 160 Oe and 180 Oe for the Si and Ge samples respectively. However, there is a clear distinction in how much the coercivity increases with patterning for the different substrate samples. This is in the region of $200 - 300$ Oe for Ge samples and $450 - 700$ Oe for Si samples: the patterning process causes a larger increase in H_C, with greater variation, on samples grown directly on Si. This could be explained by the inherent roughness of Ge. On one hand, Ge texturing introduces larger numbers of defects in the film compared with the relatively smooth Si, which limits the effect of any additional defects induced by milling. Additionally, patterning a film with a low density of defects will result in a population of discs where only a small number contain the original defects. The other discs may, as a result, have larger coercive fields than the film. This effect will be less prominent coming from the Ge film with its higher density of defects.

If we now come back to the main objective of this experiment, the investigation into the effect of pattern size on the SAF behaviour, we observe matching trends between bead diameter and H_J or H_C for the Si and Ge samples. For coupling there is a general trend of higher, or less reduced, H_J with decreasing bead size. It is notable that this trend is more distinct at smaller sizes: there is an obvious drop in H_J between the 100 nm and 200 nm Ge samples and the 200 nm and 500 nm Si samples, whilst the larger size samples show little variation. Coercivity sees a relationship of decreasing H_C with increasing bead size, with a steeper gradient for the Si samples than the Ge counterparts. There is a small drop in the average H_C for the 100 nm Si sample, however, the error bars still overlap with that of the 200 nm sample, so this may not be significant. These results agree with the proposed theories for changes in hysteresis from films to nanodiscs: the introduction of pinning defects from the milling process combined with the reduction in the presence of the original nucleation defects induces increased slanting in transitions, through an increased spread of switching fields. This is in addition to the general increase in coercivity and loss of coupling strength caused by an introduction of magnetostatic interactions. It is reasonable that smaller nanostructures are more strongly affected by these features, due to their smaller

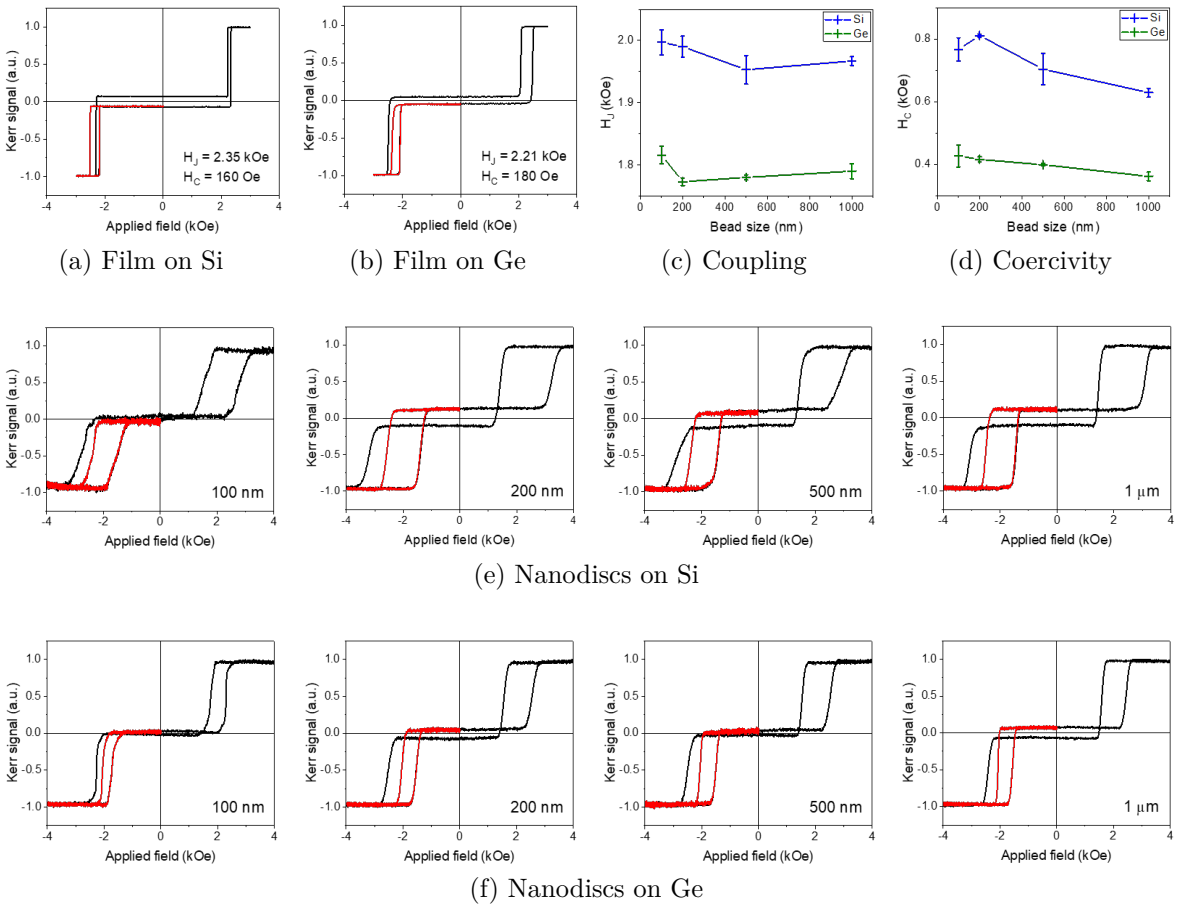

(a) Film on Si (b) Film on Ge (c) Coupling (d) Coercivity

(e) Nanodiscs on Si

(f) Nanodiscs on Ge

Figure 5.18: Major (black) and minor (red) MOKE loops of a SAF stack in (a) & (b) thin film form and in (e) & (f) milled disc form, grown on top of Si and Ge. The variation of (c) H_J and (d) H_C with disc size are shown for the Si and Ge samples.

film area and larger edge-to-area ratio. The fact the trends in H_J and H_C with disc diameter are moderate indicates that these structures are all below the threshold for a significant change in parameters from film to discs.

5.3.3 Varying the SAF stack

Varying coupling with Pt interlayer

To further study the effect of patterning on the magnetic behaviour of SAFs, and understand how this might impact nanodiscs manufactured for applications, we grew a series of thin films with different coupling strengths, mediated by the Pt interlayer thickness, t_{Pt}. For each t_{Pt} a film on Si, a film on Ge and a set of 500 nm milled discs were made. The SAF stack was grown in the form $Ta(2)/Pt(2)/CoFeB(0.9)/Pt(t_{Pt})/Ru(0.9)/Pt(t_{Pt})/CoFeB(0.9)/Pt(2)/Ta(2)$ with thicknesses in nm and where t_{Pt} was varied between $0.37 - 0.69$ nm. The MOKE loops taken from each set of samples are displayed in Figures 5.19a – 5.19c. Coupling and coercivity fields extracted from the major and minor loops are plotted against t_{Pt} in Figures 5.19d – 5.19h.

We see the expected relationship between coupling and t_{Pt} for all three sample sets: H_J decreases exponentially with increasing t_{Pt} (see Section 4.2.2, [30]). The Si and Ge samples give very similar results, but the disc samples exhibit lower values, with a divergence that gradually increases with decreasing t_{Pt}. If we look at the fitting parameters, we find some variation across the different sample sets. Maximum H_J, at $t_{Pt} = 0$, somewhat decreases from 17 ± 3 kOe for Si to 14 ± 4 kOe for Ge, although these do overlap in error. For the discs, we find a further drop to a maximum $H_J = 8 \pm 4$ kOe, which still fits within error of the Ge sample set. In the case of decay length (t_d), we find similar values for Si and Ge: 0.19 ± 0.02 nm and 0.22 ± 0.06 nm respectively. We find an increase for the fit of the discs, but also a larger error: $t_d = 0.28 \pm 0.17$ nm. So, these all match within error, which indicates that patterning doesn't have a particularly significant effect on the variation of coupling with t_{Pt}.

Looking at coercivity, the Si and Ge samples are relatively consistent, sitting at around 200 Oe. However, there is a very large difference between the H_C values of the films and those calculated for the discs, for both the top (H_{C1}) and bottom (H_{C2}) CoFeB layers. We observe a significant overall increase in H_{C1} and H_{C2} for the discs, alongside strong positive correlations with t_{Pt}, which cause a dramatic divergence (up to around $\sim$ 1.5 kOe) away from the coercivity of the thin films. The main source of this relationship between coercivity and t_{Pt} is general to the nanodisc populations: increasing t_{Pt} likely increases the (111) texture of the film, which will increase the PMA. Although this has little impact on a thin film, where magnetic reversal is driven by nucleation and propagation of domain walls, nanodiscs require nucleation within each particle to reverse. The increase in PMA therefore yields an increase in coercivity with t_{Pt}.

We plotted the two different switching fields against t_{Pt}: the anti-parallel to parallel (AP–P) and the parallel to anti-parallel (P–AP) switches, as shown in Figures 5.19g

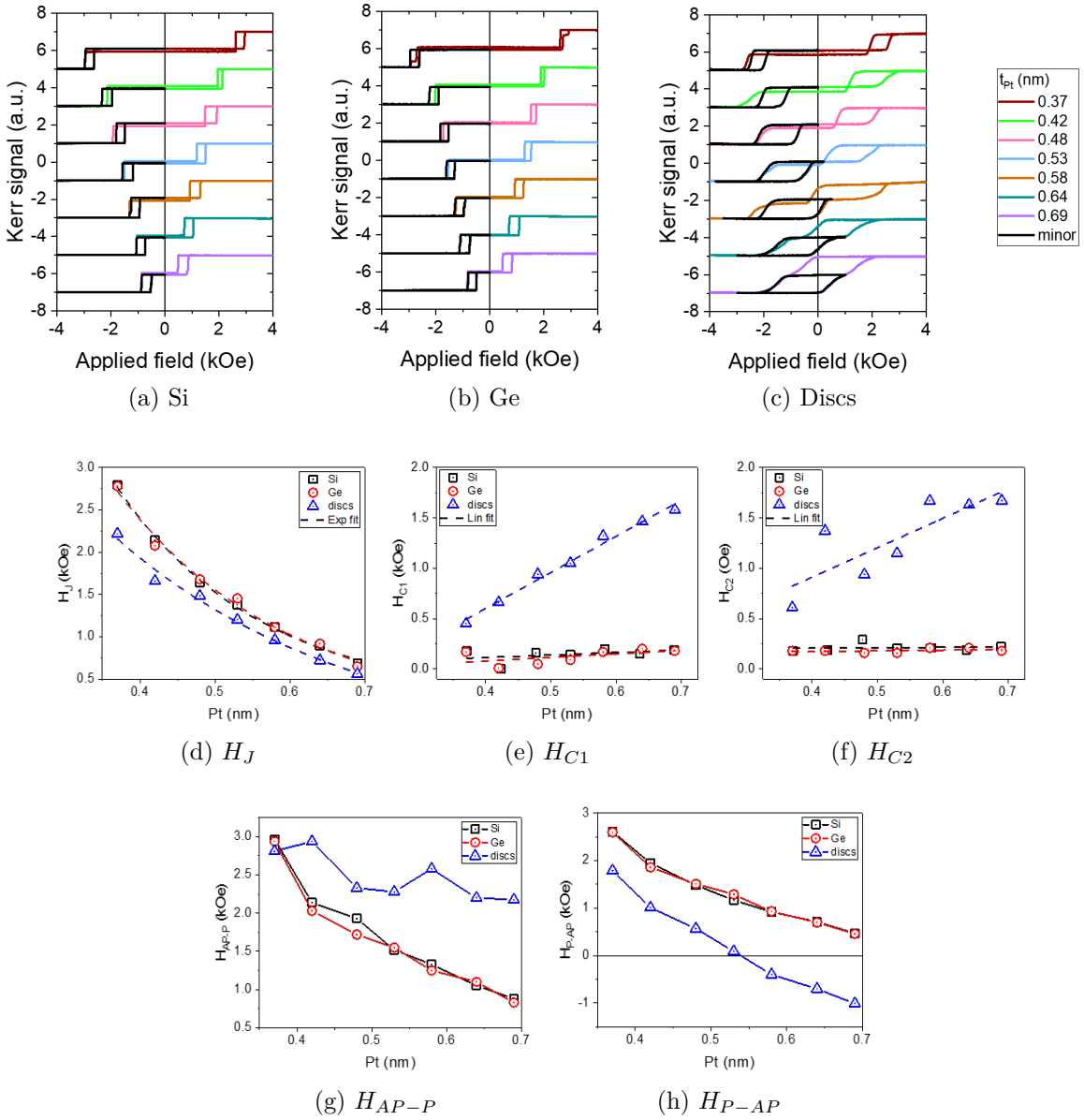

(a) Si (b) Ge (c) Discs

(d) H_J (e) H_{C1} (f) H_{C2}

(g) H_{AP-P} (h) H_{P-AP}

Figure 5.19: MOKE loops of a SAF film series with varied Pt interlayer thickness (t_{Pt}). The series was grown on top of (a) Si and (b) Ge, and also (c) grown on Ge and milled into 500 nm discs. Variation of (d) coupling, (e) top and (f) bottom layer coercivity, (g) AP–P transition field and (h) P–AP transition field with t_{Pt} for both sets of films and the nanodiscs.

and 5.19h respectively. We defined the switching field value as the end of each switch. Here, we can see that the increase in coercivity for the nanodiscs leads to both an increase in field for the AP–P switch and a decrease for P–AP, when compared with the films, with some divergence as t_{Pt} increases. Looking at the MOKE loops, those taken of the nanodiscs exhibited significantly sloped transitions in both directions, which is a major contributor to the changes in switching fields. This is explained by an increase in pinning sites, due to defects induced by milling, and an increase in spread of properties across the nanodisc population.

The discrepancy in the switching between films and discs is more varied in the AP–P case. AP–P transitions are driven by defects that create local regions of FM

coupling or low AF coupling in the film: pinholes in the interlayers will promote the P state and nucleate an AP–P transition. In addition to the general increase in coercivity from magnetostatic interactions, the large increase in the slope of the AP–P switching field (from the films to the discs) drives the effective switching field (the end of the transition, so the highest of all the individual disc switching fields) higher. This is through an increased spread in magnetic properties across the population of discs, supporting our theory that patterning reduces the likelihood of nucleation sites.

Conversely, P–AP nucleation is created in regions of the film with locally higher AF coupling. This type of defect is caused by a locally lower Pt thickness, or orange peel coupling: in the case of a high anisotropy SAF film waviness in the layer structure (which could be induced by our Ge texturing) creates localised sites of strong AF coupling [13]. Again, the patterning process reduces the likelihood of these nucleation sites, lowering the effective switching field through an increased spread in coupling field across the disc population.

The P–AP graph clearly shows which nanodisc samples have conserved their AP remanence state: those that still have a H_{P-AP} above zero, namely where $t_{Pt} < 0.55$ nm. These results provide important knowledge for the manufacturing of nanodiscs for liquid applications where the agglomeration of particles outside of an applied field, which occurs when they do not have an AP remanence state, generally reduces or prevents efficient and effective use. We have therefore found a limitation in the production of SAF nanodiscs on the more weakly coupled, lower switching field end of the spectrum.

Weakly coupled SAFs

An alternative method for tuning the coupling strength of a SAF is tuning the Ru layer thickness. To investigate the potential of accessing functional, lower switching field SAF nanodiscs by utilising the 2nd AF coupling peak, a small series of PM SAF films and 500 nm discs were grown in the form $Ta(2)/Pt(2)/CoFeB(t_{CoFeB})/Pt(t_{Pt})/Ru(2)/Pt(t_{Pt})/CoFeB(t_{CoFeB})/Pt(2)/Ta(2)$ with thicknesses in nm and where $t_{CoFeB} = 0.8$ or 1 and $t_{Pt} = 0.21$, 0.27 or 0.32.

MOKE was used to analyse the magnetic behaviour of all samples: the loops and extracted coupling and coercivity fields are presented in Figure 5.20. We observe the characteristic trend of decreasing H_J with increasing t_{Pt}, as well as larger values of H_J for the thinner CoFeB samples [30]. Additionally, there is a decrease in H_J from the films to the discs, corresponding with the findings for the 1st AF peak SAFs.

We see the same overall trend in coercivity with these 2nd AF peak SAFs as for the 1st AF peak SAFs; there is a general rise in coercivity from films to discs, alongside an increasing H_C with t_{Pt} for the discs. Again, we have calculated H_{C1}, the coercivity field of the top CoFeB layer, and H_{C2}, the coercivity field of the bottom layer. As before, we observe an increase in coercivity with t_{Pt} for both H_{C1} and H_{C2}, with a steeper gradient for the discs than the films. This follows our previous argument that increasing t_{Pt} induces stronger PMA, and thus leads to larger coercivity in the nanodiscs. In the case

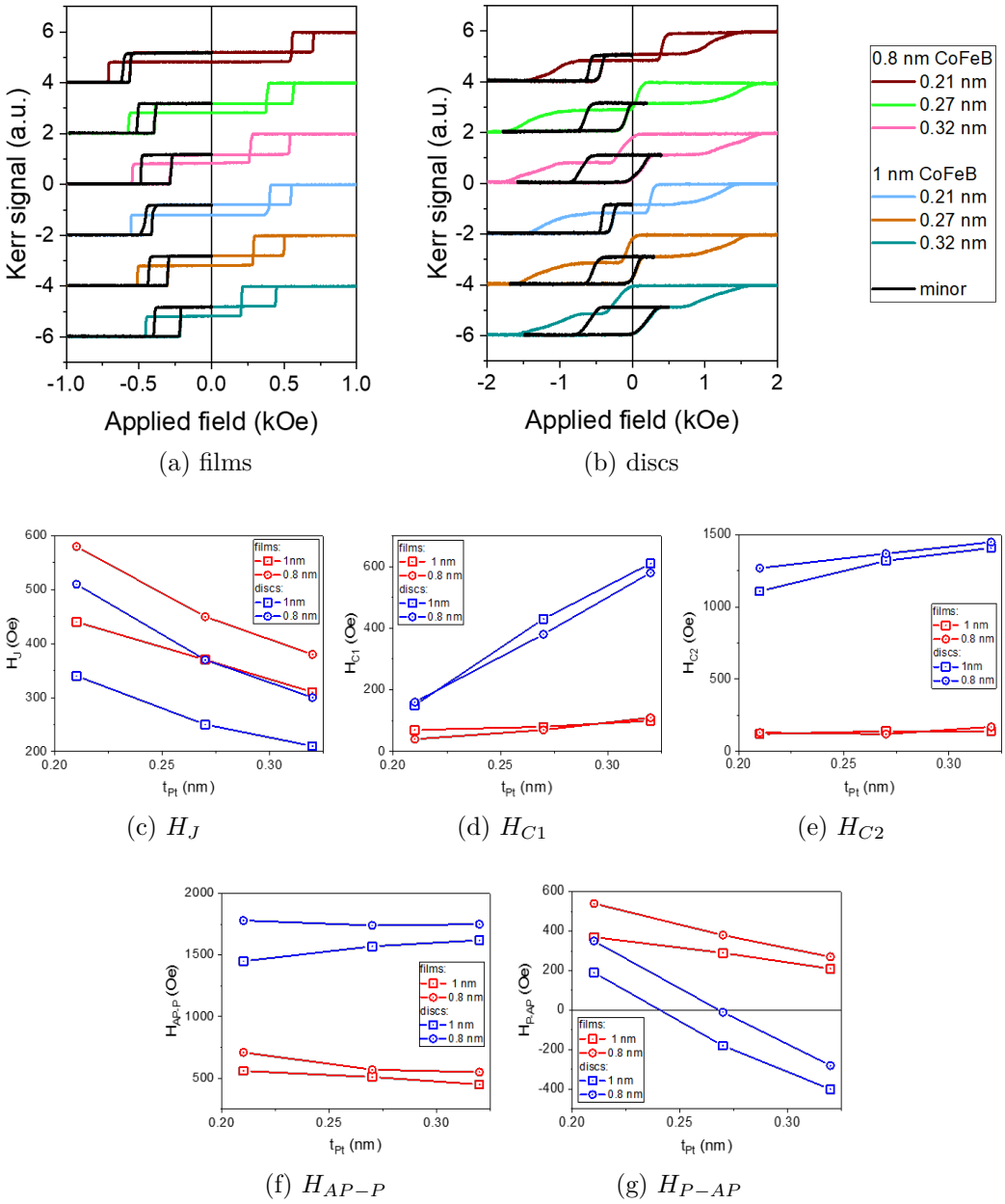

(a) films (b) discs

(c) H_J (d) H_{C1} (e) H_{C2}

(f) H_{AP-P} (g) H_{P-AP}

Figure 5.20: MOKE loops of a series of SAF stacks grown using 2nm Ru, with varied CoFeB (0.8 and 1 nm, marked in legend) and Pt interlayer thicknesses, in (a) film and (b) nanodisc form. Variation of (d) coupling, (e) top and (f) bottom layer coercivity (linear fits added to guide the eye), (g) AP–P transition field and (h) P–AP transition field with t_{Pt} for the films and nanodiscs.

of the discs, H_{C2} is consistently much higher than H_{C1}. This creates a much larger increase in coercivity from the thin film to the discs for the bottom CoFeB layers than the top layers. This feature is once more explained by inherent roughness: the bottom CoFeB layer is closer to the Ta buffer, which leads to a lesser induction of growth defects than in the top CoFeB layer. Consequently, the top layer is less affected by the patterning process than the bottom layer and H_{C1} comes out consistently lower.

Once more we have plotted the AP–P and P–AP switching fields with respect to t_{Pt}. Similarly to the 1st AF peak SAFs, H_{P-AP} consistently drops after the patterning

process, and there is a divergence as t_{Pt} increases. This divergence results in negative values of H_{P-AP} for the nanodiscs, which leads to a loss of the AP remanence state in all but the $t_{Pt} = 0.21$ nm samples. For H_{AP-P}, we again find an increase from films to discs, however this increase is much more consistent across the samples. These results indicate that although there is a more restricted range for the production of nanodiscs with a successfully conserved AP state, by using the 2nd AF peak it is possible to create functional SAF nanodiscs that switch in the lower field range.

Comparison of 1st and 2nd AF peak particles

We have observed a clear increase in coercivity from films to discs in both sets of SAFs. We also discussed a general behaviour of increasing coercivity with increasing t_{Pt} across all of the discs. Moreover, there appears to be differences in the coercivity behaviour between the 1st and 2nd AF peak samples. To more easily compare these field parameters, H_{C1} and H_{C2} are plotted against t_{Pt} for both sets of SAFs. The graphs, for thin films and nanodiscs separately, are shown in Figure 5.21.

Starting with the films (top row), we note that plotting the data from these samples separately to that of the nanodiscs has revealed a trend that was indistinct in the earlier figures: there is a similar positive correlation of coercivity with t_{Pt} as that previously seen for the nanodiscs. This trend appears with larger gradients across the H_{C1} data (left) than the H_{C2} data (right). This is understandable as decreasing t_{Pt} induces more defects in the stack and thus creates more nucleation sites. This effect is more prevalent in the top CoFeB layers as they are further from the Ta smoothing layer and directly on top of the Pt interlayers. We note that the $t_{Pt} = 0.37$ nm sample is an outlier from the general trend in H_{C1} for the 1st peak films: the top layer exhibits a much higher coercivity, $\sim$ 170 Oe, than the other films at the lower end of the t_{Pt} series (black points).

The other interesting observation is the large drop in H_{C1}, of $\sim$ 100 Oe, when we transition from the 2nd (red and blue) to the 1st AF peak samples (black). The same drop is not present in the H_{C2} graph: here, the 1st peak data appears to follow on from the 2nd peak's. This could be explained by the use of the thicker Ru layer in the 2nd peak films, which limits any extra defects induced by the Pt interlayers in the top CoFeB layer (H_{C1}), increasing coercivity through a reduction in pinholes or orange peel coupling.

Moving on to the discs (bottom row), when we compare H_{C1} (left) and H_{C2} (right) for the 1st AF peak SAFs (black) the numbers are generally similar, with an overall trend of increasing coercivity with t_{Pt}. The 2nd peak SAFs (red and blue) exhibit this same trend with t_{Pt}, however as was discussed previously, there is a large increase in value from H_{C1} to H_{C2} of $\sim$ 1000 Oe. As we found with the films, there is a similar sized drop in H_{C1} (left) from the 2nd peak (red and blue) to the 1st peak (black) samples. Conversely to the films, we see a large drop of $\sim$ 600 Oe in the H_{C2} (right) values from 2nd to 1st Ru peak. This indicates that the 2nd AF films are more affected by the

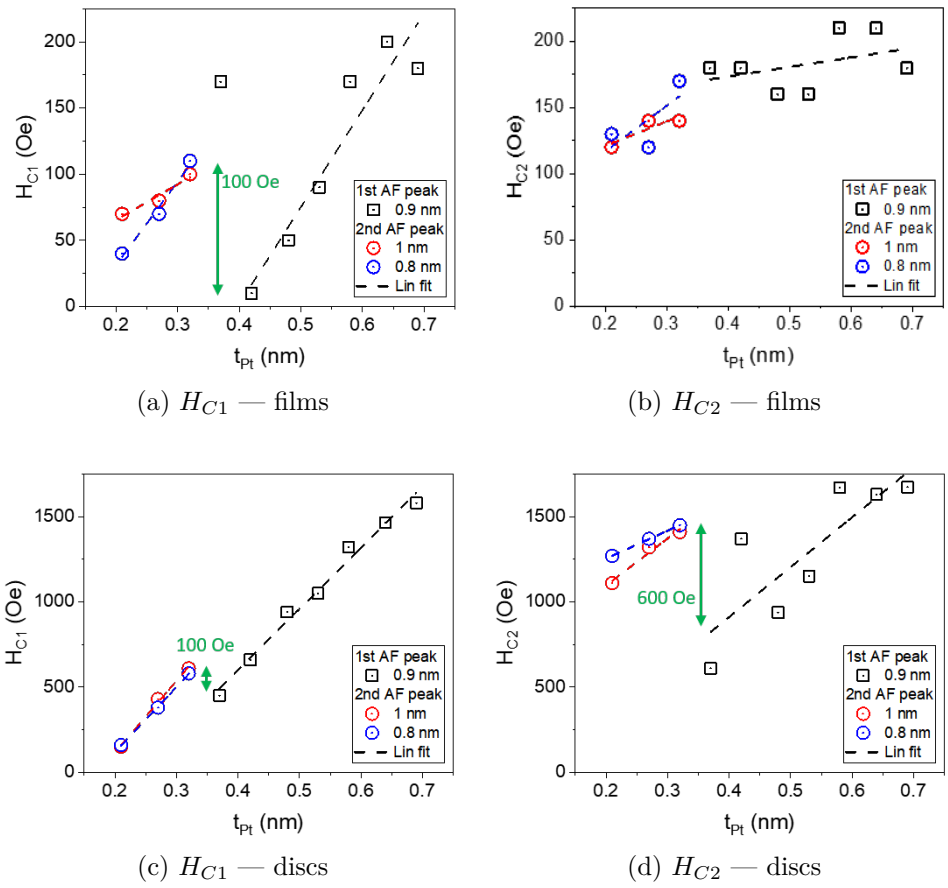

(a) H_{C1} — films (b) H_{C2} — films

(c) H_{C1} — discs (d) H_{C2} — discs

Figure 5.21: Variation of coercivity, with t_{Pt}, for the 1st and 2nd AF peak SAFs. Legend identifies samples by CoFeB thickness. Linear fits are added to guide the eye.

patterning process than the thinner t_{Pt} end of the 1st AF series. Thicker Ru limits pinhole defects in the 2nd AF films and thus reduces the likelihood of the presence of nucleation sites in the nanodiscs. As with Si vs Ge, this leads to a greater change in coercivity on patterning.

Earlier, it was mentioned that the changes in the SAF magnetic state, through the process of patterning, can affect the functionality of magnetic particles. Significantly, large changes in the coercivity in more weakly coupled SAFs can lead to the loss of the zero remanence state that prevents particle agglomeration. Thus, it is useful to further probe the impact these changes might have on magnetic particles that are being tuned towards an application, namely those engineered with a particular switching field. By plotting the changes in switching field parameters from films to discs with respect to the coupling strength of the films, instead of t_{Pt}, we can study the SAF behaviours through a metric that is more applicable to design for application.

Figure 5.22 displays the results for both change (ΔH_J) and fractional change ($\Delta H_J / H_J\ film$) in coupling strength, for the 1st and 2nd AF peak SAFs. ΔH_J shows a clear negative correlation with $H_J\ film$, across the sample sets. By translating this into fractional change, and calculating the mean and standard deviation across the full data set, we find that this trend originates from a general change in behaviour caused by patterning. The transformation of a SAF stack from a thin film to nanodiscs generates

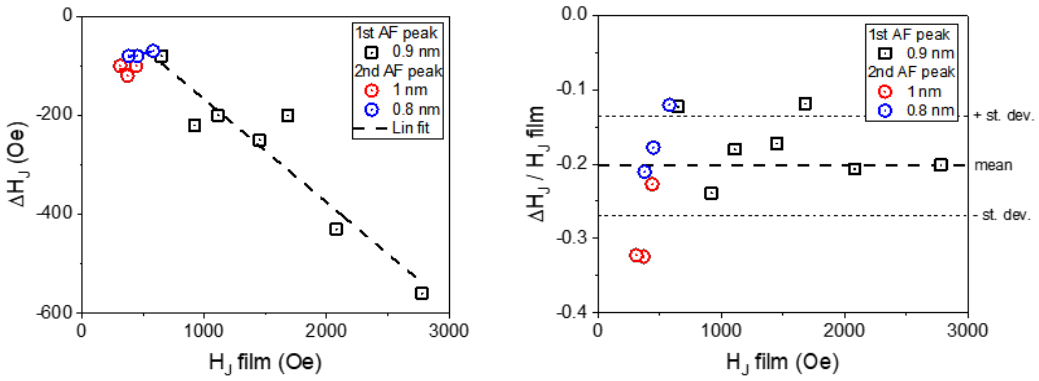

(a) ΔH_J (b) $\Delta H_J / H_J\ film$

Figure 5.22: (a) The change in coupling from SAF films to discs, for the 1st and 2nd peak AF samples, versus the H_J of the films. (b) The fractional change in coupling versus the H_J of the films. Legend identifies samples by CoFeB thickness. The mean, -0.202, and one standard deviation, 0.067, from the mean are marked with horizontal lines.

a common percentage decrease in coupling strength of $20 \pm 7\%$. This is the influence of the magnetostatic interactions favouring the parallel configuration of the CoFeB moments.

Across the disc samples, there is an inverse correlation between ΔH_C and $H_J\ film$ (see Figure 5.23). As expected from earlier analysis, there is a large increase in ΔH_C from the top (H_{C1}) to bottom (H_{C2}) CoFeB layers in the 2nd AF peak SAFs (red and blue), in the region of 1000 Oe. The 1st peak SAFs (black) exhibit a more similar range of ΔH_C across the series, with a relatively small rise in value from ΔH_{C1} to ΔH_{C2} (~ 200 Oe on average). Looking at just the bottom CoFeB layers (H_{C2}) , there is a relatively small step down in ΔH_{C2} as we transition from the 1st to the 2nd AF peak Ru SAFs, moving down in $H_J\ film$. The equivalent step for the top CoFeB layers (H_{C1}) is much larger: as $H_J\ film$ is decreased and we move from the 1st peak SAFs to the 2nd peak set, there is a big drop in ΔH_{C1} of over 1000 Oe. This is explained by the top CoFeB layer being further away from the smoothing effect of Ta, which instills more roughness in its interfaces. This effect will be more prevalent the thinner t_{Pt} is (lowest in the 2nd AF films), as the added inherent defects will limit the changes caused by the patterning process. This leads to a much smaller change in coercivity in the 2nd AF discs compared with the weakest coupled 1st AF discs.

Overall, these results indicate that the process of patterning a thin film into nanodiscs has a smaller impact on the magnetic properties of a SAF coupled by 2 nm of Ru than one coupled by 0.9 nm Ru. Significantly, this leads to a higher potential for conserving the zero remanence state in more weakly coupled SAFs. Thus, if an application requires the use of SAF particles with lower switching fields, and hence lower coupling strengths, it may be beneficial to utilise the 2nd AF coupling peak in the SAF stack. The ability to efficiently and controllably generate torque at field strengths below 1 kOe is very useful in applications where it is challenging to apply strong fields. This is

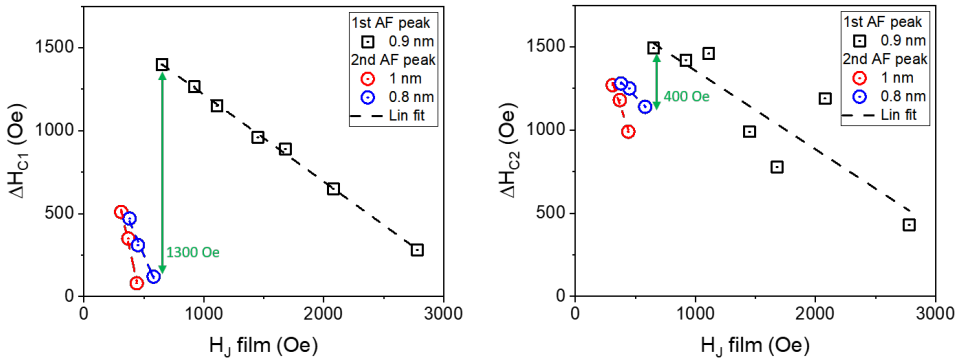

(a) ΔH_{C1} (b) ΔH_{C2}

Figure 5.23: The change in coercivity for the (a) top and (b) bottom layers of the 1st and 2nd AF peak samples, versus the H_J of the films. Legend identifies samples by CoFeB thickness.

relevant to lab-on-chip technologies, where for practicality and cost effectiveness it is desirable to keep applied field strengths low. This includes point-of-care microfluidic devices for the sorting of analytes or other biological species [47].

5.4 Conclusion

This chapter has introduced an efficient and robust fabrication method for the production of thin film based magnetic particles ranging from 100 nm–1 μm. The implementation of NSL in combination with ion milling generates high yields of well-defined nanodiscs. Spread and yield of particles is easily tuned through the spin coating parameters and dilution of the PS beads. The choice of Ge as the sacrificial layer has been shown to conserve the engineered magnetic properties of PM SAFs, without compromising ease of lift off.

Modification of parameters, including milling power and PS bead size, during the production of nanodiscs, revealed the mechanisms behind the changes in magnetic hysteresis from PM SAF films to particles. Major contributions originate from the induction of defects by ion interactions during the milling process, along with the reduction in likelihood in nucleation sites in nanostructures in comparison with a continuous film. Additionally, the inherent change from continuous film to nanostructures generates hysteretic changes, in particular through the induction of magnetostatic interactions. However, we have demonstrated that we maintain key magnetic properties during the patterning process: namely tunable switching, an AP remanence state and low field susceptibility. This shows PM SAF particles, made using this method, to be suitable candidates for biological applications.

The exploration of PM SAFs with varied coupling strength revealed a limitation in the use of 1st AF peak SAFs in the production of nanodiscs: particles that are more weakly coupled do not maintain their AP state at remanence. By modifying the coupling layers and implementing the 2nd AF peak (in combination with ultrathin Pt

interlayers) to produce weakly coupled SAFs, we show that it is still possible to create functional nanodiscs that are activated in the low field regime. This is highly relevant for biotech applications that cannot utilise strong magnetic fields, such as lab-on-chip devices.

The next chapter will continue to investigate the magnetic behaviour of PM SAF particles, but will move to studying them in a liquid environment. The added degree of freedom in the form of mechanical reconfiguration opens up new areas of the particle energy landscape and leads to the discovery of novel transitions and self-assembly behaviour. This opens up more properties that may be exploited in biological and other fluidic applications.

References

[1] H. W. Deckman and J. H. Dunsmuir. Natural lithography. *Applied Physics Letters*, 41(4):377–379, 1982.

[2] John C. Hulteen and Richard P. Van Duyne. Nanosphere lithography: A materials general fabrication process for periodic particle array surfaces. *Journal of Vacuum Science & Technology A: Vacuum, Surfaces, and Films*, 13(3):1553–1558, 1995.

[3] N Persat and A Dinia. Strong temperature dependence of the interlayer exchange coupling strength in Co/Cu/Co sandwiches. *Phys. Rev. B*, 56(5):2676–2679, aug 1997.

[4] Stephen Y. Chou, Peter R. Krauss, Wei Zhang, Lingjie Guo, and Lei Zhuang. Imprint Lithography with 25-Nanometer Resolution. *J. Vac. Sci. Technol. B*, 15(6):2897 – 2904, 1997.

[5] R. P. Cowburn, D. K. Koltsov, a. O. Adeyeye, and M. E. Welland. Single-Domain Circular Nanomagnets. *Physical Review Letters*, 83(5):1042–1045, 1999.

[6] Andreas Jordan, Regina Scholz, Peter Wust, Horst Fähling, and Roland Felix. Magnetic fluid hyperthermia (MFH): Cancer treatment with AC magnetic field induced excitation of biocompatible superparamagnetic nanoparticles. *Journal of Magnetism and Magnetic Materials*, 201(1-3):413–419, 1999.

[7] R Hyndman, P Warin, J Gierak, J Ferré, J N Chapman, J P Jamet, V Mathet, and C Chappert. Modification of Co/Pt multilayers by gallium irradiation - Part 1: The effect on structural and magnetic properties. *Journal of Applied Physics*, 90(8):3843–3849, sep 2001.

[8] Paul A. Liberti, Chandra G. Rao, and Leon W.M.M. Terstappen. Optimization of ferrofluids and protocols for the enrichment of breast tumor cells in blood. *Journal of Magnetism and Magnetic Materials*, 225(1-2):301–307, jan 2001.

[9] D.K. Kim, Y. Zhang, W. Voit, K.V. Rao, and M. Muhammed. Synthesis and characterization of surfactant-coated superparamagnetic monodispersed iron oxide nanoparticles. *Journal of Magnetism and Magnetic Materials*, 225(1-2):30–36, jan 2001.

[10] Wolf K. Hofmann, Sven De Vos, Martina Komor, Dieter Hoelzer, William Wachsman, and H. Phillip Koeffler. Characterization of gene expression of CD34 + cells from normal and myelodysplastic bone marrow. *Blood*, 100(10):3553–3560, 2002.

[11] QA A Pankhurst, J Connolly, S K Jones, and J Dobson. Applications of magnetic nanoparticles in biomedicine. *Journal of Physics D-Applied Physics*, 36(13):R167–R181, 2003.

[12] Y. Lalatonne, J. Richardi, and M. P. Pileni. Van der Waals versus dipolar forces controlling mesoscopic organizations of magnetic nanocrystals. *Nature Materials*, 3(2):121–125, feb 2004.

[13] J. Moritz, F. Garcia, J. C. Toussaint, B. Dieny, and J. P. Nozières. Orange peel coupling in multilayers with perpendicular magnetic anisotropy: Application to (Co/Pt)-based exchange-biased spin-valves. *Europhysics Letters*, 65(1):123–129, 2004.

[14] Tobias Neuberger, Bernhard Schöpf, Heinrich Hofmann, Margarete Hofmann, and Brigitte von Rechenberg. Superparamagnetic nanoparticles for biomedical applications: Possibilities and limitations of a new drug delivery system. *Journal of Magnetism and Magnetic Materials*, 293(1):483–496, may 2005.

[15] Ajay Kumar Gupta and Mona Gupta. Synthesis and surface engineering of iron oxide nanoparticles for biomedical applications. *Biomaterials*, 26(18):3995–4021, jun 2005.

[16] V Baltz, A Bollero, B Rodmacq, B Dieny, J.-P. Jamet, and J Ferré. Multilevel magnetic nanodot arrays with out of plane anisotropy: the role of intradot magnetostatic coupling. *The European Physical Journal - Applied Physics*, 39(1):33–38, 2007.

[17] Hans Fredriksson, Yury Alaverdyan, Alexandre Dmitriev, Christoph Langhammer, D. S. Sutherland, Michael Zäch, and Bengt Kasemo. Hole-Mask Colloidal Lithography. *Advanced Materials*, 19(23):4297–4302, dec 2007.

[18] Wei Hu, Robert J. Wilson, AiLeen Koh, Aihua Fu, Anthony Z. Faranesh, Christopher M. Earhart, Sebastian J. Osterfeld, Shu-Jen Han, Liang Xu, Samira Guccione, Robert Sinclair, and Shan X. Wang. High-Moment Antiferromagnetic Nanoparticles with Tunable Magnetic Properties. *Advanced Materials*, 20(8):1479–1483, apr 2008.

[19] S. E. A. Gratton, Patricia A. Ropp, Patrick D. Pohlhaus, J. Christopher Luft, Victoria J. Madden, Mary E. Napier, and Joseph M. DeSimone. The effect of particle design on cellular internalization pathways. *Proceedings of the National Academy of Sciences*, 105(33):11613–11618, aug 2008.

[20] Jon Dobson. Remote control of cellular behaviour with magnetic nanoparticles. *Nature Nanotechnology*, 3(3):139–143, mar 2008.

[21] T. A. Moore, I. M. Miron, G. Gaudin, G. Serret, S. Auffret, B. Rodmacq, A. Schuhl, S. Pizzini, J. Vogel, and M. Bonfim. High domain wall velocities induced by current in ultrathin Pt/Co/AlOx wires with perpendicular magnetic anisotropy. *Applied Physics Letters*, 93(26):262504, dec 2008.

[22] Quentin A. Pankhurst, N. T. K. Thanh, S. K. Jones, and Jon Dobson. Progress in applications of magnetic nanoparticles in biomedicine. *Journal of Physics D: Applied Physics*, 42(22):224001, nov 2009.

[23] Jochen F. Peter, Angela M. Otto, and Bernhard Wolf. Magnetic particles as Powerful Purification Tool for High Sensitive Mass Spectrometric Screening Procedures. *Proteomics*, 2009.

[24] Wei Hu, Robert J. Wilson, Christopher M. Earhart, Ai Leen Koh, Robert Sinclair, and Shan X. Wang. Synthetic antiferromagnetic nanoparticles with tunable susceptibilities. *Journal of Applied Physics*, 105(7):7–10, 2009.

[25] H. Joisten, T. Courcier, P. Balint, P. Sabon, J. Faure-Vincent, S. Auffret, and B. Dieny. Self-polarization phenomenon and control of dispersion of synthetic antiferromagnetic nanoparticles for biological applications. *Applied Physics Letters*, 97(25):253112, 2010.

[26] Dong-Hyun Kim, Elena a Rozhkova, Ilya V Ulasov, Samuel D Bader, Tijana Rajh, Maciej S Lesniak, and Valentyn Novosad. Biofunctionalized magnetic-vortex microdiscs for targeted cancer-cell destruction. *Nature materials*, 9(2):165–71, feb 2010.

[27] Ai Leen Koh, Wei Hu, Robert J Wilson, Christopher M Earhart, Shan X Wang, and Robert Sinclair. Structural and magnetic characterizations of high moment synthetic antiferromagnetic nanoparticles fabricated using self-assembled stamps. *Journal of applied physics*, 107(9):9B522, 2010.

[28] W Alayo and E Baggio-Saitovitch. Study of the interlayer coupling and its temperature dependence in spin valves with Ru and Cu spacers. *Journal of Applied Physics*, 107(7):73909, apr 2010.

[29] Yanyan Zhu, Zongzhi Zhang, Bin Ma, and Q Y Jin. Thermal stability of CoFeB/Pt multilayers with perpendicular magnetic anisotropy. *Journal of Applied Physics*, 111(7):07C106, feb 2012.

[30] R. Lavrijsen, A. Fernández-Pacheco, D. Petit, R. Mansell, J. H. Lee, and R. P. Cowburn. Tuning the interlayer exchange coupling between single perpendicularly magnetized CoFeB layers. *Applied Physics Letters*, 100(5):052411, jan 2012.

[31] Elina A Vitol, Valentyn Novosad, and Elena A Rozhkova. Microfabricated magnetic structures for future medicine: from sensors to cell actuators. *Nanomedicine*, 7(10):1611–1624, 2012.

[32] O Osman, S Toru, F Dumas-Bouchiat, N M Dempsey, N Haddour, L-F Zanini, F Buret, G Reyne, and M Frénéa-Robin. Microfluidic immunomagnetic cell separation using integrated permanent micromagnets. *Biomicrofluidics*, 7(5):54115, jan 2013.

[33] S. Leulmi, H. Joisten, T. Dietsch, C. Iss, M. Morcrette, S. Auffret, P. Sabon, and B. Dieny. Comparison of dispersion and actuation properties of vortex and synthetic antiferromagnetic particles for biotechnological applications. *Applied Physics Letters*, 103(13):132412, 2013.

[34] Jian Chen, Peitao Dong, Di Di, Chaoguang Wang, Haoxu Wang, Junfeng Wang, and Xuezhong Wu. Controllable fabrication of 2D colloidal-crystal films with polystyrene nanospheres of various diameters by spin-coating. *Applied Surface Science*, 270:6–15, 2013.

[35] C Fowley, Z Diao, C C Faulkner, J Kally, K Ackland, G Behan, H Z Zhang, A M Deac, and J M D Coey. Local modification of magnetic anisotropy and ion milling of Co/Pt multilayers using a He+ion beam microscope. *Journal of Physics D: Applied Physics*, 46(19):195501, 2013.

[36] Hung Chun Wu, Ming Dong Bao, and Kung Jeng Ma. Fabrication of size-tunable hierarchical CrN nanohole arrays for two-dimensional nanomould using modified nanosphere lithography. *Micro and Nano Letters*, 9(8):491–495, 2014.

[37] J C Read, P M Braganca, N Robertson, and J R Childress. Magnetic degradation of thin film multilayers during ion milling. *APL Materials*, 2(4):46109, apr 2014.

[38] T Vemulkar, R Mansell, D C M C Petit, R P Cowburn, and M S Lesniak. Highly tunable perpendicularly magnetized synthetic antiferromagnets for biotechnology applications. *Applied Physics Letters*, 107(1):012403, jul 2015.

[39] P. Tiberto, G. Barrera, F. Celegato, G. Conta, M. Coïsson, F. Vinai, and F. Albertini. Ni 80 Fe 20 nanodisks by nanosphere lithography for biomedical applications. *Journal of Applied Physics*, 117(17):17B304, may 2015.

[40] E. A. Périgo, G. Hemery, O. Sandre, D. Ortega, E. Garaio, F. Plazaola, and F. J. Teran. Fundamentals and advances in magnetic hyperthermia. *Applied Physics Reviews*, 2(4):041302, dec 2015.

[41] Bogdan Parakhonskiy, Mikhail V. Zyuzin, Alexey Yashchenok, Susana Carregal-Romero, Joanna Rejman, Helmuth Möhwald, Wolfgang J. Parak, and Andre G. Skirtach. The influence of the size and aspect ratio of anisotropic, porous CaCO3 particles on their uptake by cells. *Journal of Nanobiotechnology*, 13(1):53, dec 2015.

[42] Yu Cheng, Megan E. Muroski, Dorothée C.M.C. Petit, Rhodri Mansell, Tarun Vemulkar, Ramin A. Morshed, Yu Han, Irina V. Balyasnikova, Craig M. Horbinski, Xinlei Huang, Lingjiao Zhang, Russell P. Cowburn, and Maciej S. Lesniak. Rotating magnetic field induced oscillation of magnetic particles for in vivo mechanical destruction of malignant glioma. *Journal of Controlled Release*, 223:75–84, feb 2016.

[43] M Goiriena-Goikoetxea, A García-Arribas, M Rouco, A V Svalov, and J M Barandiaran. High-yield fabrication of 60 nm Permalloy nanodiscs in well-defined magnetic vortex state for biomedical applications. *Nanotechnology*, 27(17):175302, apr 2016.

[44] Attarad Ali, Hira Zafar, Muhammad Zia, Ihsan ul Haq, Abdul Rehman Phull, Joham Sarfraz Ali, and Altaf Hussain. Synthesis, characterization, applications, and challenges of iron oxide nanoparticles. *Nanotechnology, Science and Applications*, Volume 9:49–67, aug 2016.

[45] Rhodri Mansell, Tarun Vemulkar, Dorothée C. M. C. Petit, Yu Cheng, Jason Murphy, Maciej S. Lesniak, and Russell P. Cowburn. Magnetic particles with perpendicular anisotropy for mechanical cancer cell destruction. *Scientific Reports*, 7(1):4257, 2017.

[46] T. Vemulkar, E. N. Welbourne, R. Mansell, D. C. M. C. Petit, and R. P. Cowburn. The mechanical response in a fluid of synthetic antiferromagnetic and ferrimagnetic microdiscs with perpendicular magnetic anisotropy. *Applied Physics Letters*, 110(4):042402, 2017.

[47] Elizabeth Rapoport and Geoffrey S.D. Beach. Architecture for Directed Transport of Superparamagnetic Microbeads in a Magnetic Domain Wall Routing Network. *Scientific Reports*, 7(1):17–23, 2017.

[48] Abhishek Chandramohan, Nikolai V. Sibirev, Vladimir G. Dubrovskii, Michael C. Petty, Andrew J. Gallant, and Dagou A. Zeze. Model for large-area monolayer coverage of polystyrene nanospheres by spin coating. *Scientific Reports*, 7(1):40888, feb 2017.

[49] Kaarjel K. Narayanasamy, Melissa Cruz-Acuña, Carlos Rinaldi, James Everett, Jon Dobson, and Neil D. Telling. Alternating current (AC) susceptibility as a particle-focused probe of coating and clustering behaviour in magnetic nanoparticle suspensions. *Journal of Colloid and Interface Science*, 532:536–545, 2018.

[50] Yong Li, Xiangjun Jin, Pengfei Pan, Fu Nan Tan, Wen Siang Lew, and Fusheng Ma. Temperature-dependent interlayer exchange coupling strength in synthetic antiferromagnetic (Pt/Co)2/Ru/(Co/Pt)4 multilayers. *Chinese Physics B*, 27(12):127502, 2018.

Chapter 6

Magneto-mechanical behaviour of particles in liquid

6.1 Introduction

This work has so far thoroughly characterised the magnetic reversal of PM AF coupled thin films, demonstrated their patterning into robust disc-shaped particles and studied the consequences of patterning on the magnetic properties of the films. As these discs are engineered for the purpose of being used in biological and other liquid-based applications, it stands to reason that their behaviour should be studied in a fluid environment. This environment opens up the energy landscape for the discs, delivering a new degree of freedom in the form of physical orientation. Under the influence of applied fields, this has lead to the emergence of novel magneto-mechanical transitions [12]. Furthermore, the liquid suspension of discs forms a multi-particle system with the exhibition of inter-particle interactions, which generates self-assembly [12]. Accordingly, these particles have interesting implications across a range of research fields including organisation of biological systems, soft-robotics, assembly of nanostructures and smart materials [13].

The ability of a liquid suspension of magnetic micro- and nanoparticles to dynamically self-assemble under the application of a magnetic field has been well-established [5, 9, 13]. So far, the vast majority of work on this behaviour has employed magnetically simple superparamagnetic or ferromagnetic particles, stabilised by surface functionalisation, as the fundamental magnetic building block of the system. Under the application of uniaxial applied fields such systems can only form static, linear chains. One way that researchers have achieved more complex self-assembly in these types of systems is through the application of alternating magnetic fields, often in conjunction with liquid properties, e.g. surface tension [9–11, 13]. Additionally, the magnetic building blocks have been engineered with some chirality [14] or flexibility [6], which leads to the formation of more complex configurations.

PM AF coupled micro- and nanodiscs offer a more complex magnetic system to be exploited in dynamic self-assembly. Here, the balance between the exchange cou-

pling (EC) and perpendicular magnetic anisotropy (PMA), and their interplay with an applied field, generates torques on the moments of the magnetic layers [15], which can be transferred into mechanical rotations [12]. An earlier study began to probe the magneto-mechanical and self-assembly behaviour of PM AF coupled systems, leading with the exploration of the perfectly balanced, SAF case [12]. This work discovered novel transitions of SAF microdiscs under the influence of a uniaxial applied magnetic field sequence. These included abrupt mechanical rotations and the canting of magnetic moments, which allowed access to different magnetic saturation processes in order to lower particle energy. Furthermore, these transitions enabled the particles to form reconfigurable magnetic chains, and transduce torque from uniaxial fields. A more detailed discussion of this work is provided in Section 2.2.2. These findings open up a new possibility for more complex and dynamic self-assemblies, with only simple, uniaxial applied magnetic fields required to manipulate the system. Hence, the behaviour demonstrated by this type of particle offers an attractive platform for fluid-based micro- and nanodevices or dynamically self-assembled complex architectures [12].

Following on from the study of the perfectly balanced SAFs, we extended the investigation to the case with an imbalance in moment: the synthetic ferrimagnetic (SFi) system. This chapter begins with an assessment of this type of particle, with a very slight moment imbalance, in a parallel to the SAF study. It then goes on to a wider exploration of the PM AF coupled particle energy landscape, through a macrospin model. Here, we focus on the pre-saturation state of SFi discs and how this is affected by the balance of the EC and PMA energies, and the moment imbalance. Additionally, a novel transition is revealed for particles with a particularly strong EC/weak PMA. The final two sections of this chapter centre around real PM AF coupled particles, which have been made using our new version of nanodisc fabrication (see Section 5.2.2). The characterisation of their behaviour in liquid suspensions, under the application of uniaxial magnetic fields, is accomplished through a series of experimental techniques: liquid VSM, optical microscopy (OM) and reflectivity measurements.

6.2 Magneto-mechanical behaviour of SFi particles in liquid

Note: The work in this section was done in collaboration with T. Vemulkar (Prof. Cowburn's group). T. Vemulkar took the VSM measurements and ran the simulations.

6.2.1 Experimental observations

Following on from the experimental observations of PM SAF particles in liquid (Section 2.2.2), the magneto-mechanical behaviour of particles with a small asymmetry in moment were explored. A set of 2 μm discs, fabricated using the photoresist pillar method, were created from SFi film described by $[Ta(2)/Pt(2)]_3/[Ta(2)/Pt(2)/CoFeB(1.2)/Pt(0.5)/Ru(0.9)/Pt(0.5)/CoFeB(\approx 1.21)/\ Pt(2)]_2/Ta(2)/[Pt(2)/Ta(2)]_3$

with thicknesses in nm. The EA liquid VSM loops of this film is displayed in Figure 6.1a. The additional steps seen in the AP–P and P–AP transitions of the film are due to a slight variation in the coercivity and coupling field between the two individual bilayers in the SFi stack. These are the result of variations in the growth conditions during the sputtering process. From the minor loop we extract the lower value of the coupling field, $H_J \approx 1.43$ kOe, and for simplicity we will use this for the entire film. The slight difference in thickness, $\sim 1\%$, between the two CoFeB layers is highlighted in Figure 6.1b: the asymmetry manifests as a small, slanted transition around zero field and is another consequence of variations in the film growth conditions. The HP VSM loop of the film is shown in Figure 6.1c, from which we extract a saturation field (H_{Sat}) of ~ 9.50 kOe. We assume that the anisotropy and M_S are not affected by the asymmetry and that they are constant across the CoFeB layers.

The liquid VSM loop of the SFi discs in Figure 6.1d shows a linear response at low fields (regime II), followed by a distinct and coercive transition to saturation (regime III), which is very similar to that observed in the case of the SAF discs in Section 2.2.2. There is however a difference in the very low field response (regime I) of the SFi discs compared with the SAFs; Figure 6.1e shows that under an applied field of ~ -50 Oe, the particles align their EA parallel with the field direction. This behaviour

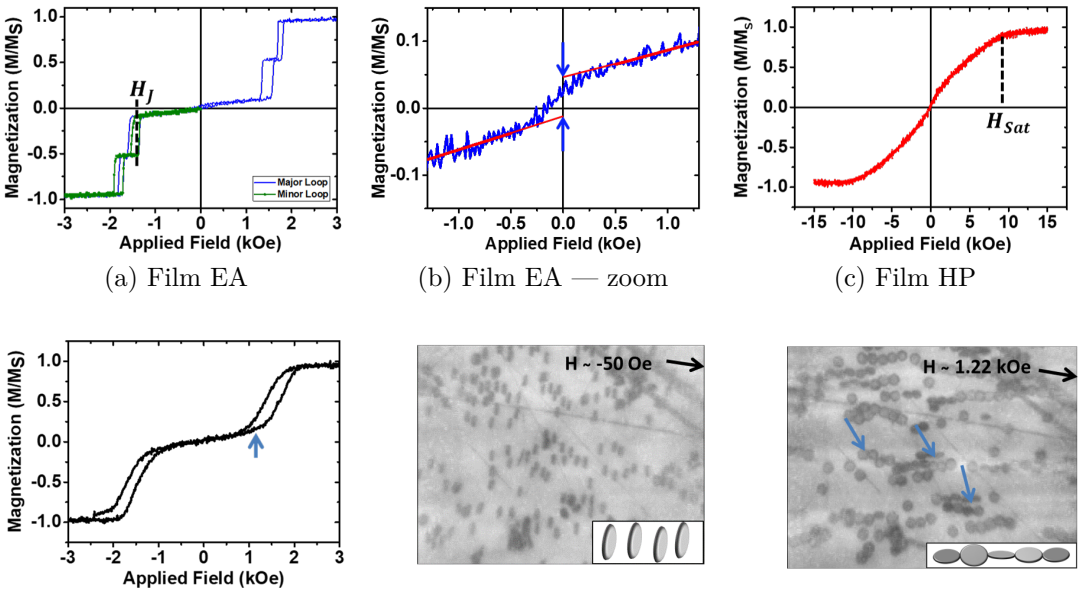

(a) Film EA (b) Film EA — zoom (c) Film HP

(d) Discs in liquid (e) -50 Oe (f) 1220 Oe

Figure 6.1: Figure adapted from [12]. (a) The EA VSM loop of the SFi film with effective coupling field, H_J, indicated. (b) The low field response of the film (rising field only for clarity), with the blue arrows highlighting the degree of ferrimagnetism. (c) The HP VSM loop of the film with saturation field, H_{Sat}, indicated. (d) The liquid VSM loop of the suspension of the SFi microdiscs with identical stack structure to the SFi film (blue arrow indicates an applied field of 1.22 kOe). 100× OM images (taken using the OM-magnet set up described in (Section 3.3.1)) of the SFi microdisc suspension under applied fields, H, of (e) ~ -50 Oe and (f) ~ 1.22 kOe (field direction indicated by the black arrows). The blue arrow in (d) indicates the field in (f). The inset schematics depict the particle configurations.

is the result of the small imbalance in moment in the SFi system. This is not clearly evident in the hysteresis in Figure 6.1d due to the particularly small signal size of this transition (the resulting magnetisation jump is only twice the imbalance in magnetic moment) and an increase in noise from film to liquid measurements. This transition is due to a 180° rotation of the SFi discs as the applied field goes through zero. As the field is increased into regime II, the linear regime, the SFi discs rotate in a magneto-mechanical transition to align their HP parallel with the field direction. This behaviour is shown at an applied field of $\sim$ 1.22 kOe (highlighted by the blue arrow in Figure 6.1d) in the image in Figure 6.1f, where the discs are chaining side-to-side. A second magneto-mechanical transition occurs as the SFi discs saturate, at high fields $>$ 1.50 kOe. This leads to the third regime whereby the particles realign their EA with the field direction and chain in the face-to-face configuration analogous with the SAF discs.

6.2.2 Comparing with the model

Using the same model as was implemented in the macrospin simulations for the SAF microdiscs (detailed in Section 2.1.3), we examined the magnetic response of the SFi bilayer system. The energy and hysteresis versus applied field plots are shown in Figure 6.2 for the EA, HP and rotationally unconstrained global responses. The inset of Figure 6.2a shows how regime I (low field) manifests in the energy profile: here, the EA process is the lowest in energy, and thus the global response follows the same path. The inset of Figure 6.2b shows that in the magnetic hysteresis of the EA and global responses, the energy minimisation in regime I gives rise to a small, sharp transition as the field goes through zero. In the real thin film, we noted that the equivalent realignment of the larger moment with the field direction manifested as a slanted transition in the EA VSM loop. This is due to this magnetic reversal process occurring via the nucleation and propagation of magnetic domains [3]. In the case of the fluid suspension of the SFi microdiscs, the added degree of freedom of mechanical rotation generates a magneto-mechanical transition: a sharp 180° rotation realigning the larger moment with the field direction (see regime I in Figure 6.2c).

As the field is increased further, the system enters the regime II (mid-field, linear regime). Here, the HP process exhibits lower energy than the EA process, which leads to the global magnetisation process to follow that of the HP. This appears similar to the behaviour found for the SAF particles (see Section 2.2.2). However, if we take a closer look at the energy profile in the inset in Figure 6.2a, we observe that the global energy is in fact lower than both the EA and HP processes. This indicates a difference in the SFi configuration during the linear regime compared with the SAFs, which exhibit a HP alignment with the field. By extracting the angles of both layer moments and of the particle itself, we reveal a novel magneto-mechanical transition in regime II of the SFi system. As is demonstrated in Figure 6.2c, the particle EA continuously rotates away from the field direction as the field increases. This behaviour is accompanied by a simultaneous rotation of the two layer moments, with both canting away from the

EA, in a manner that favours the larger moment in the field direction.

Finally, regime III occurs once the field is increased above the saturation field of the system. Here, the EA process is again the lowest in energy and is identical to the global response. As with SAF particles, a magneto-mechanical transition occurs at saturation: the SFi disc abruptly rotates to realign its EA with the field direction and both layer moments transition into the parallel state (aligning with EA and field, see regime III in Figure 6.2c).

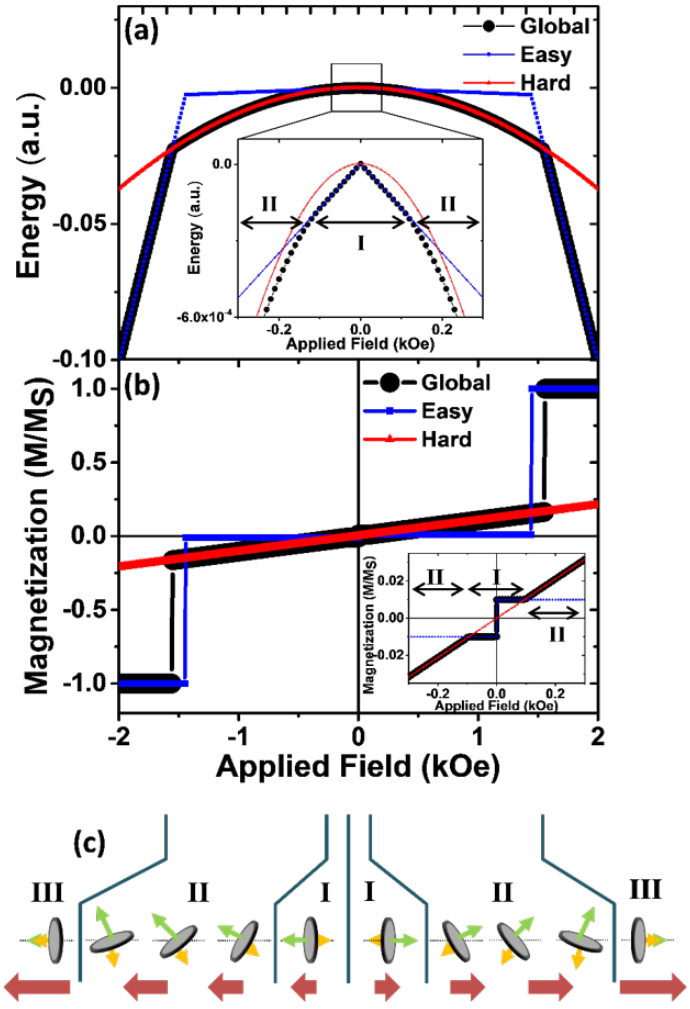

Figure 6.2: Figure taken from [12]. (a) Minimum energy curves for the EA (blue), HP (red) and global (black) responses of the SFi system using the magnetic parameters extracted from the thin film in Figure 6.1. (b) The corresponding simulated hysteresis loops for each response type. (c) A schematic depiction of the orientations of an individual disc and its layer moments (green and yellow arrows) with respect to the applied field (red arrows) across three regimes.

6.3 Exploring the AF particle energy landscape — macrospin simulations

6.3.1 The system

To further study the AF coupled particle system and investigate the magneto-mechanical behaviours these particles exhibit, the same macrospin model (see Figure 6.3a and 2.1.3) was used in conjunction with a larger array of parameters: a range of the EC-to-PMA ratio, J/Kt, which affects the magnetic reversal through the balance of system energies (see Section 2.1.3), and the degree of ferrimagnetism. The degree of ferrimagnetism was taken to be $\beta = (t_1 - t_2)/(t_1 + t_2)$, where $t_1 \geq 1$ nm is the thickness of layer 1 and $t_2 = (2 - t_1)$ nm is the thickness of layer 2 (see Figure 6.3b). This kept the average thickness t constant at 1 nm. A range J/Kt was then achieved by taking a constant value of the PMA, $K = 1 \times 10^6$ Oe emu cm^{-3}, and varying the EC, J.

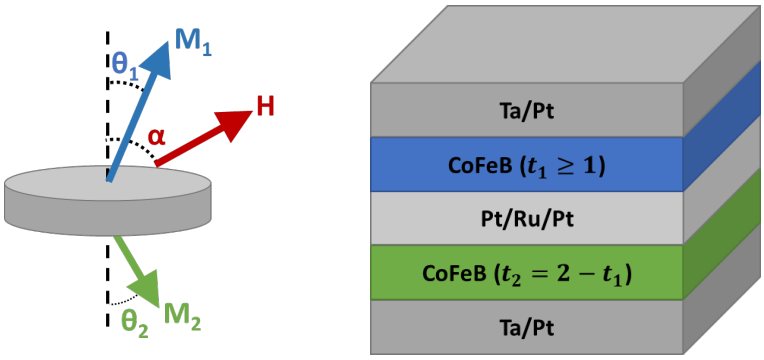

(a) Bilayer system (b) AF coupled stack

Figure 6.3: (a) A schematic showing the angles which are unconstrained in the Monte Carlo simulation: the angle between the fixed EA (dotted line) and applied field (H), α, and the angles between the moments of the CoFeB layers (M_1 and M_2) and the EA, θ_1 and θ_2. (b) The formation of the coupled bilayer stack used in the simulations of coupled bilayer particles in liquid, where the thicknesses of the CoFeB layers are t_1 and t_2.

6.3.2 A study of the pre-saturation state

The first study made was into how J/Kt and β affect the state of an AF coupled particle immediately before the magneto-mechanical switch to the saturated state. Previous work showed that a perfect SAF ($\beta = 0$) is in a configuration such that its EA is perpendicular to the field direction and the layer moments cant towards the HP/field direction [12]. Earlier (Section 6.2.2), we showed that a SFi system with a very small imbalance ($\beta \approx 0.004$) continuously rotates both its EA (away from the field) and layer moments (away from the EA) up to the point of saturation. To investigate the potential variation in the angles α, and θ_1 and θ_2 (field to EA and layer moments to EA respectively — see Figure 6.3a) immediately before saturation, macrospin simulation

were performed across an array of J/Kt and β. The thicknesses used for layer 1 were t_1 = 1–1.4 nm (steps of 0.01 nm) such that t_2 = 1–0.6 nm, producing the β range 0–0.4. A range of $J/Kt = 0.1$–1 was achieved by varying J between 0.01–0.1 Oe emu cm^{-2} in steps of 0.02 Oe emu cm^{-2}.

Figure 6.4 displays the phase diagrams generated for α, θ_1 and θ_2 across the array of β versus J/Kt. We find that the SFi particles in the top left zone of the phase diagrams (high β, low J/Kt) stay in the configuration with their EA and layer moments aligned along the field. An example of such a particle, with $\beta = 0.3$ and $J/Kt = 0.2$, is highlighted in Figure 6.5a. The hysteresis loop in this case exhibits strong, sharp switches through zero field and to saturation at $H \approx 300$ Oe. There is no presentation of the linear response previously found in the weak SFi system (see Section 6.2). The schematic depicts the state of the particle immediately before saturation where α, θ_1 and θ_2 are all zero. This indicates that either a strong enough imbalance or a low enough J/Kt will extinguish the canted state in the SFi system.

If we move across the phase diagrams, keeping β the same, but increasing J/Kt, we find a re-emergence of the off-axis canted state. Figure 6.5b demonstrates the response of a SFi with $J/Kt = 0.9$. The strong switch through zero field is identical to that of the case in Figure 6.5a. The transition to saturation is also similar, but occurs at the much higher field value of $H \approx 1.3$ kOe, which is an expected result of increasing J/Kt . Before saturation, there is a brief exhibition of the linear response, and thus the canted state, in the region of $1.2 < H < 1.3$ kOe. Just before the switch, the particle EA makes an angle $\alpha \approx 20°$ to the field, whilst the layer moments slightly cant away from the EA with angles of $\theta_1 \approx 5°$ and $\theta_2 \approx 9°$. The large percentage difference in canting between the two moments here is the result of their strong imbalance.

If instead we keep J/Kt the same at 0.2 and reduce β, we also find SFi systems that exhibit the canted particle state. Figure 6.5c shows the response of the case with $\beta = 0.05$. The reduction in degree of ferrimagnetism results in a much smaller signal in the transition through zero field. We again find only a short range of fields which induce the linear response: $120 < H < 220$ Oe. Conversely, due to a significant difference in β between case b and c, we find a much higher level of particle canting in the configuration of the particle just before saturation, with $\alpha \approx 53°$. The low value of β also leads to a negligible difference in the canting of the layer moments, with $\theta_1 \approx \theta_2 \approx 4°$. The reduction of moment canting in this case, despite the greater particle rotation, is due to the lower value of J/Kt: the energy balance is shifted towards maximising anisotropy, making it more unfavourable to angle the moments away from the EA than it is favourable to further increase alignment with the field. The switch to saturation is once again found at a lower field: $H \approx 220$ Oe. This is slightly lower than that found for case a as here the system is in a slightly less favourable configuration, with the moments canted and not parallel with the field direction, such that a lower field strength is able to saturate the disc.

The final case we explore takes the lower value of $\beta = 0.05$ and the higher value of $J/Kt = 0.9$. In Figure 6.5d we again observe the smaller switch around zero field. The

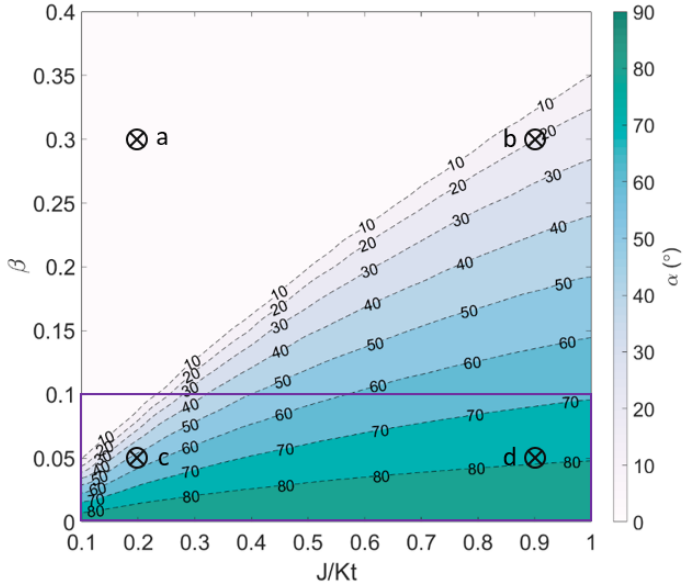

(a) α

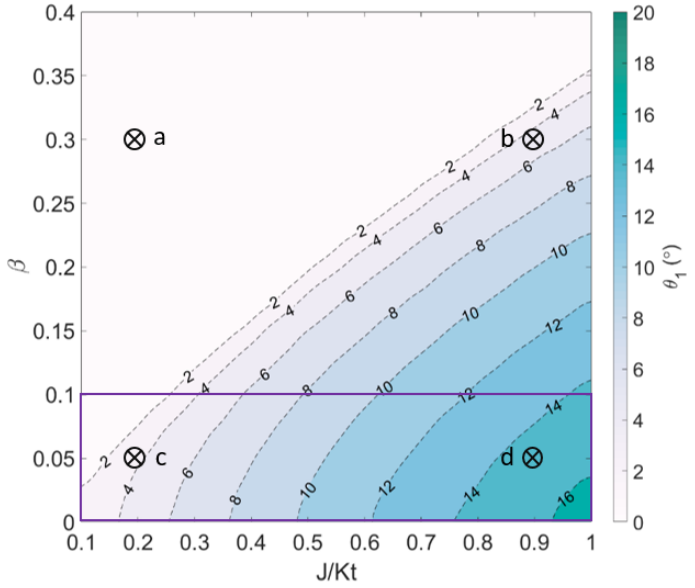

(b) θ_1

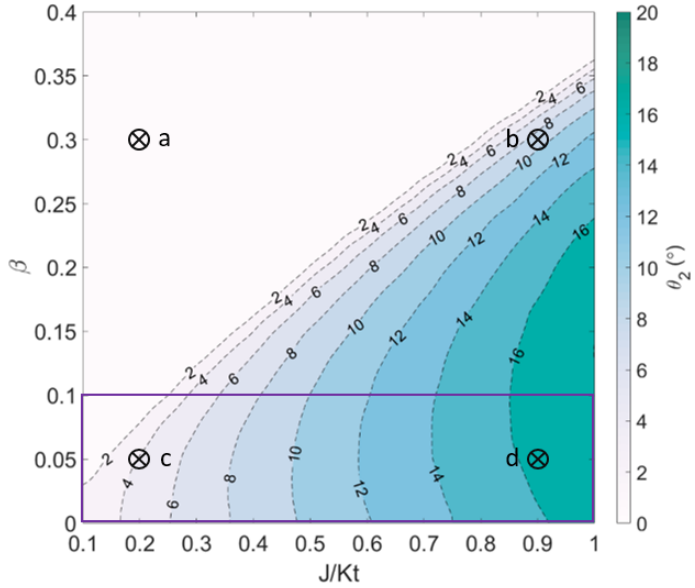

(c) θ_2

Figure 6.4: Phase diagrams of the angles (a) α, (b) θ_1 and (c) θ_2 at the point just before particle saturation across a range of degrees of ferrimagnetic strength (β) and EC/PMA ratios (J/Kt).

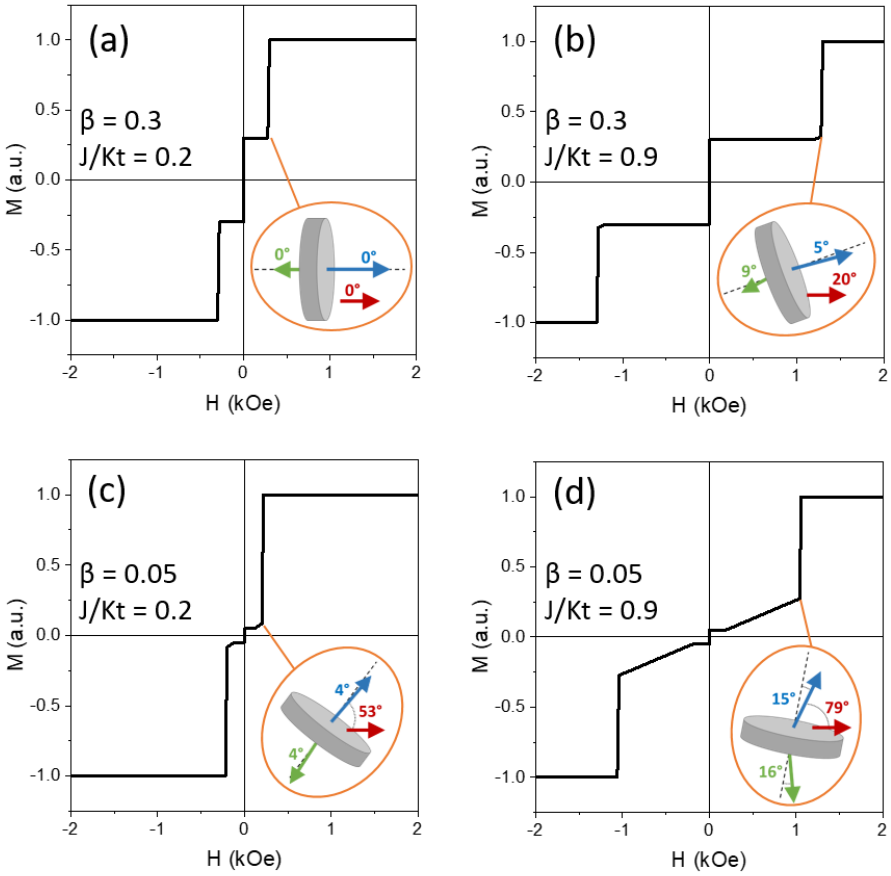

Figure 6.5: Four different SFi particle systems picked out from the phase diagrams in Figure 6.4. The simulated liquid response and a schematic of the particle at the point before saturation are shown. The angles α (red), θ_1 (blue) and θ_2 (green) are included, $M_1 \geq M_2$.

lower β, higher J/Kt combination leads to a much larger range of field, $0.18 < H < 1.06$ kOe, in which the canted particle state is induced. With a more prolonged regime of this state, with the particle continuously rotating, it is not surprising to find the particle close to a HP alignment just before saturation, with $\alpha \approx 79°$. Furthermore, we find a slightly higher level of moment canting, with $\theta_1 \approx 15°$ and $\theta_2 \approx 16°$. This behaviour is due to the higher J/Kt moving the energy balance to favouring the AF coupled state over the PM state, allowing increased canting of the moments towards the field direction (and thus rotation of EA away from the field) to maximise the Zeeman energy and minimise the consequence on the exchange energy. The minimal degree of ferrimagnetism leads to only a 1° difference in canting between the two layer moments. Saturation occurs at $H \approx 1.06$ kOe. Again, this is slightly lower than that found for the other $J/Kt = 0.9$ case, due to the increase in moment canting and mechanical rotation.

6.3.3 The pre-saturation state — low β regime

In a further study of the effects of J/Kt and β on the pre-saturation state of SFi particles, we focused on the low β regime across the range $\beta = 0$–0.1 (highlighted by

the purple boxes in Figure 6.4). To achieve this range with an increased number of data points, the CoFeB layer thicknesses were varied as: t_1 = 1–1.1 nm, with steps of 0.002 nm, such that t_2 = 1–0.9 nm. The same range of J/Kt, with the same step size, was used. The phase diagrams generated for α, θ_1 and θ_2 across this array of parameters are displayed in Figure 6.6. In this low β regime, the moment angles in the pre-saturation state are roughly constant along lines of equal J/Kt. Conversely, increasing moment angles are found with increasing J/Kt along lines of equal β. In the case of the angle of particle to the field (α), we find increasing angles with both increasing J/Kt and β.

To help visualise the particle configurations in these pre-saturation states with varied J/Kt and β we have taken two lines across the phase diagrams (see Figure 6.6) and drawn up the disc schematics in Figure 6.7, which highlight the three angles α, θ_1 and θ_2 for a selection of SFi discs. First, we look at the horizontal line: variation in J/Kt with $\beta = 0.02$. Here we find an increase in α with increasing J/Kt , as the discs align their HP more with the field direction. Additionally, there is a larger rate of change at the lower end of the J/Kt range: α increases by ∼17° from ∼64° to ∼81° as J/Kt increases from 0.1 to 0.3, whilst there is just a ∼1° increase (∼85–86°) as J/Kt increases from 0.7 to 0.9. Looking at the moment angles, we find only small differences between them across the board, due to the low value of β creating only a small imbalance in moment. This difference widens with increasing J/Kt, however the percentage difference remains at $\sim$ 4%. This is because θ_1 and θ_2 increase with increasing J/Kt and α: θ_1 ranges from ∼2.3–15.2° and θ_2 ranges from ∼2.4–15.8°. The SFi particle behaviour results from the competing PMA and EC energies. Lower values of J/Kt make it more favourable for the particle system to prioritise aligning the layer moments along the EA, which limits the canting of the moments. Hence, to minimise energy, the disc rotates its EA through a smaller angle away from the field direction, minimising Zeeman through alignment of the stronger moment with the field. As J/Kt increases, the energy balance shifts such that it becomes less unfavourable to cant the moments away from the EA. This allows the particle to minimise its energy by satisfying Zeeman more effectively: a larger mechanical rotation of the particle into a more HP alignment with the field means that both layers can cant towards the field direction.

Next, we consider a vertical line across the phase diagrams in Figure 6.6, with variation in β and $J/Kt = 0.3$. The left-hand case in Figure 6.7b depicts the perfect SAF case, whereby the lack of imbalance leads to $\theta_1 = \theta_2 \approx 7°$ as the particle aligns its EA perpendicular to the field before saturation. As β is increased, the difference in value of θ_1 and θ_2 gradually increases in both absolute value and percentage, up to $\sim$ 0.8° or $\sim$ 22%. This occurs as the overall canting of the moments reduces with increasing β: ∼7.0–3.7° and 7.0–4.5° for θ_1 and θ_2 respectively. Simultaneously, the particle mechanically rotates through smaller angles, becoming less HP aligned in the pre-saturation state: the minimum angle found, at $\beta = 0.1$, was $\alpha \approx 35°$. This behaviour across this varied range of β, is again explained by the balance of

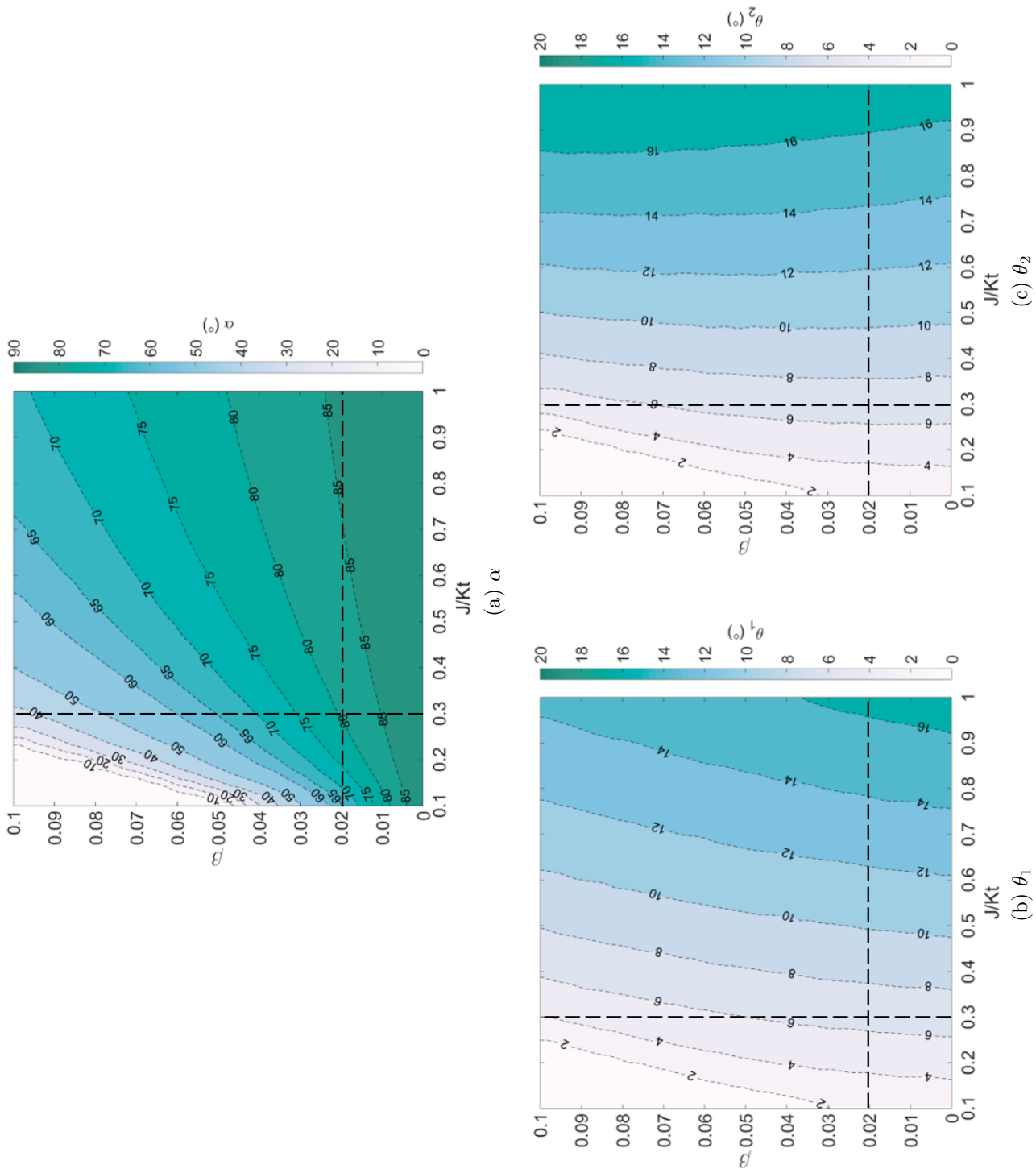

(a) α (b) θ_1 (c) θ_2

Figure 6.6: Phase diagrams of the angles (a) α, (b) θ_1 and (c) θ_2 at the point just before particle saturation across a smaller range of degrees of ferrimagnetic strength (β), area highlighted by the purple boxes in Figure 6.4) and the same range of EC/PMA ratios (J/Kt).

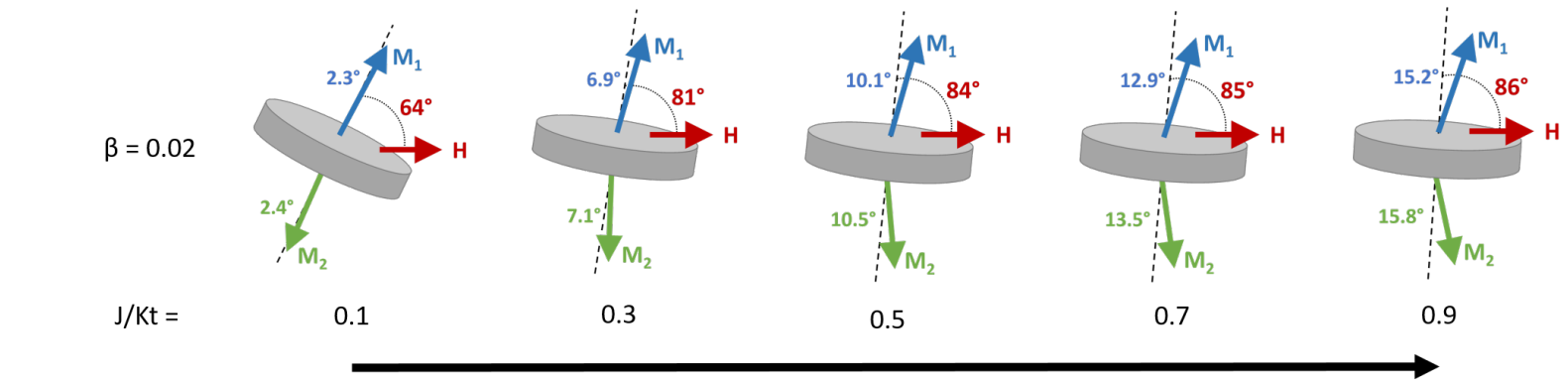

(a)

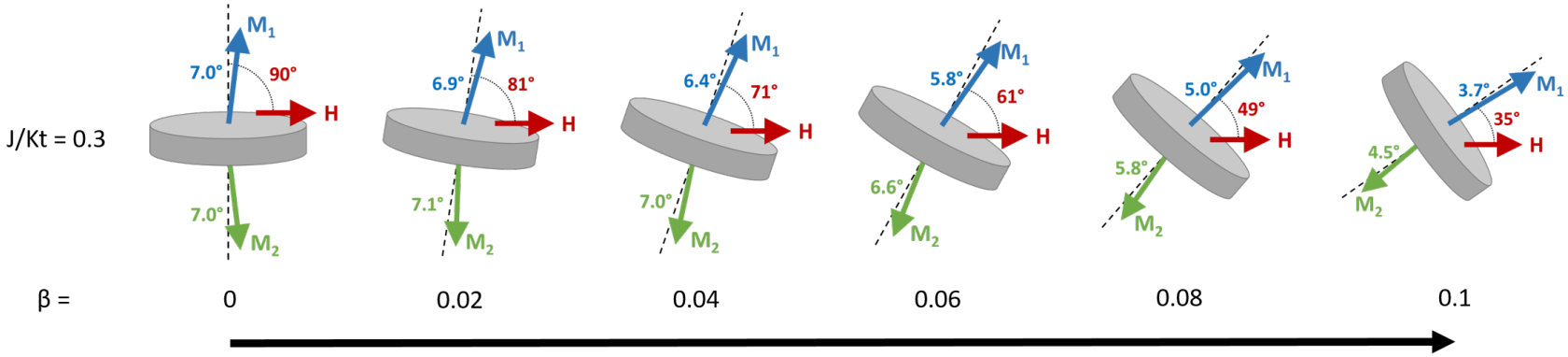

(b)

Figure 6.7: Disc schematics of a series of particles (a) with $\beta = 0.02$ and and range of J/Kt and (b) with $J/Kt = 0.3$ and a range of β (corresponding to the dotted lines in the diagrams in Figure 6.6). The angles α (red), θ_1 (blue) and θ_2 (green) are included, $M_1 \geq M_2$.

energies. Here, as J/Kt is kept constant, the limiting factor is the Zeeman energy, or the alignment of moment with field. As the imbalance in the layer moments is increased, it becomes more favourable to maximise the alignment of the higher moment with the field over the alignment of the lower moment. To achieve this, the particle itself rotates through smaller angles, such that the EA remains more in the direction of the field. In turn, this makes it less favourable for the layer moments to cant — it is better to minimise the PMA energy. However, the lower moment layer sees a relatively large percentage increase in angle relative to the other layer, as its strength is reduced along with its alignment being forced away from the field direction.

6.3.4 Expanding J/Kt — the emergence of a spin-flop transition

The final study made into the magneto-mechanical behaviours of SFi particles in liquid took a narrower range of β (0, 0.05 and 0.2) and an extended range of J/Kt (0.5, 2 and 4), and explored the configurations of the discs from remanence to saturation. The field-moment responses, alongside schematics of the discs across the field ranges, for each pair of parameters is shown in Figure 6.8.

First, we consider the first column of cases, with $J/Kt = 0.5$, a familiar ratio from the earlier sections. The $\beta = 0$ case exhibits the classic SAF behaviour, with two distinct regimes: the HP alignment, moments canted regime; and the full EA alignment saturation regime. Increasing β to 0.05 reveals the additional low-field regime, whereby the particle aligns its EA with the field, such that the larger moment is parallel with the field. This creates the characteristic low signal, sharp switch around zero field. The SFi disc then exhibits continuous rotation towards a more HP alignment with the field, as the layer moments cant away from the EA, up to saturation where a sharp magneto-mechanical transition results in the full EA alignment state. This is consistent with previous findings (see Section 6.2, [12]) for similar SFi systems. Further increasing β up to 0.2 results in the off-axis regime being extinguished, as was discussed earlier in Section 6.3.2. In this case, the disc remains with its EA parallel to the field across the full range, with the switch to saturation being exclusively magnetic. The mechanical rotation through zero field remains, but induces a bigger change in M signal due to the larger inherent imbalance.

The middle column of Figure 6.8 displays the behaviour of three types of disc with $J/Kt = 2$, a larger ratio than has been previously considered. In the SAF case, the increase in J/Kt leads to an increase in canting of the layer moments before saturation. This is because the increase in J/Kt makes it less unfavourable for the moments to rotate away from the EA, and hence more favourable overall to align the moments more with the field direction to minimise Zeeman energy. The saturation field of the system also increases due to the increase in J/Kt: to minimise EC energy, the AP state is more favourable than the P state across a larger range of field values. The two cases with non-zero β exhibit the same increase in saturation field. They both also present

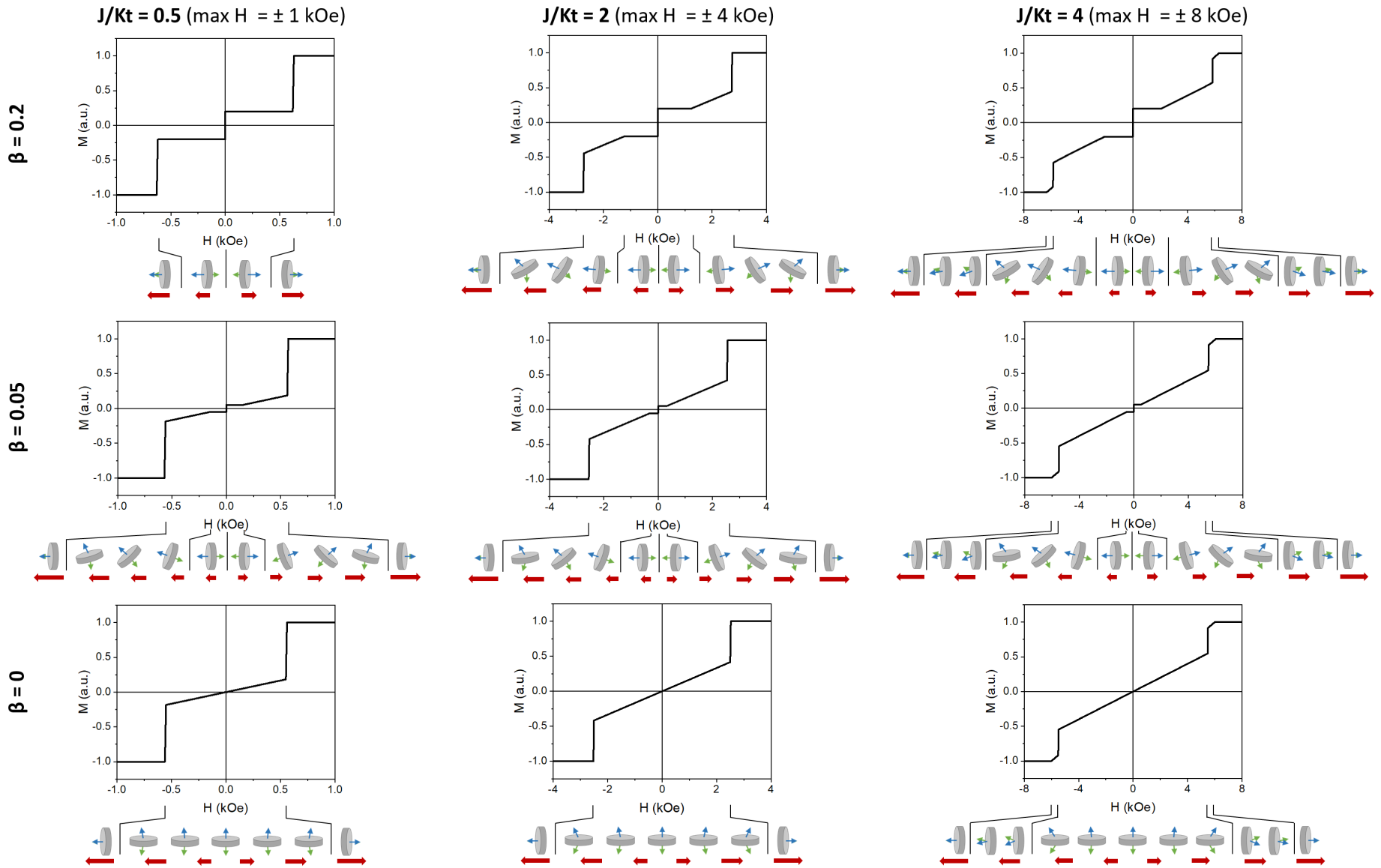

Figure 6.8: Simulated liquid responses with accompanying disc schematics for a larger range of J/Kt. The angle of the discs relative to a linear, increasing applied field (red arrows) is displayed and the direction of the moment of each CoFeB layer is shown (blue and green arrows, $M_1 \geq M_2$).

with the three regime behaviour: the higher value of J/Kt means that even in the $\beta = 0.2$ case, the off-axis configuration is favourable in the mid-field range. This is due to the canting of the layer moments being less unfavourable, such that the lower energy state involves minimising Zeeman through the magneto-mechanical transition into the off-axis configuration. The key differences between the $\beta = 0.05$ and $\beta = 0.2$ cases are the characteristic, larger signal switch through zero, followed by the exhibition of the low-field regime/EA alignment through a larger field range for $\beta = 0.2$.

The last column of Figure 6.8 corresponds to $J/Kt = 4$, which is a significantly higher ratio than previously studied. Practically, it would be challenging to create discs with such a ratio using this SFi system. Nevertheless, it is interesting to further explore the theoretical energy landscape of the system, in pursuit of novel magneto-mechanical behaviour. Across the series of β, we find the same changes in transitions and configurations in the low- and mid-field regimes as for the $J/Kt = 2$ discs: increase in signal strength of the zero-field transition, increase in field range for the low-field regime and a decrease in HP alignment in the pre-saturation state, all with increasing β. However, by raising J/Kt to 4, we reveal a change in the switch to saturation, through the discovery of an additional transition in the M-H response: a short, linear response after the second high field switch. This new behaviour is present for all three values of β. Looking at the corresponding disc schematics, we can understand how this new M-H response manifests. The sharp, vertical switch corresponds with a similar magneto-mechanical transition to that found before: the disc abruptly and mechanical rotates to realign its EA with the field direction. The difference in this case is that although the layer moments also undergo an abrupt rotation, they do not initially lie parallel with the field direction. Instead, they position themselves canted either side of the EA, and then continuously rotate into EA alignment as the field increases further: this corresponds with the linear response found in the M-H plot.

We have therefore discovered the ability of SFi particle systems to undergo spin-flop transitions in liquid, induced by sufficiently high J/Kt, which is above the critical limit for spin-flop in thin films ($J/Kt = 2$ [2, 4]). We suggest that this delay in manifestation is due to the expression of the HP/off-axis regime in the mid-field range, which suppresses the desire for the system to saturate via spin-flop. Akin to the other SFi canted state, there is some variation in the particle configuration during this transition with different values of β. The moment imbalance induces an imbalance in the canting angle of the moments: the disc again favours a better alignment of the larger moment with the EA, to maximise the anisotropy term, such that the lower moment cants through a larger angle. In addition, although it is not obvious by eye, the non-zero β discs do not align their EA perfectly parallel to the field in spin-flop canted state. They then rotate continuously into the parallel configuration as the layer moments relax into the EA. This is a more prominent effect for the higher β disc, as the disc again favours a better alignment of the larger moment with the field direction to maximise the Zeeman term, but even here the initial angle is very small at $\sim 1.1°$. The variation in the initial state of the disc with β, during the spin-flop transition, is

demonstrated via the schematics in Figure 6.9.

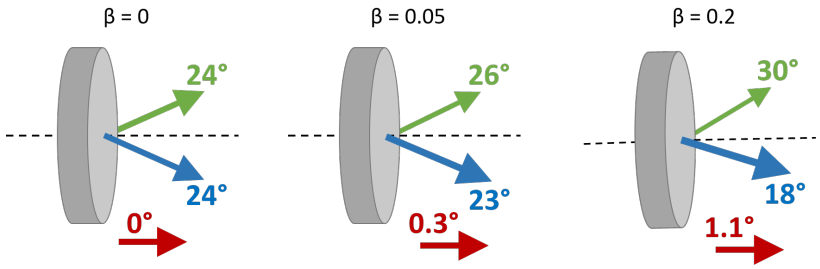

Figure 6.9: The initial canted state in the spin-flop transition for the three types of disc in Figure 6.8 with $J/Kt = 4$ and $M_1 \geq M_2$. The angles α (red), θ_1 (blue) and θ_2 (green) are noted.

6.4 Exploring the AF particle energy landscape — experimental observations

Note: all stray field calculations in this section were performed by D. C. M. C. Petit (Prof. Cowburn's group).

6.4.1 Particle interactions

As we shift from exploring PM AF coupled systems via simulations to via experimental observations, we introduce a number of additional factors that will affect the energy landscape. One major alteration is the switch from a single particle to a multi particle system. The inherent moment of magnetic particles translates into a stray field, which can influence the behaviour of adjacent particles, leading to inter-particle interactions. A number of parameters affect a particle's stray field, including magnetisation (strength and direction) and size. The stray field of one particle experienced by another is related to their separation by a decay term. This means that in a chain, every particle experiences a summation of the stray fields from all of the other particles in that chain, where more distance particles contribute less to the total. In this chapter a method based on [1] will be used to estimate the maximum stray fields of our PM AF coupled discs with EA saturation.

We have previously mentioned the concept of self-polarisation [7], as a phenomenon that induces magnetic agglomeration of particles after the application and then removal of an applied field, even if they exhibit a zero remanence state. This phenomenon is where the stray fields of particles are large enough that they sustain the chaining of particles even when the external applied field is switched off. It has been found that for the case of an in plane SAF particle, which has a susceptibility that can be controlled by magnetic thickness, self-polarisation is observed above a certain susceptibility threshold: above this threshold the particles gradually agglomerate, below it, they redisperse in zero field [7]. Conversely, in the case of our PM AF coupled particles, which have

low susceptibility in low fields, self-polarisation would require the stray field to exceed the coupling field.

In this chapter we observe various deviations in behaviour of our particles from the model predictions. To explain these deviations, we will be considering the potential effects of stray fields and particle interactions, and how these might influence the magnetic reversal of our PM AF systems.

6.4.2 1st AF peak nanodiscs — a range of J

To experimentally investigate the characteristics of PM AF coupled particles across a range of J a series of 500 nm magnetic discs were fabricated from 1st AF peak coupled stacks that are described by: $Ta(2)/Pt(2)/CoFeB(0.9)/Pt(t_{Pt})/Ru(0.9)/Pt(t_{Pt})/CoFeB(0.9)/Pt(2)/Ta(2)$, with thicknesses in nm and where t_{Pt} was varied between $0.42 - 0.69$ nm. These particles were then studied using a selection of liquid measurements (VSM, reflectivity and OM) to probe their magneto-mechanical behaviour.

Liquid VSM

The EA VSM loops of the original thin films and nanodiscs before lift off are displayed in Figure 6.10 alongside liquid VSM measurements of the nanodiscs suspended in water. It should be noted that the response of the discs on chip around remanence may not represent the particle behaviour alone: it is possible for there to be an additional ferromagnetic response originating from redeposited material from the milling process.

While t_{Pt} creates a characteristic gradient in coupling strength across the thin film series, this translates into some increased variation in magnetic reversal upon patterning into nanodiscs. As discussed in the previous chapter (Section 5.3), there is a large increase in coercivity from the films to discs, which results in the loss of the AP state at remanence in the samples with the weakest coupling. The patterning process also induces variation in magnetic reversal across the population of particles, which leads to more smeared transitions in their VSM loops. Consequently, when the nanodiscs are suspended in liquid and subjected to an applied field, they exhibit a spread of magneto-mechanical behaviours. This has resulted in a series of varied VSM loops, some of which display novel responses for AF coupled particles.

In the liquid loops of the more strongly coupled samples, we observe a similar trend of decreasing saturation field with decreasing coupling strength to the films or discs on chip. We find evidence of moment imbalances in the $t_{Pt} = 0.48$ and 0.53 nm samples, driving 180° rotation of discs through zero field. It is not possible to ascertain if this is also the case in the $t_{Pt} = 0.42$ nm sample: any potential moment imbalance is less than the noise base in the signal. Overall, these three samples exhibit the linear field response followed by a steeper switch to saturation, as was previously found for AF coupled discs ([12], Section 6.2.1). In the case of the $t_{Pt} = 0.53$ nm discs, the P–AP magnetic reversal differs somewhat to the two strongest coupled samples: there is no

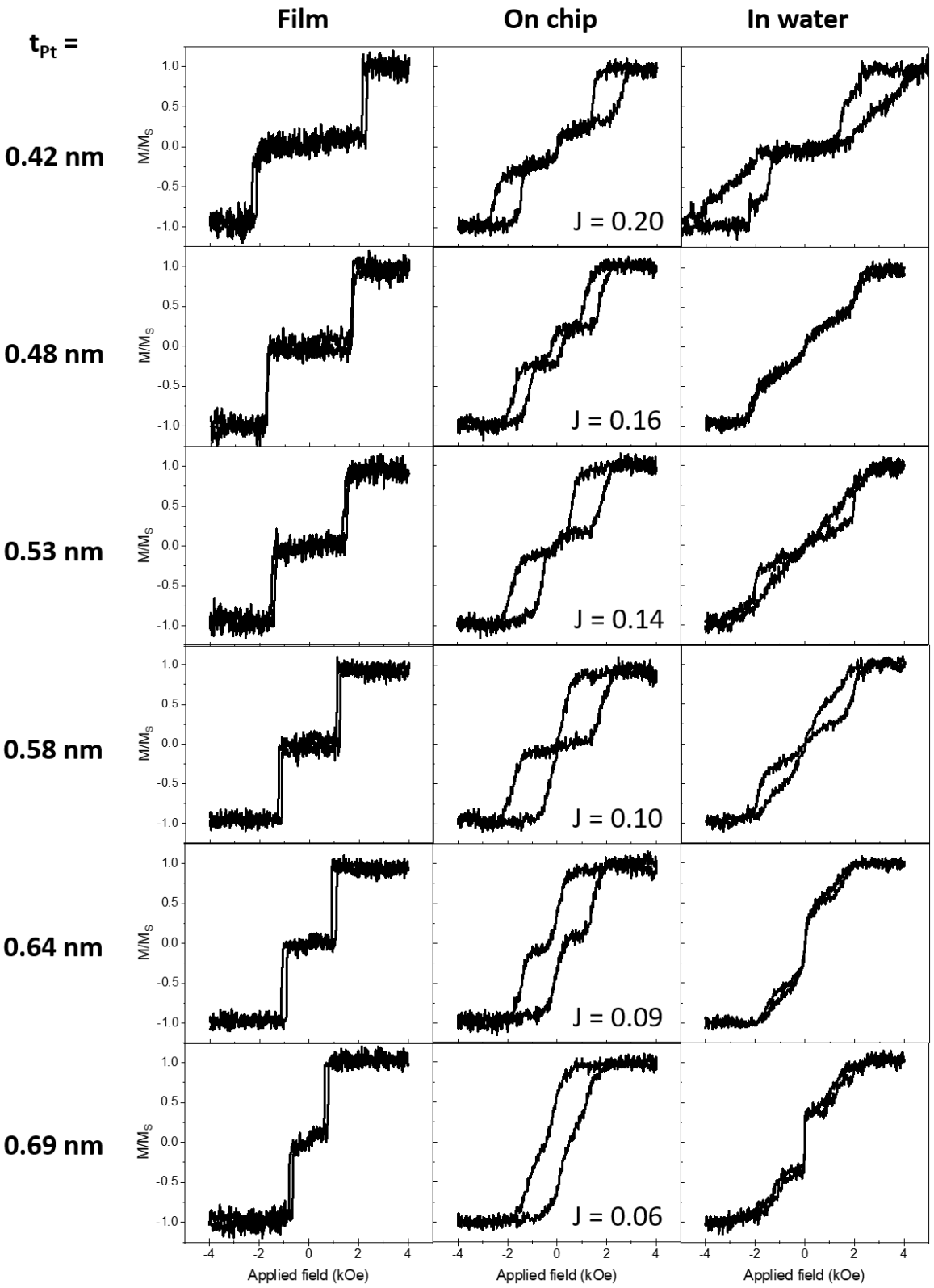

Figure 6.10: Normalised VSM loops of the Pt interlayer series of 1st AF peak thin films (left) and nanodiscs before (middle) and after (right) lift off. For the nanodiscs values of J (Oe emu cm^{-2}), calculated using the average coupling fields, are displayed alongside the 'on chip' loops.

presentation of a relatively steep transition, instead, we find a relatively linear response all the way back to zero field. This indicates that the transition could be more of a HP-like response.

As coupling strength is reduced again, the AP state at remanence becomes less stable. In the 'on chip' measurement of the $t_{Pt} = 0.58$ nm sample the AP state definitely did not exist at remanence in the higher FSR MOKE loop (see Figure 5.19 in Section 5.3.3), but is just about present in the quasi-static VSM loop. Further reduction in coupling then causes the AP state at remanence to completely disappear. In the case of the $t_{Pt} = 0.64$ and 0.69 nm samples, this has translated into a particularly strong switch through zero field in the liquid response, which is clearly larger than a switch resulting from a SFi moment imbalance.

A large increase in coercivity is a key driver for the loss of AP state. We previously discussed (Section 5.3) that a strong factor in this increase is variation in switching fields across the populations of discs. If we look, for example, at the 'on chip' VSM loop of the $t_{Pt} = 0.64$ nm sample, it appears that the P–AP transitions cross $H = 0$. This indicates that a proportion of the population could still exhibit an AP state at remanence, while the rest do not. We suggest that the liquid response of a particle that does not have an AP state at remanence would be limited to a purely mechanical switch through zero field, to conserve a parallel EA and moment alignment with the field direction and satisfy the Zeeman energy. This would translate into a seemingly FM signal in a VSM measurement. The particles that do exhibit an AP state at remanence would behave in the same manner as other SAF or SFi discs, as previously discussed (Sections 2.2.2 and 6.2.1). The liquid VSM loop that we would find for a population of discs that contains a mixture of these two types of particle would be a superposition of the two different M-H responses, which reflects the shape of the response found for $t_{Pt} = 0.64$ and 0.69 nm samples. Furthermore, we suggest that the $t_{Pt} = 0.58$ nm sample shows a similar response, but weighted more towards the SFi type behaviour, due to the more highly coupled film generating a larger ratio of particles with a robust AP state.

Our current model for AF coupled discs does not fully represent all of the constraints on a single particles, namely, it does not include coercivity. This does not present a significant problem in the systems that exhibit a zero remanence state: although the locations of switches will be inconsistent, the overall behaviour of a disc should be well-represented. However, in the case of a system that has an extinguished zero remanence state, due to higher coercivity in the particles versus the film, our model is no longer able to minimise the system energy in a way that accurately represents a real disc. It would be interesting to adapt our model to include coercivity, and better represent a wider range of AF coupled systems, so as to deepen our understanding of the particle transitions and how they diverge from EA responses.

Further insight into the magneto-mechanical behaviour of these types of particle could be gained through the imaging under applied fields. To make such a study as constructive as possible, it would be optimal to use slightly larger particles (as was done

in Section 6.2.1), such that they are much easier to visualise with OM. Nevertheless, in the next section we utilise OM and reflectivity measurements to explore the magneto-mechanical behaviour of one of the sets of 1st AF peak 500 nm discs that maintains its zero remanence state.

Reflectivity and OM

To gain further understanding of the magneto-mechanical behaviour of these particles in liquid the sample with the strongest AF coupling ($t_{Pt} = 0.42$ nm) was measured with the reflectivity and OM set ups with integrated applied fields (both described in Section 3.3). To recap the principal of the reflectivity measurements: highest signal is induced by a maximum incidence of the light on the disc faces, corresponding with a HP alignment with the field; low signal is induced by a side on alignment of the discs with the light, corresponding with an EA alignment with the field. By measuring/imaging the suspension in a direction perpendicular to a slowly ramping field it is hence possible to assess changes in particle orientation and self-assembly.

Figure 6.11a displays the reflectivity response of this disc suspension, alongside the corresponding portion of the liquid VSM response, with the rising field response in red and the falling field response in blue. A large peak is found as the field is increased, which then levels out before dropping down to the baseline. This peak in the signal corresponds with the discs aligning their HP with the field. The drop in signal indicates particle saturation. As the field ramps back down the signal stays low until ~ 1.5 kOe, indicating a maintenance of the EA alignment. The discs then exhibit a peak in signal, as they return to the linear regime and realign their HPs with the field. The transition between the saturated and linear regimes occurs at a lower field value in the falling field response due to the coercivity in the system. We also find a jump in signal around zero field, which indicates a ferrimagnetic state: the particles align their EA with the field again in the low field regime and rotate 180° around zero, as seen in Section 6.2.1.

Due to their size (~ 500 nm diameter, ~ 12 nm thick) it is not trivial to focus on individual nanodiscs with the OM, however their self-assembly helps to reveal the disc orientations across the population. Figure 6.11b displays snapshots of OM videos at four different applied field values, which are indicated in the corresponding VSM and reflectivity responses in Figure 6.11a.

Under the remanent field of the dipole electromagnet (~ 10 Oe), as seen in image 1, the nanodiscs are very difficult to see. This corresponds well with the response seen in the reflectivity measurement: in the low field regime we determined that the nanodiscs aligned their EA with the field direction due to an inherent ferrimagnetism, this would make them very challenging to observe in the OM as their thickness is significantly smaller than the lens resolution and the wavelength of the incident light.

In the second image, the applied field has risen to ~ 2.4 kOe. Here, we just distinguish the speckling of the nanodiscs across the image. This indicates that they have switched to an off-axis alignment with the field (not HP due to the SFi characterisation—

see Section 6.2.2). This matches well with the findings in the reflectivity and liquid VSM responses: this field location corresponds with the peak in the reflectivity data and the sloped AP–P transition in the VSM loop.

After the field has reached a maximum, causing the particles to saturate, we ramp it back down and look at the third field value of ~ 2.2 kOe. The VSM and reflectivity data suggest that the nanodiscs are still in an EA alignment with the field here. Again, this matches with the OM observation: the nanodiscs are in the formation of long face-to-face chains which line along the field direction.

Finally, we look at a further reduced field at ~ 1.3 kOe. In the VSM loop, this lies towards the bottom of the P–AP transition. In the reflectivity response, the signal at this field has risen back above the baseline. In the OM image we observe a scattering of the nanodiscs away from the previous chain locations. Their relatively strong visibility supports the theory that they exhibit some HP field alignment during the P–AP transition.

Overall this work demonstrates the convenience of the reflectivity measurement, and how it is highly complementary to the OM imaging of nanodiscs, which are challenging to resolve optically. We have shown that this technique offers a simple method to assess the magneto-mechanical transitions of PM discs, even on the nanoscale, under applied fields. The implementation of a laser for measurement is transferable to devices for applications, e.g. magnetic sorting.

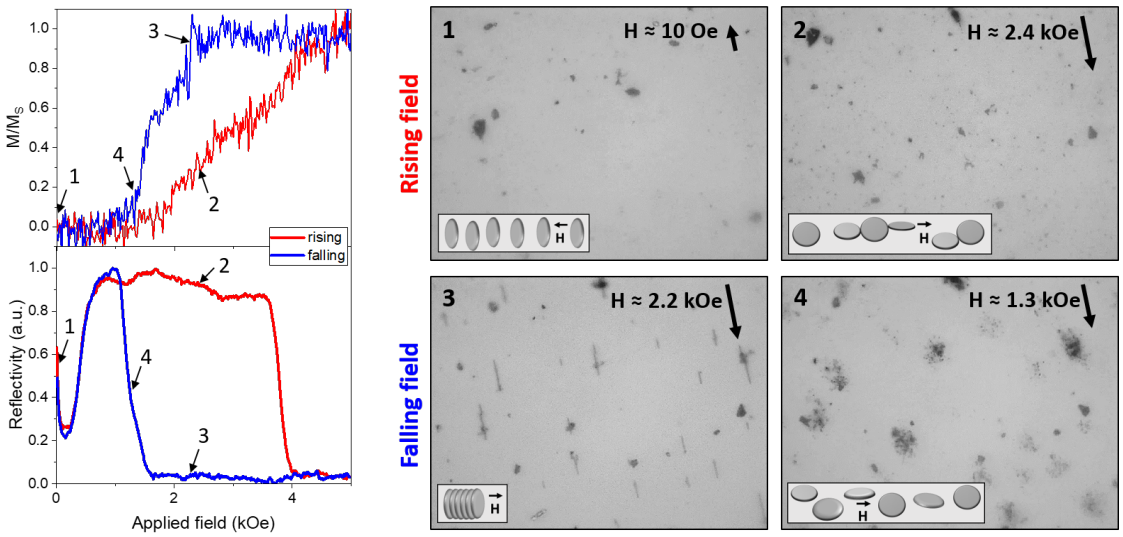

(a) VSM and reflectivity (b) OM images and schematics

Figure 6.11: Liquid observations of the 1st AF peak discs with 0.42 nm Pt. (a) The liquid VSM and reflectivity measurements, with arrows indicating the fields represented by the 100× OM images in (b). Disc schematics depict the orientations and interactions of the discs during the different regimes.

6.4.3 2nd AF peak nanodiscs — low J particles

To experimentally investigate the characteristics of PM AF coupled particles with particularly low J a series of 500 nm magnetic discs were fabricated from 2nd AF peak coupled stacks of the form $Ta(2)/Pt(2)/CoFeB(t_{CoFeB})/Pt(t_{Pt})/Ru(2)/Pt(t_{Pt})/CoFeB(t_{CoFeB})/Pt(2)/Ta(2)$ with thicknesses in nm and where $t_{CoFeB} = 0.8$ or 1 and $t_{Pt} = 0.21$, 0.27 or 0.32. These particles were then studied using a selection of liquid measurements (VSM, reflectivity and OM) to probe their magneto-mechanical behaviour.

Liquid VSM

The EA VSM loops of the original thin film and nanodiscs before lift off are displayed in Figure 6.12 alongside liquid VSM measurements of the nanodiscs suspended in water. The nanodiscs on chip across these mini-series also show an increase in coercivity and a smearing of the transitions in comparison with the thin films. However, as discussed in Section 5.3.3, patterning has a smaller impact on the magnetic properties of 2nd AF peak nanodiscs compared with 1st AF peak nanodiscs with low J. Consequently, whilst we do still lose the AP state at remanence as the coupling strength is reduced in the 2nd peak samples, it has been possible to fabricate nanodiscs with a conserved AP state and relatively low saturation fields by utilising the 2nd AF peak. Furthermore, we demonstrate with the VSM responses that this translates into disc suspensions that maintain the distinct switching behaviour, which is desirable for applications such as magnetic sorting.

The transformation of the liquid loops, with change in coupling strength, is very similar to that found for the 1st AF nanodiscs. For convenience, we have labeled the liquid loops with letters (see Figure 6.12), which we will refer to. If we first focus on the 0.8 nm CoFeB mini-series, we find two samples with a conserved AP state at remanence: a) and b). Both of these exhibit SFi behaviour in the low field regime: a small switch is present through zero field. This imbalance is also evident in the EA loops of the corresponding thin films, with neither expressing zero moment at remanence. These two disc suspensions then show a linear field response, followed by a strong switch to saturation, as is characteristic of SFi systems (see section 6.2.1). The sample c), which does not have a zero remanence state, exhibits different magneto-mechanical behaviour. The switch through zero-field has a much stronger signal, although not as strong as the samples in 1st AF peak series that did not have a zero remanence state (see Section 6.4.2). As the field rises, we find a linear regime, which indicates some presence of an off-axis field alignment. This is followed by a sharp switch to saturation, just like that seen in a) and b). Conversely, there is some disparity in the liquid VSM response as the field ramps down from saturation back to remanence. Namely, there is more of a two-stage P–AP transition in c): a relatively steep drop in moment, followed by a more moderate slope until the sharp zero-field switch. Given the shape of the corresponding 'on chip' loop for c), where we observe a somewhat unstable AP state

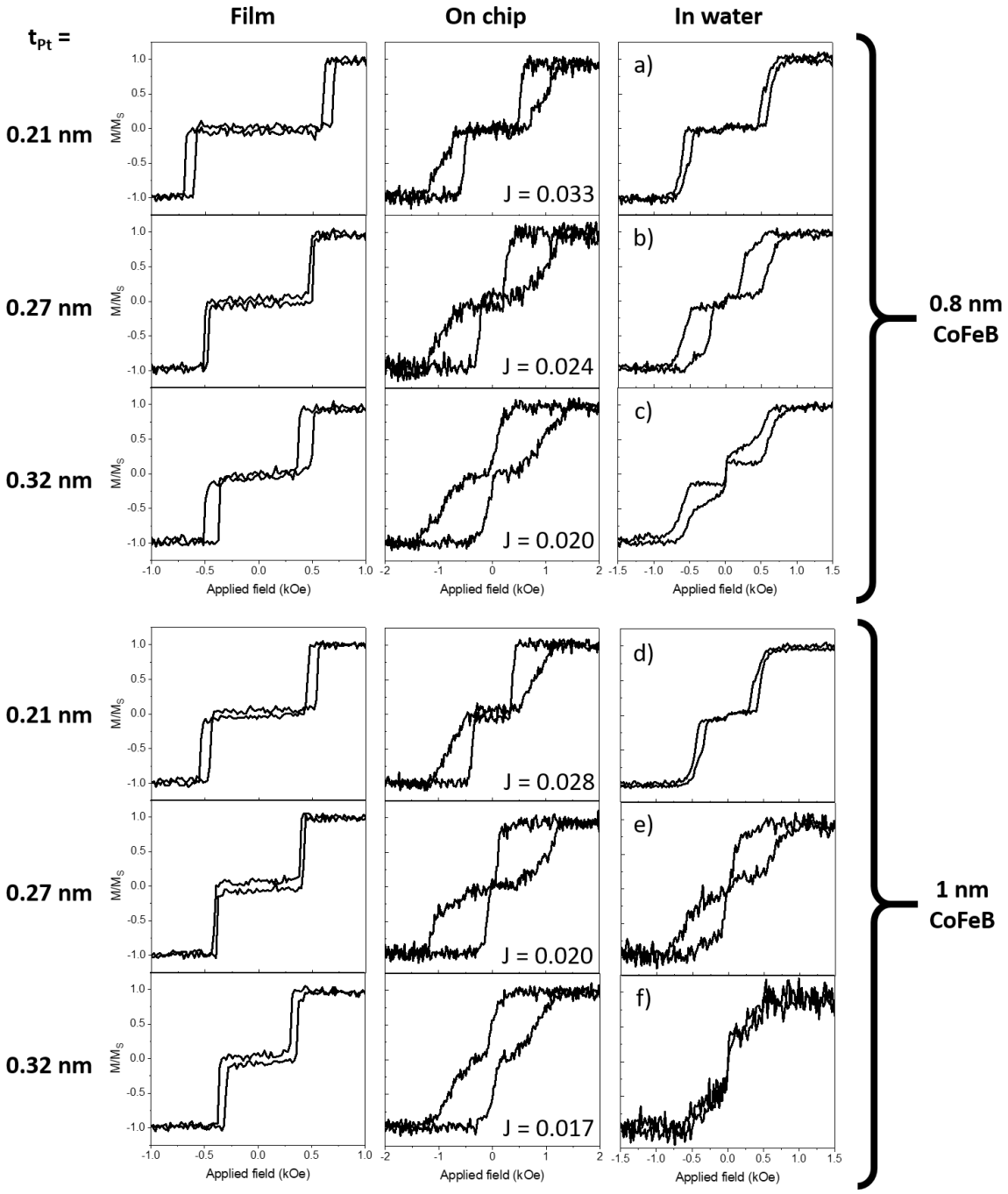

Figure 6.12: Normalised VSM loops of the Pt interlayer series of 2nd AF peak thin films (left) and nanodiscs before (middle) and after (right) lift off. For the nanodiscs, values of J (Oe emu cm^{-2}) calculated using the average coupling fields are displayed alongside the 'on chip' loops.

at remanence, we suggest that the differences in the shape of the liquid loop is again the result of particle variation: some particles exhibit an AP state at remanence, while others do not. Consequently, c) is a superposition of a SFi type loop, like a) or b), with an FM type loop.

We now move to the 1 nm CoFeB mini-series, which present with slightly lower coupling than their 0.8 nm CoFeB counterparts (highlighted by the values of J noted by the disc on chip VSM loops). Liquid VSM loop d) is almost identical to a), but

with a slightly lower saturation field ($\sim$ 580 Oe rather than $\sim$ 770 Oe). The EA 'on chip' counterpart of e) is similar to that of c) (which makes sense given their equal J), with the AP state at remanence appearing unstable (it also did not exist in the MOKE loop shown in Figure 5.20 of Section 5.3.3). Consequently, the resulting liquid VSM response is also similar (albeit noisier in the case of e)), with a notably increased signal in the zero-field switch from d). The final sample in the mini-series, f), has the most distinct loss of zero remanence state of the 2nd AF peak nanodiscs. As a result, the liquid VSM loop displays the same shape as the two weakest coupled 1st AF nanodiscs (see Section 6.4.2): a particularly strong switch through zero field, followed by a strong, relatively linear response up to saturation. Again, we attribute this to an increase in the proportion of discs that do not exhibit a zero remanence state.

Studying these types of particle with OM would give further insight into their magnetic reversal in liquid. However, as mentioned previously for the 1st AF peak nanodiscs, this would be a more effective study if the discs were of a larger size and hence easier to visualise. Nevertheless, in the next section we utilise OM and reflectivity measurements to explore the magneto-mechanical behaviour of one of the sets of 2nd AF peak nanodiscs that has relatively strong coupling.

Reflectivity and OM

The 2nd AF peak nanodiscs with 1 nm CoFeB and 0.21 nm Pt were further assessed in their liquid suspension via the reflectivity and OM-magnet set ups (see Section 3.3). This uncovered some variation in the magneto-mechanical behaviour of the system, in comparison to that observed in the liquid VSM measurements.

The reflectivity response and OM snapshots of the suspension at four different points in the measurement are displayed in Figure 6.13. In Figure 6.13a, we find a distinct mismatch in the point of saturation in the reflectivity versus VSM responses: unlike with the 1st AF nanodiscs in Section 6.4.2, the steep drop in reflectivity occurs at a much higher field ($H \approx 1.3$ kOe) than saturation of moment occurs in the VSM loop ($H \approx 600$ Oe). To investigate this, we first compare the configuration of the discs in the OM images with the reflectivity response.

In image 1 of Figure 6.13b, under the remanent field of the dipole, the discs align their EA parallel to the field direction. This indicates a slight imbalance in the layer moments and makes them particularly difficult to focus on at this point due to their thickness ($\sim$ 12 nm). The EA alignment is confirmed through a visible 180° rotation of the discs under the OM as the field goes through zero.

As the field is ramped up, the discs go through the first magneto-mechanical transition, rotating their EA away from the field direction. In the reflectivity, this manifests as a relatively steep rise up to a strong peak. We suggest that the slope in the reflectivity signal is the result of either: the spread of switching fields across the particle population; the manifestation of the canted state, which will lead to a continuous rotation in the case of a SFi system (see Section 6.2.2); or a combination of the two. In the

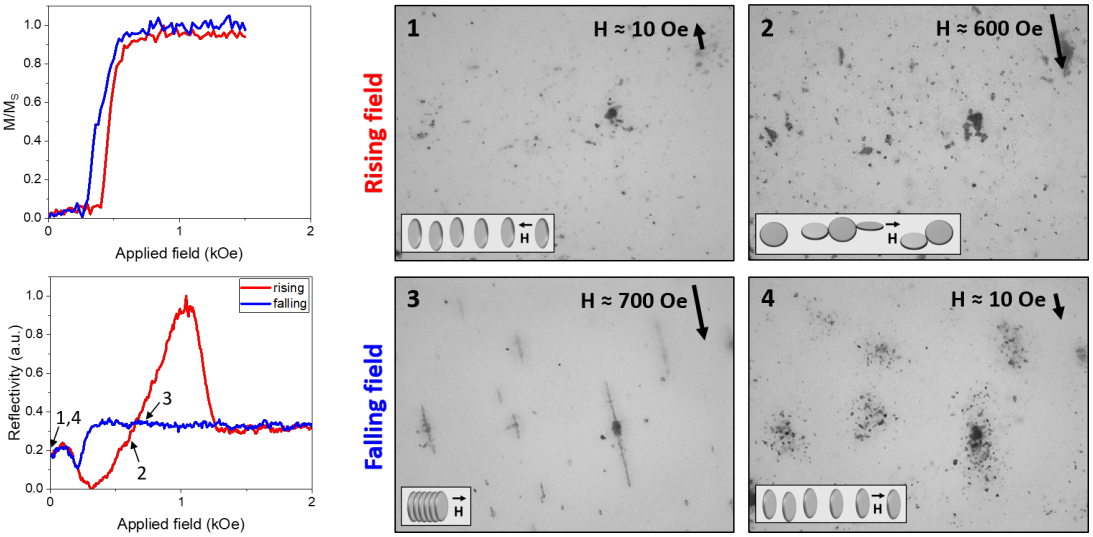

(a) VSM and reflectivity (b) OM images and schematics

Figure 6.13: Liquid observations of the 2nd AF peak discs with 1 nm CoFeB and 0.21 nm Pt. (a) The liquid VSM and reflectivity measurements, with arrows indicating the fields represented by the 100× OM images in (b). Disc schematics depict the orientations and interactions of the discs during the different regimes.

OM, the transition is visualised as an emergence of the nanodiscs: their rotation means that the light is now incident more on their faces which offer a comparatively much larger surface area, hence making them easier to focus on and distinguish. This effect is shown in image 2 of Figure 6.13b at a field value of ~ 600 Oe. As noted before, this field was strong enough to saturate the nanodiscs in the VSM measurement. However, this is not what we find in the OM, which instead appears to correspond well with the reflectivity response so far. Further ramping up of the field causes the steep drop in reflectivity noted earlier, indicating the saturation of the nanodiscs as they realign their EAs with the field direction. This second magneto-mechanical transition is also observed in the OM imaging.

As the field is ramped back down, the particles maintain the EA configuration. Image 3, which corresponds with a field of ~ 700 Oe, demonstrates the long, face-to-face chain formations of the particles in this regime. Eventually, the particles dissociate from each other, as shown in image 4. At the same point in the reflectivity we observe a small drop in the signal. We suggest that this indicates that although the discs maintain their EA alignment with the field, there is a difference between the reflectivity of chained and unchained particles, while in the same side-on alignment with the laser.

This is a different behaviour to that observed for the 1st AF peak nanodisc sample in Section 6.4.2, which transitioned back to the AP state via the HP configuration. The strong difference in coupling strength is the key difference in between the two samples, and thus plays a role here. The other factor that leads to this changed behaviour, which separates the real system from the model, is particle interactions. We have just noted the formation of long face-to-face chains by the 2nd AF peak discs. Through a stray field calculation (see Section 6.4.1) we find the field experienced by a particle at

the end of a chain, due to the magnetic moment of the other particles in the chain, as a function of chain length. The results of these calculations for both the 1st and 2nd AF peak discs are presented in Figure 6.14a. In the calculations, the key differences between the discs are the overall particle thickness (slightly larger for the 2nd AF discs) and total moment (also slightly higher for the 2nd AF discs). Here, we see that in the small chain regime, for both sets of discs, the total field rises dramatically each time another disc is added. They both then reach maximum stray fields in the region of 900 Oe, with that of the 2nd AF peak discs being slightly higher. This is a relatively large field value, however, the coupling field of the 1st AF discs is significantly higher ($\sim$ 3 kOe looking at the liquid VSM). On the other hand, the coupling field of the 2nd AF peak discs is lower than the total stray field ($\sim$ 500 Oe looking at the liquid VSM). This means that these discs can generate some level of self-polarisation (see Section 6.4.1), making the chained state more favourable, which delays their P–AP switch enough to suppress the linear regime in the falling field response. However, the self-polarisation effect is not strong enough to prevent the dissociation of the particles under zero field, despite the fact that only a chain length of 10 particles is required to reach a stray field that exceeds the coupling field. This is explained by the fact that the stray field calculations are based on a perfect face-to-face alignment of completely flat discs: in reality, there will be imperfect lateral alignment and extension of inter-particle distances. Consequently, our calculation is only an estimate of the maximum possible interaction, and the fact that the 2nd peak discs express a dissociated state proves that this is an overestimate.

As noted earlier, a key difference between the responses of the 1st and 2nd AF peak nanodiscs during the liquid measurements is the lack of correspondence between the reflectivity and OM with the VSM, in the case of the 2nd AF peak sample. One significant difference in the conditions during VSM, compared with reflectivity or OM, is the vibration of the disc suspension at 75 Hz. We propose that, as such vibration

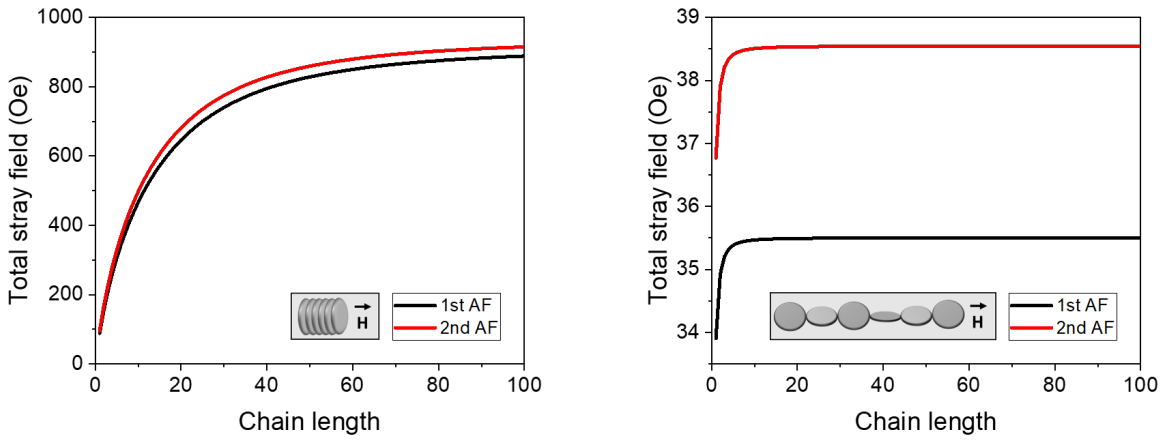

(a) Face-to-face (b) Side-to-side

Figure 6.14: The cumulative stray field experienced by a 500 nm disc at the end of (a) face-to-face and (b) side-to-side particle chains, as a function of chain length.

could be capable of disrupting particle chain formation, the discrepancy in responses could be linked to the effects of particle interactions and chaining, as we have just seen in the suppression of the HP alignment. However, we note that the stray fields involved in the side-to-side chaining of the discs (the configuration prior to saturation) will be significantly smaller than those we have calculated for face-to-face chains. This is demonstrated in Figure 6.14b: although slightly higher than for the 1st AF disc counterpart, the maximum total stray field in a 2nd AF disc side-to-side chain does not exceed 40 Oe. Hence, this will not be nearly large enough to induce a saturation of moment along the HP, which would be the requirement for the side-to-side chaining becoming more favourable than a magneto-mechanical switch to EA saturation.

Alternatively, it is possible that the vibration of the sample in the VSM provides the nanodiscs with a mechanical perturbation that allows them to more easily (i.e. at lower applied fields) overcome energy barriers and change configuration. An alternative way of measuring the variation in magnetic moment with applied field, without sample vibration, would be via a superparamagnetic quantum interference device (SQUID). Comparison of SQUID data of the nanodisc suspensions with our VSM, reflectivity and OM data would help us to understand these systems even more.

Another condition that should be considered is the FSR used during the different measurements. VSM measurements could be described as quasi-static: the field is ramped in chosen steps, with a pause at each value. In the case of our liquid VSM measurement of the 2nd AF peak discs, we approximate an effective FSR of 2.5 Oe/s. A similar method of field application was used during the OM imaging, but the parameters produced an effective FSR of ~ 40 Oe/s. A continuous ramp method was used in the case of reflectivity, at a FSR of 30 Oe/s. The OM and reflectivity measurements thus use an FSR that is an order of magnitude higher than that of the VSM. Although this variation will only induce a relatively minimal change on the dynamics of magnetic reversal (i.e. there will not be a large change in EA switching field — see the variation in similar films in Section 4.3.3), it is possible that this difference in FSR is enough to have much larger consequences on the mechanical behaviour of the particles. In particular the interactions between particles will be affected: increased timescale leads to increased chaining.

Given this discovery, we note that the reflectivity measurements employed in this work might have been important in portraying the behaviour of the particles outside of a vibrating environment, which better represents the conditions in an application scenario (e.g. microfluidic chip or biomedical device). Additionally, our set up for these measurements allows us a greater variation in FSR application, which could be exploited to examine the FSR dependence of the magneto-mechanical transitions. This further demonstrates this measurement technique as complementary to those previously used, to assess PM nanoparticles.

The assessment of a larger range of coupled particles could provide insight into the magneto-mechanical behaviours studied here. It would be more convenient to undertake such experiments with particles with a larger diameter, such that their

orientations were easier to analyse with OM. It could however be interesting to compare the behaviour of particles of different sizes, that have been fabricated from the same thin film stack.

6.5 Particles with multiple coupling strengths

To investigate the possibility of manufacturing PM particles with multiple switching fields, two different multilayer thin film stacks were grown and patterned into 1 μm discs via nanosphere lithography with ion milling. The first is a double SAF bilayer, in the form $Ta(2)/[Pt(2)/CoFeB(0.9)/Pt(x)/Ru(0.9)/Pt(x)/CoFeB(0.9)/Pt(2)/Ta(2)]_2$, where $x = 0.45$ and 0.3 and thicknesses are in nm. The second is a triple SAF bilayer, in the form $Ta(2)[/Pt(2)/CoFeB(0.6)/Pt(x)/Ru(0.9)/Pt(x)/CoFeB(0.6)/Pt(2)/Ta(2)]_3$, where $x = 0.55$, 0.4 and 0.3 and thicknesses are in nm. By using different Pt interlayer thicknesses in each bilayer the SAFs possess layers with different coupling strengths and therefore multiple switching fields. The design of these SAF structures was further discussed in Section 4.2.3.

6.5.1 Dual bilayer SAFs

Locating magnetic switches

As can be seen in the VSM loops in Figure 6.15, by carefully choosing the Pt interlayers such that the coupling fields ($H_J \approx 1370$ and 2520 Oe) are well separated, it is possible to create a thin film with two, well-defined pairs of switches either side of remanence. Furthermore, such a film can be patterned into particles that, despite increases in coercivity, conserve this distinct switching behaviour. The average coupling fields of the discs on chip are extracted to be 1080 Oe and 2170 Oe, slightly lower than those of the corresponding film. This observation is consistent with effects discussed in Section 4.2.3 and is attributed to the patterning process inducing defects in the coupling interlayers ($Pt/Ru/Pt$), leading to a reduction in coupling strength. It also seems that these transitions are distinguishable in the VSM measurement of the disc suspension. To better quantify how the individual bilayer switching translates from films, to discs on chip, to discs in liquid we take the derivative of the VSM loops (Savitzky Golay smoothed with polynomial order 1 and a window of 10) and locate peaks that are associated with the transitions in each version of the SAF.

Alongside the VSM loops, Figure 6.15 displays the Gaussian fitted peaks of the derivatives in the rising (red) and falling (blue) field responses. Each peak is labeled with its FWHM. All forms of the double SAF exhibit two separable peaks corresponding with both AP–P and P–AP transitioning. However, there is a very clear decrease in the lower field peak from the film to the discs on chip and in both of the peaks in the suspended discs. Additionally, these peaks are wider, with larger FWHMs. This corresponds with the more sloped transition observed in the VSM responses. There are notable shifts in the centres of the peaks from the film to disc forms of the double

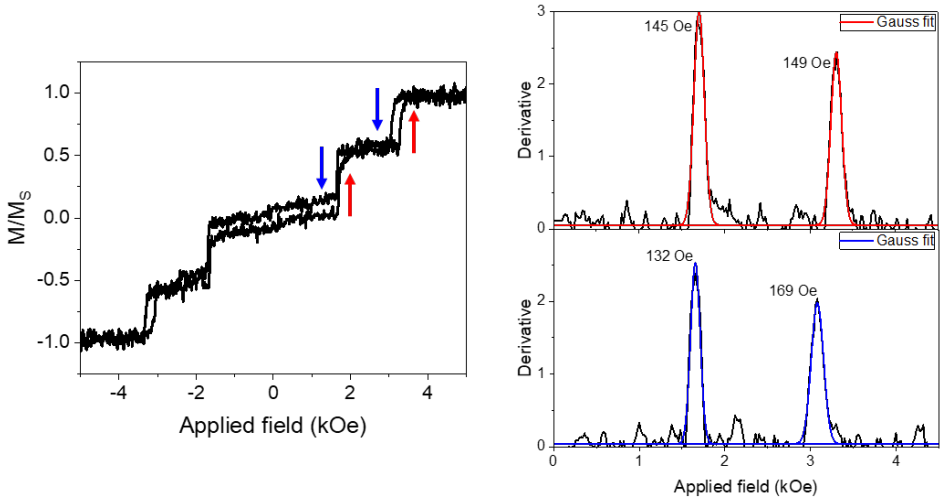

(a) Thin film

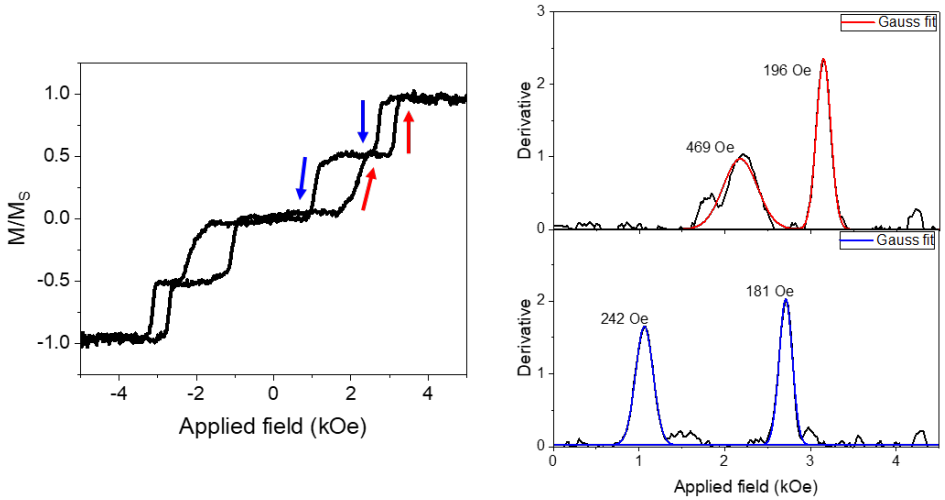

(b) Discs on chip

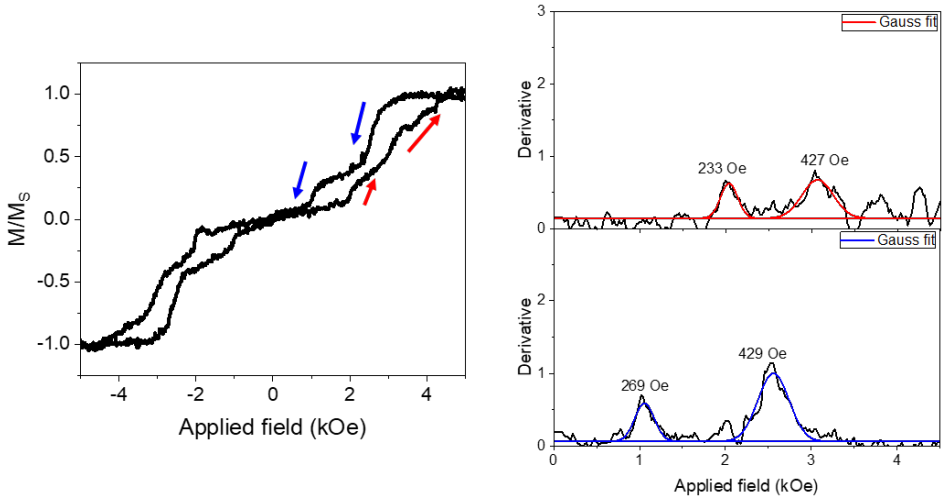

(c) Discs in liquid

Figure 6.15: The VSM loops (left) of the double SAF stack in (a) film and (b) & (c) disc form. The derivative with Gaussian fit of peaks of the rising (red) and falling (blue) field sections of the loops are displayed to the right. Each peak is labeled with its FWHM.

SAF, which corresponds with the increase in coercivity mentioned earlier. This, as well as the smearing of the transitions in the disc VSM, is mainly the result of measuring a large population of particles; as discussed in more detail in the previous chapter (see Section 5.3.1), the fabrication process induces variation in the magnetic properties across the set of discs.

Macrospin simulations

We adapted the PM AF coupled particle system modeled in Section 2.1.3 to include two magnetically independent, but mchanically coupled CoFeB bilayers, as is shown in Figure 6.16a. Using this, the liquid response of a double bilayer particle was then simulated. To simplify, it was assumed that the particles were perfect SAFs, with no imbalances in moment between the different CoFeB layers, and that M_S and K were also consistent across the layers. The values $J = 0.20$ Oe emu cm^{-2} and $J = 0.11$ Oe emu cm^{-2} were extracted from the minor MOKE loops taken of each bilayer in the thin film (see Figure 4.7a in Section 4.2.3) and implemented in the model.

The resulting M-H response in liquid is presented in Figure 6.16b, accompanied by some disc schematics that demonstrate the configuration of the disc and layer moments with respect to the field. Up to the point of the first sharp switch ($H \approx 1.7$ kOe), the system exhibits the classic linear response, with the disc aligning its HP with the field and all the layer moments canting away from the EA/towards the field direction. In this regime, due to the different values of J, the layer moments pairs cant at different angles. The moments in the bilayer with $J = 0.11$ cant to a maximum angle of $\sim 10°$. The moments in the bilayer with $J = 0.20$ cant to a maximum angle of $\sim 8°$: the higher coupling strength means that a stronger field is required to cant the moments

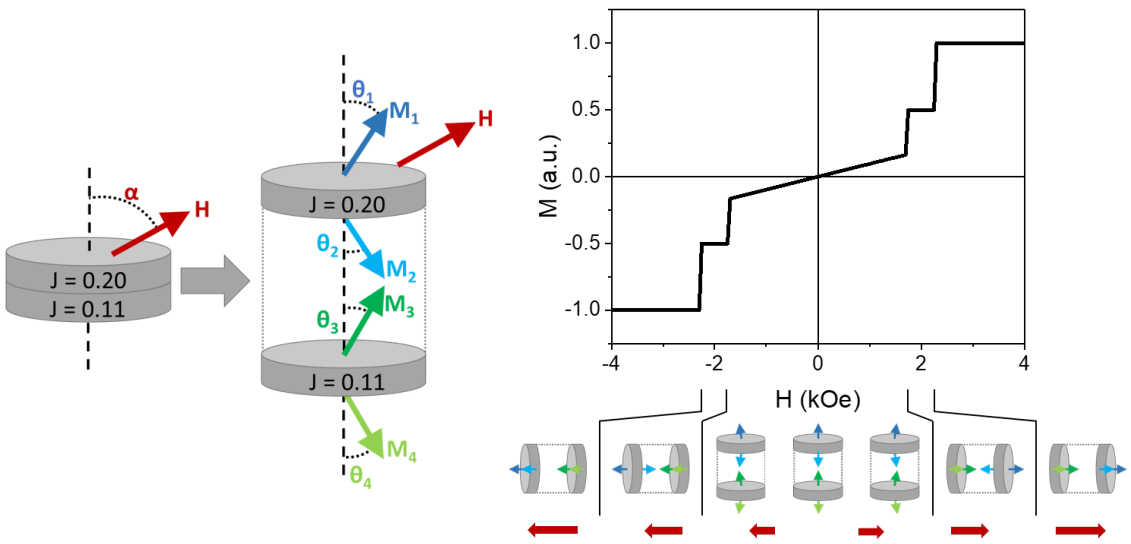

(a) Double bilayer system (b) Simulated liquid response

Figure 6.16: (a) A schematic of the system used to model the double bilayer stack. (b) The simulated liquid hysteresis alongside disc schematics. The arrows correspond to the moments of each CoFeB layer and the applied field, as labeled in (a).

to the same angle as the $J = 0.11$ moments.

The first sharp switch comprises a magneto-mechanical transition, similar to that seen in the AP–P transition observed for SAFs with a single coupling field (see Section 2.2.2), whereby the disc abruptly rotates to align its EA parallel with the field direction. The key difference in the case of this double SAF system lies with the configuration of the layer moments. The bilayer with the lower coupling saturates with both layer moments switching to the parallel configuration with the EA and field, as has been seen previously. However, the applied field is not yet high enough to saturate the bilayer with the higher coupling. Therefore, as the more highly coupled CoFeB layers experience the mechanical rotation, they too undergo a rotation of their magnetic moments, returning them into the AP state along the EA. This disc configuration remains until the higher saturation field ($H \approx 2.3$ kOe), which induces the purely magnetic, sharp AP–P transition of the more highly coupled bilayer.

Experimental observations in liquid

The suspension of dual bilayer discs was assessed using the reflectivity and OM-magnet set-ups to further explore their magneto-mechanical behaviour in liquid under applied field: the results of which are displayed in Figure 6.17. Once again, we find a strong match between the particle behaviour in reflectivity measurements and OM images. The reflectivity response shown in Figure 6.17a looks very similar to that found for the 1st AF peak, single bilayer in Figure 6.11a. We observe the same large, relatively flat peak in the rising curve, which corresponds with a HP alignment of the disc with the field, as is shown in image 2 of Figure 6.17b. We note that the reflectivity signal exhibits a brief period of a more moderate rise prior to this flat peak, which most likely corresponds to some spread in the particle properties, or the expression of an SFi canted rotation (as was suggested for the 2nd AF peak discs). We also find similar behaviour to the 1st AF discs in the low-field regions of both the rising and falling sections of the curve: a small jump in reflectivity at zero field, which indicates a ferrimagnetic-driven 180° rotation; and a peak in reflectivity as the field ramps down towards zero, which corresponds with the P–AP transition occuring via the HP configuration. Finally, as seen previously, the full saturation field in the liquid VSM (to plot of Figure 6.17a) corresponds with the steep drop in reflectivity during the rising field, and thus the mechanical rotation of discs to align their EAs parallel with the field (see image 3 of Figure 6.17b).

However, the experimental response does not match that of the simulation in the previous section. Specifically, the simulation predicts a 90° mechanical rotation of these discs at the saturation field of the bilayer with the lower J, which would induce a drop in reflectivity to occur at the same field. However, we experimentally observe the reflectivity drop at what appears to be the saturation field of the higher J bilayer.

There are a few effects that might have the potential to delay the mechanical rotation in the real system compared with the theoretical one. The first potential

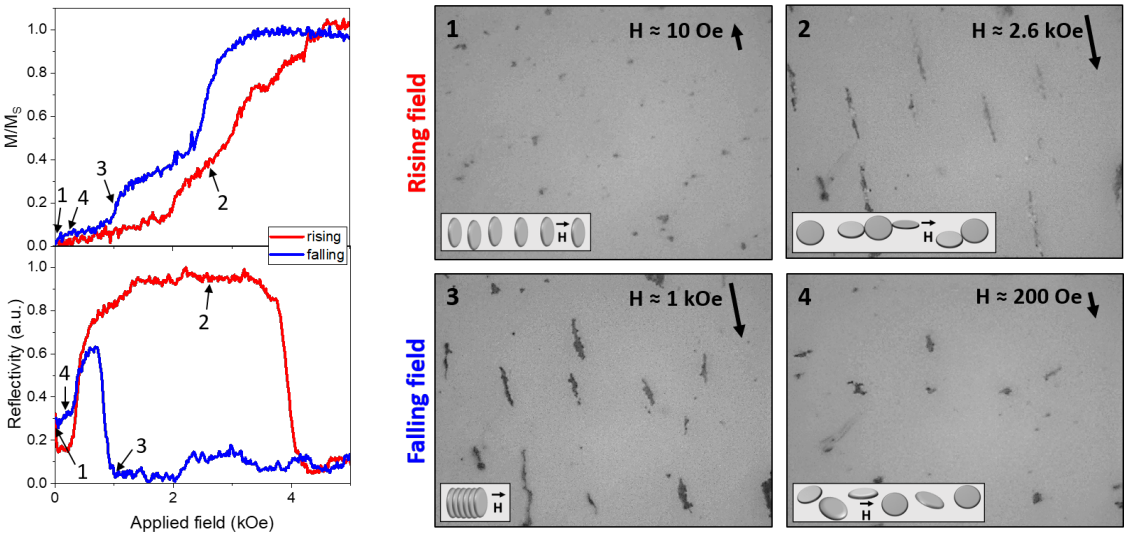

(a) VSM/reflectivity (b) OM images and disc schematics

Figure 6.17: Liquid observations of double bilayer SAF particles. (a) A zoom in of the liquid VSM response (top) compared with a reflectivity measurement of the discs. The black arrows highlight the field points that correspond with the 100× OM images of the disc suspension in (b). Disc schematics indicate the disc orientations relative to the field.

effect originates from the fact that the real system involves a suspension containing thousands of particles. The modeled system is based on the behaviour of a single particle, and hence excludes the effects of any inter-particle interactions. There are therefore additional effects involved in the real system that are not included in the model, which could delay the mechanical switch. We note, from the analysis in Figure 6.15c and Section 6.5.1, that there is evidence of two switches being present in the rising and falling response of the liquid VSM measurement. This indicates the possibility that the VSM response of the disc suspension more closely matches the simulated response.

One key difference in the conditions of the particle suspension during VSM, as discussed previously in Section 6.4.3, is the sample vibration at 75 Hz. It is possible that this vibration is disruptive to chain formation. Consequently, the discs exhibit behaviour closer to that of the single disc in the simulation.

Another difference between the different measurement types, also discussed in Section 6.4.3, is FSR. Here, we again used a much lower FSR during VSM ($\sim$ 2.5 Oe/s) compared with reflectivity (60 Oe/s) and OM ($\sim$ 40 Oe/s). This will also have consequences on the chaining effects, as an increased timescale could allow interactions to manifest more substantially. This idea could be tested with varied FSR measurements, potentially via the reflectivity set up.

The second effect also follows on from the 75 Hz sample vibration in the VSM measurements only. As mentioned in section 6.4.3, this vibration will increase the overall energy of the particles, which could lower the energy barriers enough for the nanodiscs to make transitions at lower applied fields. SQUID measurements could provide useful insight into the behaviour of this system, as an alternative method of

analysing the change in moment with field without sample vibration.

6.5.2 Triple bilayer SAFs

Locating magnetic switches

By using thinner layers of CoFeB (0.6 nm) we are able to create a triple bilayer stack with three distinct and well separated coupling fields ($H_J \approx 1190$, 2480 and 3580 Oe); the coupling strength induced in a CoFeB bilayer is a thickness dependent effect, such that a pair of 0.6 nm layers of CoFeB exhibit a higher coupling field than a pair of 0.9 nm layers [8]. Hence, the use of thinner CoFeB both expands the range of accessible coupling fields and also increases the spread between them. The EA VSM result of the engineered thin film stack is shown in Figure 6.18a, alongside the derivatives of the rising and falling field responses. The Gaussian fitted peaks highlight the marked clarity and separation of the switches. As was discussed in Section 4.2.3, the bilayer with the strongest coupling, which is also at the top of the stack, exhibits less sharp transitions than the other two. This is due to increased defects, caused by the particularly thin Pt interlayer and increased roughness higher up the stack, which leads to a more nucleation dominated transition and increased domain wall pinning. This behaviour is reflected in the switch peaks: the two highest field peaks are noticeably lower in height and, in particular in the falling field, there is an increase in the FWHM.

Figure 6.18b shows the EA VSM and corresponding derivative plot of the same thin film stack, but now patterned into 1 μm discs. As we observed with the dual bilayer samples, the patterning process has induced an increase in coercivity in the two bilayers with lower coupling fields. This is not the case with the bilayer with the strongest coupling, which indicates that the behaviour of the transition is dominated by the defects that were already present in the thin film stack. Nevertheless, the VSM and derivative peaks demonstrate that the distinct switching behaviour is conserved from the film to the discs. As was seen for the dual bilayer discs, there is also a loss of sharpness in the transitions, which is reflected in the increased FWHMs of the peaks in the derivative plots. Again these results are consistent with the effects discussed in Section 5.3.1, which attribute the an increase in defects during by the patterning process to the changes in magnetic reversal.

After lifting the triple bilayer discs off substrate and suspending them in water, a liquid VSM measurement is made to assess if the switching behaviour is maintained in fluid. 6.18c shows the resulting loop, alongside the derivative plots with the discernible peaks fitted. In the rising field, although there is a further increase in the smearing of the transitions, we observe three switches in the VSM loop and three corresponding peaks in the derivative plot. However, in the falling field, the highest field switch is conserved whilst the lower two appear to have merged together. The increased smearing of the transitions is the result of measuring a large population of particles (as discussed previously in Section 5.3.1). Furthermore, the added degree of freedom provided by the ability to mechanically rotate in water opens up the energy landscape of the triple

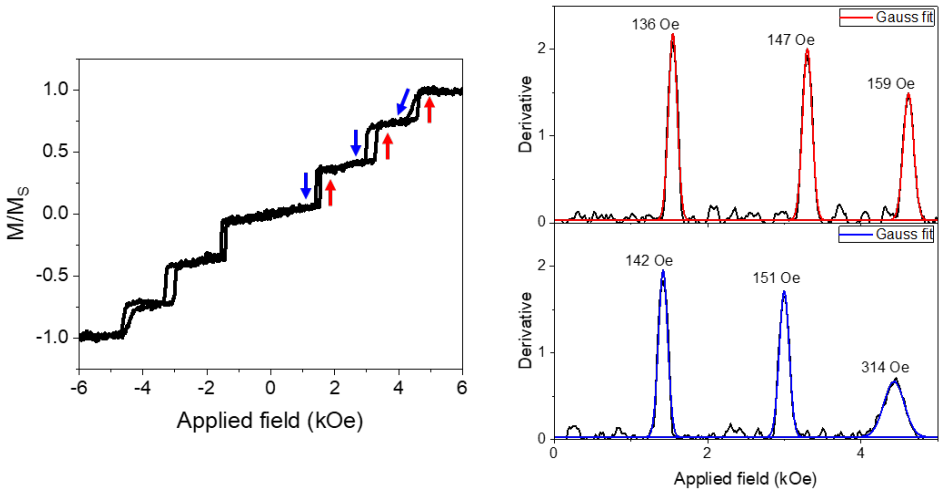

(a) Thin film

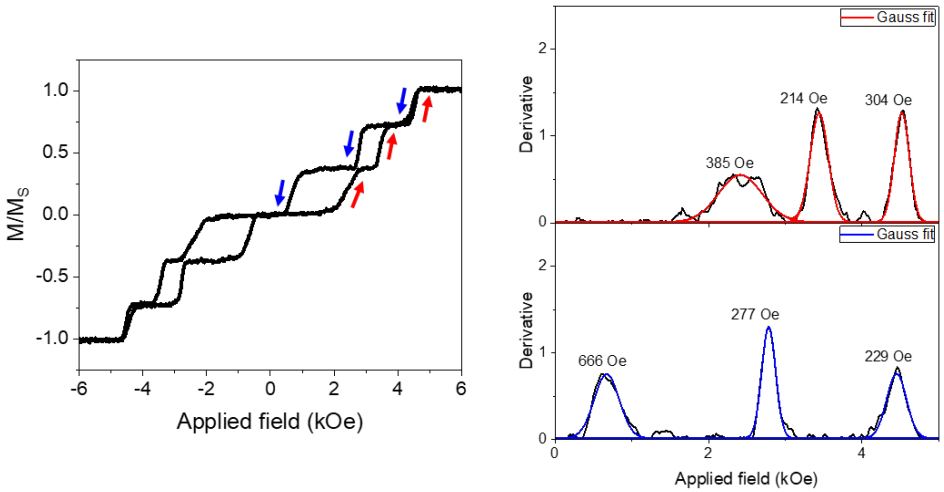

(b) Discs on chip

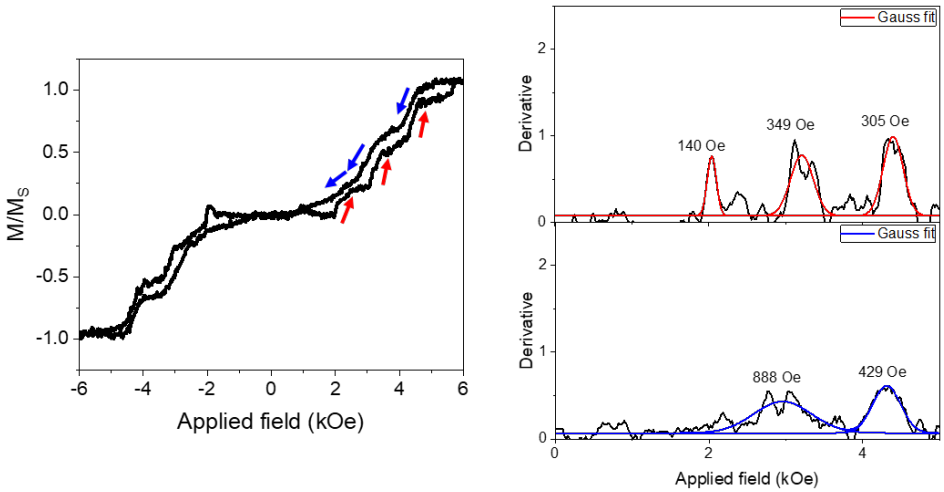

(c) Discs in liquid

Figure 6.18: The VSM loops (left) of the triple SAF stack in (a) film and (b) & (c) disc form. The derivative with Gaussian fit of the rising (red) and falling (blue) field sections of the loops are displayed to the right.

bilayer and induces a broader range of transitions. These include off-EA alignments with the field direction, causing layer moments to cant continuously across a range of field, which produces linear field responses (see Section 2.2.2). It is therefore not unexpected that the superposition of a varied population of discs, displaying a series of varied transitions, creates less distinct switching behaviour in the VSM response. Nevertheless, the conservation of three discernible switches in the rising field response of the triple bilayer discs illustrates that these particles could be employed in magnetic sorting applications, including multiplexed sorting.

Macrospin simulations

The PM AF coupled particle system modeled in Section 2.1.3 was further modified to include three magnetically independent, but mechanically coupled CoFeB bilayers, as is shown in Figure 6.19a. As was done earlier with the dual SAF system (Section 6.5.1), to simplify, it was assumed that there were no imbalances in moment between the CoFeB layers, and that M_S and K were consistent. Coupling fields were extracted from the minor MOKE loops of the thin film (see Figure 4.7b in Section 4.2.3) and used to calculate three values of exchange energy, which were then implemented into the triple bilayer model: $J = 0.19$, 0.13 and 0.06 Oe emu cm^{-2}.

The M-H liquid response of the system is shown in Figure 6.19b, alongside disc schematics that demonstrate the configuration of the disc and its layer moments with respect to the field direction. The result is very similar to that found in the dual SAF simulation. A linear response with a HP field alignment of the disc and canting moments up to the first sharp switch ($H \approx 1.4$ kOe). Again, the different moment pairs cant to different maximum angles: $\theta_1 = \theta_2 \approx 5.9°$, $\theta_3 = \theta_4 \approx 7.0°$ and $\theta_5 = \theta_6 \approx 9.1°$. Like in the dual SAF case, the first transition is magneto-mechanical, with the disc abruptly aligning its EA with the field direction and simultaneously realigning all

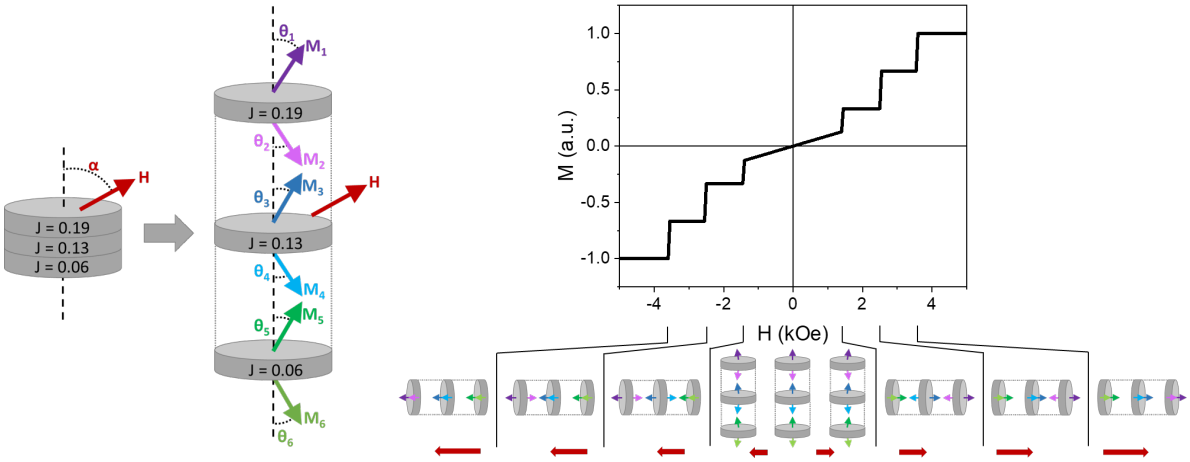

(a) Triple bilayer system (b) Simulated liquid response

Figure 6.19: (a) A schematic of the system used to model the triple bilayer stack. (b) The simulated liquid hysteresis alongside disc schematics. The arrows correspond to the moments of each CoFeB layer and the applied field, as labeled in (a).

moments along the EA. Here, the lowest J moments exist in the saturated, P state, whilst the other two bilayers have returned to the AP state. The following switches, at $H \approx 2.5$ kOe and $H \approx 3.6$ kOe, are purely magnetic AP–P transitions of the middle and highest J bilayers respectively.

Liquid observations

To further explore the magneto-mechanical behaviour of the real triple bilayer discs, and compare it with the simulated response, the liquid suspension was analysed with the reflectivity and OM-magnet set-ups. The rising and falling field reflectivity responses of the discs is compared against the liquid VSM loop in Figure 6.20a. Figure 6.20b shows four OM snapshots of the disc suspension, which correspond with four different field values, as labeled in Figure 6.20a.

Overall, the behaviour is very similar to that found for the dual bilayer discs. The discs presented in image 1 are randomly orientated as they are not under the influence of an applied field. In the reflectivity measurement, a small rise in signal near zero field corresponds with an 180° mechanical rotation, indicating a SFi state. The typical large reflectivity peak is then found in the rising field response, with signal dropping back down at a field that appears to correspond with the full saturation field of the discs in the VSM loop. Image 2 demonstrates the side-to-side chaining configuration of the discs in the field range of the reflectivity peak. After saturation, as shown in Image 3, we find that the discs have mechanically rotated to orient their EAs with the field direction and the chains have collapsed into face-to-face configurations. Image 4 illustrates the dissociation of the discs once the falling field has reached a low enough

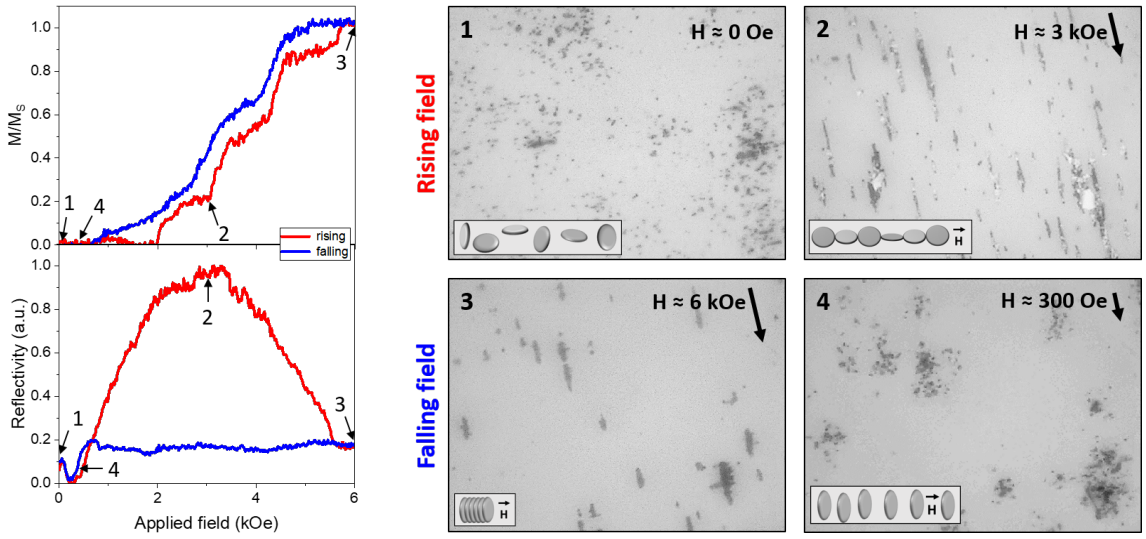

(a) VSM/reflectivity (b) OM images and disc schematics

Figure 6.20: Liquid observations of triple bilayer SAF particles. (a) A zoom in of the liquid VSM response (top) compared with a reflectivity measurement of the discs. The black arrows highlight the field points that correspond with the 100× OM images of the disc suspension in (b). Disc schematics indicate the disc orientations relative to the field.

field strength; we infer from the further reduction in the reflectivity signal, from the saturation level, that the EA of the discs are parallel to the field direction in this case as seen for the 2nd peak nanodiscs in Section 6.4.3.

One difference between the reflectivity responses of the triple and double bilayer discs is that the transitions between the EA and HP alignments for the double bilayers discs are significantly sharper. As has been noted previously, one major contributor to this lack of sharpness (in the case of the triple bilayer discs) will be the spread of magnetic properties across the population of discs. In the case of the triple bilayer discs, which are patterned from a thin film stack with a greater number of layers and switching fields, there is likely to be a greater spread of properties, and therefore more sloped transitions. In the case of the first transition up to the reflectivity peak, there is also the potential for an off-axis SFi rotation to contribute to the slope—as we have mentioned for both the double bilayer and 2nd AF peak discs (also see Section 6.2.2 and Figure 6.21). In light of this, we suggest the possibility of a novel canted state that could contribute to the slope of the second transition: from the peak in reflectivity down to saturation. We have illustrated our suggestion for the series of particle transitioning in Figure 6.21—from the AP EA alignment, up to the reflectivity peak, and back down to the saturated EA alignment. The new suggested canted state, occurring between the reflectivity peak and saturation, involves the unsaturated bilayers remaining in an AP canted state, whilst the saturating bilayers exhibit a spin-flop configuration (similar to that found in Section 6.3.4). A configuration like this could occur in liquid in order to minimise the system energy in the case of imbalances between the six layer moments, which is a likely feature of the magnetic stack. However, all of our bilayers should exist in the spin-flip regime, particularly in the case of those with lower J. It is therefore unfavourable for those bilayers to saturate via spin-flop in a canted configuration, and thus more likely that it is the spread of properties across the particle population that creates the sloped transition into the parallel state.

A major difference between the reflectivity of the triple and double bilayer discs is the lack of HP alignment in the falling field response of the triples. Previously, when we compared 1st AF peak discs with 2nd AF peak discs, we found a similar difference (see Section 6.4.3). We explained this by strong inter-particle interactions combined with

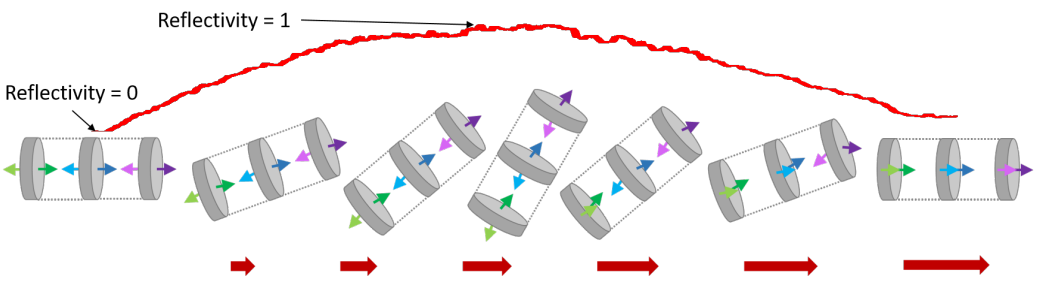

Figure 6.21: A schematic of a triple bilayer disc transitioning via the SFi canted regime up to a peak in its reflectivity signal (shown above), and then transitioning via alternative canted states into its saturated state. The arrows correspond to the moments of each CoFeB layer and the applied field, as labeled in Figure 6.19a.

weak coupling, in the case of the 2nd AF discs, which made the face-to-face chaining configuration more favourable and suppressed any HP alignment in the falling field response. So, in the case of the triple bilayer discs, compared with the double bilayer discs, we will again consider whether particle chaining is having an effect.

Figure 6.22 presents the field experienced by a particle at the end of a face-to-face chain, due to the magnetic moment of the particles, as a function of chain length. Here, the stray field calculations have been made with the particles possessing the same total magnetic moment (4×0.9 nm CoFeB for the double bilayer and 6×0.6 nm for the triple bilayer), but spread across a larger effective magnetic thickness for the triple bilayer discs (the effective magnetic thickness includes the full multilayer stack, minus the Ta buffer layers on either end). We find that the triple bilayer discs actually experience lower stray fields, for a chain length greater than 11, than the double bilayer discs. However, as we saw previously with the 2nd AF peak discs, it is the stray field relative to coupling field that is important in the suppression of the linear regime. In the case of the both disc types, the lowest coupling field is ~ 1.5 kOe, which is higher than the maximum total stray fields of ~ 950 Oe for the doubles and ~ 550 Oe for the triples. Although, these fields are roughly the same order of magnitude, which suggests that inter-particle interactions in these systems could be capable of affecting switching behaviour. It is not however clear why we have found a difference between the response of the double and triple bilayer discs, as these results indicate that they should behave in the same way. We suggest that the simplifications of our model for calculating stray fields, such as assuming perfect face-to-face alignment within a chain, could be masking a greater variation in interactions between the two disc types, which might lead to a difference in behaviour during their falling field response in liquid.

The key agreement between the dual and triple bilayer discs is their lack of correspondence between the simulated and real responses. The triple bilayer disc model, just like the dual disc model, predicts the abrupt mechanical rotation into the EA alignment at the saturation field of the lowest J bilayer. However, in reality, the discs appear to go through this transition at the final saturation field of the magnetic stack. Conversely,

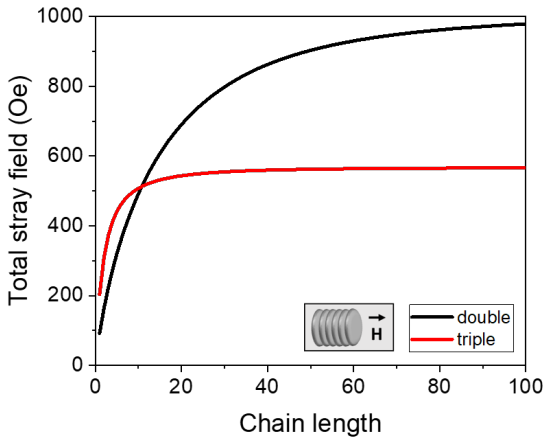

Figure 6.22: The cumulative stray field experienced by a 1 μm disc at the end of a face-to-face particle chain, as a function of chain length.

the liquid VSM response exhibits three clearly identifiable transitions, as discussed in Section 6.5.2, which matches better with the M-H response of the simulation. This indicates that the magneto-mechanical behaviour exhibited during this measurement of the real disc suspension is different to that in the reflectivity and OM. Consequently, we suggest that this difference stems from major difference in measurement conditions between the VSM and reflectivity/OM: namely the 75 Hz sample vibration and FSRs, as discussed in Section 6.5.1. As has been mentioned before, SQUID and FSR dependence data should shed more light on the behaviour of this system.

6.6 Conclusion

This chapter has made a thorough investigation into the magneto-mechanical behaviour of PM AF coupled particle systems under uniaxial applied magnetic fields. The novel transitions of these particles have been probed, through macrospin simulations and experimental analysis, whilst exploring their variation with a selection of parameters including EC, PMA and moment imbalance.

First, we extended the research from the simple SAF case to the moment imbalanced SFi case. This revealed an additional transition through zero field, in form of a 180° particle rotation. Furthermore, we demonstrated that even a relatively small imbalance in moment induces an alteration in the particle configuration during the linear field response: whilst a SAF disc exhibits perfect HP alignment to the field, with equal moment canting, a SFi disc continuously rotates its EA away from the field, up to a maximum angle $\alpha < 90°$, which is driven by an imbalance in moment canting. By conducting macrospin simulations across a broader range systems, we showed that the ultimate configuration that a SFi disc reaches, just before the point of saturation, is influenced by both the degree of ferrimagnetism and the balance between the EC and PMA energies. More extensive simulations uncovered another new transition, for discs with particularly strong EC/weak PMA, which manifests in a very high field regime with spin-flop characteristics.

An alternative exploration into the energy landscape of PM AF coupled particles was then made experimentally, utilising liquid VSM, reflectivity and OM measurements. Here, we investigated the effect of coupling strength on particle behaviour. This included how the loss of a zero remanence state transforms magnetic reversal, with some alteration to the more familiar SFi transitions, and thus does not result in a ferromagnetic response. Additionally, we considered the particles with multiple coupling strengths and found that it was possible to engineer thin films with two or three distinct coupling fields, which were conserved upon their patterning into magnetic discs and subsequent release into liquid.

Reflectivity measurements were found to be particularly useful in the assessment of particles that were challenging to distinguish with an OM. As these require a very simple optical set up, this work demonstrates the potential for this novel technique of the assessment of magnetic particle to be implemented in applications. Moreover,

a discrepancy was discovered between the magnetic response of particles under the conditions of a VSM versus in our custom reflectivity and OM-magnet set-ups. Further investigation is required into this phenomena, however, our work indicates that the reflectivity method is perhaps more appropriate, or at least offers new insight, in characterising the mechanical behaviour of particles for application driven studies.

Overall, the work in this chapter has developed our understanding of PM AF coupled particle systems, experimentally and theoretically. It illustrates the range of possible transitions and configurations, which are accessed by the application of simple uniaxial fields. This demonstrates these systems as attractive platforms for biological and other fluidic applications, including in the dynamic self-assembly of complex architectures, multiplexed magnetic sorting and soft robotics.

References

[1] G. Akoun and J.-P. Yonnet. 3D analytical calculation of the forces exerted between two cuboidal magnets. *IEEE Transactions on Magnetics*, 20(5):1962–1964, sep 1984.

[2] P. J. H. Bloemen, H. W. van Kesteren, H. J. M. Swagten, and W. J. M. de Jonge. Oscillatory interlayer exchange coupling in Co/Ru multilayers and bilayers. *Physical Review B*, 50(18):13505–13514, nov 1994.

[3] Gyung Min Choi, Il Jae Shin, Byoung Chul Min, and Kyung Ho Shin. Perpendicular magnetic tunnel junctions with synthetic ferrimagnetic pinned layer. *Journal of Applied Physics*, 108(7), 2010.

[4] B. Dieny and J P Gavigan. Minimum energy versus metastable magnetisation processes in antiferromagnetically coupled ferromagnetic multilayers. *J. Phys.:Condens. Matter*, 2(1):187–194, 1990.

[5] Randall M. Erb, Hui S. Son, Bappaditya Samanta, Vincent M. Rotello, and Benjamin B. Yellen. Magnetic assembly of colloidal superstructures with multipole symmetry. *Nature*, 457(7232):999–1002, 2009.

[6] Cécile Goubault, Fernando Leal-Calderon, Jean Louis Viovy, and Jérôme Bibette. Self-assembled magnetic nanowires made irreversible by polymer bridging. *Langmuir*, 21(9):3725–3729, 2005.

[7] H. Joisten, T. Courcier, P. Balint, P. Sabon, J. Faure-Vincent, S. Auffret, and B. Dieny. Self-polarization phenomenon and control of dispersion of synthetic antiferromagnetic nanoparticles for biological applications. *Applied Physics Letters*, 97(25):253112, 2010.

[8] R. Lavrijsen, A. Fernández-Pacheco, D. Petit, R. Mansell, J. H. Lee, and R. P. Cowburn. Tuning the interlayer exchange coupling between single perpendicularly magnetized CoFeB layers. *Applied Physics Letters*, 100(5):052411, jan 2012.

[9] A. Snezhko, I. S. Aranson, and W. K. Kwok. Surface wave assisted self-assembly of multidomain magnetic structures. *Physical Review Letters*, 96(7):1–4, 2006.

[10] A. Snezhko, M. Belkin, I. S. Aranson, and W. K. Kwok. Self-assembled magnetic surface swimmers. *Physical Review Letters*, 102(11):2–5, 2009.

[11] Alexey Snezhko and Igor S. Aranson. Magnetic manipulation of self-assembled colloidal asters. *Nature Materials*, 10(9):698–703, 2011.

[12] T. Vemulkar, E. N. Welbourne, R. Mansell, D. C. M. C. Petit, and R. P. Cowburn. The mechanical response in a fluid of synthetic antiferromagnetic and ferrimagnetic microdiscs with perpendicular magnetic anisotropy. *Applied Physics Letters*, 110(4):042402, 2017.

[13] George M. Whitesides. Self-Assembly at All Scales. *Science*, 295(5564):2418–2421, mar 2002.

[14] D. Zerrouki, J. Baudry, D. Pine, P. Chaikin, and J. Bibette. Chiral colloidal clusters. *Nature*, 455(7211):380–382, 2008.

[15] Jian Gang Zhu. Spin valve and dual spin valve heads with synthetic antiferromagnets. *IEEE Transactions on Magnetics*, 35(2 PART 1):655–660, 1999.

Chapter 7

PM SAFs in a magnetic combination cancer therapy

Note: This work was done in collaboration with M. Stanton (Prof. Cowburn's group), I. Rodrigo (BCMaterials and the Department of Electricity and Electronics, University of the Basque Country) and D. Valdés (Balseiro Institute, National University of Cuyo and the Magnetic Resonance Laboratory, Bariloche Atomic Centre). ***In vitro*** *treatment experiments were supported by B. Herrero de la Parte (Department of Surgery, Radiology and Physical Medicine, University of the Basque Country). The work was completed for the IEEE Magnetics Society, as a winning student-led project from their 2018 Summer School.*

7.1 Introduction

Cancer is a leading cause of death across the world: it estimated that cancer claimed 9.6 million lives in 2018 alone [34]. Cancer cells are highly resilient, which makes tackling the disease incredibly challenging. In order for a therapy to be successful in attacking cancer, it ideally combines a high level and persistent toxicity to cancer cells with a low negative effect on other, healthy cells in the body. This will destroy the cancer, prevent recurrence or metastasis, and limit undesirable side effects to a patient. Two common treatments that are currently used in medicine, and often in combination, are chemo- and radio-therapy. Together they apply a persistent, body-wide treatment alongside doses of the more focused radiation, which is often successful in fighting a range of cancers. However, it is well known that these aggressive methods also have a negative impact on healthy tissue, which induces unpleasant side effects in patients. Accordingly, there is a lot of research being conducted into alternative treatments, and how different therapies may be combined, with the aim of improving cancer destruction and reducing adverse side effects.

Perpendicularly magnetised (PM) synthetic antiferromagnetic (SAF) microdiscs (MDs) have previously been demonstrated as viable candidates for the magneto-mechanical destruction (MMD) of cancer cells. In this therapy the particles are ac-

tuated in a low-frequency, rotating magnetic field, which creates high torques that can effectively damage and kill cancer cells [16, 19]. There is potential for this treatment option to have great efficacy: efficient killing of cancer cells, alongside scope for the avoidance of negative effects on healthy tissue through the use of well-established cell targeting technology. Another approach, which is more well-established and is already appearing in clinical trials, is magnetic hyperthermia. Here, magnetic iron oxide nanoparticles (IONPs) induce cytotoxic heating of cells under the application of high frequency AC magnetic fields [8, 22, 24]. In addition to research on these particle-based methods as stand alone treatments, there are also studies being made into them as supplementary or synergistic methods to the more conventional chemo- or radio-therapies [10, 15, 21, 28].

This project aimed to investigate the potential for creating a 'magnetic combination' or solely particle based therapy, providing a novel, drug-free approach to the treatment of cancer. We endeavoured to take the hyperthermia and MMD concepts, which are not currently totally effective at killing cancer cells, and explore whether their integration would create a more successful treatment.

7.2 SAF particle design

The MDs were fabricated via a simple top-down lithography process: a PM SAF stack was sputtered on to 2 μm photoresist pillars and then released into solution by dissolving away the resist in acetone [31]. An SEM image of the resulting MDs is shown in Figure 7.1b. The magnetic stack used is described by $Au(10)/[Ta(2)/Pt(4)/CoFeB(0.9)/Pt(0.4)/Ru(0.9)/Pt(0.4)/CoFeB(0.9)/Pt(4)]_{10}/Au(10)$, with thicknesses in nm (see Figure 7.1a). The Ru layer provides strong AF coupling, through the RKKY interaction [3, 23], which gives the MDs a zero remanence state and prevents their agglomeration in water in zero applied field. The Pt layers force the magnetisation of the discs out of plane, creating a single EA, which provides the necessary lever to transform magnetic torque into mechanical torque in a rotating field [11, 16, 31]. The Pt interlayers have been made as thin as possible, without compromising the sharpness of the magnetic switching, to maximise the AF coupling and therefore preserve the zero remanence state [14]. The amorphous Ta acts as a smoothing layer, promoting sharp switching [29]. The main motif of the stack is repeated 10× to increase the net moment of the discs, therefore increasing their potential torque. Finally, the stack is capped on both sides with Au, for bio-compatibility.

Analysis of a thin film, sputtered concurrently with the MDs, was used to characterise the magnetic properties of the chosen stack. Figures 7.1c and 7.1d show the MOKE and VSM measurements respectively. The arrows alongside the MOKE loop represent the magnetisation direction of the two sets of CoFeB layers (bottom layers before Ru, top layers after Ru). From the MOKE data, we can determine the saturation field, $H_S = 2300$ Oe, the coupling field, $H_J = 1800$ Oe, and the coercivity field $H_C = 500$ Oe. With the addition of the VSM measurements, we can calculate

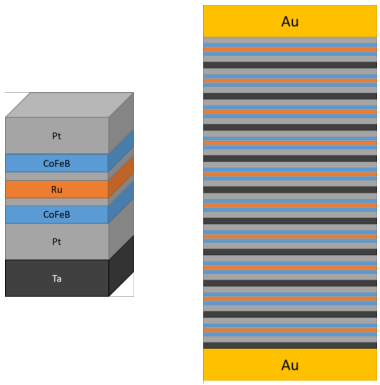

(a) Magnetic stack

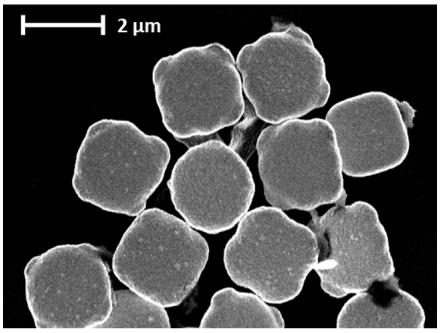

(b) Lifted discs

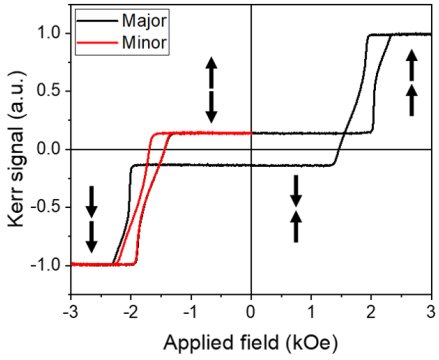

(c) MOKE of film

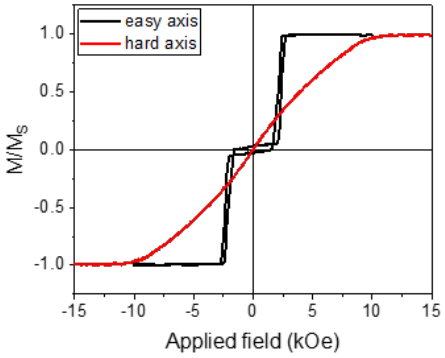

(d) VSM of film

Figure 7.1: (a) A schematic of the multilayer sputter stack used to create the microdiscs, which takes the form $Au/[Ta/Pt/CoFeB/Pt/Ru/Pt/CoFeB/Pt]_{10}/Au$ (b) An SEM image of microdiscs that have been lifted and redeposited for imaging. (c) A MOKE loop taken of the thin film form of this stack, with arrows indicating the magnetisation direction the two sets of CoFeB layers. (d) EA and HP VSM measurements of the thin film, normalised by M_S.

the anisotropy field, $H_K = 6700$ Oe, and find the magnetic saturation $M_S \approx 1100$ emu/cm^3. In the EA VSM loop, there is a very small net moment observed at remanence, which is $\sim 3\%$ of the M_S. This is likely due to roughness in the large multilayer stack, creating a slight imbalance in the volume of CoFeB in each set of layers.

7.2.1 Particle torque

Energy simulations of a single PM SAF MD under an applied magnetic field were conducted to investigate the potential torque that could be applied to cells, using the same method as in [16]. Here, the macrospin model detailed in Section 2.1.3 (and used throughout Chapter 6), was used to generate the full energy landscape of a MD under a particular applied field. The minimum energy configuration of the CoFeB layer moments was then found for the range of alpha (0–180°), the angle between the field and the EA. Using the definition of the magnetic torque, $\boldsymbol{T} = \boldsymbol{m} \times \boldsymbol{H}$, the magnitude

of the torque could then be calculated using:

$$T = MH_K \sin(\alpha - \theta) \tag{7.1}$$

where H_K is the anisotropy field, and θ is the angle between the net layer moment M (for all ten bilayers) and the EA (assuming that the two CoFeB layers are equal, for simplicity).

As is seen in the graph in Figure 7.2, there are strong variations in maximum possible torque with both applied field strength and with alpha, the angle between the EA of the MD and the field direction. To maximise the effectiveness of an MMD therapy on cancer cells, the treatment is carried out using a 10 kOe rotating field. Under these conditions, the MDs can apply a maximum torque of $\sim$ 40 fNm, which translates to a maximum force of $\sim$ 40 nN. This is a significantly higher force than the 100s of pN required to rupture a cell membrane, as quoted in the literature [13].

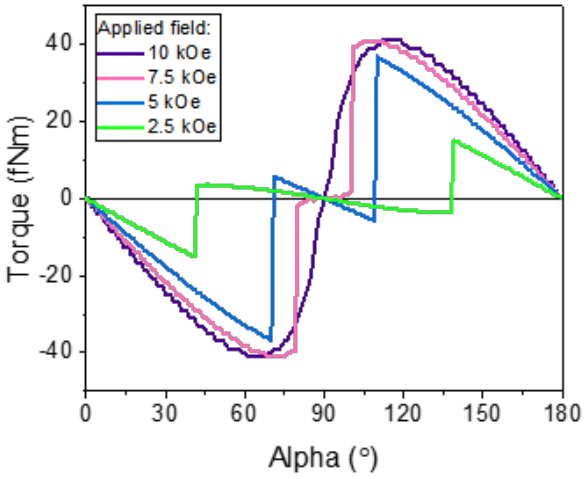

Figure 7.2: The simulated torque of a single MD when its EA is at an angle, alpha, to the field direction, for a range of applied field strengths.

7.3 Combining SAF MDs with IONPs

Note: the synthesis and characterisation of the IONPs were carried out by D. Valdés with the help of I. Rodrigo. The optical microscopy and SEM imaging were performed jointly with M. Stanton. The calorimetry and AC hysteresis measurements and analysis were completed by I. Rodrigo.

7.3.1 Synthesis and characterisation of IONPs

The fabrication of IONPs, for the magnetic hyperthermia aspect of the combined therapy, was done through a standard chemical synthesis method. Under reflux conditions, iron (III) acetylacetonate was thermally decomposed in the presence of oleic acid, using

Benzyl ether as a solvent, for 40 min. This created oleic acid coated IONPs, which are hydrophobic. The IONPs were imaged by TEM (see Figure 7.3a) and *ImageJ* software was used to analyse the size distribution of the particles through the assessment of particle area (see Figure 7.3b). This determined an average IONP diameter of 26 ± 1 nm.

The particles were made hydrophilic, and therefore more bio-compatible, by coating with two different compounds: DSPE-mPEG-2000 (PEG) and dextran (dex) [17]. To ascertain the organic mass fraction (proportion of PEG/dex molecules) of the coated IONPs, a thermogravimetric or mass loss test was carried out: the particles were heated up to $\sim$ 900 ℃ over a period of $\sim$ 90 mins and their mass was recorded as a percentage of the original mass. The results are displayed in Figure 7.3c. Both samples exhibit two distinct decreases in mass at $\sim$ 250 ℃ and $\sim$ 700 ℃. These correspond with decomposition of oleic acid into H_2O, CO_2, H_2, O_2 and graphite; and graphite respectively. The total mass loss, and therefore coating proportion, was quantified as 22.20% and 21.96% for dex- and PEG-IONPs respectively.

The coated IONPs were characterised magnetically using VSM measurements, with the resulting loops shown in Figure 7.3d. Both curves strongly resemble typical super-

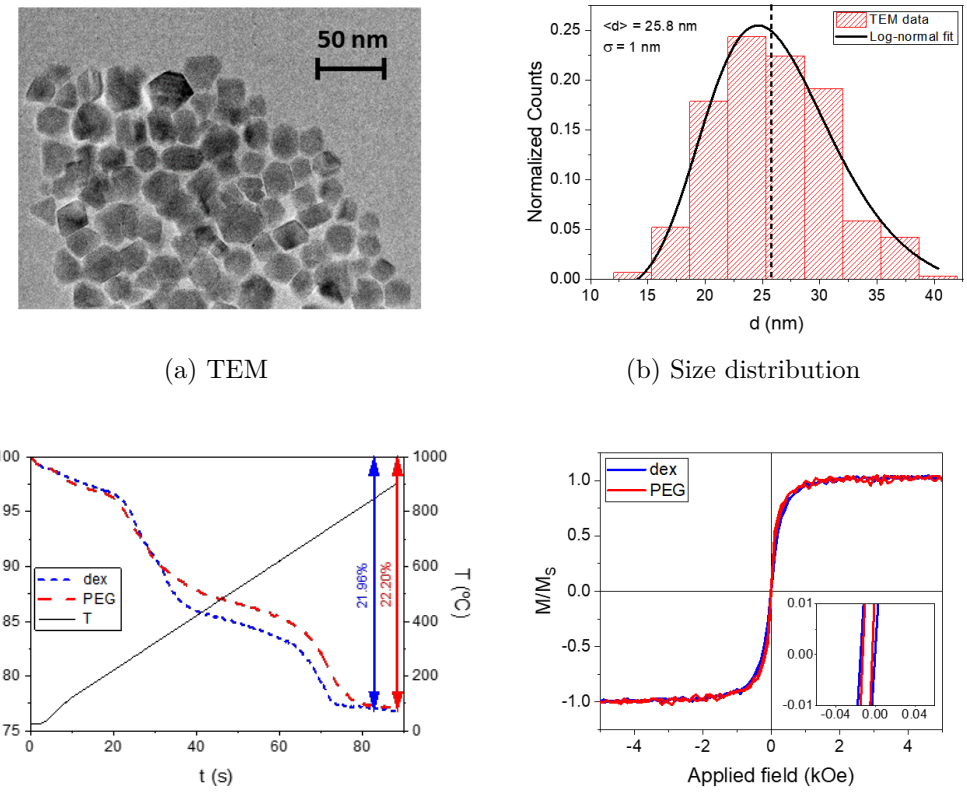

(a) TEM

(b) Size distribution

(c) Mass loss

(d) VSM

Figure 7.3: (a) A TEM image of uncoated IONPs. (b) The size distribution by diameter (d) of the uncoated IONPs: they have an average diameter (<d>) of 25.8 nm with standard deviation (σ) of 1 nm. (c) The percentage mass of the coated IONPs over time (blue and red) as temperature, T, (black) is increased, causing the removal of the coating. (d) VSM measurements of the coated IONPs.

paramagnetic behaviour, but with a very small amount of hysteresis around remanence (see inset in Figure 7.3d). This may be due to particles being in a blocked state at room temperature: particle magnetisation does not flip repeatedly, as it would if it were superparamagnetic, resulting in the particles exhibiting a net moment at remanence [1]. The M_S of the particles was calculated from a Langevin fit, giving 73 ± 1 emu/g and 74 ± 1 emu/g for dex- and PEG-IONPs respectively. These findings indicate that the coatings do not have an effect on the magnetic behaviour of the particles.

7.3.2 IONP-MD behaviour in liquid

VSM analysis

Before carrying out *in vitro* experiments that utilise combinations of MDs and IONPs, we made some investigations into how the different particles interact with each other in a simplified fluid environment. The liquid VSM data in Figure 7.4 compares the magnetic responses of MD-IONP mixtures suspended in water with the responses of the individual samples under the same conditions. The shape of the liquid VSM loop of the MDs has some variation from that of the EA loop taken of the corresponding thin film [30]. As previously discussed in Chapter 6, this is a result of increasing the freedom of movement of the discs, thus allowing them to rotate mechanically under the applied field in order to minimise their energy. They are therefore able to access new parts of their energy landscape, which creates different chaining configurations and alters their magnetic behaviour in comparison with a corresponding thin film [30].

Looking at the liquid VSM loops of the MD-IONP mixtures, shown in Figure 7.4, they both take the general form of a superposition of the loops from the separate components. This is not unlike the results we found in Sections 6.4.2 and 6.4.3 for mixtures of particles with and without zero remanence states. To further probe the behaviour of these particles mixtures under applied fields, and discover how they interact with each other, we imaged them using OM.

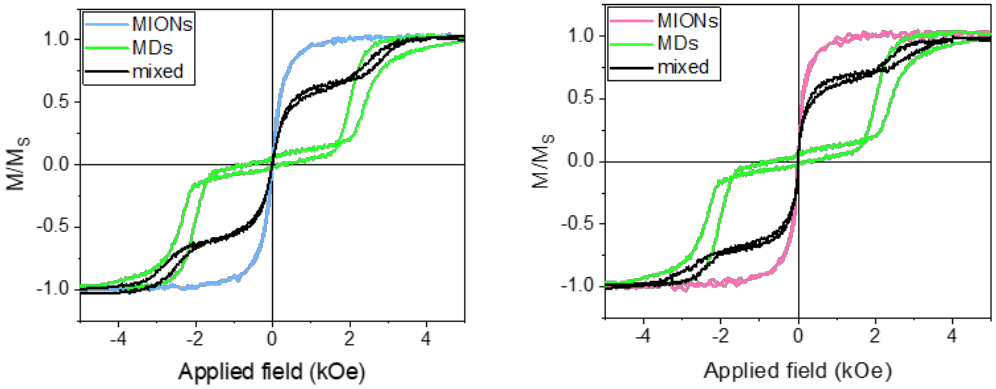

(a) MDs and dex-IONPs (b) MDs and PEG-IONPs

Figure 7.4: Liquid VSM measurements of the MDs, dex-IONPs and PEG-IONPs both individually and in two MD-IONP mixtures. Magnetic moment has been normalised by respective M_S.

Particle imaging

To image the particles in similar conditions to those experienced with the VSM, droplets of the particle suspensions were deposited on Si chips and placed in the OM-magnet set up (see Section 3.3.1). The dipole here was capable of applying a field strong enough to saturate all particles. The interactions between MDs and IONPs are driven by the dipolar fields that are generated by the particles themselves. At remanence, the MDs exhibit very low dipolar fields, resulting from the small imbalance in moment which was found in the EA VSM, low enough that the MDs do not agglomerate outside of applied fields. Conversely, under higher applied fields and particularly when saturated, the MDs exhibit a relatively high dipolar field. This creates the characteristic particle chaining as discussed in [30] and Section 6.2. In Figure 7.5b, which depicts the MD mixture with the PEG-IONPs, we observe a very similar behaviour as that of a simple MD suspension: at very low fields, the particles are dispersed, and when the field strength is increased, the MDs form chains along the field direction.

However, the behaviour of the MD mixture with the dex-IONPs is quite different: the presence of the IONPs in this case has a significant effect on the chaining response. Figure 7.5a shows that under the higher field strength, the two particle types form long inter-particle chains along the field direction: minimising the energy of the system by maximising the alignment of both particle magnetisations with the magnetic flux. This is not dissimilar to the response seen by the PEG-IONP sample, however there

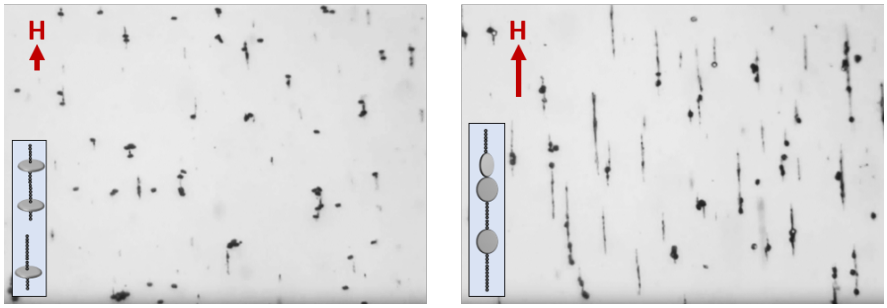

(a) MDs and dex-IONPs

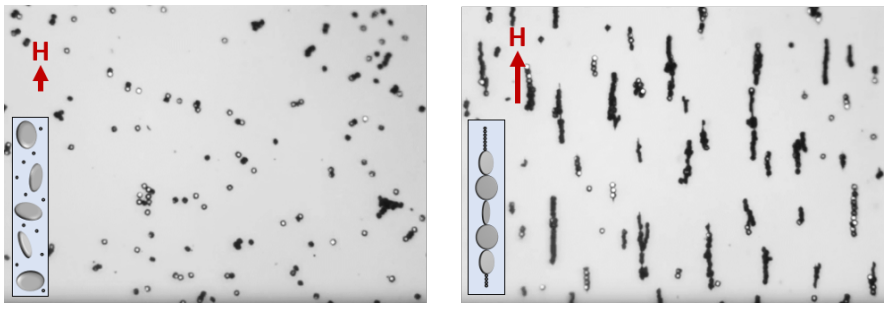

(b) MDs and PEG-IONPs

Figure 7.5: Optical microscope images taken at 100× magnification of the two MD-IONP mixtures suspended in water. DC fields of ∼ 30 Oe (left) and ∼ 3500 Oe (right) were applied in the vertical direction of the image. Red arrows indicate the applied field direction.

is an obvious increase in the inclusion of the dex-IONPs in the chains. The more prominent difference in behaviour is at lower field strengths: again we do not observe direct interactions between MDs, however, the dex-IONPs still form small clumps and chains between themselves and the MDs. This is the result of the IONPs exhibiting a magnetic moment significantly larger than that of the MDs, even under a low applied field. The explanation as to why we see this additional chaining with the dex-IONPS, but not the PEG-IONPS, comes down to the molecules used in their coatings. The PEG molecules are much larger than the dextran molecules, thus the hydrodynamic volume of the PEG-IONPs is greater. This has two key effects: a reduction in the ability of the particles to rotate in order to orient their magnetic moment, and increased shielding or particle separation. These effects will reduce the dipolar interactions between the particles, therefore preventing PEG-IONPs from chaining under lower applied fields.

SEM images

SEM images of samples of the MD-IONP mixtures further confirm the conclusions formed about the particle interactions. Figure 7.6 shows images of particle suspensions that were saturated in a magnetic field (parallel to substrate surface), removed from the applied field and then left to dry out on the Si substrate. The dex-IONP sample, shown in Figure 7.6a, contains distinct chains of the IONPs, which stem from and connect up the MDs. It is interesting that these chains are still very prevalent, despite the lack of applied field during the drying process. This firstly indicates that the

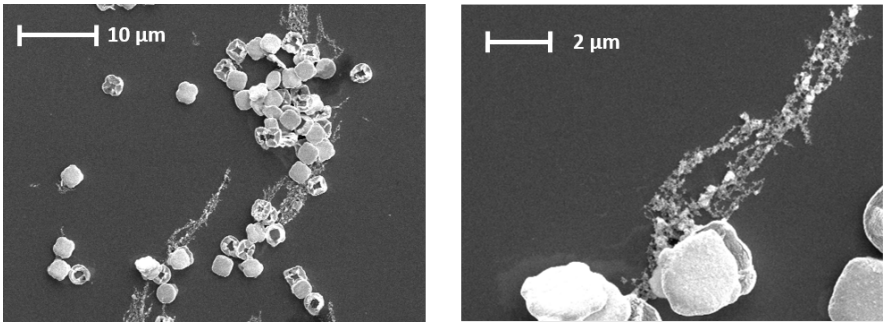

(a) MDs and dex-IONPs

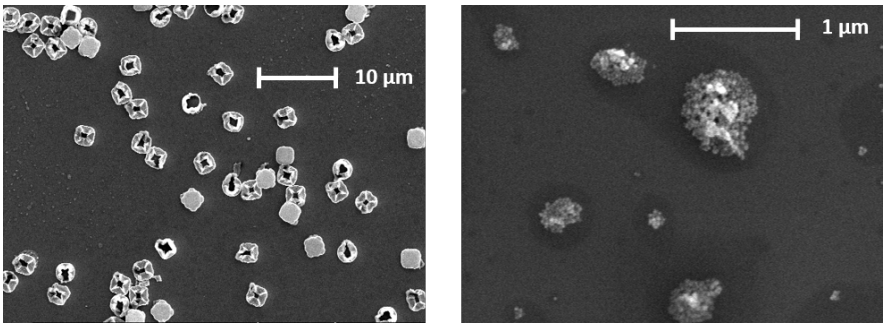

(b) MDs and PEG-IONPs

Figure 7.6: SEM images of the particle mixtures dried out on a Si substrate after the application and removal of a magnetic field.

dipolar fields from the MDs are sufficient to cause IONP interactions, which could be possible due to the high susceptibility of the IONPs [12], and secondly suggests that the dextran coating could be physically sticky to both itself and the Au coating of the MDs. This would allow the chains to be retained after drying, despite the turbulence caused during water evaporation.

As expected from the optical imaging results, the PEG-IONP sample does not exhibit the same chaining patterns. In Figure 7.6b we can see a dispersion of MDs, alongside small clusters of the PEG-IONPs, with no apparent inter-particle interactions. The IONP aggregation could stem from a number of causes: such physical binding between the coating or surface interactions caused by the sample drying process.

7.3.3 Magnetic hyperthermia

Before applying treatments to cancer cells *in vitro* we characterised the magnetic hyperthermia capabilities of the different particles. We used a combination of calorimetric and alternating current (AC) hysteresis measurements, made using a custom built AC magnetometer [7], the results of which are displayed in Figure 7.7. The concentration of dex- and PEG-IONPs were 0.39 mg/ml and 0.45 mg/ml respectively. The MD concentration was 0.1 mg/ml.

Calorimetry

Heating curves were obtained by inserting a fibre optical thermometer into a vial of particles suspended in water, while an AC magnetic field with an amplitude of 226 Oe and a frequency of 301 kHz was applied for 10 mins. The graph in Figure 7.7a shows that the MD sample does not generate any heat, as is described in the literature [16] - the decrease in temperature we observe is due to the cooling of the magnet. The dex- and PEG-IONP samples experienced temperature increases of 12 °C and 15.6 °C respectively. We note that the same effect from the cooling of the magnet could mean that these values are an underestimate of the temperature increase. As such, we cannot assume these are absolute values related to the heating capabilities of the IONPs. However, as each experiment here has been conducted in the same way, it is still relevant to compare the results.

From the calorimetry data, specific absorption rate (SAR) values were extracted using the standard formula [2]:

$$SAR = \frac{C}{m_{IONP}} \left| \frac{dT}{dt} \right|_{t=0} = \frac{C}{m_{IONP}} \psi \tag{7.2}$$

where C is the heat capacity of the whole sample, m_{IONP} is the total mass of particles and ψ is the initial slope of the heating curve. This gave 340 W/g for dex-IONPs and 400 W/g for PEG-IONPs. This indicates that although both IONP samples are effective at generating heat, the PEG-IONPs have a greater heating efficiency than the

dex-IONPs.

AC hysteresis

To investigate further, the AC hysteresis loops of all three sets of particles, separately suspended in water, were measured at a field frequency of 301 kHz with increasing field intensity (0–226 Oe). The results are displayed in Figures 7.7b - 7.7d. As expected, after the results from the calorimetry experiment and from the literature [16], the MDs were unable to align with the field under such a high AC frequency, therefore no significant AC magnetic response is observed (Figure 7.7b), compared to the IONPs. We also note that the field amplitude is much smaller than the switching field of the MDs. However, both IONP samples produced typical sets of AC hysteresis loops. In Figure 7.7c, we see a series of somewhat tilted and stretched loops from the dex-IONPs, with decreased areas. Analogous AC loops have been observed previously for systems of dipolar interacting IONPs with randomly oriented axes [6, 20, 26], which reflects the chaining behaviour observed of the dex-IONPs during optical microscopy (see Section 7.3.2). The loops produced from the PEG-IONPs , shown in Figure 7.7d, are more square in shape. Both simulations and measurements of non-interacting, randomly oriented magnetite particles with uniaxial anisotropy have previously generated similar hysteretic responses [5, 18, 20, 27].

By comparing the AC hysteresis of a PEG-IONP-MDs with PEG-IONPs alone, as is shown in Figure 7.7e, we find that the the MDs have an effect on the magnetic response of the IONPs: there is a small increase in area of the AC loop. This is likely due to inter-particle interactions causing some modification of the IONP assembly under field. As the change in the shape of the hysteresis loop is small, it demonstrates that although MDs have some effect on the behaviour of IONPs, the MDs do not have a significant effect on the hysteresis of the PEG-IONPs.

SAR analysis

SAR versus field strength curves were extracted from the AC hysteresis measurements of the IONPs using the equation [25]:

$$SAR = -\frac{f}{c} \cdot \mu_0 \oint M(t).dH \tag{7.3}$$

where f is the field frequency and c is the IONP mass concentration (mass/sample volume). The results are presented in Figure 7.7f.

Both curves take the same shape, with small SAR values at low magnetic fields, followed by a more rapid increase with field strengths above ~ 100 Oe. This trend was previously reported for nanoparticles large enough to maintain permanent magnetic dipoles [5], which was observed in the VSM data (see Section 7.3.1). As was calculated from the calorimetry experiment, the PEG-IONPs produced higher SAR values than the dex-IONPs. However, there is a discrepancy between the SAR values calculated from the calorimetry and magnetometry: reading from the curves in Figure 7.7f, we

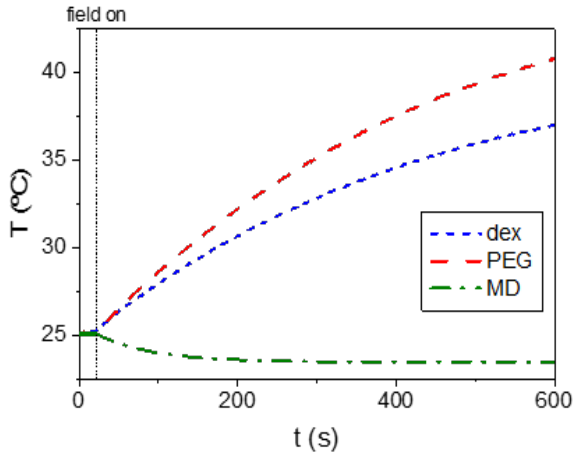

(a) Heating curves

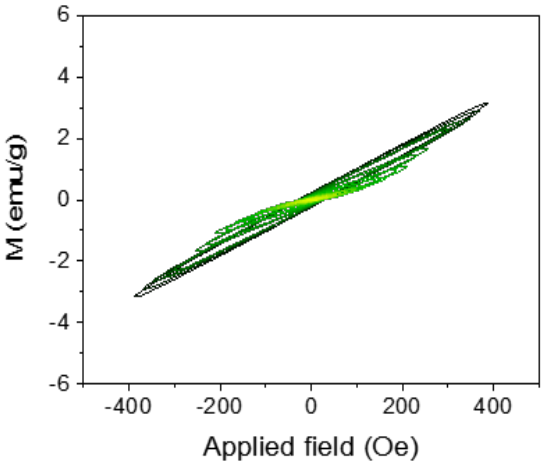

(b) AC hysteresis - MDs

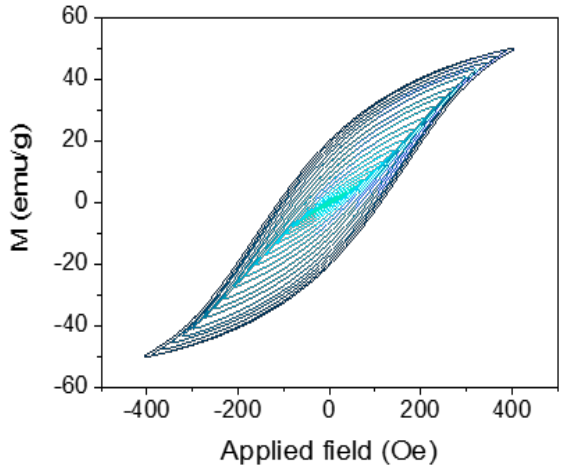

(c) AC hysteresis - dex-IONPs

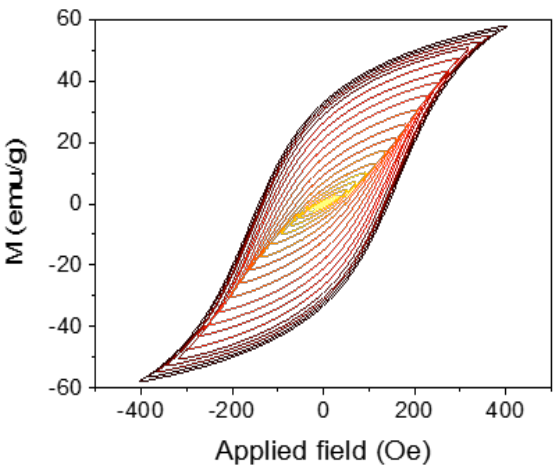

(d) AC hysteresis - PEG-IONPs

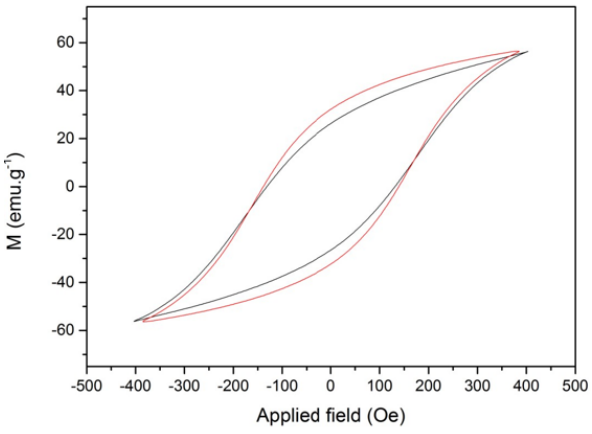

(e) AC hysteresis - PEG-IONPs and MDs

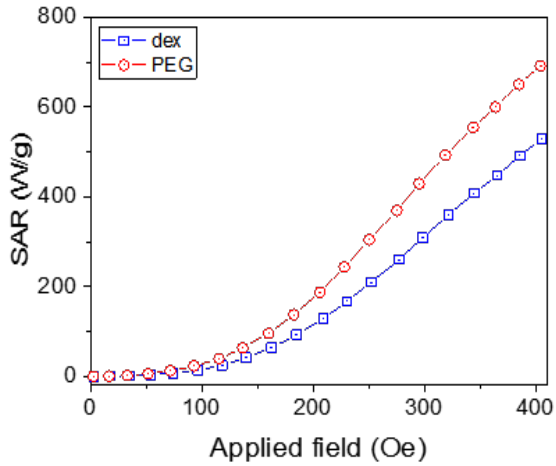

(f) SAR

Figure 7.7: A characterisation of the hyperthermia capabilities of the particles when suspended in water. (a) Temperature, T, curves for each particle type under an applied AC magnetic field with a magnitude of 226 Oe and a frequency of 301 kHz over time, t. (b) - (d) AC hysteresis loops of the three particle types under applied fields with a frequency of 301 kHz. (e) AC hysteresis loops of a PEG-IONP and MD mixture (red) compared with PEG-IONPs alone (black). (f) SAR curves for the IONPs.

find smaller values for SAR at 226 Oe as was found from the calorimetry data. In the case of calorimetry, SAR is determined from the initial slope of the temperature versus time curve. However, multiple factors may influence this slope, and thus the calculated SAR value, including: volume of fluid, thermal properties of the container (as we observed with the magnetic cooling), positioning of the temperature sensor, sample geometry, coil geometry, power density and heating time [9, 32]. For example, sample geometry may create a non-uniformity in the generated magnetic field, and as SAR is proportional to squared field strength a small difference in field may result in a significant difference in SAR [9]. This makes calculating the SAR values from the AC magnetometry a more reliable and accurate method.

7.4 *In vitro* experiments

Note: The SEM imaging was performed jointly with M. Stanton. The TEM was carried out by I. Rodrigo. The majority of the cytotoxicity experiments are the work of I. Rodrigo and D. Valdés. The ***in vitro*** *treatment trials were a joint effort between all collaborators, with the statistical analysis performed by I. Rodrigo and D. Valdés. B. Herrero de la Parte supported all of the culturing and analysis of cells.*

The following in vitro studies were made on rat colorectal cancer cells, of the cell line CC531. Colorectal, or bowel, cancer originates in the epithelial cells of the intestines and its cause is generally attributed to old age and lifestyle factors (e.g. diet or smoking) [4]. In 2018 it was the third most common cancer (1.80 million cases) and the second most common cause of cancer death (862 000 deaths) [34]. Traditional treatments include some combination of surgery, radiation therapy, chemotherapy and molecularly targeted therapy [33].

7.4.1 Particle internalisation

SEM analysis

To investigate the internalisation of particles by the CC531 cells, we first utilised SEM imaging. A culture of cells that had been grown on a glass coverslip and incubated with both MDs and PEG-IONPs was fixed with paraformaldehyde, dried and sputter coated with Au. Figure 7.8 shows two SEM images of the same cell, one taken at a beam voltage of 5 keV and the other at 20 keV. Due to the significantly small size of the IONPs and the strong presence of salt crystals (originating from the cell culture medium or PBS washing medium), it is not possible to locate the PEG-IONPs in these images. In the 5 keV image, Figure 7.8a, it is not trivial to locate the MDs, however the morphology of the cell surface can be seen. When the beam voltage is increased to 20 keV, as seen in 7.8b, the higher energy electrons are able to pass further through the sample: they penetrate the Au coating and the cell membrane, revealing the locations of the highly reflective MDs. This result indicates that the MDs have been internalised by the cell, however TEM imaging was required to confirm this.

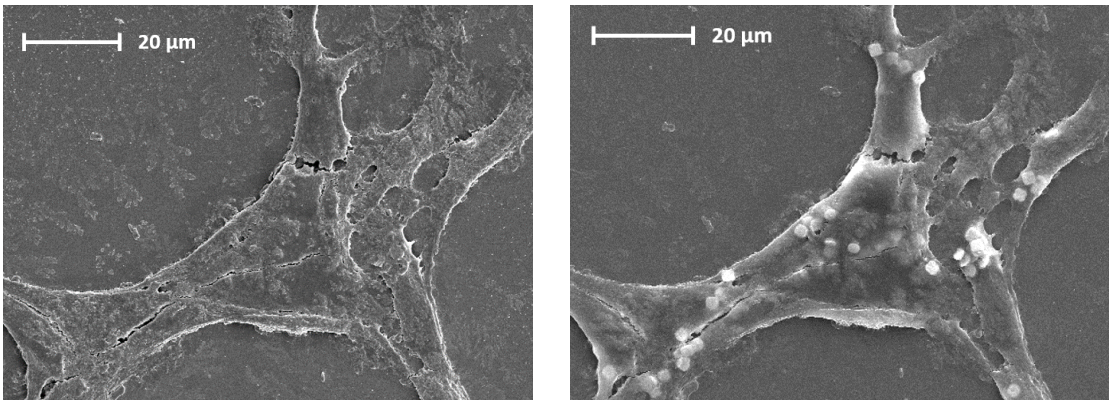

(a) 5 keV (b) 20 keV

Figure 7.8: SEM images of CC531 cells that were incubated with MDs and PEG-IONPs, taken with two different SEM beam voltages.

TEM analysis

CC531 cells were again incubated with a mixture of MDs and IONPs, and were then explored with TEM imaging. Looking at the images shown in Figure 7.9, it is clear that the MDs (the large, curved, black forms - zoomed in image on left) have been internalised by this cell. This is consistent with previous studies [15, 16]. Internalisation of MDs was observed regularly across the cell population in the TEM imaging. It is noted that the size of MDs is quite large relative to the cell size and that their shape is quite irregular: future work might consider a modification in their fabrication to make them smaller and more uniform. The cell shown in Figure 7.9 has also taken up some of the IONPs (the clusters of small, black grains - zoomed in on right). These appear to be encased in a vesicle, but it is unclear if the MDs are too. The internalisation of the IONPs through the cell population is not as regular as for the MDs: the IONPs were often collected outside of the cell membranes. We speculate that there is a potential correlation between cells that have internalised one or more MDs and the increased frequency of IONP uptake; perhaps, what is most likely a substantial event in the

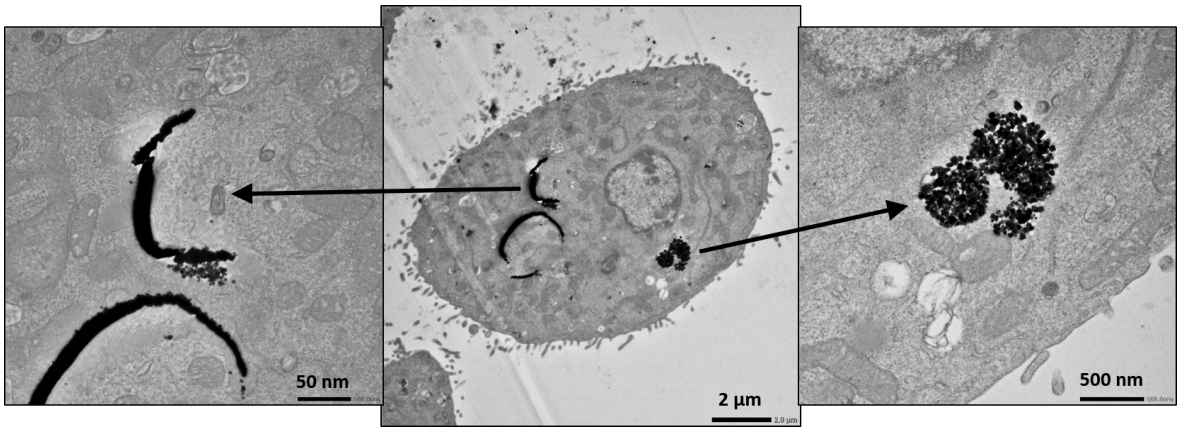

Figure 7.9: TEM images of a CC531 cell that was incubated with MDs (magnified on left) and IONPs (magnified on right).

engulfing of a relatively large MD, promotes or aids the uptake of IONPs. However, to confirm this, large scale analysis across a sizeable cell population would be required, which was beyond the scope of this work.

7.4.2 Cytotoxicity

Before any treatment experiments were performed it was important to assess whether the presence of the particles alone had any negative effect on the viability of CC531 cells.

IONPs

The cytotoxicity of the IONPs was evaluated using a standard trypan blue assay. The trypan blue assay is a dye exclusion method: dead cells are stained, but live cells are not. Viable cells are very selective towards which compounds they internalise. However, cell death results in a loss of membrane integrity, allowing the trypan blue dye to enter and stain the cell. This technique for assessing cytotoxicity does not determine the nature of cell death, nor does it include cells that are in the process of dying.

Cell numbers were found through image cytometry (using a NucleoCounter NC-100). Cell viability was calculated relative to control samples, using Equation 7.4 where $N_{culture}$ is the number of viable cells in a test sample and $N_{control}$ is the number of viable cells in the control sample.

$$Viability = \frac{N_{culture}}{N_{control}} \times 100\% \tag{7.4}$$

The results are displayed in Figure 7.10a. After an incubation period of 24 hrs with a particle concentration of 0.5 mg/ml, the dex-IONP sample has a cell viability of $91 \pm 2\%$ and the PEG-IONP sample has a cell viability of $59 \pm 1\%$. These results indicate that the dex-IONPs have little effect on the cells, however, the PEG-IONPs have a significantly toxic effect. We note that previous studies have also found that IONPs coated with mPEG molecules are much more toxic than those coated with dextran [17].

MDs and mixtures

To further investigate particle cytotoxicity, we utilised MTT assays to assess the effects of MDs and MD-IONP mixtures. The MTT assay is a colourmetric assay that assesses the metabolic activity of cells, which is related to their viability. A type of cellular oxidoreductase enzyme is capable of reducing a particular cell permeable dye to a coloured compound - the indicator molecule. Quantification of the presence of the indicator is made by spectrophotometry, relative to that in a control sample of cells, is used to assess the percentage of viable cells in a test sample.

Here, the IONPs were again used at a concentration of 0.5 mg/ml and the MDs were tested at 20 particles/cell. 24 hrs after the addition of particles, the MTT stock

solution was added to the cell cultures and incubated for 2 hrs. The cells were then lysed with DMSO (perforating the cell membranes) to release the indicator molecules. Absorbance readings were taken at 540 nm with a spectrophotometer (Multiskan EX) to quantify the presence of the indicator. From this, cell viability was calculated relative to control samples using Equation 7.5, where $A_{culture}$ is the absorbance measured from a test sample, $A_{control}$ is the absorbance from the control sample and A_{blank} is the background absorbance measured from an empty well plate.

$$Viability = \frac{A_{culture} - A_{blank}}{A_{control} - A_{blank}} \times 100\% \tag{7.5}$$

From the results shown in Figure 7.10b we can see that the cell viabilities were $90 \pm 7\%$, $79 \pm 15\%$ and $55 \pm 14\%$ for the MD, MD-dex-IONP and MD-PEG-IONP samples respectively. This again indicates that the PEG-IONPs are significantly cytotoxic, but that the MDs and dex-IONPs are both suitable to continue with for our *in vitro* testing. We concluded that the PEG-IONPs are not good candidates for the *in vitro* treatment experiments for two key reasons: firstly, it would be hard to separate out the numbers of cancer cells killed by any treatments from those harmed by just the IONP presence; secondly, if research progressed to any *in vivo* trials, there would be a concern that the IONPs could have a toxic effect on healthy cells.

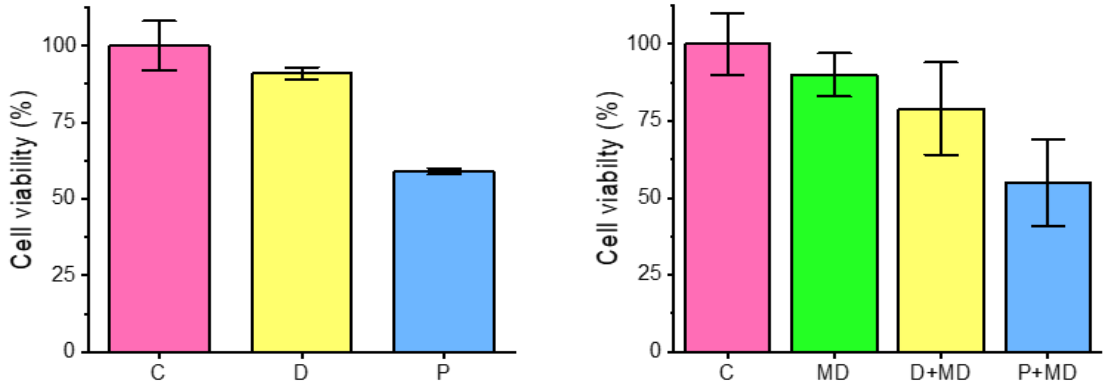

(a) IONPs (b) MDs and IONPs

Figure 7.10: Cell viability percentages for cells that have been incubated for 24 hrs with each particle type individually (MDs, D = dex-IONPs, P = PEG-IONPs), plus two MD-IONP mixtures. Control samples (C) contained no particles.

7.4.3 *In vitro* treatment trial

We carried out a preliminary *in vitro* treatment experiment, which started with incubating the CC531 cells (5000/well in 96-well plates) with the particles, individually and in MD-IONP mixtures, for 24 hrs to give the cells time to internalise the particles. We used a IONP concentration of 0.5 mg/ml and 20 MDs/cell, the same as in the cytotoxicity assays. We then carried out a series of treatments on the various samples, using two different custom-built therapy set ups, separately and in tandem. The

magnetic hyperthermia system applied a linear AC magnetic field with a strength of 226 Oe and a frequency 301 kHz over a period of 10 mins; we will refer to this as the high frequency, low field (HFLF) therapy. The MMD was initiated by the application of rotating magnetic field, with a much higher strength of 10 kOe and a much lower frequency of 20 Hz, also for 10 mins; we will refer to this as the slow rotation, high field (SRHF) therapy. Four repeats (four wells) of each set of conditions were used, with treatments applied to multiple wells at the same time, while ensuring field homogeneity. Control samples, without any particles added to the cells, were also prepared for comparison. After a 5 hr incubation period, MTT assays were used to assess the cell viability of the samples, using the same method as described above in the cytotoxicity experiments. It should be noted that with the assessment of cell viability being made after just 5 hrs, it is probable that the full cell damage will not have been accounted for: the effects of apoptosis and reactive oxygen species triggered cell death can take longer to emerge.

Figure 7.11 displays all of the cell viability results from the treatment trial. For the dex-IONP only samples, as seen in Figure 7.11a, we can see that under the SRHF treatment the IONPs have no effect on the cells. This was expected due to their very small size and minimal anisotropy, which leads to highly inefficient torque application. Conversely, the dex-IONPs have a much greater effect in the HFLF treatment: we observe a reduction in cell viability of $\sim 25\%$ for HFLF application only and $\sim 40\%$ for the combined treatment. We therefore see some promising results from the IONPs in the cancer therapy, however, this reduction in cell viability is not yet good enough for a successful treatment.

The results for the MD only samples are presented in Figure 7.11b. Here we confirm that the MDs do not exert any hyperthermic effect on the cancer cells, with no decrease in viability in the HFLF samples. However, the SRHF treatment application with the MD samples does induce a decrease in cell viability. Under the current conditions, we observe a decrease in viability of only $\sim 11\%$ for both the SRHF only and combined treatment samples, which is much lower than that required for a successful treatment.

We now move onto the combined particle samples, the results of which are displayed in Figure 7.11c, where the aim was to increase the destruction of cancer cells by joining the forces of hyperthermic and MMD effects. In all of these samples a mixture of dex-IONPs and MDs were present and the two treatments were applied both individually and in tandem. The HFLF only sample of this set shows a similar decrease in cell viability, $25 \pm 6\%$, as was observed for the equivalent dex-IONP only sample. Likewise, the SRHF only sample of this set shows a similar decrease in viability, $12 \pm 1\%$, as we found for the equivalent MD only sample. For the combined treatment samples, we indeed see a greater decreases in cell viability of $37 \pm 6\%$ and $32 \pm 3\%$, which doesn't appear to be particularly affected by the order of the treatment application. A final observation is the reduced standard deviation in the mixed particle samples (in particular the SRHF + HFLF sample) compared with the single type samples. We hypothesize that this could be a result of the increased IONP uptake with parallel MD internali-

sation, as we detected in the TEM images; an increase in IONP internalisation would induce a more consistent application of hyperthermia. Further studies are required to demonstrate if this is a statistically significant effect.

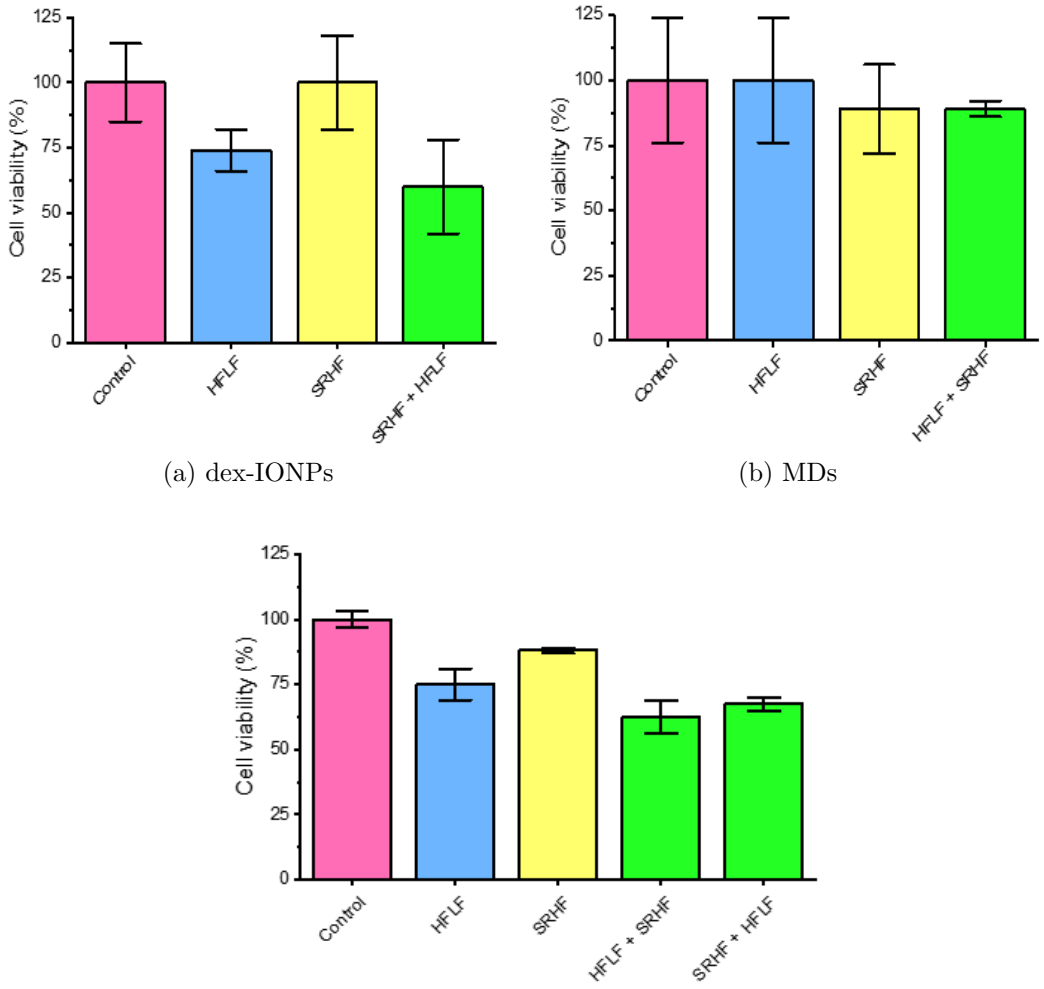

(a) dex-IONPs

(b) MDs

(c) dex-IONPs and MDs

Figure 7.11: Cell viabilities calculated after the different treatments (HFLF and SRHF), plus controls (C).

7.5 Conclusions and future work

This project provided a preliminary study into the concept of a magnetic particle based cancer treatment, involving the combination of magnetic hyperthermia and MMD. Chemically synthesised IONPs, coated with two different molecules, were shown to have promising hyperthermic properties, but no MMD effect. PM SAF MDs were fabricated through a top-down process, which created particles that were tailored towards the MMD application with theoretically sufficient torque production, but did not exhibit any significant hyperthermic effects. Imaging of the particles revealed different chaining behaviours, dependent on the functional coating of the IONPs, which led to changes in the magnetic behaviour of the IONPs under high frequency AC fields. *In vitro*

studies showed that the CC531 cancer cells were capable of internalising both types of particle. Additionally, the MDs and dex-IONPs did not appear to exert a significant cytotoxic effect, however, it was discovered that the PEG-IONPs were cytotoxic and therefore unsuitable for cell treatments. An initial cancer treatment trial using the dex-IONPs and MDs gave evidence that, under the chosen experimental parameters, the individual treatments cause small therapeutic effects and when combined this effect was somewhat enhanced. These results provide a proof of concept for the magnetic combination therapy: we have proven that it is possible to combine the two different particle-based treatments, that this combination can increase cell death from that of the individual treatments, and that there is a possible synergistic effect originating from the interaction between the two different particle types.

However, this is a very early study into this combined particle therapy concept. There were significant constraints, due to the framework of the project (as set by the IEEE Magnetics Society), which lead to the majority of the work being performed during two weeks of allocated time in which all collaborators were present (in Cambridge, then in Leioa). This allowed for the preparation and some characterisation of the particles before this period and for post-processing of data to be made afterwards, but there was no scope for significant preparatory or follow-up studies to be made for the *in vitro* work. This leaves considerable opportunity for the continuation of research into this concept of the 'magnetic combination therapy'.

Future research on this project will need to begin with work on optimising the hyperthermia and MMD treatments individually, before returning to combined therapy trials. This should start with increased adaptation of the particles for each of their applications. On the side of the IONPs, this would involve two key threads: formation and properties of the iron-oxide core, and the use and composition of the IONP coating. Here the aims would be to promote particle internalisation, limit particle agglomeration outside of applied magnetic fields and tailor the AC hysteretic response towards an increased heating response. The outcome of these modulations should be a more efficient and effective hyperthermic effect on cancer cells. Tailoring of the MDs for MMD would involve editing of the magnetic sputter stack and the fabrication method, to develop a potentially more suitable disc shape, mainly to target improvements in the application of torque. This could include utilising the fabrication method detailed in Section 5.2.2 to transfer from the use of MDs to nanodiscs. These adaptations would aim to improve the killing efficiency of the MMD application.

A crucial stage in future research on this project is the optimisation of the treatment application parameters for hyperthermia and MMD individually. In previous work higher levels of cell death have been achieved, for example MMD has been show to cause 62% damage to cancer cells with just one minute of treatment application [16], which demonstrates scope for increasing therapeutic effect via the individual treatments. The set ups used for each treatment should be satisfactory, as they had already been designed for purpose as part of other research projects. The main variables that should be explored, to achieve more a more therapeutic effect, are: the length of time

that a treatment is applied, potential repetitions of such applications, and the number/concentration of particles added to the cells. As an example, in a previous study on the use of MDs in a SRHF therapy, it was found that the use of 50 particles/cell had a significantly larger therapeutic effect that 20 particles/cell [19]. The method of assessing cell viability should also be considered: a technique that takes into account both cell necrosis and apoptosis would be an ideal candidate.

Once a more effective solution has been outlined for each of the individual treatments, it will be possible to return to the combined therapy testing. Due to our finding that the killing of cancer cells by hyperthermic IONPs is more consistent in the presence of MDs, the combined therapy work should start with tests on cultures incubated with particle mixtures, but under the implementation of one treatment system only. This will investigate the potential synergy between the different therapies, which will most likely originate from inter-particle interactions, since we found that the particles do not exhibit significant effects under the fields they are not designed to work under. Here, it may be worth exploring particle ratios and, again, time periods of treatment application. Finally, to complete a thorough *in vitro* study into the combined therapy concept, a series of trials involving the two sets of particles and the two treatment applications should be made. Using all the previous groundwork, optimising all the parameters involved in the hyperthermia and MMD separately, it can be hypothesised that a significantly improved therapeutic effect could be observed. If successful, it might be considered worthwhile to move on to *in vivo* testing.

References

[1] A Aharoni. *Introduction to the Theory of Ferromagnetism*. International Series of Monographs on Physics. Clarendon Press, 2000.

[2] Irene Andreu and Eva Natividad. Accuracy of available methods for quantifying the heat power generation of nanoparticles for magnetic hyperthermia. *International Journal of Hyperthermia*, 29(8):739–751, 2013.

[3] S. Bandiera, R. C. Sousa, S. Auffret, B. Rodmacq, and B. Dieny. Enhancement of perpendicular magnetic anisotropy thanks to Pt insertions in synthetic antiferromagnets. *Applied Physics Letters*, 101(7):072410, aug 2012.

[4] FT Bosman. Chapter 5.5: Colorectal Cancer. In BW Stewart and CP Wild, editors, *World Cancer Report*, pages 392–402. The International Agency for Research on Cancer, World Health Organisation, 2014.

[5] J. Carrey, B. Mehdaoui, and M. Respaud. Simple models for dynamic hysteresis loop calculations of magnetic single-domain nanoparticles: Application to magnetic hyperthermia optimization. *Journal of Applied Physics*, 109(8), 2011.

[6] Diego F. Coral, Pedro Mendoza Zélis, Marzia Marciello, María Del Puerto Morales, Aldo Craievich, Francisco H. Sánchez, and Marcela B. Fernández Van Raap. Effect of Nanoclustering and Dipolar Interactions in Heat Generation for Magnetic Hyperthermia. *Langmuir*, 32(5):1201–1213, 2016.

[7] E. Garaio, J. M. Collantes, F. Plazaola, J. A. Garcia, and I. Castellanos-Rubio. A multifrequency eletromagnetic applicator with an integrated AC magnetometer for magnetic hyperthermia experiments. *Measurement Science and Technology*, 25(11), 2014.

[8] Rudolf Hergt, Silvio Dutz, Robert Müller, and Matthias Zeisberger. Magnetic particle hyperthermia: Nanoparticle magnetism and materials development for cancer therapy. *Journal of Physics Condensed Matter*, 18(38), 2006.

[9] S Huang, S-y Wang, A Gupta, D-A Borca-Tasciuc, and S J Salon. On the measurement technique for specific absorption rate of nanoparticles in an alternating electromagnetic field. *Measurement Science and Technology*, 23(3):035701, mar 2012.

[10] Mark Hurwitz and Paul Stauffer. Hyperthermia, radiation and chemotherapy: the role of heat in multidisciplinary cancer care. *Seminars in oncology*, 41(6):714–729, dec 2014.

[11] M T Johnson, P J H Bloemen, F J A den Broeder, and J J de Vries. Magnetic anisotropy in metallic multilayers. *Reports on Progress in Physics*, 59(11):1409–1458, 1996.

[12] H. Joisten, T. Courcier, P. Balint, P. Sabon, J. Faure-Vincent, S. Auffret, and B. Dieny. Self-polarization phenomenon and control of dispersion of synthetic antiferromagnetic nanoparticles for biological applications. *Applied Physics Letters*, 97(25):253112, 2010.

[13] Dong-Hyun Kim, Elena a Rozhkova, Ilya V Ulasov, Samuel D Bader, Tijana Rajh, Maciej S Lesniak, and Valentyn Novosad. Biofunctionalized magnetic-vortex microdiscs for targeted cancer-cell destruction. *Nature materials*, 9(2):165–71, feb 2010.

[14] R. Lavrijsen, A. Fernández-Pacheco, D. Petit, R. Mansell, J. H. Lee, and R. P. Cowburn. Tuning the interlayer exchange coupling between single perpendicularly magnetized CoFeB layers. *Applied Physics Letters*, 100(5):052411, jan 2012.

[15] Selma Leulmi Pichot, Sabrina Bentouati, Saif S. Ahmad, Marios Sotiropoulos, Raj Jena, and Russell Cowburn. Versatile magnetic microdiscs for the radio enhancement and mechanical disruption of glioblastoma cancer cells. *RSC Advances*, 10(14):8161–8171, 2020.

[16] Rhodri Mansell, Tarun Vemulkar, Dorothée C. M. C. Petit, Yu Cheng, Jason Murphy, Maciej S. Lesniak, and Russell P. Cowburn. Magnetic particles with perpendicular anisotropy for mechanical cancer cell destruction. *Scientific Reports*, 7(1):4257, 2017.

[17] M. L. Mojica Pisciotti, E. Lima, M. Vasquez Mansilla, V. E. Tognoli, H. E. Troiani, A. A. Pasa, T. B. Creczynski-Pasa, A. H. Silva, P. Gurman, L. Colombo, G. F. Goya, A. Lamagna, and R. D. Zysler. In vitro and in vivo experiments with iron oxide nanoparticles functionalized with DEXTRAN or polyethylene glycol for medical applications: Magnetic targeting. *Journal of Biomedical Materials Research - Part B Applied Biomaterials*, 102(4):860–868, 2014.

[18] Alicia Muela, David Muñoz, Rosa Martín-Rodríguez, Iñaki Orue, Eneko Garaio, Ana Abad Díaz De Cerio, Javier Alonso, José Ángel García, and M. Luisa Fdez-Gubieda. Optimal Parameters for Hyperthermia Treatment Using Biomineralized Magnetite Nanoparticles: Theoretical and Experimental Approach. *Journal of Physical Chemistry C*, 120(42):24437–24448, 2016.

[19] Megan E. Muroski, Ramin A. Morshed, Yu Cheng, Tarun Vemulkar, Rhodri Mansell, Yu Han, Lingjiao Zhang, Karen S. Aboody, Russell P. Cowburn, and Maciej S. Lesniak. Controlled Payload Release by Magnetic Field Triggered Neural Stem Cell Destruction for Malignant Glioma Treatment. *PLOS ONE*, 11(1):e0145129, jan 2016.

[20] Zohreh Nemati, Javier Alonso, Irati Rodrigo, Raja Das, Eneko Garaio, José Ángel García, Inaki Orue, Manh Huong Phan, and Hariharan Srikanth. Improving the Heating Efficiency of Iron Oxide Nanoparticles by Tuning Their Shape and Size. *Journal of Physical Chemistry C*, 122(4):2367–2381, 2018.

[21] Takayuki Ohguri, Hajime Imada, Hiroyuki Narisada, Katsuya Yahara, Tomoaki Morioka, Keita Nakano, Yasuhiro Miyaguni, and Yukunori Korogi. Systemic chemotherapy using paclitaxel and carboplatin plus regional hyperthermia and hyperbaric oxygen treatment for non-small cell lung cancer with multiple pulmonary metastases: Preliminary results. *International Journal of Hyperthermia*, 25(2):160–167, 2009.

[22] D. Ortega Ponce and Quentin Pankhurst. Magnetic Hyperthermia. In P. O'Brien, editor, *Nanoscience*, page 6088. Royal Society of Chemistry, 2012.

[23] S. S.P. Parkin. Systematic variation of the strength and oscillation period of indirect magnetic exchange coupling through the 3d, 4d, and 5d transition metals. *Physical Review Letters*, 67(25):3598–3601, 1991.

[24] E. A. Périgo, G. Hemery, O. Sandre, D. Ortega, E. Garaio, F. Plazaola, and F. J. Teran. Fundamentals and advances in magnetic hyperthermia. *Applied Physics Reviews*, 2(4):041302, dec 2015.

[25] R.E. Rosensweig. Heating magnetic fluid with alternating magnetic field. *Journal of Magnetism and Magnetic Materials*, 252(6 I):370–374, nov 2002.

[26] D. Serantes, D. Baldomir, C. Martinez-Boubeta, K. Simeonidis, M. Angelakeris, E. Natividad, M. Castro, A. Mediano, D. X. Chen, A. Sanchez, L. I. Balcells, and B. Martínez. Influence of dipolar interactions on hyperthermia properties of ferromagnetic particles. *Journal of Applied Physics*, 108(7), 2010.

[27] R. P. Tan, J. Carrey, and M. Respaud. Magnetic hyperthermia properties of nanoparticles inside lysosomes using kinetic Monte Carlo simulations: Influence of key parameters and dipolar interactions, and evidence for strong spatial variation of heating power. *Physical Review B - Condensed Matter and Materials Physics*, 90(21):1–12, 2014.

[28] Jacoba van der Zee, Dionisio González, Gerard C van Rhoon, Jan DP van Dijk, Wim LJ van Putten, and Augustinus AM Hart. Comparison of radiotherapy alone with radiotherapy plus hyperthermia in locally advanced pelvic tumours: a prospective, randomised, multicentre trial. *The Lancet*, 355(9210):1119–1125, apr 2000.

[29] T. Vemulkar, R. Mansell, D. C. M. C. Petit, R. P. Cowburn, and M. S. Lesniak. The effect of underlayers on the reversal of perpendicularly magnetized multilayer thin films for magnetic micro- and nanoparticles. *Journal of Applied Physics*, 121(4):043908, 2017.

[30] T. Vemulkar, E. N. Welbourne, R. Mansell, D. C. M. C. Petit, and R. P. Cowburn. The mechanical response in a fluid of synthetic antiferromagnetic and ferrimagnetic microdiscs with perpendicular magnetic anisotropy. *Applied Physics Letters*, 110(4):042402, 2017.

[31] T Vemulkar, R Mansell, D C M C Petit, R P Cowburn, and M S Lesniak. Highly tunable perpendicularly magnetized synthetic antiferromagnets for biotechnology applications. *Applied Physics Letters*, 107(1):012403, jul 2015.

[32] Shu Yi Wang, Shujuan Huang, and Diana Andra Borca-Tasciuc. Potential sources of errors in measuring and evaluating the specific loss power of magnetic nanoparticles in an alternating magnetic field. *IEEE Transactions on Magnetics*, 49(1):255–262, 2013.

[33] Colon Cancer Treatment (PDQ®) (https://www.cancer.gov/types/colorectal/patient/colon-treatment-pdq#section/all), 2014.

[34] Cancer (https://www.who.int/en/news-room/fact-sheets/detail/cancer), 2010.

Chapter 8

Conclusions and outlook

8.1 The aims of this thesis

Magnetic particles offer a powerful tool for the remote control of specific components and wider systems in soft matter applications. From the manipulation of cells and sub-cellular components, to investigate their intrinsic properties or influence their behaviour [1, 2, 4–6, 14]; to the fabrication of magnetically actuated composites and dynamically self assembled architectures [3, 15]; to biotechnology solutions for cell separation, microfluidic mixing and biosensing [9, 10, 13]; magnetic actuation has been established as an important technique across the field of biology.

Perpendicularly magnetised (PM), synthetic antiferromagnetic (SAF) particles have been demonstrated as a strong candidate for use in applications involving magnetic actuation in soft matter systems [8, 11, 12]. They offer a selection of highly desirable characteristics, including: strong uniaxial anistropy, a zero remanence state, variable magnetic moment and tunable switching [12]. An investigation into PM SAF particle behaviour in liquid, under the influence of simple uniaxial applied fields, also revealed interesting magneto-mechanical transitions and dynamic self-assemblies [11]. These could be exploited in a number of actuation based applications, such as soft robotics or the organisation of biological components.

One particular application that PM SAFs particles have been shown to be successful in, is the magneto-mechanical destruction of cancer cells. This area of research was pioneered with a different type of planar particle, a magnetic vortex microdisc (MD) [6], which offered an exciting development for a localised, non-pharmaceutical cancer therapy. Since then, it has been shown that due to the uniaxial symmetry of PM SAFs, they are capable of inducing a more effective therapeutic effect than vortex MDs [8]. Additionally, a study into a potential combination cancer treatment revealed a synergistic effect between the application of magneto-mechanical destruction and radiotherapy [7]. Specifically, the gold coated SAF MDs acting as intracellular emitters of secondary electrons, enhanced the effect of radiotherapy, on top of providing their characteristic mechanical disruption through exertion of torque.

The goal of this thesis was to build on the innovative research that has engineered

PM SAF particles and begun to explore how their properties and behaviour might be exploited. We intended to put together a robust toolbox, for the design and fabrication of flexible magnetic nanodiscs, which can be tailored for use across a suite of biological applications. To achieve this, we studied the design of PM SAF multilayers, worked on optimising their translation into functional nanoparticles, and implemented a range of techniques to thoroughly characterise their magnetic and mechanical behaviours.

8.2 Design development of multilayer thin films

In Chapter 4, we highlighted the key parameters that may affect the magnetic properties of PM SAF coupled thin films. Through this discussion we aimed to demonstrate the flexibility of the systems, and exhibit how they can be tailored towards a variety of applications.

Initially, we studied how the different components of our multilayer heterostructures influence their magnetic hysteresis. In particular, we focused on the variation of the AF coupling, via the thicknesses of the Ru and Pt interlayers for coarse and fine control respectively, showing how it is possible to produce films with a wide range of switching fields. This ability is crucial to a plethora of applications, including magnetic sorting and sensing. Furthermore, we demonstrated the ability to engineer films with up to ten distinct switching fields, which could be interesting for the concept of multiplexed sorting. We also showed that by stacking up repeats of our bilayer motif, we can efficiently increase magnetic moment, without compromising our other magnetic properties. For force and torque based applications, this simple method of tuning moment is highly beneficial.

We then went on to explore how external parameters may affect the magnetic reversal of PM SAF films. The majority of this investigation focused around underlayers, which will become a necessary addition to our deposition stack for the fabrication of PM SAF particles, as they will enable their lift-off into solution. We established Ge as a strong candidate for the production of robust PM SAFs, with the key components of their magnetic hysteresis being well-conserved for potential applications. On a physics level, we did uncover that Ge induces some interesting effects in the nucleation and propagation of domains during magnetic transitions. In addition, by exploiting the field sweep rate dependence of PM SAF switching, we revealed the manifestation of AP–AP transitions in highly coupled SAFs and the potential for dynamic selective switching in weakly coupled SAFs. Such behaviours might be of interest in applications such as race track memory or magnetic sensing, and data storage respectively.

8.3 Optimisation and effects of particle fabrication

In Chapter 5, we presented an efficient and robust fabrication method for the production of thin film based magnetic nanoparticles. By implementing nanosphere lithogra-

phy with polystyrene beads we were able to achieve a range of diameters from 1 μm, roughly the lower limit of traditional optical lithography methods, down to 100 nm. Our choice of a spin coating application of the beads provided a simple method to tune their spread, via the spin parameters, which led us to generate a particularly high yield of particles. Using the beads as a direct mask during the ion milling process, we were able to efficiently produce well-defined, planar nanoparticles. Finally, following on from our investigation in Chapter 4, we made use of Ge as our sacrificial layer. We were hence able to fabricate PM SAF nanodiscs with robust magnetic properties, which could be easily lifted off into solution.

We explored how the patterning of PM SAF thin films into nanodiscs affects the magnetic reversal of the system. Through the modification of fabrication parameters, such as milling power and bead size, we were able to probe the causes behind hysteretic changes, which included increased coercivity and loss of sharpness of switching. A major contributor to this was the induction of defects in the multilayer films, through the interaction of ions during the milling process. Additionally, the patterning of a continuous film into nanostructures generates a spread in magnetic properties across the particle population: magnetic reversal is driven by growth defects in the multilayer, which become distributed across the particle population. Nevertheless, our work demonstrated the ability to maintain the key properties of our films during their translation into nanodiscs: namely tunable switching, a zero remanence state and low field susceptibility.

Due to the effects of patterning, we found that variation in coupling strength and coercivity can lead to the loss of the zero remanence state. This occurs in systems that are coupled at the strongest AF coupling peak, but which have their switching field reduced by a relatively thick Pt interlayer. By altering the design of the interlayer motif and using the 2nd strongest AF peak with a thinner Pt interlayer, we put together an alternative method for creating particles with a smaller switching field. We then found that the patterning process had a smaller impact on the hysteresis of these nanodiscs. Therefore, we showed that it is possible to create functional nanodiscs that are activated in the low field regime. This is highly relevant to biotechnology applications where a low strength magnetic field is required, such as in lab-on-chip devices.

8.4 Characterisation of in-liquid particle behaviour

Chapter 6 extended the investigation into the magneto-mechanical behaviour of PM AF coupled particles in liquid suspensions and under the influence of uniaxial magnetic fields. This was undertaken via a combination of macrospin simulations and experimental analysis, to examine PM AF systems with varied magnetic parameters. Through this we developed our understanding of these systems, as both single particles and particle suspensions. We presented these systems as attractive platforms for a range of soft matter applications, including magnetic sorting, soft robotics and dynamic self assembly.

Our study began with the case of an AF system with a small imbalance in moment: a synthetic ferrimagnetic (SFi) particle. We found that SFis with a very small imbalance experience similar magneto-mechanical transitions to perfectly balanced SAFs, leading to the same dynamic self-assemblies. However, there were some differences in the particle configurations, driven by the imbalance: an EA field alignment in low fields, leading to a 180° mechanical rotation through zero field; and continuous rotation of the HP towards the field prior to saturation, rather than an perfect HP alignment.

By conducting macrospin simulations across a broader range of PM AF systems, we showed how the degree of ferrimagnetism and the ratio of coupling to anisotropy energies can affect the ultimate SFi configuration before the point of saturation. More extensive simulations uncovered an additional, novel transition in discs with particularly strong coupling or particularly weak anisotropy. This manifested at particularly high fields as a spin-flop type transition, notably at a much higher coupling to anisotropy ratio than is seen in thin film systems.

Liquid VSM, OM and reflectivity measurements were used to experimentally explore the energy landscape of PM AF particles with varied coupling strengths. We determined that for weakly coupled particles that seemed to have lost their zero remanence state, the hysteretic response of the population in liquid was the result of a superposition of those particles that did and those that did not retain an AP state at remanence. Additionally, we found that it was possible to engineer thin films with multiple, distinct switching fields, which were conserved during patterning and subsequent release into liquid. This has interesting implications in the area of multiplexed sorting of soft matter systems.

Our innovative use of reflectivity to measure the orientation of PM AF particles under applied fields was found to be particularly useful in the case of our 500 nm discs, which are challenging to resolve with an OM. Moreover, we uncovered a discrepancy between the magnetic responses of particles under the conditions of a VSM, versus reflectivity and OM. Our work indicates that the magneto-mechanical transitions of PM SAFs are affected by external parameters such as field sweep rate and particle interactions.

8.5 Magnetic combination therapy

Chapter 7 summarised a project on the original concept of a ‘drug free’ cancer treatment, through the combination of magnetic hyperthermia and magneto-mechanical destruction. Despite this being a very early study, our results indicate the potential for a synergistic effect between the two therapies. This suggests that the concept of a combined magnetic particle treatment is worth further consideration, and could be developed into a strong method of fighting cancer, while limiting negative side effects to patients.

We started this project by assessing the efficacy of the individual particles: iron oxide nanoparticles (IONPs) and the PM SAF MDs. We established that the IONPs

had promising hyperthermic properties, but no mechanically destructive effect. We also designed the MDs to have a sufficiently high torque for mechanical destruction, but they did not exhibit significant hyperthermic effects. Imaging of particle mixtures, under the application of uniaxial applied fields, revealed variation in chaining behaviour with the type of functional coating of the IONPs. This also manifested in changes in the magnetic hysteresis on the IONPs under high frequency AC fields.

In vitro studies, utilising SEM and TEM imaging, demonstrated that cancer cells can internalise both types of particle. They also showed that although IONPs with a dextran coating and MDs did not appear to induce cytotoxicity, and were therefore suitable for therapeutic use, IONPs with a PEG coating did. A preliminary treatment trial provided a proof of concept for the magnetic combination therapy: the individual treatments a small therapeutic effect, which is enhanced when combined.

8.6 Outlook

This thesis provides significant development into the design and characterisation of PM AF particles. Starting with the foundation, the PM SAF thin film, we extended scope for flexibility in the system, for application driven magnetic properties. We worked on optimising the translation of these films into magnetic particles, overcoming some of the limitations of previous fabrication methods such as size and yield. We studied the magnetic behaviour of our particles on chip and released into solution, demonstrating the ability to fabricate functional PM AF particles. In the process of studying the particles in liquid, we revealed some interesting and novel physics, in the form of variable magneto-mechanical transitions and configurations. We finished by showing the potential for PM SAF particles, in combination with iron oxide NPs, in an original 'drug free' cancer treatment.

To provide a more comprehensive analysis of the PM AF coupled system, increase our grasp on how such particles might behave in a liquid environment and learn how best to tailor them for particular applications, there are a few areas in which further study would be beneficial. The first area is that of our designed magnetic properties, from the thin film to the nanodiscs. Although we have been quite thorough in manipulating our multilayers to vary the AF coupling, we have not really explored the other key characteristic of our magnetic system: the PMA. As we have noted, this property is crucial to the most efficient transduction of torque, which is highly desirable for magnetic actuation purposes. In future work, it would be worth exploring how this could be manipulated, such as through the use of Co/Pt systems, which offer higher interfacial anisotropy that CoFeB/Pt counterparts (as the PMA arises from the Co-Pt interface). While we have spent time probing the switching behaviour of the PM AF films, down to the domain level, we have not undertaken such experiments on our particles. It would be very interesting to compare the nucleation and propagation behaviour of magnetic reversal of the particles with the films, which could be possible with magnetic force microscopy measurements. This would provide more insight into

how the magnetic hysteresis is altered by the patterning process.

The second area that should be considered for additional study, is the materials and methods of particle fabrication. On the side of materials, a lot of energy has been put into the engineering of magnetic multilayers with desirable, tunable properties. However, we must note the issue of toxicity when proposing the use of such materials for applications *in vivo*. Unlike iron oxide NPs, which have been implemented into clinical applications, not all of the metallic layers that we have utilised are biologically compatible. Research into potential applications must be mindful of this. However, there is still a wide range of biological applications that this type of particle would be well suited to, not excluding the biomedical sector, such as in point-of-care microfluidic devices. On the side of fabrication, although we have made significant progress in increasing the yield of thin film based particle on the nanoscale, further efforts would be necessary to manufacture quantities that would be relevant for commercial applications. Having said that, our implementation of the spin coating method for generating our lithography mask is highly amenable to industrial fabrication methods, and presents the potential for increasing the yield (via tuning of spin parameters) without having to look to alternatives.

The variation in magneto-mechanical behaviour of PM AF particles in liquid, with respect to parameters such as degree of ferrimagnetism and coupling-to-anisotropy ratio, opens up another interesting avenue of study. This has possible implications to exciting applications such as the dynamic self assembly of complex soft matter structures. To explore the energy landscape of our magnetic system in more detail, it could be meaningful to introduce coercivity into our model. This could be achieved by using a steepest descent minimisation method. This would allows us to simulate single particle behaviour that was more representative of the reality.

In our work, we highlighted a number of external parameters to our system, which appeared to have an effect on the behaviour of our particles. In particular, we uncovered different exhibitions of the previously characterised magneto-mechanical transitions, depending on whether we measured the particles via VSM or by an optical method. We noted that the two key differences in conditions during these measurements were field sweep rate and mechanical vibration. To better understand the mechanisms behind the alterations that these conditions cause to the energy landscape, we suggest two parallel investigations: measurement of liquid suspensions via a SQUID, to eliminate sample vibration and compare directly with VSM; and a series of FSR dependence measurements, spearheaded with the reflectivity set up. Additionally, we mentioned the influence of interparticle interactions on magnetic reversal. A more in depth investigation into the potential fields exerted by particles, on others, in the different chaining configurations would certainly be beneficial here.

Finally, on the subject of our novel cancer therapy concept, we previously discussed in detail the future work that should be undertaken to develop this concept into a more established, effective treatment option. To summarise, it is important to first optimise the separate therapies, hyperthermia and mechanical-disruption, such that

they are individually more efficient at killing cancer cells. Afterwards, the notion of a synergy between the two can be explored. Here, it would be beneficial to investigate the possible mechanisms behind this, with interparticle interactions seeming to be a likely possibility. This could lead to the development of a combined treatment that was more effective than the sum of its individual components.

The PM AF coupled system generates uniquely characterised particles, which exhibit a range of interesting and tunable behaviours. Rather than being perfectly suited to a singular, major application, they instead offer a selection of desirable properties that could be tailored to and exploited by a suite of different applications across the field of biology and beyond. In particular, the configurations and transitions demonstrated by these particles are highly interesting to applications involving magnetic or mechanical actuation, or dynamic self-assembly.

References

[1] F.H.C. Crick and A.F.W. Hughes. The physical properties of cytoplasm. *Experimental Cell Research*, 1(1):37–80, 1950.

[2] Jon Dobson. Remote control of cellular behaviour with magnetic nanoparticles. *Nature Nanotechnology*, 3(3):139–143, mar 2008.

[3] Randall M. Erb, Joshua J. Martin, Rasam Soheilian, Chunzhou Pan, and Jabulani R. Barber. Actuating Soft Matter with Magnetic Torque. *Advanced Functional Materials*, 26(22):3859–3880, 2016.

[4] Steven Hughes, Stuart McBain, Jon Dobson, and A J El Haj. Selective activation of mechanosensitive ion channels using magnetic particles. *Journal of the Royal Society, Interface / the Royal Society*, 5(25):855–63, 2008.

[5] J M Kanczler, H S Sura, J Magnay, D Green, R O Oreffo, J P Dobson, and A J El Haj. Controlled differentiation of human bone marrow stromal cells using magnetic nanoparticle technology. *Tissue Eng Part A*, 16(10):3241–3250, 2010.

[6] Dong-Hyun Kim, Elena a Rozhkova, Ilya V Ulasov, Samuel D Bader, Tijana Rajh, Maciej S Lesniak, and Valentyn Novosad. Biofunctionalized magnetic-vortex microdiscs for targeted cancer-cell destruction. *Nature materials*, 9(2):165–71, feb 2010.

[7] Selma Leulmi Pichot, Sabrina Bentouati, Saif S. Ahmad, Marios Sotiropoulos, Raj Jena, and Russell Cowburn. Versatile magnetic microdiscs for the radio enhancement and mechanical disruption of glioblastoma cancer cells. *RSC Advances*, 10(14):8161–8171, 2020.

[8] Rhodri Mansell, Tarun Vemulkar, Dorothée C. M. C. Petit, Yu Cheng, Jason Murphy, Maciej S. Lesniak, and Russell P. Cowburn. Magnetic particles with

perpendicular anisotropy for mechanical cancer cell destruction. *Scientific Reports*, 7(1):4257, 2017.

[9] QA A Pankhurst, J Connolly, S K Jones, and J Dobson. Applications of magnetic nanoparticles in biomedicine. *Journal of Physics D-Applied Physics*, 36(13):R167–R181, 2003.

[10] Quentin A. Pankhurst, N. T. K. Thanh, S. K. Jones, and Jon Dobson. Progress in applications of magnetic nanoparticles in biomedicine. *Journal of Physics D: Applied Physics*, 42(22):224001, nov 2009.

[11] T. Vemulkar, E. N. Welbourne, R. Mansell, D. C. M. C. Petit, and R. P. Cowburn. The mechanical response in a fluid of synthetic antiferromagnetic and ferrimagnetic microdiscs with perpendicular magnetic anisotropy. *Applied Physics Letters*, 110(4):042402, 2017.

[12] T Vemulkar, R Mansell, D C M C Petit, R P Cowburn, and M S Lesniak. Highly tunable perpendicularly magnetized synthetic antiferromagnets for biotechnology applications. *Applied Physics Letters*, 107(1):012403, jul 2015.

[13] Elina A Vitol, Valentyn Novosad, and Elena A Rozhkova. Microfabricated magnetic structures for future medicine: from sensors to cell actuators. *Nanomedicine*, 7(10):1611–1624, 2012.

[14] N. Wang, J.P. P Butler, and D.E. E Ingber. Mechanotransduction across the cell surface and through the cytoskeleton. *Science (New York, N.Y.)*, 260(5111):1124–1127, 1993.

[15] George M. Whitesides. Self-Assembly at All Scales. *Science*, 295(5564):2418–2421, mar 2002.

Chapter 9

List of publications

- *The mechanical response in a fluid of synthetic antiferromagnetic and ferrimagnetic microdiscs with perpendicular magnetic anisotropy*, T. Vemulkar, **E. N. Welbourne**, R. Mansell, D. C. M. C. Petit, and R. P. Cowburn, Appl. Phys. Lett. 110, 042402 (2017)
- *High-yield fabrication of perpendicularly magnetised synthetic antiferromagnetic nanodiscs*, **E. N. Welbourne**, T. Vemulkar, and R. P. Cowburn, under review

Appendix A

Supplementary Figures to Chapter 4

Here we present some Figures to supplement the discussion in Section 4.3.3, in which we investigate the presence of AP–AP transitions in strongly coupled SAF thin films.

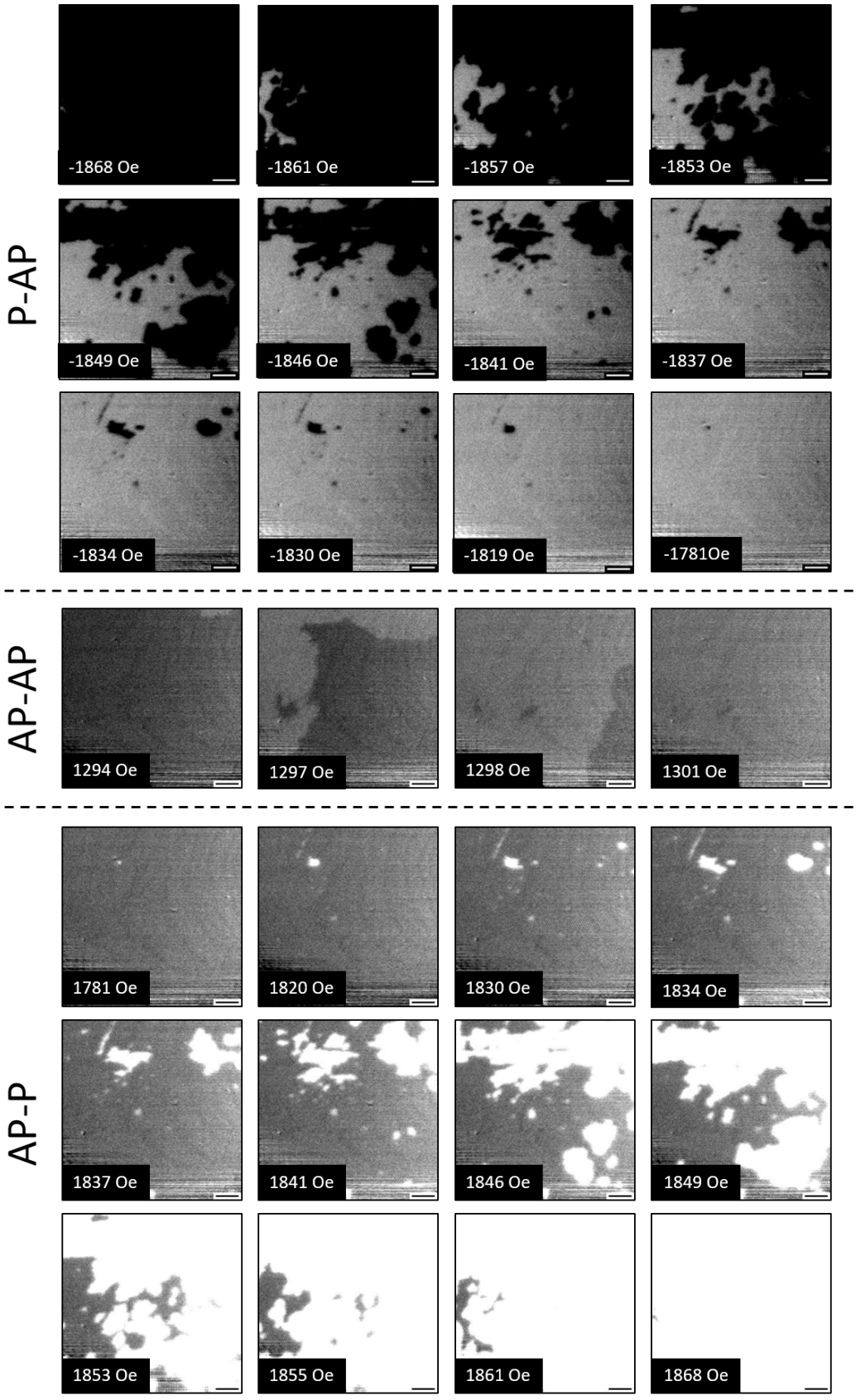

Figure A.1: Domain images of the thin film $Ge/Ta(2)/Pt(2)/CoFeB(0.9)/Pt(0.42)/Ru(0.9)/\ Pt(0.42)/CoFeB(0.9)/Pt(2)/Ta(2)$ during the P–AP, AP–AP and P–AP transitions. The scale bar is 50 μm.